Summer 2026

Gems & Gemology

Volume LXII

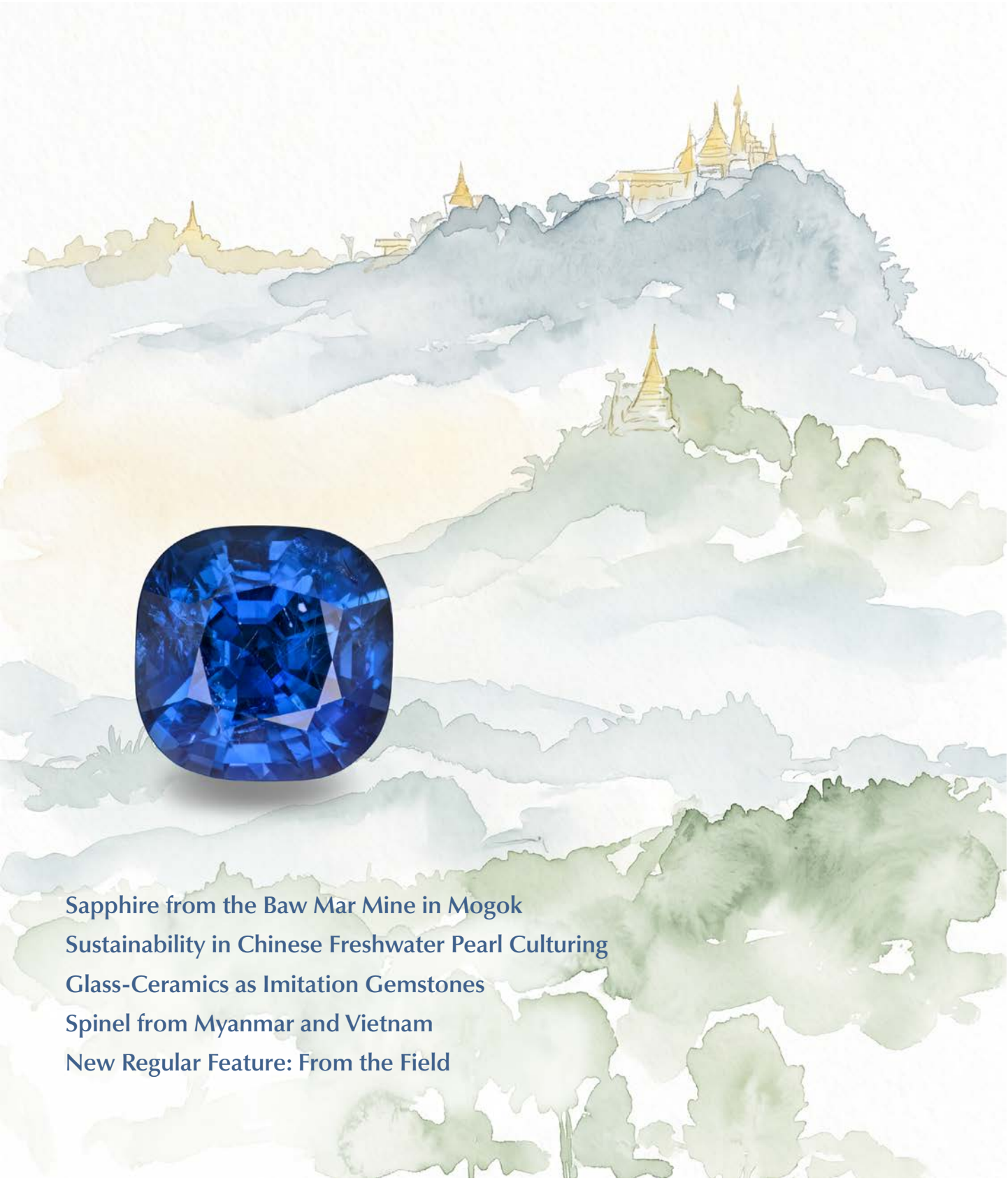

Sapphire from the Baw Mar Mine in Mogok
Sustainability in Chinese Freshwater Pearl Culturing
Glass-Ceramics as Imitation Gemstones
Spinel from Myanmar and Vietnam
New Regular Feature: From the Field

The Quarterly Journal of the Gemological Institute of America

GEMS & GEMOLOGY

Summer 2026
VOLUME 62, No. 2

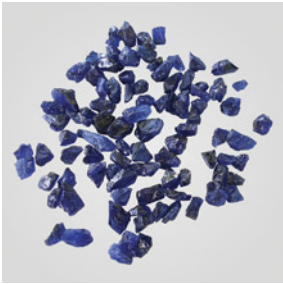

p. 131

p. 179

p. 192

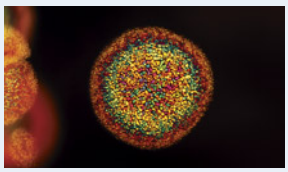

p. 211

p. 215

Editorial

113 Baw Mar Sapphire, China's Freshwater Pearl Industry, Glass-Ceramic Imitation Gemstones, and Red and Orange Spinel from Myanmar and Vietnam
Duncan Pay

Feature Articles

114 Gemological, Geochemical, and Geochronological Study of Sapphire from the Baw Mar Mine in Mogok, Myanmar
Arkar Moe Myint, Pitsanupong Kanjanapayont, Khin Zaw, Karsten Goemann, Jeffrey Oalmann, Abhisit Salam, and Bhuwadol Wanthanachaisaeng
Presents detailed identification characteristics of blue sapphire from the Baw Mar deposit in the Mogok Stone Tract and estimates the timing of the sapphire's formation.

136 Policy-Driven Sustainability in China's Freshwater Pearl Culturing Industry
Qishen Zhou, Yalan Xu, Deyi Xu, Jingping Hu, and Mancun Zhao
Traces the evolution of China's freshwater pearl culturing industry since 1949, exploring how environmental regulation and sustainable development can result in a shift from volume-driven production to higher-quality, environmentally responsible outputs.

164 Glass-Ceramics as Imitation Gemstones: A Study on a Silicon-Aluminum-Magnesium-Zinc System
Wasura Soonthorntantikul, Wim Vertriest, and Karen Avakyan
Characterizes silicon-aluminum-magnesium-zinc glass-ceramics and proposes identification criteria to distinguish these imitations from natural and laboratory-grown gemstones.

178 Characterization of Red and Orange Spinel from Myanmar and Vietnam
Boonyapak Aksorn, Thitiphan Assawincharoenkij, Doan Thi Anh Vu, Dietmar Schwarz, Bhuwadol Wanthanachaisaeng, and Chakkaphan Sutthirat
Examines the gemological properties of red and orange spinel from Mogok, Myanmar, and Lang Chap and An Phu in Vietnam, using trace element chemistry to evaluate geographic origin.

Regular Features

192 From the Field
Travel with GIA's field gemology team to northern Vietnam as they explore local mining and trading communities, revealing the connection between gemstones and their origins.

200 Lab Notes
Atypical color center in natural pinkish brown diamond • Carved natural diamond panther face • Large South Sea bead cultured pearl with *mille-feuille* structure • Microscopic marine organisms in South Sea cultured pearls • Reversible photochromism in a heat-treated Sri Lankan sapphire • Heat-treated red spinel

208 *G&G* Micro-World
Twinned calcite with realgar inclusions • "Fungal hyphae" in a mabe pearl • Leaf-like imprint on non-nacreous pearl • Reticulated pattern on pearls' surfaces • Two-phase inclusion in peridot • Colorful mosaic pattern in heated orange sapphire • "Shooting stars" in sapphire • Vesuvianite in sapphire • Distinctive fluorescent crystal inclusions in spinel • Quarterly Crystal: Chromite in diamond

214 Gem News International
Determination of aquamarine in a Brazilian pegmatite plate • Rare colors of Chinese freshwater cultured pearls • Six-rayed star quartz containing exsolved rutile needles • An unusual yellow raindrop turquoise • In Memoriam: Harold Van Pelt

Editorial Staff

Editor-in-Chief
Duncan Pay

Editorial Manager
Brooke Goedert

Editor
Erica Zaidman

Senior Technical Editor
Jennifer Stone-Sundberg

Technical Editor
Tao Z. Hsu

Assistant Editor
Erin Hogarth

Editors, Lab Notes
Shane F. McClure
Sally Eaton-Magaña
Artitaya Homkrajae

Editors, Micro-World
Tyler Smith
John I. Koivula
Nathan Renfro

Editors, Gem News
Gagan Choudhary
Guanghai Shi

Editor, From the Field
Wim Vertriest

Editors, Colored Stones Unearthed
Aaron C. Palke
James E. Shigley

Editor, Diamond Reflections
Evan M. Smith

Contributing Editors
James E. Shigley
Raquel Alonso-Perez

Editor-in-Chief Emerita
Alice S. Keller

Production Staff

Supervisor, Multimedia Design
Michael Creighton

Multimedia Designer
Christopher Bonine

Photo Producer, Multimedia Designer
Emily Lane

Illustrator
Russel Samson

Video Production
Pedro Padua

Editorial Review Board

Ahmadjan Abduriyim
Tokyo, Japan

Timothy Adams
San Diego, California

Philippe Belley
St. John's, Canada

James E. Butler
Washington, DC

Alan T. Collins
London, UK

Aurélien Delaunay
Paris, France

Dona Dirlam
Redwood Falls, Minnesota

Sally Eaton-Magaña
Carlsbad, California

John L. Emmett
Brush Prairie, Washington

Emmanuel Fritsch
Nantes, France

Eloïse Gaillou
Paris, France

Al Gilbertson
Carlsbad, California

Gaston Giuliani
Nancy, France

Lee A. Groat
Vancouver, Canada

Yunbin Guan
Pasadena, California

George Harlow
New York, New York

Richard W. Hughes
Bangkok, Thailand

Jaroslav Hyršl
Prague, Czech Republic

Dorrit Jacob
Canberra, Australia

A.J.A. (Bram) Janse
Perth, Australia

Mary L. Johnson
San Diego, California

Robert E. Kane
Helena, Montana

Stefanos Karampelas
Thessaloniki, Greece

Lore Kiefert
Lucerne, Switzerland

Simon Lawson
Maidenhead, UK

Ren Lu
Wuhan, China

Thomas M. Moses
New York, New York

Laura Otter
Vienna, Austria

Aaron C. Palke
Carlsbad, California

Ilene Reinitz
Chicago, Illinois

Nathan Renfro
Carlsbad, California

Sudarat Saeseaw
Bangkok, Thailand

Karl Schmetzer
Petershausen, Germany

Andy Shen
Wuhan, China

Guanghai Shi
Beijing, China

Elisabeth Strack
Hamburg, Germany

Nicholas Sturman
Bangkok, Thailand

Tim Thomas
Portland, Oregon

D. Brian Thompson
Florence, Alabama

Fanus Viljoen
Johannesburg, South Africa

Wuyi Wang
New York, New York

Christopher M. Welbourn
Reading, UK

Chunhui Zhou
New York, New York

J.C. (Hanco) Zwaan
Leiden, The Netherlands

GEMS & GEMOLOGY

gia.edu/gems-gemology

Customer Service
(760) 603-4200
gandg@gia.edu

Subscriptions
Copies of the current issue may be purchased for $35.95 plus shipping. Subscriptions are $95.99 for one year (4 issues) in the U.S. and $119.99 elsewhere. Canadian subscribers should add GST. Discounts are available for renewals, group subscriptions, GIA alumni, and current GIA students. To purchase print subscriptions, visit store.gia.edu or contact Customer Service. For institutional rates, contact Customer Service.

Database Coverage
Gems & Gemology's impact factor is 2.4, according to the 2025 Journal Citation Reports by Clarivate Analytics (issued June 2026). *G&G* is abstracted in Thomson Reuters products (Current Contents: Physical, Chemical & Earth Sciences and Science Citation Index—Expanded, including the Web of Knowledge) and other databases. For a complete list of sources abstracting *G&G*, go to gia.edu/gems-gemology, and click on "Publication Information."

Manuscript Submissions
Gems & Gemology, a peer-reviewed journal, welcomes the submission of articles on all aspects of the field. Please see the Author Guidelines at gia.edu/gems-gemology or contact the editors (gandgeditorial@gia.edu). Letters on articles published in *G&G* are also welcome. Please note that Field Reports, Lab Notes, Micro-World, Gem News International, Colored Stones Unearthed, Diamond Reflections, From the Field, Charts, and In the Spotlight are not peer-reviewed sections but do undergo technical and editorial review.

Copyright and Reprint Permission
Abstracting is permitted with credit to the source. Libraries are permitted to photocopy beyond the limits of U.S. copyright law for private use of patrons. Instructors are permitted to reproduce isolated articles and photographs/images owned by *G&G* for noncommercial classroom use without fee. Use of photographs/images under copyright by external parties is prohibited without the express permission of the photographer or owner of the image, as listed in the credits. For other copying, reprint, or republication permission, please contact the editors.

Gems & Gemology is published quarterly by the Gemological Institute of America, a nonprofit educational organization for the gem and jewelry industry.

Postmaster: Return undeliverable copies of *Gems & Gemology* to GIA, The Robert Mouawad Campus, 5345 Armada Drive, Carlsbad, CA 92008.

Our Canadian goods and service registration number is 126142892RT.

Any opinions expressed in signed articles are understood to be opinions of the authors and not of the publisher.

About the Cover

A 7.63 ct sapphire from the Baw Mar deposit in Myanmar is featured on the cover against a watercolor rendering of the Mogok Valley located near the mine. Blue sapphires from this deposit are highlighted in the lead article of this issue. Photo by Robert Weldon; sapphire courtesy of Ye Minn Htoom.

Printing is by L+L Printers, Carlsbad, CA.

GIA World Headquarters The Robert Mouawad Campus 5345 Armada Drive Carlsbad, CA 92008 USA

© 2026 Gemological Institute of America All rights reserved.

ISSN 0016-626X

FSC www.fsc.org MIX Paper from responsible sources FSC® C006300

Baw Mar Sapphire, China's Freshwater Pearl Industry, Glass-Ceramic Imitation Gemstones, and Red and Orange Spinel from Myanmar and Vietnam

Welcome to our Summer 2026 issue! Dip into our feature articles, covering a variety of gem materials from East and Southeast Asia as well as glass-ceramic gem imitations. We also introduce readers to a brand-new column on field gemology.

In our first paper, a team of researchers led by Arkar Moe Myint report on blue sapphires from Baw Mar, Myanmar, highlighting their color, clarity, and unique internal features. The authors use a combination of laser ablation–inductively coupled plasma–mass spectrometry and uranium-lead dating of a zircon inclusion to estimate that the sapphires formed in a magmatic environment 54 to 65 million years ago.

"A new column, From the Field,*…brings a recent Vietnam expedition to vivid life…"*

Next, Dr. Qishen Zhou and colleagues contribute a sustainability study of freshwater pearl culturing in China. Although the world's leader in freshwater pearl culture, much of China's pearl industry has historically generated low profits. Environmental regulations initially posed challenges for producers but also encouraged sustainable practices and better quality, which the authors indicate might present new business opportunities for the industry.

GIA's Dr. Wasura Soonthorntantikul and coauthors present a paper on glass-ceramics—manufactured materials that closely mimic the color and appearance of natural gemstones. The team provides an identification guide, using refractive index, distinct chemistry, and unique infrared and luminescence features that remain consistent across a wide variety of gem imitations.

In our final article, Boonyapak Aksorn and fellow researchers examine red and orange spinel from Myanmar and Vietnam, finding that the gems share similar basic properties but differ in chemical makeup. While trace elements can help identify origin, the authors note that distinguishing some orange spinels remains challenging.

A new column, *From the Field*, offers a firsthand look at GIA's field gemology expeditions, where geologists connect with local mining communities to better understand the gemstones, their origins, the people behind their production, and their journey to market. During these expeditions, the team gathers samples for GIA's reference collection to support origin determination and other studies. In this installment, the column brings a recent Vietnam expedition to vivid life through dramatic photographs, short videos, and captions documenting the local mining and trading scene.

Our regular sections offer a variety of noteworthy content as well. Interesting gem materials featured in *Lab Notes* include a natural diamond carved to resemble a panther's face, an enormous cultured pearl measuring more than 40 millimeters, and a heated red spinel submitted as a ruby. Some of the wonders revealed in this iteration of *Micro-World* are "fungal hyphae" in a mabe pearl, colorful mosaic patterns and "shooting stars" in sapphire, and distinctive fluorescent inclusions in spinel. Our *Gem News International* section documents rare Chinese freshwater cultured pearl colors, a six-rayed star quartz, and more.

We hope you enjoy this issue's content!

Duncan Pay | Editor-in-Chief | dpay@gia.edu

Gemological, Geochemical, and Geochronological Study of Sapphire from the Baw Mar Mine In Mogok, Myanmar

Arkar Moe Myint, Pitsanupong Kanjanapayont, Khin Zaw, Karsten Goemann, Jeffrey Oalmann, Abhisit Salam, and Bhuwadol Wanthanachaisaeng

This study presents detailed fingerprinting studies to characterize blue sapphire from the Baw Mar deposit in the Mogok Stone Tract, Myanmar. These sapphires typically range from 2 to 8 mm, with some reaching up to 15 cm in length. The gem-quality blue sapphires studied often exhibited distinct pleochroism, ranging from greenish blue to violet blue, and were relatively inclusion-free. In some of the samples, microscopic observations revealed multiple twinning planes associated with tiny whitish needle-like inclusions such as boehmite. Unlike sapphires from other Mogok locations, needle-like rutile inclusions were rare in the Baw Mar samples. A critical new observation from this study was the presence of ilmenite silk needles aligned in three distinct directions, or "three-directional ilmenite silk," which may indicate a unique crystallization environment or exsolution mechanism distinct from other sapphire localities. Microscopic observations, combined with spectroscopic and chemical analysis, can be used to distinguish Baw Mar blue sapphires from those found in other localities including different Mogok locations. The trace element variations of Baw Maw sapphires appear to result from magmatic heterogeneity, possibly related to melt evolution, fractional crystallization, or minor interaction with metasomatic fluids within the intrusive host rocks. The observed geochemical signatures in Baw Mar sapphires are best explained by formation in a magmatic system, likely linked to syenitic pegmatite intrusions, with internal chemical variability rather than metamorphic overprinting. Laser ablation–inductively coupled plasma–mass spectrometry and uranium-lead dating of a single zircon inclusion in one sapphire sample suggests that the timing of sapphire formation in the Baw Mar area ranged between 54 and 65 million years ago.

Sapphires, particularly blue sapphires, have long held a prominent place in the global gemstone market and continue to attract strong demand and sustained consumer interest. Their enduring appeal is driven by their aesthetic qualities, durability, cultural significance, and close association with historically important gem-producing regions.

In Myanmar, sapphire occurs in both primary deposits (in syenitic pegmatite) and secondary placer deposits (locally called *byon*) along the Mogok Stone Tract, also known as the Mogok Valley. This is one of the most recognized gem fields in the world, renowned for ruby, sapphire, spinel, peridot, and extremely rare minerals such as johachidolite and painite (Thu, 2007; Zaw, 2017). The Mogok Stone Tract is set in the misty and picturesque mountainous region of northern Myanmar. In recent years, several studies have been conducted on sapphire from different regions of Mogok (e.g., Phyu, 2009; Kan-Nyunt et al., 2013; Soonthorntantikul et al., 2017; Chen et al., 2021; Phyu et al., 2021). Sapphires from Mogok are prized for their extraordinary color and remarkable clarity. The Baw Mar deposit has been of particular interest due to the discovery of high-quality sapphires with intense blue color and exceptional clarity (Kan-Nyunt et al., 2013).

See end of article for About the Authors and Acknowledgments.
Gems & Gemology, Vol. 62, No. 2, pp. 114–134,
https://doi.org/10.5741/GEMS.62.2.114
© 2026 Gemological Institute of America

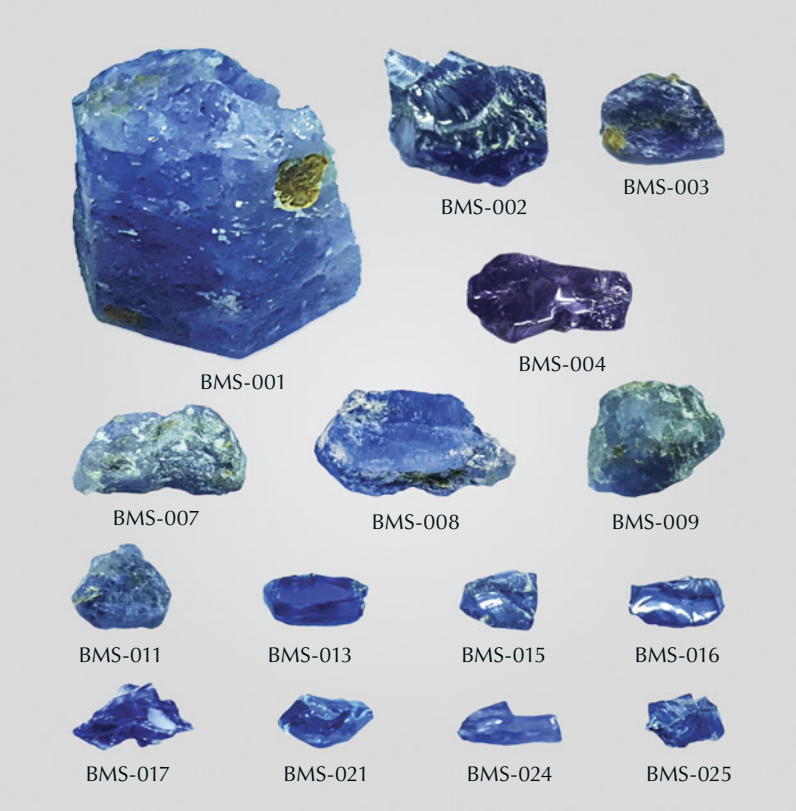

Figure 1. A selection of 15 studied sapphire samples from Baw Mar, ranging from 0.210 to 4.075 ct, as described in table 1. Photos by Arkar Moe Myint.

Baw Mar is located northwest of Kyatpyin village, west of Mogok Township, and 17 km from Mogok (22°55'39.9" N, 96°24'43" E). The deposit is comprised of Baw Mar North and Baw Mar South. The area is surrounded by diverse mountains, shaping it into a basin. The Baw Mar primary deposit lies in the mountain range known locally as the "Koe Wun Tin." Due to its elevation of about 1200 m above sea level, the locality has a relatively cool climate. Subtropical conditions, with an average rainfall of about 200–250 cm annually, result in highly weathered outcrops along the hillsides where mining operations are conducted.

Previous reports have described the Baw Mar mine, the mining techniques employed, and preliminary gemological observations of the sapphires recovered (Kan-Nyunt et al., 2013; Soonthorntantikul et al., 2017). The present article reinforces the existing understanding of this material from previous studies with a combination of standard gemological and microscopic observations with analytical methods, including laser ablation–inductively coupled plasma–mass spectrometry (LA-ICP-MS), Raman spectroscopy, Fourier-transfer infrared (FTIR) spectroscopy, ultraviolet/visible/near-infrared (UV-Vis-NIR) spectroscopy, and scanning electron microscopy equipped with energy-dispersive spectrometry (SEM-EDS) and an automated material identification and classification system (AMICS). The study seeks to refine the characterization of Baw Mar sapphires (figure 1) and establish a preliminary framework for interpreting their origin and timeframe for formation, contributing to a comprehensive genetic and geochronological model.

In Brief

- "Three-directional ilmenite silk" in Baw Mar sapphires may reflect a distinctive crystallization or exsolution history.
- Trace element variations are most consistent with magmatic history, possibly linked to melt evolution, fractional crystallization, and minor metasomatic fluid interaction.
- Uranium-lead dating of a single zircon inclusion in one sapphire sample suggests that Baw Mar sapphire formation occurred between 54 and 65 Ma.

Regional Geology. Geotectonically, the Baw Mar area lies within the Mogok Metamorphic Belt (MMB) (figure 2), which spans in age from the Jurassic to the Miocene and contains numerous primary

Figure 2. Regional geological map of north-central Myanmar, highlighting the study site. The Baw Mar area is situated at the western end of the Mogok Metamorphic Belt. Modified from Barley et al. (2003).

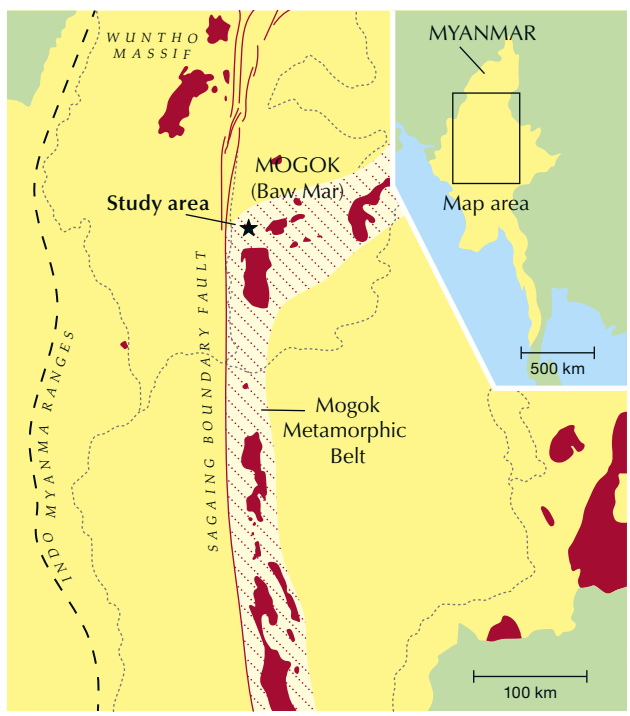

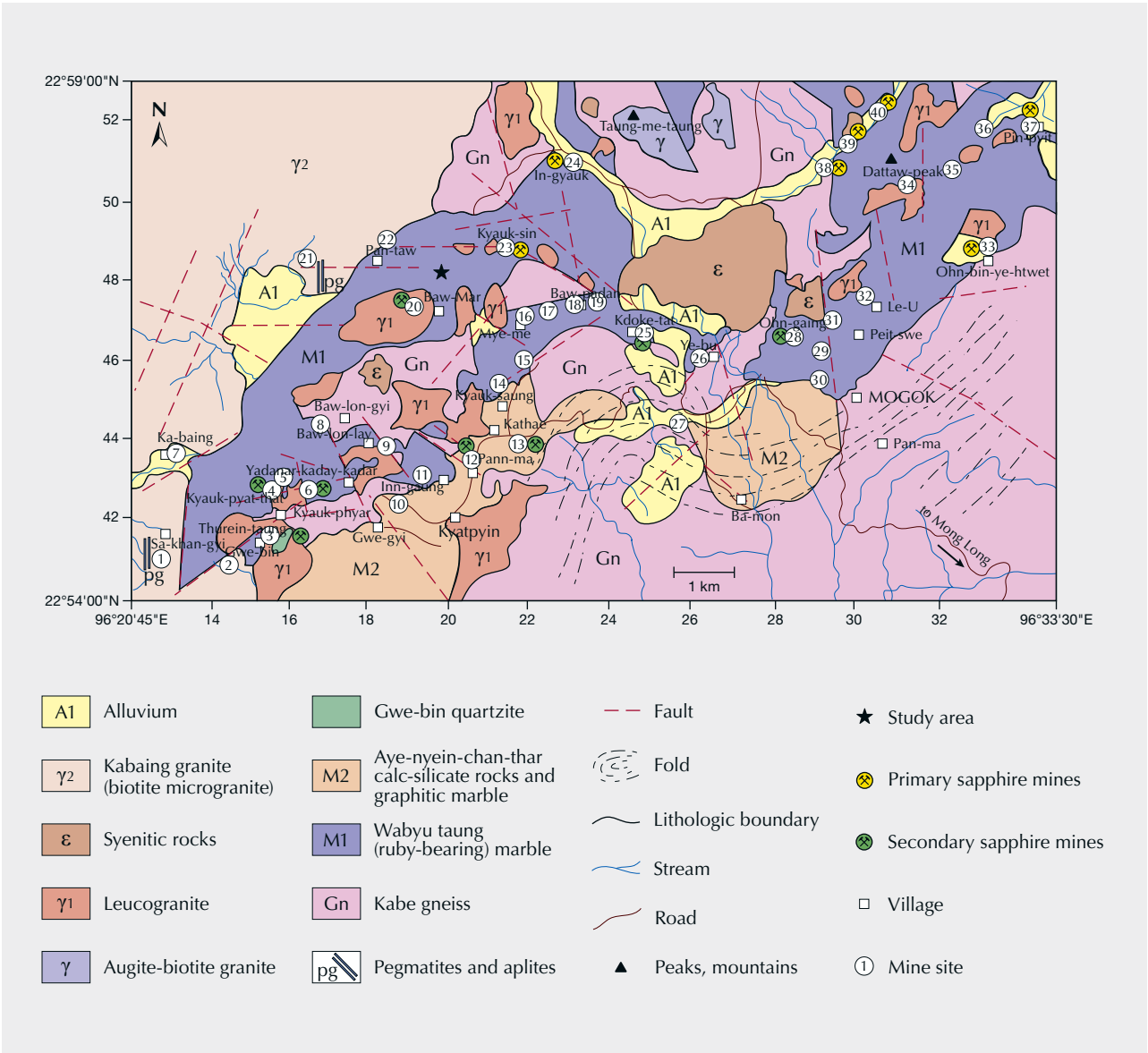

A1	Alluvium		Gwe-bin quartzite	— —	Fault	★	Study area
γ2	Kabaing granite (biotite microgranite)	M2	Aye-nyein-chan-thar calc-silicate rocks and graphitic marble		Fold	⊗	Primary sapphire mines
ε	Syenitic rocks	M1	Wabyu taung (ruby-bearing) marble		Lithologic boundary	⊗	Secondary sapphire mines
γ1	Leucogranite	Gn	Kabe gneiss		Stream	□	Village
γ	Augite-biotite granite	pg	Pegmatites and aplites		Road	①	Mine site
				▲	Peaks, mountains		

Figure 3. Local geological map of the Baw Mar sapphire deposit area. Modified from Zaw et al. (2015), Thu and Zaw (2017), and Chen et al. (2021).

and secondary ruby and sapphire deposits (Barley et al., 2003; Zaw et al., 2015; Searle et al., 2017; Zaw, 2017; Crow et al., 2023). The MMB is characterized by a sequence of magmatic and metasedimentary rocks exhibiting a wide range of metamorphic grades, from low to high grades, culminating in the upper amphibolite-granulite facies. The dominant unit is banded gneiss (with biotite, garnet, sillimanite, and oligoclase), interspersed with quartzite and bands and lenses of marble (Zaw et al., 2015; Thu and Zaw, 2017; Sutherland et al., 2019; Searle et al., 2020; Lamont et al., 2021). Marbles are major host rocks for the highest quality "pigeon's blood" ruby, together with spinel, forsterite, diopside, phlogopite, and graphite. The metamorphic rocks are associated with alkaline rocks (mostly sodic nepheline syenite and syenitic pegmatite), which host exceptionally high-quality royal blue sapphires.

Searle et al. (2020) identified the syenite intrusion host rocks as charnockite-syenite and recorded a wide age range, from Jurassic (170–168 Ma) to late Cretaceous to early Paleocene (~68–63 Ma) and late

Eocene–Oligocene (44–21 Ma) for syenite samples. Min (2016) reported a uranium-lead zircon age of 57.81 ± 0.5 Ma (Lower Paleocene) for the sapphire-bearing nepheline syenite in the Ondan area, 40 km west of the Mogok area. The Mogok metamorphic and syenitic rocks are accompanied by a mafic-ultramafic suite of peridotite, minor gabbro, and norite with unknown ages (Min, 2016). Post-collisional biotite granites near Mogok at Kabaing yielded a uranium-lead zircon age of 19 Ma (Zaw et al., 2015; Searle et al., 2020).

Local Geology. The geological formations in the Baw Mar area comprise metamorphic units including gneiss, calc-silicate, and marble, which have been penetrated by dikes and small intrusions of granitic and syenitic composition (Thu, 2007; Thu and Zaw, 2017; Chen et al., 2021) (figure 3). Granitic rocks include leucogranite and biotite microgranite. The outcrops are limited in extent and poorly exposed. Leucogranite occurs as small pockets associated with sapphire-bearing nepheline syenite and syenitic pegmatite.

Most of the workings consist of small, gently sloping shafts (*al-ter*) and vertical shafts (*lay-bin-twin* or *le bin*) that measure 1.5 × 1.5 m and up to 30 m deep (figure 4, A and B). Non-sapphire-bearing leucogranite dikes and granitic pegmatite veins intruded weathered gneiss, visible at ground level in exposed rock surfaces (figure 4, C and D). The

Figure 4. A: Horizontal shafts that gently slope down through the intruded pegmatitic syenite body at Baw Mar. B: Vertical shafts through the overburden biotite gneiss body to the sapphire-bearing syenitic pegmatite. Both shafts measure 1.5 × 1.5 m. C: A recent view of mining areas at Baw Mar shows small-scale shafts covered with tents. D: Contact between host biotite garnet gneiss and intruded syenitic pegmatite (outlined). The tape measure shown is extended to 1.5 m. Photos by Arkar Moe Myint.

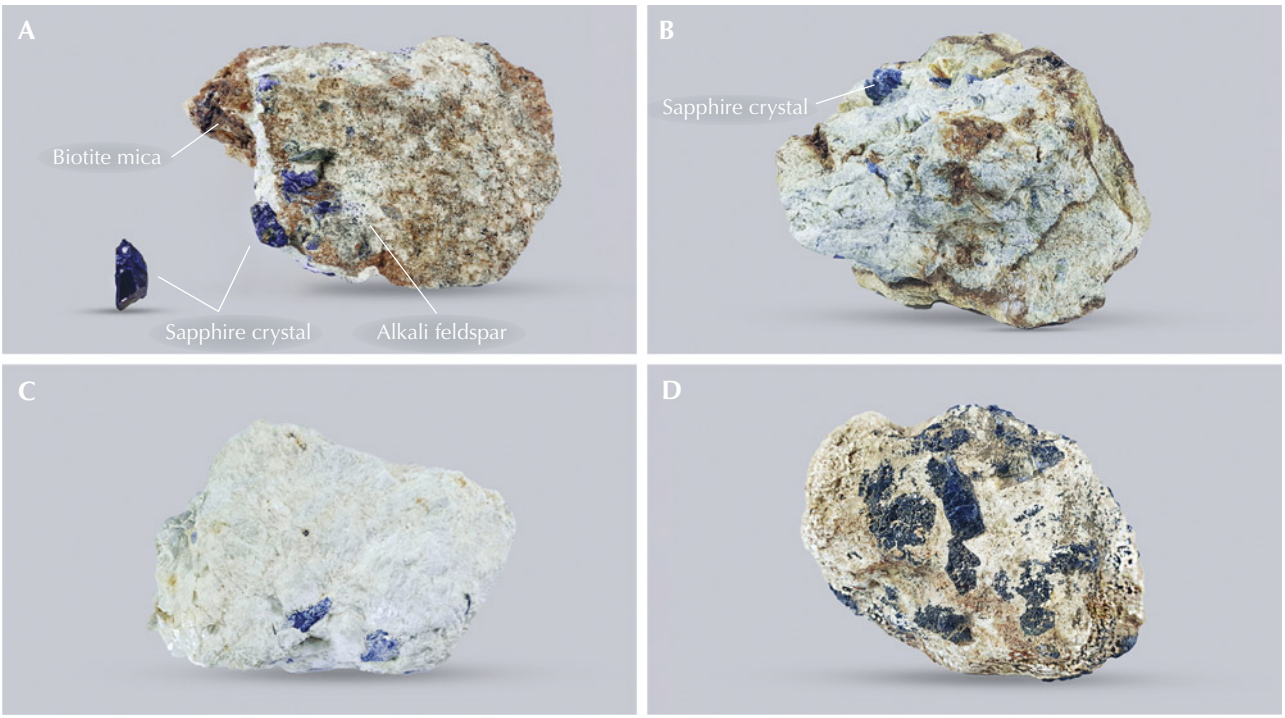

Figure 5. A: Sapphire-bearing syenitic pegmatite from Baw Mar (~55 × 43 × 39 mm) consisting of alkali feldspar, biotite, garnets, and some opaque minerals. The 4.34 ct gem-quality sapphire was extracted from the displayed matrix. B: Syenitic pegmatite (~50 × 46 × 39 mm) with high-quality sapphire crystals. C: Sapphire-bearing kaolinite matrix from Baw Mar (~32 × 30 × 40 mm), a common alteration product of alkali feldspar. D: Sapphire-bearing syenitic pegmatite (~44 × 40 × 40 mm) with some biotite and partially oxidized weathered surfaces. Photos by Arkar Moe Myint.

recently mined area also shows exposed leucogranite in contact with syenite boulders. High-quality blue sapphire is retrieved from this syenite (figure 5, A and B), which, like the pegmatite, has intruded weathered gneiss, as well as from pockets formed at the exposed leucogranite. These sapphires are embedded in clay lenses (feldspar altered to kaolinite) and surrounded by biotite mica and chlorite (figure 5, C and D). They are intimately associated with syenite and are often up to 4 cm in size (figure 6).

Most exposures in the Baw Mar area are highly weathered. The main igneous unit consists of biotite microgranite, which intruded biotite-garnet gneisses and their related rocks. Granitic pegmatites formed small dikes and veins at the margins of the biotite microgranite and the surrounding metamorphic rocks. Some nepheline syenites formed dikes that intruded marble and skarn zones, and these can be found at the contact between igneous intrusions and marble in the Baw Mar area.

Figure 6. Left: A high-quality sapphire crystal from Baw Mar (~15 × 18 × 9 mm) with alkali feldspar matrix. Right: A low-grade translucent sapphire crystal shown by a local miner. Photos by Arkar Moe Myint.

MATERIALS AND METHODS

Samples. For this investigation, a total of 200 sapphires were collected by author AMM from primary deposits at small mines in the Baw Mar area during two field trips in June 2023 and January 2024. Of these, 85 samples (BMS-001 to BMS-045 and BMS-080 to BMS-120) were selected for standard gemological testing and microscopic observation of internal features based on size and diaphaneity (ranging from transparent to translucent). The size, color, and transparency of representative sapphire samples are listed in table 1 (again, see figure 1). Twenty samples (BMS-001 to BMS-015, BMS-023 to BMS-026, and BMS-093) were selected, based on uniformity of color and clarity, for UV-Vis-NIR spectroscopy.

Standard Gemological Testing. Gemological properties of the 85 samples, including refractive index (RI), specific gravity (SG), and UV fluorescence, were determined using standard gemological equipment. A gemological microscope was used to study their internal features.

Spectroscopy. Raman microspectrometry analysis was performed at the Gem and Jewelry Institute of Thailand (GIT) in Bangkok for the identification of inclusions using a Renishaw inVia confocal Raman microscope and a Dilor Super LabRam spectrometer equipped with a holographic notch filter, gratings of 600 and 1800 lines/mm, and a liquid nitrogen-cooled CCD detector (with a resolution of 2000 × 450 pixels).

TABLE 1. Characteristics of representative blue sapphires from Baw Mar.

Sample no.	Weight (ct)	Color	Diaphaneity	UV fluorescence	Inclusions
BMS-001	4.075	Blue	Translucent	Inert to long-wave and short-wave	Graphite, rutile
BMS-002	1.826	Blue	Transparent	Inert to long-wave and short-wave	K-feldspar, mica flakes, rutile
BMS-003	1.203	Blue	Transparent	Inert to long-wave and short-wave	Albite, rutile
BMS-004	0.871	Purplish blue	Transparent	Long-wave: Very weak red Short-wave: Inert	Graphite, rutile, mica flakes
BMS-007	2.625	Blue	Translucent	Inert to long-wave and short-wave	Rutile, apatite, zircon
BMS-008	2.475	Blue	Transparent	Inert to long-wave and short-wave	Zircon?
BMS-009	2.757	Greenish blue	Translucent	Inert to long-wave and short-wave	Graphite, rutile
BMS-011	0.806	Blue	Semitransparent	Inert to long-wave and short-wave	Negative crystals, apatite, graphite
BMS-013	0.264	Blue	Transparent	Inert to long-wave and short-wave	Albite, mica flakes
BMS-015	0.251	Light blue	Transparent	Inert to long-wave and short-wave	Negative crystals, apatite, rutile
BMS-016	0.210	Blue	Transparent	Inert to long-wave and short-wave	Rutile, apatite, zircon
BMS-017	0.357	Blue	Transparent	Inert to long-wave and short-wave	Rutile, apatite, zircon
BMS-021	0.272	Blue	Transparent	Inert to long-wave and short-wave	K-feldspar, negative crystals
BMS-024	0.229	Blue	Transparent	Inert to long-wave and short-wave	Dark flakes, fluid inclusions, mica
BMS-025	0.256	Blue	Transparent	Inert to long-wave and short-wave	Fluid inclusions, fluid fingerprints

Each analysis consisted of a 30 s single accumulation with the sample excited by a 5 mW 514 nm Spectra-Physics 2017 argon-ion laser.

UV-Vis-NIR polarized spectra were collected at GIT using a Cary 5000 spectrophotometer in the 200–800 nm range with a scan speed of 600 nm/min. The 20 selected samples were prepared into wafers with polished surfaces oriented perpendicular to the *c*-axis. The optical path lengths ranged from 1.230 to 4.551 mm and were measured using a Mitutoyo 395-371-32 spherical micrometer (1-inch range, spherical anvil and spindle).

Mineral Identification. At the University of Tasmania's Central Science Laboratory (Sandy Bay, Australia), an FEI MLA650 scanning electron microscope (SEM) with a tungsten source was used to identify the host, associated minerals, and mineral inclusions in nine sapphires (BMS-007, BMS-012, BMS-013, BMS-014, BMS-016, BMS-019, BMS-025, BMS-039, and BMS-099). The samples were mounted in epoxy resin, polished, and coated with a 20 nm layer of carbon. The SEM was equipped with a Bruker Quantax Esprit 1.9.4 energy-dispersive X-ray spectrometry (EDS) system and two XFlash 5030 silicon drift detectors with 133 eV energy resolution. Analytical conditions included an accelerating voltage of 20 kV and a beam current of approximately 7 nA, yielding a total EDS X-ray intensity of around 600,000 cps and a dead time of ~30% on quartz. Data was acquired and processed using Bruker's Automated Material Identification and Classification System (AMICS) software, version 3.0.0.249. Backscattered electron (BSE) imaging contrast and brightness were adjusted on gold metal and epoxy. The Particle Mapping method was used with 512 × 512 pixel imaging resolution, 1.536 mm field of view, and ~4 s acquisition time per frame (corresponding to a pixel size of 3 × 3 μm^2). In addition, a Gatan PanaCL-F detector on the same SEM instrument was used to acquire a cathodoluminescence (CL) image of a single zircon inclusion. This zircon inclusion was later analyzed by LA-ICP-MS and subjected to uranium-lead dating.

Trace Element Analysis and Geochronological Dating. Trace element analyses (ppm to ppb levels) of 10 samples (BMS-001, BMS-003, BMS-007, BMS-009, BMS-014, BMS-023, BMS-024, BMS-025, BMS-028, and BMS-093) were conducted using LA-ICP-MS at GIT. The system paired an iCAP RQ ICP-MS with an NWR-213 LA device operating at a wavelength of 213 nm. The laser conditions included a 55 μm diameter laser spot size, a fluence of ~10 J/cm^2, and a repetition rate of 10 Hz. Three spots were analyzed for each sample. The ICP-MS was operated at a forward power of ~1550 W, with a typical helium carrier gas flow of 0.75 L/min and an argon plasma gas flow of 14 L/min. Calibration was performed using NIST 612 and NIST 610 glasses as external standards and aluminum as the internal standard. Total acquisition time was 120 s: 30 s of laser warm-up, 60 s of ablation time, and 30 s of washout, with a 0.03 s integration time. Masses for the following isotopes were measured: ^{9}Be, ^{24}Mg, ^{47}Ti, ^{51}V, ^{53}Cr, ^{57}Fe, and ^{69}Ga.

Sapphire sample BMS-019, which contained the single zircon inclusion (identified by SEM-AMICS), was further analyzed at the Center for Ore Deposit and Earth Sciences (CODES), University of Tasmania. This analysis used an ASI RESOlution S-155 ablation system with a Coherent COMPexPro 110 argon-fluorine excimer laser (193 nm wavelength and 20 ns pulse width), coupled to an Agilent 7900 quadrupole ICP-MS. Details of additional analytical conditions are described in Thompson et al. (2018).

Each analysis on the zircon began with a blank gas measurement, followed by 30 s of analysis time once the laser was switched on. Ten laser spots were ablated using a 30 μm spot diameter, a 5 Hz repetition rate, and an energy density of ~2 J/cm^2. Ablation was performed in a helium atmosphere with a flow rate of 0.35 L/min. The ablated particles and helium gas were mixed with argon gas flowing at 1.05 L/min and nitrogen gas at 2.5 mL/min, respectively, before being carried to the plasma torch. The following isotopes were measured: ^{31}P, ^{49}Ti, ^{56}Fe, ^{89}Y, ^{91}Zr, ^{93}Nb, ^{139}La, ^{140}Ce, ^{141}Pr, ^{146}Nd, ^{147}Sm, ^{153}Eu, ^{157}Gd, ^{159}Tb, ^{163}Dy, ^{165}Ho, ^{166}Er, ^{169}Tm, ^{172}Yb, ^{175}Lu, ^{178}Hf, ^{181}Ta, ^{204}Pb, ^{206}Pb, ^{207}Pb, ^{208}Pb, ^{232}Th, and ^{238}U. Each isotope was measured every 0.25 s except for the lead isotopes, which were measured with a longer counting time of 0.75 s.

Data reduction was performed using LADR software (Halpin et al., 2014; Norris and Danyushevsky, 2018). For each analysis, a subset was selected for quantification. Corrections for downhole fractionation, instrument drift, and mass bias for lead-to-uranium ratios were calculated using zircon 91500, a commonly used reference material for uranium-lead chronology (Wiedenbeck et al., 1995). Instrument drift and mass bias correction factors for the ^{207}Pb/^{206}Pb ratio were calculated using the lead isotopic values of NIST 610 glass (Baker et al., 2004). Trace element abundances in the zircon were calibrated using NIST 610 glass (Jochum

et al., 2011), with ^{91}Zr as the internal standard element and assuming stoichiometric proportions for zircon. The zircon 91500 and the NIST 610 glass calibration standards were analyzed in duplicate at the beginning, end, and every 60 minutes throughout the analytical session.

The calibration of the uranium-lead ages was validated using two standards: the Temora-2 reference zircon (Jochum et al., 2011) and the Plešovice reference zircon (Black et al., 2003), both of which were treated as unknowns. The Temora reference zircon had a measured age of 415.2 ± 2.4 Ma (95% confidence, mean square weighted deviation = 0.40, probability = 0.98) and a published age of 416.8 ± 1.1 Ma by thermal ionization mass spectrometry (TIMS) (Jochum et al., 2011). The Plešovice reference zircon had a measured age of 337.7 ± 2.0 Ma (95% confidence, mean square weighted deviation = 0.36, probability = 0.91) and a published TIMS age of 337.1 ± 0.4 Ma (Sláma et al., 2008).

Trace element abundances measured in the zircon 91500 (calibrated with NIST 610) were within the range of reported values from the GeoReM database. Uranium-lead isotopic data were corrected for common lead using the model lead composition of Stacey and Kramers (1975). Chondrite normalization was applied using the values from Sun and McDonough (1989) for trace element analyses and data handling.

Tera-Wasserburg concordia plots of $^{238}U/^{206}Pb$ versus $^{207}Pb/^{206}Pb$ were generated using an in-house application designed by CODES. The Tera-Wasserburg concordia plot is a graphical method used in uranium-lead geochronology to interpret isotopic data, particularly for the mineral zircon. It was introduced by F. Tera and G.J. Wasserburg in 1972 as a more precise way to display and correct radiogenic lead loss in uranium-lead isotopic systems. This app was written in R, utilizing IsoplotR software (Vermeesch, 2018). Since the analyzed ages obtained from all 10 laser spots were <1.5 Ga, $^{206}Pb/^{238}Pb$ ages are reported, with no ^{207}Pb correlation age.

RESULTS

Gemological Properties. The samples ranged from light blue to blue to violet blue. They had an RI of 1.760–1.768 (birefringence 0.008) and SG values ranging from 3.99 to 4.10. Nearly all the samples were inert to both long- and short-wave UV radiation because of their high iron trace element content (again, see table 1). Most showed distinct pleochroism under a dichroscope, though pleochroism was very weak and indistinct in some cases.

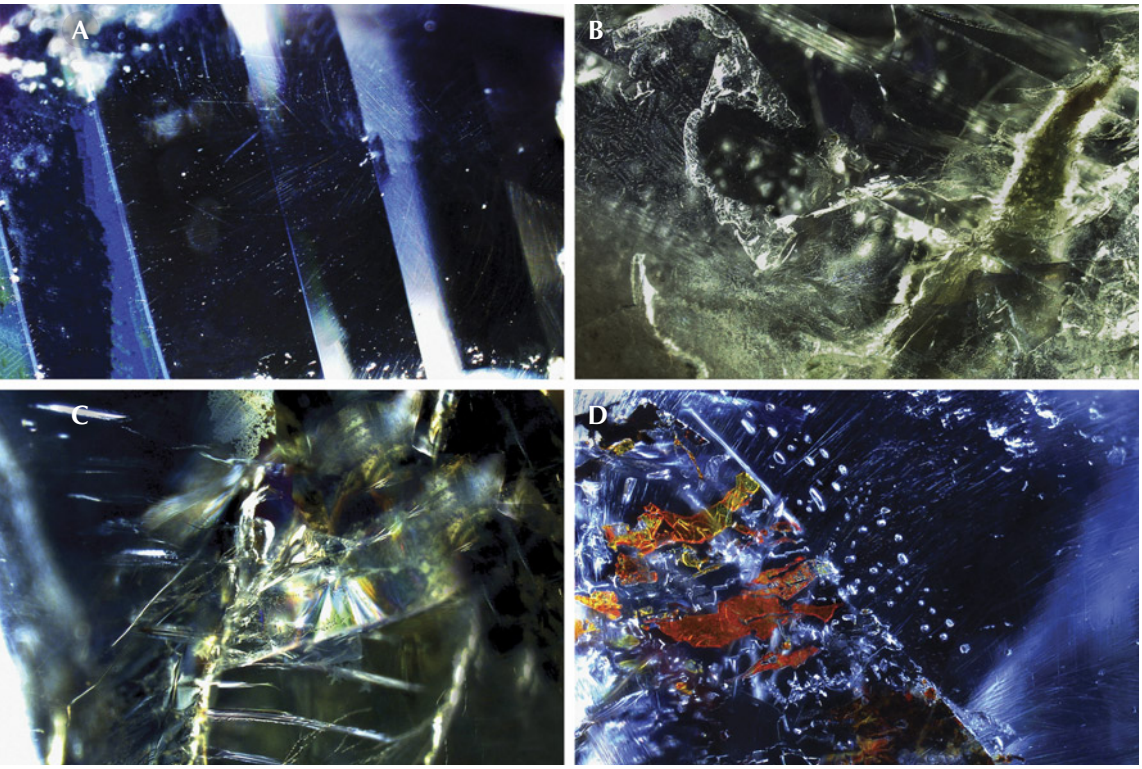

Figure 7. Internal features in sapphires from Baw Mar. A: Multiple twinning (sample BMS-003). B: Twin planes with epigenetic boehmite imprints (BMS-003). C: Thin films displaying iridescence in oblique illumination (BMS-006). D: Healed fissures filled with iron oxide fragments (BMS-011), shown in oblique and darkfield illumination. Photomicrographs by Arkar Moe Myint; fields of view 2.15 mm (A), 1.79 mm (B), 1.89 mm (C), and 1.04 mm (D).

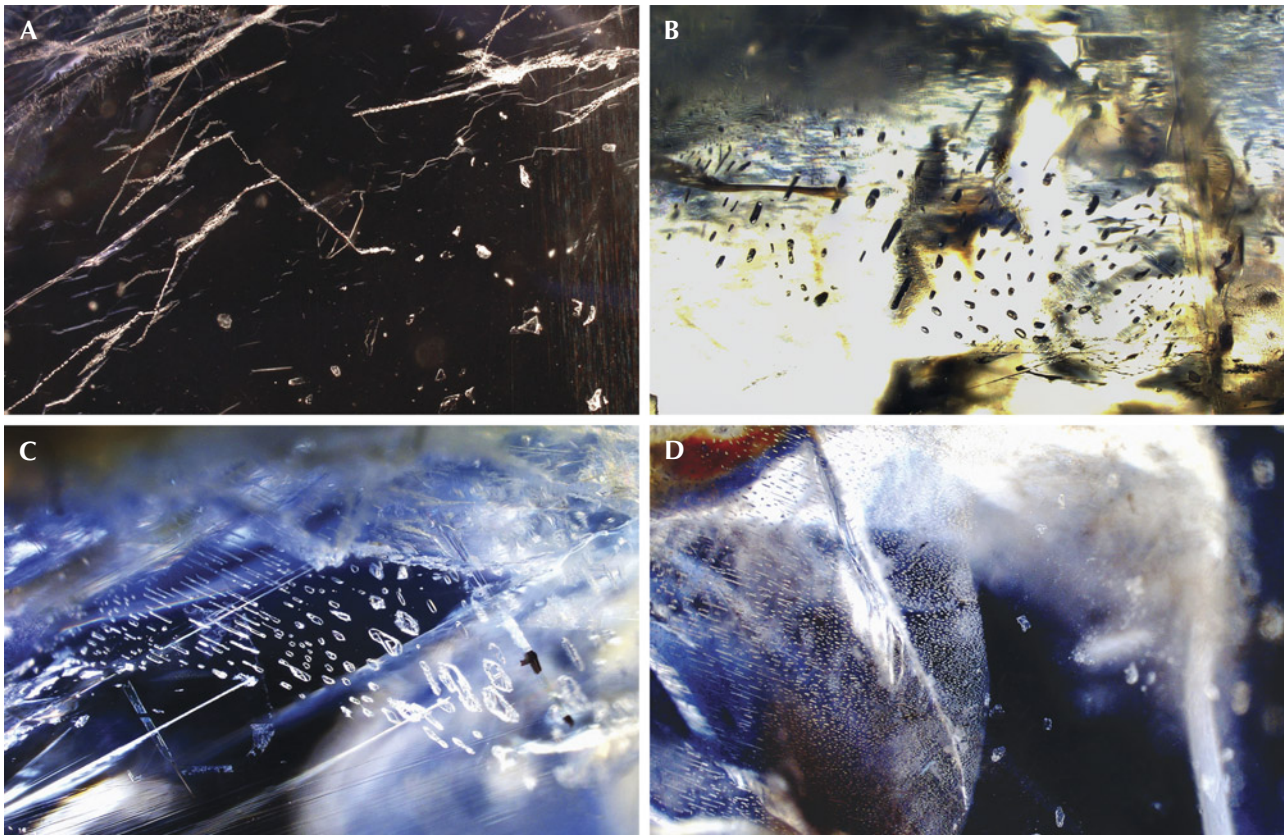

Figure 8. More internal features in sapphires from Baw Mar. A: Colorless negative crystals and whitish stringers (sample BMS-007). B: Two-phase fluid inclusions (BMS-012). C: Multi-phase inclusions (BMS-016). D: Fluid fingerprints (BMS-016), shown in oblique and darkfield illumination. Photomicrographs by Arkar Moe Myint; fields of view 1.65 mm (A), 0.75 mm (B), 0.97 mm (C), and 2.38 mm (D).

Internal Features. Microscopic observation revealed that the Baw Mar samples shared many of the inclusions seen in "classic" Mogok blue sapphires (Themelis, 2008; Giuliani et al., 2014; Hughes et al., 2017). Under magnification, the samples frequently showed multiple twin planes, usually observed oblique to the sample surfaces (figure 7A). Whitish epigenetic boehmite imprints were found along with many fractures (figure 7B). Tabular negative crystals surrounded by iridescent thin films were often observed (figure 7C). Some of the healed fissures were filled with orange iron oxide fragments and showed unusual colors along the fractures (figure 7D).

Most of the samples contained colorless, distinct negative crystals, and some exhibited arrays of whitish stringers (figure 8A). Two-phase fluid and multi-phase inclusions were also abundant (visible with oblique illumination) and could be mistaken for solid inclusions (figure 8, B and C). Fluid fingerprints, which are common in sapphires from the Mogok Stone Tract, were found in many samples (figure 8D).

Several types of solid inclusions were seen in the Baw Mar blue sapphires. The most common of these were zircon, unidentified opaque black crystals, feldspar, and mica. Reddish brown short needles (probably rutile) were frequently observed with large fluid fingerprints (figure 9A). Transparent, irregularly shaped, and colorless crystals of feldspar were commonly associated with both parallel brownish and dark green micas (magnesium biotite). Some tabular negative crystals were associated with clouds of platy brown mica (figure 9B). Also observed were three-directional sets of short, silk-like ilmenite needles (figure 9C). Transparent colorless crystals of zircon appeared as either single crystals or in clusters, usually with fingerprints or tension fractures (figure 9D).

Raman Spectroscopy. The Baw Mar samples displayed Raman shifts consistent with those of sapphires from across the Mogok region. This suggests that Raman spectroscopy has a limited role in determining the specific origin of Burmese sapphires.

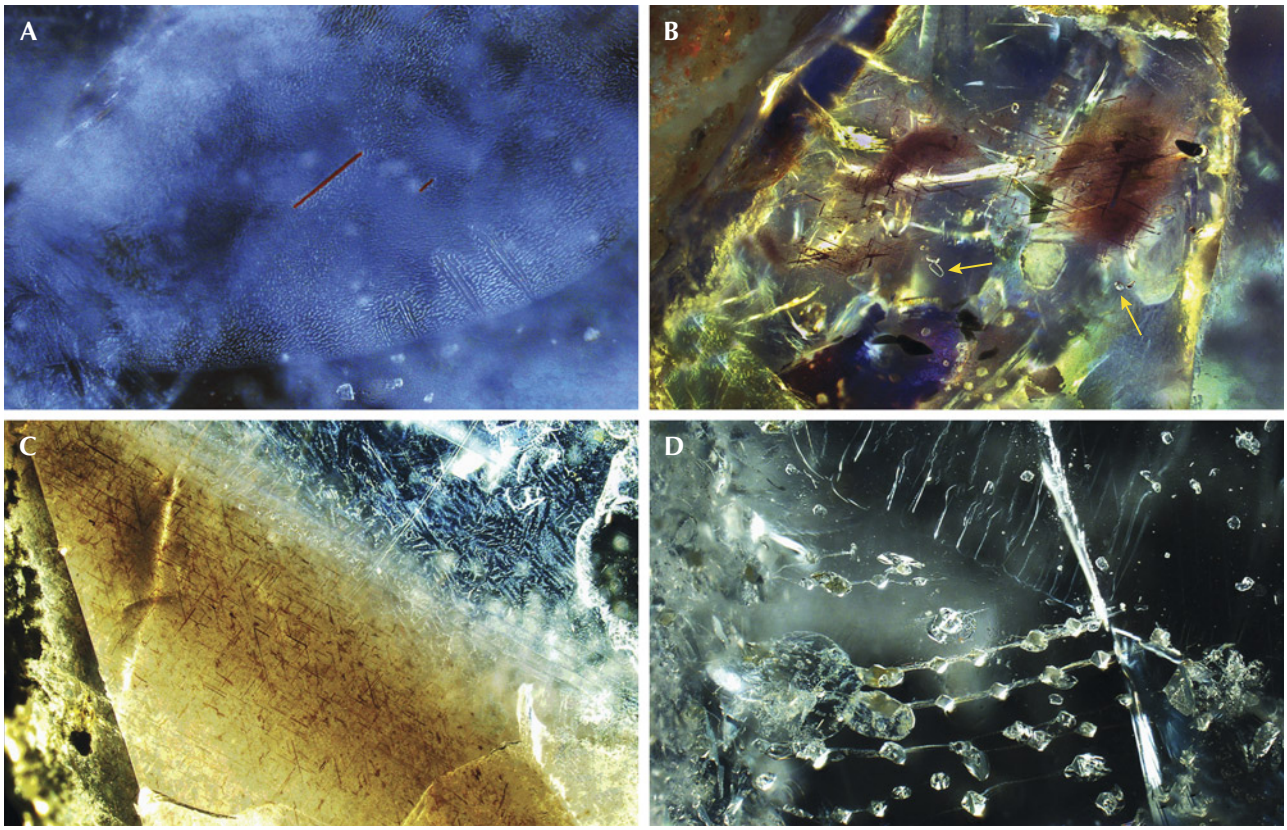

Figure 9. Solid inclusions in sapphires from Baw Mar. A: Reddish brown short rutile needles (identified by Raman) associated with a fluid fingerprint in sample BMS-025. B: Transparent, irregular-shaped, and colorless alkali feldspar (indicated by arrows) associated with brownish and platy dark green mica (magnesium biotite) in sample BMS-039. C: Three-directional sets of short, silk-like ilmenite needles in sample BMS-099 (identified by Raman). D: Arrays of zircon inclusions with tension halos and fractures in sample BMS-019, shown in oblique and darkfield illumination. Photomicrographs by Arkar Moe Myint; fields of view 0.87 mm (A), 1.66 mm (B and D), and 3.45 mm (C).

UV-Vis-NIR Spectroscopy. UV-Vis-NIR spectra were very similar across the entire set of samples. Example UV-Vis-NIR spectra from sample BMS-014 (figure 10) exhibited prominent Fe^{3+} absorption features, with a significant shoulder at 330 nm and distinct peaks at 377, 388, and 450 nm. Notably, the peak at 388 nm is higher than the 377 nm peak in the o-ray, while the opposite is observed in the e-ray. Additionally, a broad band centered at 580 nm in the o-ray and at 700 nm in the e-ray can be attributed to Fe^{2+}-Ti^{4+} intervalence charge transfer. Moreover, the o-ray spectrum displays a weak broadband at about 870 nm, associated with Fe^{2+}/Fe^{3+} clusters (Kan-Nyunt et al., 2013). Unlike other classic Mogok sapphires, the Baw Mar samples display high Fe^{3+} absorption peaks in the violet and blue regions, and most also show an intense shoulder near 340 nm.

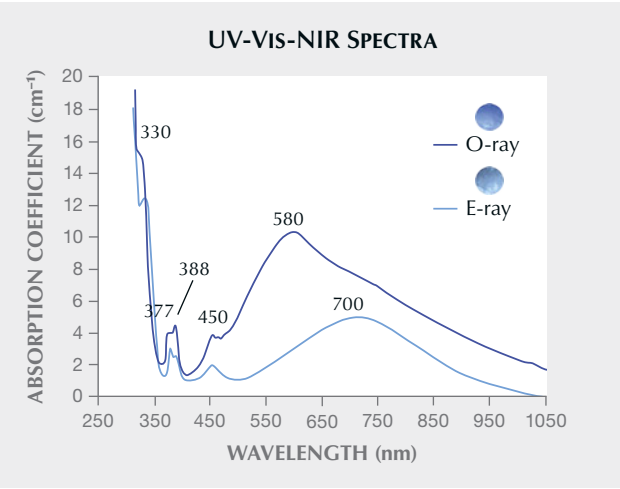

Figure 10. Polarized UV-Vis-NIR spectra of sample BMS-014, with inset color-calibrated polarized photos of the beam path area (blue and light greenish blue dichroism). The 0.25 ct sample has an optical path length of 2.234 mm.

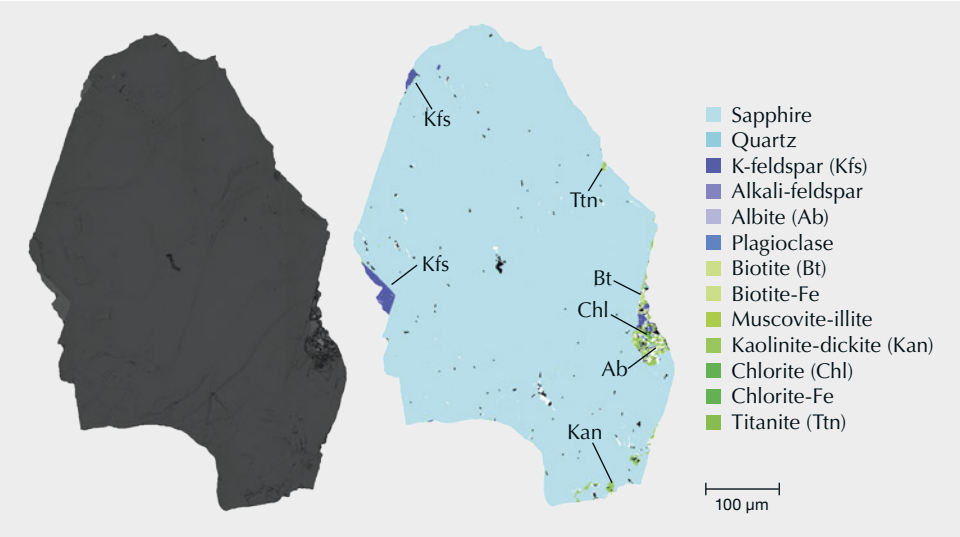

Figure 11. SEM-BSE image and AMICS mineral map of albite, K-feldspar, kaolinite, chlorite, titanite, and biotite mineral inclusions in the matrix of sample BMS-039.

The intensity of the Fe^{2+}/Fe^{3+} bands in the near-infrared region varies significantly and can sometimes be mistaken for the spectra of basaltic sapphires (Kan-Nyunt et al., 2013).

SEM-EDS. SEM-EDS automated mineralogical analyses identified molybdenite, chlorite, baddeleyite, hercynite, and pyrite as associated minerals. The BSE images and mineral maps are shown in figures 11 and 12.

LA-ICP-MS. The results of LA-ICP-MS trace element analyses for 10 blue sapphires from Baw Mar are summarized in table 2. Sample BMS-093 had distinctly different trace element ranges than the other nine samples, and therefore this sample has been excluded when discussing ranges. All of them exhibited relatively high iron contents, ranging from 944 to 2880 ppm. Magnesium content in most samples was low, ranging from 5.8 to 12.5 ppm, while gallium concentrations were moderate at 36.9 to 64.2 ppm. Vanadium concentrations were generally low, with values ranging from below the detection limit (bdl) to 0.95 ppm. Titanium varied from low to moderate levels of 7.2 to 92.0 ppm. Chromium levels were predominantly below the detection limit. Trace amounts of tungsten were detected in most of the samples but were insignificant. Other high field strength elements (including zircon, niobium, tin, hafnium, tantalum, and thorium) were in most cases either below detection limits or only slightly above.

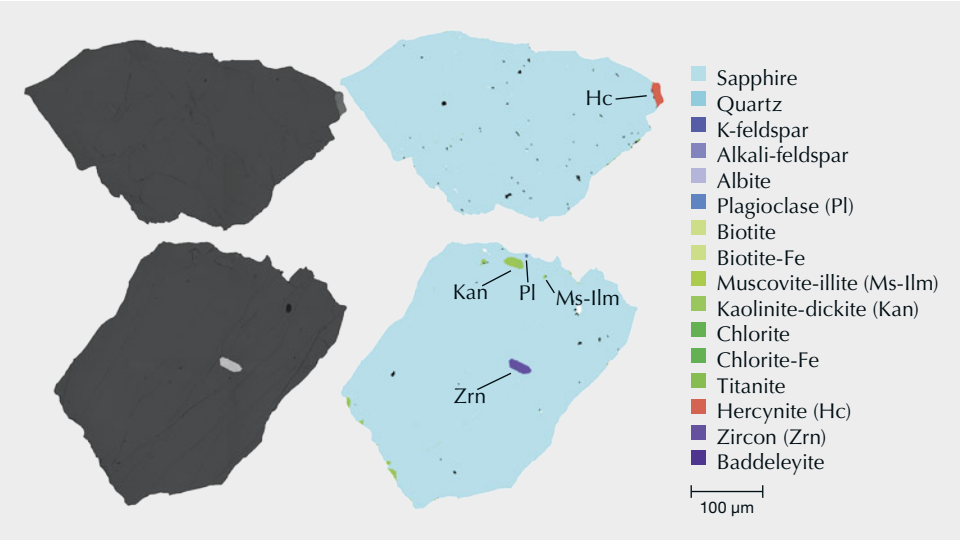

Figure 12. SEM-BSE images and AMICS mineral maps of hercynite, plagioclase, kaolinite, muscovite-illite, and zircon mineral inclusions in the matrix of sample BMS-019.

TABLE 2. Trace element chemistry (in ppm) of blue sapphires from Baw Mar, measured by LA-ICP-MS.

Sample no.	Be	Mg	Ti	V	Cr	Fe	Ga	W	Ga/Mg
	bdl[a]	6.17	20.0	0.93	bdl	2666	59.1	2.9	9.58
BMS-001	bdl	7.05	13.2	0.80	0.1	2480	63.8	3.0	9.04
	bdl	7.01	7.2	0.78	2.1	2606	60.1	2.9	8.58
	bdl	11.48	29.5	0.28	bdl	2702	55.6	2.9	4.84
BMS-003	bdl	12.52	39.1	0.65	bdl	2816	64.2	2.9	5.13
	bdl	11.76	25.2	0.54	0.8	2830	63.2	3.0	5.37
	bdl	5.82	9.2	0.28	bdl	2455	49.6	2.9	8.53
BMS-007	bdl	5.98	16.4	0.64	bdl	2316	47.2	2.9	7.90
	bdl	12.12	26.0	0.61	bdl	2431	49.6	2.9	4.09
	bdl	7.63	11.9	0.25	bdl	2461	56.7	2.9	7.44
BMS-009	bdl	8.09	7.2	0.54	bdl	2657	54.1	2.9	6.69
	bdl	6.72	13.5	0.41	bdl	2336	55.9	3.0	8.32
	bdl	7.29	23.9	0.76	bdl	2634	43.5	2.9	5.98
BMS-014	bdl	7.94	20.2	0.52	0.8	2588	48.5	2.9	6.11
	bdl	8.62	13.7	0.71	bdl	2608	50.6	2.9	5.87
	bdl	7.83	15.3	0.49	bdl	2880	47.8	2.9	6.10
BMS-023	bdl	7.79	92.0	0.81	bdl	2972	49.0	2.9	6.30
	bdl	8.20	15.9	0.60	14.8	2809	47.6	2.9	5.80
	bdl	10.14	25.2	0.77	bdl	2549	52.1	2.9	5.14
BMS-024	bdl	8.79	43.0	0.76	0.6	2708	50.3	3.0	5.72
	bdl	8.11	30.5	0.62	bdl	2612	45.6	2.9	5.62
	bdl	7.30	20.2	0.81	bdl	2459	37.1	3.0	5.09
BMS-025	bdl	7.23	34.6	0.95	0.7	2456	36.9	2.9	5.10
	bdl	7.14	23.7	0.79	bdl	2611	37.8	2.9	5.29
	bdl	6.68	18.5	0.81	bdl	2629	46.6	2.9	6.97
BMS-028	bdl	8.18	21.7	0.89	bdl	2610	47.7	2.9	5.83
	bdl	6.89	15.5	bdl	bdl	2499	44.1	2.9	6.40
	bdl	59.34	175.3	27.41	5.2	944	60.8	3.0	1.03
BMS-093	0.98	70.47	160.9	29.34	4.8	959	60.7	2.9	0.86
	bdl	61.01	194.3	30.45	5.0	980	69.9	2.9	1.15
Detection limit (ppm)	0.5	0.04	0.9	0.04	0.4	3	0.1	0.4	—

[a]*bdl = below detection limit.*
Note: Zr, Hf, Ta, and Th were analyzed but below detection limits, and they are not presented in the table.

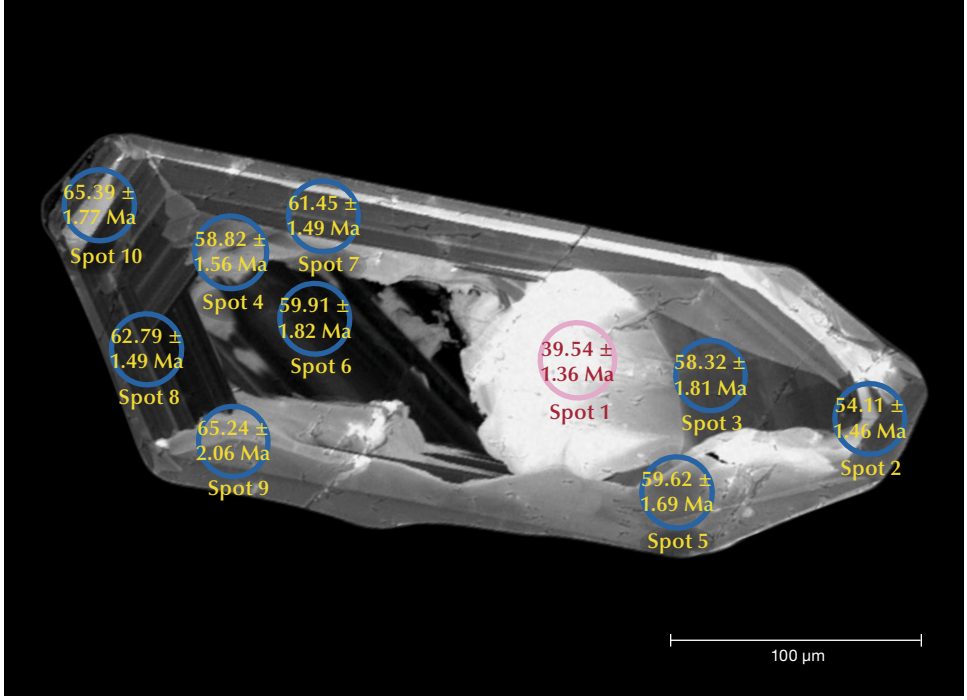

Figure 13. Cathodoluminescence image of a single zircon inclusion in sample BMS-019, showing the locations of the 10 laser ablation spots. Spot 1 is likely due to metamorphic/metasomatic overprint at 40 Ma. The other ages of 54 to 65 Ma on the zircon rims represent the age of the sapphire formation.

Geochronological Data of a Zircon Inclusion. Ten laser ablation spots were analyzed to measure the uranium and lead isotope ratios and the trace element content of the zircon inclusion in sample BMS-019, focusing on the zoning from the rim to the bright core observed by CL imaging. The zircon inclusion's morphology revealed a euhedral prismatic shape with smooth outlines. CL imaging displayed well-defined growth structures (figure 13), allowing the identification of two distinct age groups. The older age group is characterized by concentric zircon rims with overgrown, optically disrupted younger zircon layers. These zircon cores exhibit short prismatic shapes, with dimensions typically ranging from 20 to 27 µm. Fine oscillatory zoning, which represents the youngest growth phase of the inclusion, is often altered and replaced by irregular, dark to bright patches or indistinct gray areas within the zircon structure.

The oldest age, corresponding to the rim analyses from spots 2 to 10, ranges between 54.1 ± 1.6 Ma and 65.4 ± 1.8 Ma. The youngest age was

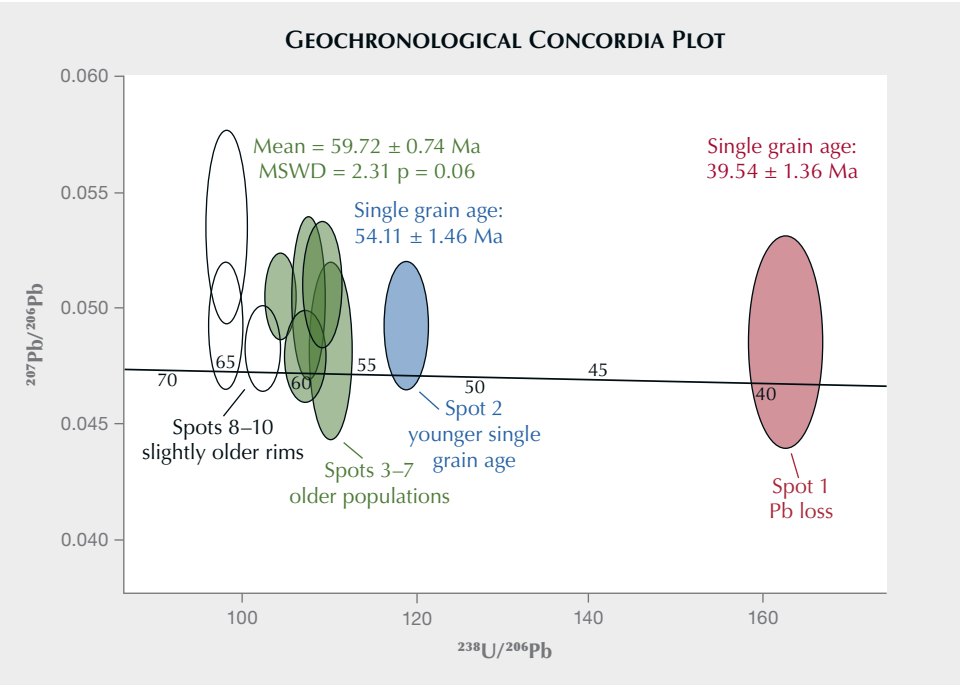

Figure 14. Geochronological concordia plot of analyses from the zircon inclusion in sample BMS-019, showing the ages of populations from the oldest age group. Spot 1 is shown in figure 13 as a bright patch with a homogeneous texture indicating a lead loss, which is likely due to metamorphic/metasomatic overprint at 40 Ma. The other ages of 54 to 65 Ma on the zircon rims represent the age of the sapphire formation. MSWD = mean square of weighted deviates; p = probability of fit.

obtained from spot 1, a CL-bright interior domain of the zircon inclusion, yielding a concordia age of 39.54 ± 1.36 Ma (figure 14). Among all analyzed spots, spot 1 shows the lowest total lead concentration. While its overall pattern is consistent with the other zircon spots, the lower absolute lead abundance and its anomalous young age may reflect a metamorphic/metasomatic overprint event resulting in potential lead loss, or partial metamictization, as suggested by Xu et al. (2012). For a summary of the zircon inclusion's uranium-lead dating results, see supplementary table S1 (https://www.gia.edu/gems-gemology/summer-2026-sapphires-from-baw-mar).

Chondrite-normalized rare earth element (REE) concentrations of the 10 spots are presented in supplementary table S2, and the corresponding spider plot is shown in figure 15.

The 10 spots from the zircon inclusion display a steep positive slope from light to heavy REEs, with strong enrichment of heavy REEs and significant depletion in light REEs. These patterns are consistent with zircon crystallization from a silicate melt, as zircon preferentially incorporates heavy REEs due to their smaller ionic radii and higher charge compatibility into the zircon lattice structure (Hoskin and Schaltegger, 2003). A positive cerium anomaly and a negative europium anomaly are pronounced in all sampled spots. The positive cerium anomaly results from the oxidation of Ce^{3+} to Ce^{4+} under oxidizing magmatic conditions, which enhances its compatibility in zircon compared to trivalent REEs. The negative europium anomaly indicates plagioclase fractionation during magma evolution, where Eu^{2+} is removed preferentially, leaving the melt, and subsequently the zircon, depleted in europium (e.g., Belousova et al., 2002; Sutthirat et al., 2020).

The uniformity in spider plot shapes across all spots suggests a common magmatic origin and supports the interpretation that these zircons crystallized from a syenite to syenite-pegmatitic melt. This is consistent with field observations of pegmatitic textures and their close genetic association with the formation of blue sapphire in Baw Mar.

Thus, the REE distribution and chondrite-normalized REE patterns provide strong evidence for a magmatic origin of the zircon inclusion, consistent with high-temperature crystallization and preservation of its primary geochemical signature.

DISCUSSION

Origin of Baw Mar Sapphire. It is widely accepted that sapphire deposits are formed through metasomatic, metamorphic, or magmatic processes. In small-scale metasomatism, desilication reactions occur primarily between silico-aluminous rocks (e.g., pegmatites and gneisses) and silica-poor rocks (e.g., ultramafic rocks

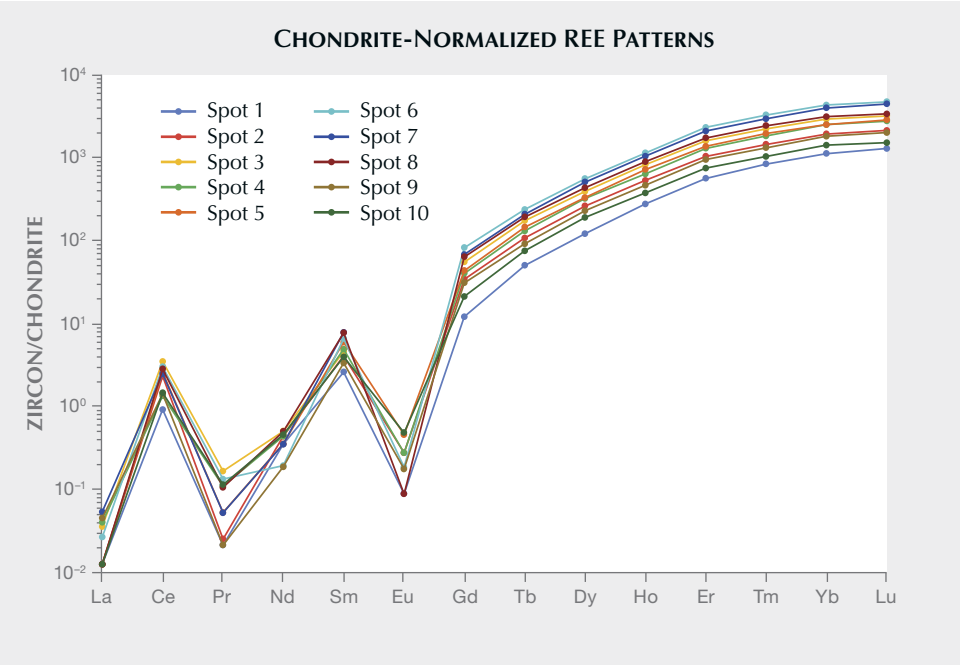

Figure 15. Chondrite-normalized REE patterns of the zircon inclusion in sample BMS-019. Chondrite data from Sun and McDonough (1989).

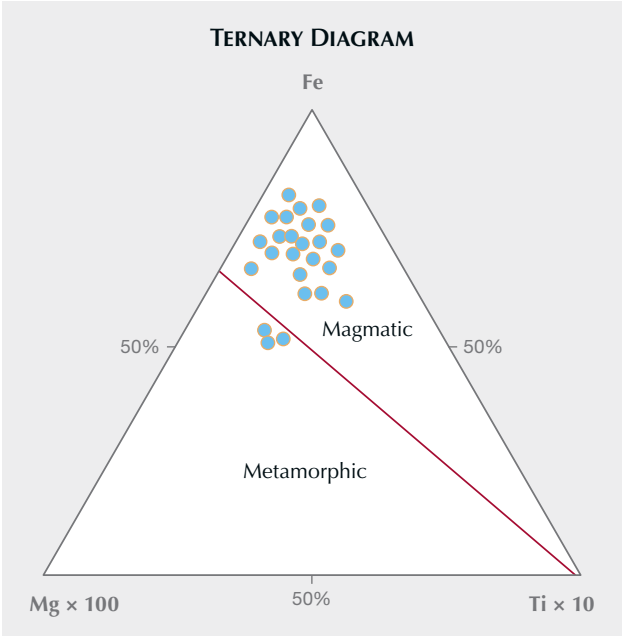

Figure 16. This ternary diagram of Fe vs. (Mg × 100) vs. (Ti × 10) shows that almost all of the sapphires analyzed (except BMS-093) fall within the magmatic field. Modified from Peucat et al., 2007.

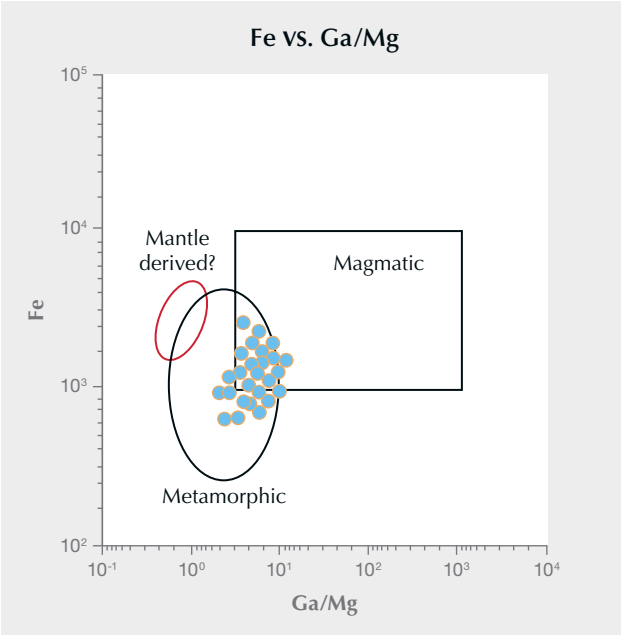

Figure 17. This Fe vs. Ga/Mg plot also indicates that most of the sapphire samples fall within the magmatic field. Modified from Peucat et al., 2007.

and metacarbonates). These reactions result in the formation of sizable sapphire deposits (Sutherland and Coenraads, 1996; Simonet et al., 2008; Sutherland and Abduriyim, 2009; Sutherland et al., 2009, 2015; Giuliani et al., 2014; Harris et al., 2017; Wong et al., 2017; Sutherland and Zaw, 2020).

The iron-magnesium-titanium ternary diagram proposed by Peucat et al. (2007) shows that most Baw Mar sapphires, including those with moderately high magnesium contents, plot consistently within the magmatic field. The exception is sample BMS-093, which lies near the edge of the magmatic domain (figure 16). The gallium-to-magnesium ratios, ranging from approximately 6 to 10, are broadly consistent with sapphires formed from alkaline magmas (Sutherland et al., 2009; Giuliani et al., 2014; Palke et al., 2019) such as syenites or alkali basalts.

Initially, a few samples that plot near or slightly within the metamorphic field on the iron versus gallium-to-magnesium ratio diagram (figure 17) were thought to reflect a later tectono-metamorphic overprint. However, upon further evaluation, the authors found no mineralogical, inclusion-based, or textural evidence (e.g., growth zoning, recrystallization textures, or associated metamorphic minerals) to support this hypothesis. Instead, the trace element variations appear to result from magmatic heterogeneity, possibly related to melt evolution, fractional crystallization, or minor interaction with metasomatic fluids within the intrusive host rocks.

This interpretation is supported by recent work by Belley et al. (2025), which demonstrated that trace element fields for magmatic sapphires can overlap with those traditionally considered metamorphic, especially when corundum crystallizes from partially molten systems. The findings from that study challenge the sharp dichotomy between magmatic and metamorphic geochemical fields, arguing for a more nuanced understanding, particularly in alkali-rich, low-silica systems, where corundum stability is sensitive to small compositional shifts. Therefore, the observed geochemical signatures in Baw Mar sapphire are best explained by formation in a magmatic system, likely linked to syenitic pegmatite intrusions, with internal chemical variability rather than metamorphic overprinting. This conclusion is consistent with field geology and previous studies that identify Baw Mar as a magmatic-related sapphire deposit (Kan-Nyunt et al., 2013; Soonthorntantikul et al., 2017).

Microscopic observations of blue sapphires from Baw Mar revealed a broad range of internal features, many of which are consistent with those found in classic Mogok sapphires mined elsewhere within the region. However, several notable differences suggest distinct geological conditions during crystal growth and post-crystallization history.

Multiple oblique twinning planes are prominent in Baw Mar sapphire. Such twinning planes are similar to those described in classic Mogok and Sri Lankan sapphires, but generally absent in Thai and Australian samples (Hughes et al., 2017; Soonthorntantikul et al., 2021). Healed fissures filled with iron oxide fragments, likely resulting from alteration of sulfide inclusions, are common in Baw Mar sapphire and occasionally found in classic Mogok and Sri Lankan sapphires, but rarely reported in samples from Thailand and Australia, as summarized in table 3 (Ferguson and Fielding, 1971; Hughes and Win, 1995;

TABLE 3. Comparison of internal features of sapphires from Baw Mar and other deposits.

Internal characteristics	Baw Mar (this study)	Baw Mar	"Classic" Mogok	Sri Lanka	Thailand	Australia
Multiple twinning	Abundant	Abundant	Abundant	Frequent	nd[a]	Rare
Healed fissures with Fe-oxide	Abundant	Frequent	Abundant	Rare	nd	nd
Short rutile needles (three directions)	Frequent	Frequent	Abundant	nd	nd	nd
Long rutile silks	nd	nd	Rare	Abundant	Frequent	Abundant
Three-directional ilmenite silk	Frequent[b]	nd	nd	nd	nd	nd
Stressed fractures	nd	Rare	nd	Rare	Abundant	Frequent
Rectilinear zigzag fingerprints	nd	Rare	nd	Abundant	nd	Rare
Negative crystals	Abundant	Abundant	Abundant	Abundant	Frequent	Frequent
Fluid fingerprints	Abundant	Abundant	Abundant	Abundant	Abundant	Abundant
K-feldspar	Abundant	Frequent	Frequent	Rare	Rare	nd
Gahnospinel	nd	nd	Rare	Rare	nd	nd
Green mica (probably Mg-biotite)	Abundant	Rare	Rare	Frequent	Rare	nd
Zircon	Frequent	Frequent	Frequent	Abundant	Rare	Frequent
Pyrochlore	nd	nd	nd	nd	Abundant	Abundant
Pyrite	Rare	Rare	Rare	Abundant	Rare	Rare
Rutile/titanite/monazite	Abundant	Frequent	Abundant	Abundant	Rare	Rare
Molybdenite	Rare	nd	Rare	Frequent	nd	Rare
Chlorite/hercynite	Rare	nd	nd	nd	nd	nd
Baddeleyite	Rare	nd	Rare	nd	nd	nd
Reference	—	Kan-Nyunt et al. (2013); Chen et al. (2021)	Gübelin and Koivula (2005); Themelis (2008); Hughes et al. (2017); Soonthorntantikul et al. (2021)	Hughes et al. (2017); Palke et al. (2019); Palke (2020)	Saeseaw et al. (2017); Palke (2020)	Sutherland and Coenraads (1996); Sutherland et al. (2009); Palke et al. (2019); Palke (2020)

[a]*nd = not detected.*
[b]*New finding from this study.*

Abduriyim and Kitawaki, 2006; Themelis, 2008; Chitty, 2009; Zwaan et al., 2015; Saeseaw et al., 2017; Palke, 2020; Soonthorntantikul et al., 2021).

A critical observation from this study of sapphires from Baw Mar is the presence of needle-like inclusions aligned in three crystallographic directions (again, see figure 9C). These inclusions are morphologically similar to classic rutile silk, which is well documented in sapphires from Mogok, Sri Lanka, and Australia (Giuliani et al., 2014; Hughes et al., 2017; Saeseaw et al., 2017; Soonthorntantikul et al., 2017). However, Raman spectroscopy confirmed that these fine needle-like inclusions forming silk patterns in several Baw Mar sapphires are composed of ilmenite, not rutile. The ilmenite needles are arranged in three distinct crystallographic directions, resembling traditional rutile silk but representing a novel ilmenite-based silk morphology. This structural alignment was observed in ~60% of the highly included samples in this study. Short needle-like ilmenite has previously been described as particles or platelets (Soonthorntantikul et al., 2017). However, three-directional ilmenite needles have not been previously reported as ilmenite silk in either Baw Mar or other Mogok sapphires. The authors therefore propose the term *three-directional ilmenite silk*, which may indicate a unique crystallization environment or exsolution mechanism distinct from other sapphire localities (Kan-Nyunt et al., 2013; Soonthorntantikul et al., 2017; Palke et al., 2019; Chen et al., 2021).

Other inclusion types observed in Baw Mar sapphire—short rutile needles, fluid fingerprints, negative crystals, and multi-phase fluid inclusions—are common features in Mogok and Sri Lankan sapphires. Long rutile silk, which is abundant in Sri Lankan and Australian sapphires, was absent in the Baw Mar samples. Solid inclusions such as zircon, feldspar, biotite, fuchsite, and occasionally molybdenite, chlorite, baddeleyite, hercynite, and pyrite—identified only by SEM-AMICS and assumed to be associated mineral inclusions—further support an igneous or metasomatic origin, consistent with field evidence indicating a pegmatitic or syenitic host rock for Baw Mar sapphire.

The absence of gahnospinel, a common inclusion in Mogok and Sri Lankan stones, and the presence of rare mineral inclusions in Baw Mar specimens highlight the geological uniqueness of this deposit. These micro-features, particularly the three-directional ilmenite silk, may offer an important microanalytical fingerprint for origin determination and advance our understanding of sapphire formation in pegmatitic-syenite-related geological settings.

Timing of Baw Mar Sapphire Formation. The formation of rubies in the Mogok area is believed to have occurred between approximately 32 and 17 Ma, likely linked to high-grade regional metamorphism. Uranium-lead dating of titanite inclusions in Mogok ruby yielded ages of 31–32 Ma, corresponding to the Oligocene (Link, 2016; Zaw et al., 2017). Similarly, secondary ion mass spectrometry (SIMS) uranium-lead dating of titanite from the host marble provided ages of 25.15 ± 0.24 Ma and 25.06 ± 0.22 Ma (Zhang et al., 2021). At the Le Oo mine, uranium-lead titanite ages from ruby-bearing marbles and meta-skarns were determined to be 21 Ma (Searle et al., 2020). Furthermore, uranium-lead ages of zircon inclusions in gem-quality ruby and spinel were found to be 22.26 ± 0.36 Ma and 22.88 ± 0.72 Ma, respectively, while zirconolite yielded uranium-lead ages ranging from approximately 35 Ma to 17 Ma (Phyo et al., 2020).

In contrast, the timing of sapphire formation in the Mogok region remains less constrained. Searle et al. (2020) reported a wide age range from Jurassic (170–168 Ma), the late Cretaceous to early Paleocene (~68–63 Ma), and late Eocene–Oligocene (44–21 Ma) for syenite intrusions in the Mogok area. Min (2016) determined a uranium-lead zircon age of 57.81 ± 0.5 Ma (Lower Paleocene) for the sapphire-bearing nepheline syenite in the Ondan area, 40 km west of the Mogok area. Shi et al. (2021) concluded SIMS uranium-lead dating of acicular rutile inclusions in sapphire at 13.43 ± 0.92 Ma, and furnace step-heating $^{40}Ar/^{39}Ar$ dating of moonstone (antiperthite) in syenites from the MMB yielded ages of 13.43 ± 0.92 and 13.55 ± 0.08 Ma. The rutile ages seem to reflect the remobilization of titanium during metamorphism rather than the actual timing of Mogok sapphire formation. Link (2016) reported a uranium-lead age of 26–27 Ma, while Elmaleh et al. (2019) documented a uranium-lead age of 67 Ma for zircon inclusions in Mogok sapphires. However, neither study includes sufficiently detailed information on sample provenance, geographic coordinates, or spatial distribution in contrast to this research. In this study, uranium-lead isotopic data from the zircon inclusion in Baw Mar sapphire BMS-019 also revealed an unexpected reverse age zoning sequence. The core (spot 1) recorded the youngest age of 39.54 ± 1.36 Ma, while the other spots

yielded older ages (54–65 Ma). In a simple magmatic setting, one would observe the oldest ages at the core, reflecting outward growth of zircon during melt crystallization.

One well-documented mechanism for a reverse age zoning sequence is the selective loss of lead from metamict cores via hydrothermal fluids. These metamict zones in zircon, which are amorphous or highly disordered, are caused primarily by radiation damage from high concentrations of naturally incorporated uranium and thorium within the crystal structure. Over time, alpha decay of these radioactive elements causes cumulative damage to the zircon crystal lattice, leading to the development of a perforated internal structure and microcracks and creating pathways for rapid fluid ingress (Xu et al., 2012) (again, see figure 17).

Radiogenic Pb^{4+} in these damaged sites is reduced to Pb^{2+} by reducing fluids and is leached out (Geisler et al., 2001; Xu et al., 2012). Comparing the total lead concentrations (in ppm) of spot 1 and spots 2–10 shows a suspiciously young $^{206}Pb/^{238}U$ age in the core, while less altered rims preserve the actual crystallization age.

In sodalite syenite from Ejinao, the type locality in south China (Xu et al., 2012), cores were found to be up to ~5 Ma younger than the rims, directly attributed to fluid-induced lead depletion. By analogy, the 39.5 Ma age in BMS-019's core likely reflects hydrothermal overprinting rather than a genuine late crystallization event.

Therefore, the range of ages from the nine spots not in the center of the zircon is interpreted as representing the primary magmatic crystallization interval for this tested zircon (and by extension, the host sapphire) during the Baw Mar syenitic pegmatite formation.

An alternative but not mutually exclusive explanation is secondary zircon recrystallization, whereby a younger zircon growth phase infills along cracks or replaces older cores during a later thermal or metasomatic (hydrothermal) pulse (Rubatto, 2002; Geisler et al., 2007). However, the bright patch (or bright phase) in the zircon grain with a 40 Ma age determination has a homogeneous texture (spot 1) and is therefore consistent with later metamorphic/metasomatic overprint (again, see figures 13 and 14).

Hence, the pronounced reversal of age zoning and the known fluid-rich environment strongly favor a lead-loss model. Therefore, the authors propose that the ages ranging from 54.1 ± 1.6 Ma to 65.4 ± 1.8 Ma, observed in the neatly zoned regions of the zircon, represent the actual timing of sapphire formation in the Baw Mar area.

CONCLUSIONS

The Baw Mar area is located in the high-grade Mogok Metamorphic Belt, which hosts numerous primary and secondary ruby and sapphire deposits, along with those of several other gems. The sapphires at Baw Mar are hosted in syenitic pegmatite that intruded the Proterozoic metamorphic rock sequence. The sapphire sizes range from 2 to 8 mm, with some reaching up to 15 cm (figure 18). Most of the Baw Mar sapphires exhibited internal characteristics that are largely consistent with those documented in previous studies of sapphires from other Mogok origins.

The most common syngenetic inclusions found in the studied Baw Mar sapphires were fluid fingerprints, as well as two-phase fluid and multi-phase inclusions. Epigenetic inclusions typically manifested as boehmite and iron oxide imprints in healed fissures. Furthermore, colorless potassium-feldspar, brownish biotite mica, greenish mica, zircon, rutile, apatite, and ilmenite were observed as protogenetic mineral inclusions, identifiable with microscopy and Raman spectroscopy. An important feature observed in the samples consisted of three-directional ilmenite silk, which may offer a microanalytical fingerprint for origin determination and advance the knowledge of sapphire

Figure 18. High-quality natural rough sapphires recently mined from the Baw Mar area, Mogok, Myanmar, ranging from approximately 5.0 × 3.5 × 4.7 mm to 17.4 × 6.6 × 5.6 mm. Photo by Arkar Moe Myint.

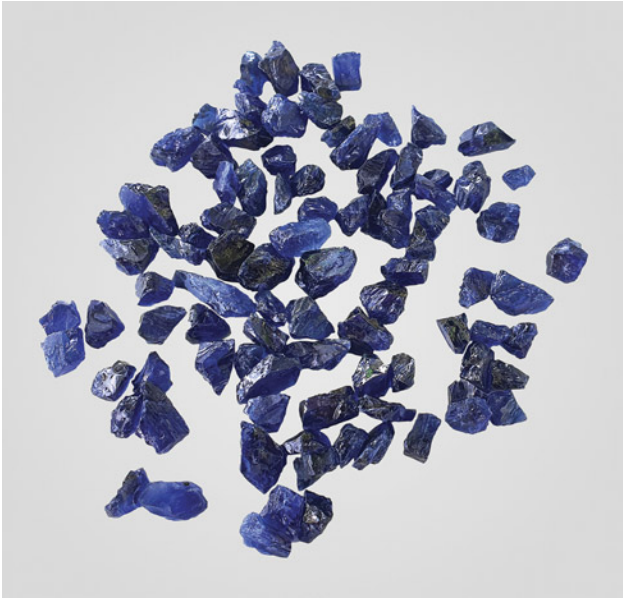

formation in pegmatitic-syenite-related geological settings. According to SEM-AMICS data analysis, biotite, magnesium biotite, chlorite, iron hydroxide, hercynite, pyrite, baddeleyite, and rutile were observed as associated minerals.

Uranium-lead dating ranging from 54.11 ± 1.6 Ma to 65.39 ± 1.77 Ma, observed in the well-defined zoning of the zircon inclusion in sample BMS-019, are interpreted as representing the timing of sapphire formation in Baw Mar. The trace element variations of the studied Baw Maw sapphires appear to result from magmatic processes, possibly related to melt evolution, fractional crystallization, or minor interaction with metasomatic fluids within the intrusive host rocks. Ongoing petrogenetic, geochemical, and geochronological investigations of sapphire-related syenitic pegmatite intrusions in the Baw Mar area will provide valuable new insights into the magmatic and metamorphic evolution of the Mogok Metamorphic Belt.

ABOUT THE AUTHORS

Arkar Moe Myint received a master's degree in geology from Chulalongkorn University in Bangkok and is currently a PhD student at the School of Earth and Environmental Sciences (SEES), Seoul National University, Korea. Dr. Pitsanupong Kanjanapayont is a professor of geology and deputy dean of the Faculty of Science, and Dr. Abhisit Salam is a retired lecturer from the Department of Geology, at Chulalongkorn University. Dr. Khin Zaw is a professor of economic geology at the School of Natural Sciences, Centre of Ore Deposit and Earth Sciences (CODES), Dr. Karsten Goemann is a senior research fellow at the Central Science Laboratory, and Dr. Jeffrey Oalmann is a manager of the CODES Analytical Laboratory, at the University of Tasmania in Sandy Bay, Australia. Dr. Bhuwadol Wanthanachaisaeng is chief of research and standard development at the Gem and Jewelry Institute of Thailand in Bangkok.

ACKNOWLEDGMENTS

The authors express their gratitude to U Thint Lwin, owner of the Baw Mar primary gem deposit, and U Mya Soe and Daw Byar, mine managers, as well as all the miners who allowed access to the gem mines and pits to support sampling. The authors also thank Chakkaphan Sutthirat (Department of Geology, Chulalongkorn University) for valuable suggestions for Baw Mar sapphire genesis continuity aligned with the syenitic melt and crystallization. We are also grateful to Sebastien Meffre and Peerapong Sritangsirikul (CODES, University of Tasmania) for insightful suggestions on zircon inclusion geochronology. Author AMM received study grants and a scholarship from the Association of Southeast Asian Nations (ASEAN) and NON-ASEAN Scholarship Program of the graduate school at Chulalongkorn University. Author PK is funded by the Thailand Science Research and Innovation Fund, Chulalongkorn University (DIS_FF_68_328_2300_089). Author AMM is deeply grateful to Jung-Woo Park (School of Earth and Environmental Sciences, Seoul National University) for his generous support in the extensive revision of this manuscript. Lastly, we would like to thank the peer reviewers for their valuable comments and suggestions, which dramatically improved the article.

REFERENCES

Abduriyim A., Kitawaki H. (2006) Determination of the origin of blue sapphire using laser ablation inductively coupled plasma mass spectrometry (LA-ICP-MS). *Journal of Gemmology*, Vol. 30, No. 1-2, pp. 23–36.

Baker J., Peate D., Waight T., Meyzen C. (2004) Pb isotopic analysis of standards and samples using a ^{207}Pb–^{204}Pb double spike and thallium to correct for mass bias with a double-focusing MC-ICP-MS. *Chemical Geology*, Vol. 211, No. 3-4, pp. 275–303, https://doi.org/10.1016/j.chemgeo.2004.06.030

Barley M.E., Pickard A.L., Zaw K., Rak P., Doyle M.G. (2003) Jurassic to Miocene magmatism and metamorphism in the Mogok metamorphic belt and the India-Eurasia collision in Myanmar. *Tectonics*, Vol. 22, No. 3, article no. 1019, https://doi.org/10.1029/2002TC001398

Belley P.M., Onodenalore O., Abdale L., Groat L.A., Fayek M. (2025) Chemical discrimination of magmatic vs. metamorphic blue corundum: The problem of corundum formed in partial melt and its implications for sapphire exploration and deposit modeling. *Lithos*, Vol. 510-511, article no. 108125, https://doi.org/10.1016/j.lithos.2025.108125

Belousova E., Griffin W., O'Reilly S.Y., Fisher N. (2002) Igneous zircon: Trace element composition as an indicator of source rock type. *Contributions to Mineralogy and Petrology*, Vol. 143, No. 5, pp. 602–622, https://doi.org/10.1007/s00410-002-0364-7

Black L.P., Kamo S.L., Allen C.M., Aleinikoff J.N., Davis D.W., Korsch R.J., Foudoulis C. (2003) TEMORA 1: A new zircon standard for Phanerozoic U–Pb geochronology. *Chemical Geology*, Vol. 200, No. 1-2, pp. 155–170, https://doi.org/10.1016/S0009-2541(03)00165-7

Chen S., Tan H., Zhang C., Teng Y., Zu E. (2021) Study on gemological characteristics of blue sapphires from Baw-Mar Mine, Mogok, Myanmar. *Crystals*, Vol. 11, No. 11, article no. 1275, https://doi.org/10.3390/cryst11111275

Chitty W. (2009) A Study of Sapphires and Rubies from Tanzania's Tunduru District. Bachelor's thesis, Kingston University, Kingston upon Thames, UK.

Crow M., Zaw K., Thu K., Belousov I., Goemann K. (2023) A review of new detrital zircon U-Pb ages from the Mogok area of Myanmar: Implications for the stratigraphy and early tectonic evolution of the Mogok Metamorphic Belt (MMB). *Earth-Science Reviews*, Vol. 242, article no. 104441, https://doi.org/10.1016/j.earscirev.2023.104441

Elmaleh E., Schmidt S.T., Karampelas S., Link K., Kiefert L., Süssenberger A., Paul A. (2019) U-Pb ages of zircon inclusions in sapphires from Ratnapura and Balangoda (Sri Lanka) and implications for geographic origin. *G&G*, Vol. 55, No. 1, pp. 18–28, https://doi.org/10.5741/GEMS.55.1.18

Ferguson J., Fielding P.E. (1971) The origins of the colours of yellow, green and blue sapphires. *Chemical Physics Letters*, Vol. 10, No. 3, pp. 262–265, https://doi.org/10.1016/0009-2614(71)80282-8

Geisler T., Schaltegger U., Tomaschek F. (2007) Re-equilibration

of zircon in aqueous fluids and melts. *Elements*, Vol. 3, No. 1, pp. 43–50, https://doi.org/10.2113/gselements.3.1.43

Giuliani G., Ohnenstetter D., Fallick A.E., Groat L.A., Fagan A.J. (2014) The geology and genesis of gem corundum deposits. In L.A. Groat, Ed., *Geology of Gem Deposits*, 2nd ed., Mineralogical Association of Canada, Short Course Series, Vol. 44, pp. 29–112, https://doi.org/10.3749/9780921294696.ch02

Gübelin E.J., Koivula J.I. (2005) *Photoatlas of Inclusions in Gemstones, Volume 2*. Opinio Verlag, Basel, Switzerland.

Halpin J.A., Jensen T., McGoldrick P., Meffre S., Berry R.F., Everard J.L., Calver C.R., Thompson J., Goemann K., Whittaker J.M. (2014) Authigenic monazite and detrital zircon dating from the Proterozoic Rocky Cape Group, Tasmania: Links to the Belt-Purcell Supergroup, North America. *Precambrian Research*, Vol. 250, pp. 50–67, https://doi.org/10.1016/j.precamres.2014.05.025

Harris S.J., Graham I.T., Lay A., Powell W., Belousova E., Zappettini E. (2017) Trace element geochemistry and metasomatic origin of alluvial sapphires from the Orosmayo Region, Jujuy Province, Northwest Argentina. *Canadian Mineralogist*, Vol. 55, No. 4, pp. 595–617, https://doi.org/10.3749/canmin.1700015

Hoskin P.W.O., Schaltegger U. (2003) The composition of zircon and igneous and metamorphic petrogenesis. *Reviews in Mineralogy and Geochemistry*, Vol. 53, No. 1, pp. 27–62, http://dx.doi.org/10.2113/0530027

Hughes R.W., Win U.H. (1995) Burmese sapphire giants. *Journal of Gemmology*, Vol. 24, No. 8, pp. 551–561.

Hughes R.W., Manorotkul W., Hughes E.B. (2017) *Ruby & Sapphire: A Gemologist's Guide*. RWH Publishing/Lotus Publishing, Bangkok, 816 pp.

Jochum K.P., Weis U., Stoll B., Kuzmin D., Yang Q., Raczek I., Jacob D.E., Stracke A., Birbaum K., Frick D.A., Günther D., Enzweiler J. (2011) Determination of reference values for NIST SRM 610–617 glasses following ISO guidelines. *Geostandards and Geoanalytical Research*, Vol. 35, No. 4, pp. 397–429, https://doi.org/10.1111/j.1751-908X.2011.00120.x

Kan-Nyunt H.-P., Karampelas S., Link K., Thu K., Kiefert L., Hardy P. (2013) Blue sapphires from the Baw Mar mine in Mogok. *G&G*, Vol. 49, No. 4, pp. 223–232, https://doi.org/10.5741/GEMS.49.4.223

Lamont T.N., Searle M.P., Hacker B.R., Htun K., Htun K.M., Morley C.K., Waters D.J., White R.W. (2021) Late Eocene-Oligocene granulite facies garnet-sillimanite migmatites from the Mogok Metamorphic belt, Myanmar, and implications for timing of slip along the Sagaing Fault. *Lithos*, Vol. 386-387, article no. 106027, https://doi.org/10.1016/j.lithos.2021.106027

Link K. (2016) Gem Notes: New age data for blue sapphires from Mogok, Myanmar. *Journal of Gemmology*, Vol. 35, No. 2, pp. 107–109.

Min M. (2016) The Mineralogical and Petrological Aspects of Igneous and Metamorphic Rocks of Ondan-Kyaukhlebein Area. PhD thesis, University of Yangon, Myanmar.

Phyo M.M., Wang H.A.O., Guillong M., Berger A., Franz L., Balmer W.A., Krzemnicki M.S. (2020) U-Pb age dating of zircon and zirconolite inclusions in marble-hosted gem-quality ruby and spinel from Mogok, Myanmar. *Minerals*, Vol. 10, No. 2, article no. 195, https://doi.org/10.3390/min10020195

Norris A., Danyushevsky L. (2018) Towards estimating the complete uncertainty budget of quantified results measured by LA-ICP-MS. Twenty-Eighth Annual Goldschmidt Conference, August 12–17, Boston, p. 1894.

Palke A.C. (2020) Coexisting rubies and blue sapphires from major world deposits: A brief review of their mineralogical properties. *Minerals*, Vol. 10, No. 5, article no. 472, https://doi.org/10.3390/min10050472

Palke A.C., Saeseaw S., Renfro N.D., Sun Z., McClure S.F. (2019) Geographic origin determination of blue sapphire. *G&G*, Vol. 55, No. 4, pp. 536–579, https://doi.org/10.5741/GEMS.55.4.536

Peucat J.J., Ruffault P., Fritsch E., Bouhnik-Le Coz M., Simonet C., Lasnier B. (2007) Ga/Mg ratio as a new geochemical tool to differentiate magmatic from metamorphic blue sapphires. *Lithos*, Vol. 98, No. 1-4, pp. 261–274, https://doi.org/10.1016/j.lithos.2007.05.001

Phyu K.M. (2009) Mineralogical and Petrological Studies of the Rocks of Twinnge Yenya Oo Area, Thabeikkyin Township, Mandalay Division. PhD thesis, University of Yangon, Myanmar.

Phyu K.M., Zaw K., Mernagh T.P, Aung T.Z. (2021) Characterisation and genesis of sapphires from the Yenya-U area, Thabeikkyin Township, Mandalay Region, Myanmar. *Journal of Gemmology*, Vol. 37, No. 8, pp. 802–815.

Rubatto D. (2002) Zircon trace element geochemistry: Partitioning with garnet and the link between U-Pb ages and metamorphism. *Chemical Geology*, Vol. 184, No. 1-2, pp. 123–138, https://doi.org/10.1016/S0009-2541(01)00355-2

Saeseaw S., Sangsawong S., Vertriest W., Atikarnsakul U., Raynaud-Flattot V.L., Khowpong C., Weeramonkhonlert V. (2017) A study of sapphire from Chanthaburi, Thailand and its gemological characteristics. *GIA Research News*, April 19, https://www.gia.edu/gia-news-research/sapphire-chanthaburi-thailand-gemological-characteristics

Searle M.P, Morley C.K., Waters D.J., Gardiner N.J., Htun U.K., Nu T.T., Robb L.J. (2017) Chapter 12: Tectonic and metamorphic evolution of the Mogok Metamorphic and Jade Mines belts and ophiolitic terranes of Burma (Myanmar). *Geological Society, London, Memoirs*, Vol. 48, No. 1, pp. 261–293, https://doi.org/10.1144/M48.12

Searle M.P., Garber J.M., Hacker B.R., Htun K., Gardiner N.J., Waters D.J., Robb L.J. (2020) Timing of syenite-charnockite magmatism and ruby and sapphire metamorphism in the Mogok Valley region, Myanmar. *Tectonics*, Vol. 39, No. 3, article no. e2019TC005998, https://doi.org/10.1029/2019TC005998

Shi G., Zhang X., Wang Y., Li Q., Wu F., He H. (2021) Age determination of oriented rutile inclusions in sapphire and of moonstone from the Mogok metamorphic belt, Myanmar. *American Mineralogist*, Vol. 106, No. 11, pp. 1852–1859, https://doi.org/10.2138/am-2021-7487

Simonet C., Fritsch E., Lasnier B. (2008) A classification of gem corundum deposits aimed towards gem exploration. *Ore Geology Reviews*, Vol. 34, No. 1-2, pp. 127–133, https://doi.org/10.1016/j.oregeorev.2007.09.002

Sláma J., Košler J., Condon D.J., Crowley J.L., Gerdes A., Hanchar J.M., Horstwood M.S.A., Morris G.A., Nasdala L., Norberg N., Schaltegger U., Schoene B., Tubrett M.N., Whitehouse M.J. (2008) Plešovice zircon – A new natural reference material for U-Pb and Hf isotopic microanalysis. *Chemical Geology*, Vol. 249, No. 1-2, pp. 1–35, https://doi.org/10.1016/j.chemgeo.2007.11.005

Soonthorntantikul W., Vertriest W., Raynaud-Flattot V.L., Sangsawong S., Atikarnsakul U., Khowpong C., Weeramonkhonlert V., Pardieu V. (2017) An in-depth gemological study of blue sapphires from the Baw Mar mine (Mogok, Myanmar), *GIA Research News*, February 24, https://www.gia.edu/gia-news-research/blue-sapphires-baw-mar-mine-mogok-myanmar

Soonthorntantikul W., Atikarnsakul U., Vertriest W. (2021) Blue sapphires from Mogok, Myanmar: A gemological review. *G&G*, Vol. 57, No. 4, pp. 292–317, https://doi.org/10.5741/GEMS.57.4.292

Stacey J.S., Kramers J.D. (1975) Approximation of terrestrial lead isotope evolution by a two-stage model. *Earth and Planetary Science Letters*, Vol. 26, No. 2, pp. 207–221, https://doi.org/10.1016/0012-821X(75)90088-6

Sun S.-S., McDonough W.F. (1989) Chemical and isotopic systematics of ocean basalts: Implications for mantle composition and processes. *Geological Society, London, Special Publications*, Vol. 42, pp. 313–345, https://doi.org/10.1144/gsl.sp.1989.042.01.19

Sutherland F.L., Abduriyim A. (2009) Geographic typing of gem

corundum: A test case from Australia. *Journal of Gemmology*, Vol. 31, No. 5-8, pp. 203–210.
Sutherland F.L., Coenraads R.R. (1996) An unusual ruby-sapphire-sapphirine-spinel assemblage from the Tertiary Barrington volcanic province, New South Wales, Australia. *Mineralogical Magazine*, Vol. 60, No. 401, pp. 623–638, https://doi.org/10.1180/minmag.1996.060.401.08
Sutherland F.L., Zaw K. (2020) Editorial for special issue "Mineralogy and Geochemistry of Ruby," *Minerals*, Vol. 10, No. 10, article no. 888, https://doi.org/10.3390/min10100888
Sutherland F.L., Zaw K., Meffre S., Giuliani G., Fallick A.E., Graham I.T., Webb G.B. (2009) Gem-corundum megacrysts from east Australian basalt fields: Trace elements, oxygen isotopes and origins. *Australian Journal of Earth Sciences*, Vol. 56, No. 7, pp. 1003–1022, https://doi.org/10.1080/08120090903112109
Sutherland F.L., Zaw K., Meffre S., Yui T.-F., Thu K. (2015) Advances in trace element "fingerprinting" of gem corundum, ruby and sapphire, Mogok area, Myanmar. *Minerals*, Vol. 5, No. 1, pp. 61–79, https://doi.org/10.3390/min5010061
Sutherland F.L., Zaw K., Meffre S., Thompson J., Goemann K., Thu K., Nu T.T., Zin M.M., Harris S.J. (2019) Diversity in ruby geochemistry and its inclusions: Intra- and inter- continental comparisons from Myanmar and eastern Australia. *Minerals*, Vol. 9, No. 1, article no. 28, https://doi.org/10.3390/min9010028
Sutthirat C., Pisutha-Arnond V., Khamloet P., Assawincharoenkij T. (2020) Multistages of original sapphire formation related to basaltic magmatism in the Bo Phloi basaltic gem field, Kanchanaburi, Western Thailand: Evidence from trace elements and ages of zircons. *Journal of Asian Earth Sciences*, Vol. 187, article no. 104068, https://doi.org/10.1016/j.jseaes.2019.104068
Themelis T. (2008) *Gems & Mines of Mogok*. Self-published, Bangkok.
Thompson J.M., Meffre S., Danyushevsky L. (2018) Impact of air, laser pulse width and fluence on U-Pb dating of zircons by LA-ICPMS. *Journal of Analytical Atomic Spectrometry*, Vol. 33, No. 2, https://doi.org/10.1039/C7JA00357A
Thu K. (2007) The Igneous Rocks of the Mogok Stone Tract: Their Distributions, Petrography, Petrochemistry, Sequence, Geochronology, and Economic Geology. PhD thesis, University of Yangon, Myanmar.
Thu K., Zaw K. (2017) Chapter 23: Gem deposits of Myanmar. *Geological Society, London, Memoirs*, Vol. 48, pp. 497–529, https://doi.org/10.1144/M48.23
Vermeesch P. (2018) IsoplotR: A free and open toolbox for geochronology. *Geoscience Frontiers*, Vol. 9, No. 5, pp. 1479–1493, https://doi.org/10.1016/j.gsf.2018.04.001
Wiedenbeck M., Alle P., Corfu F., Griffin W.L., Meier M., Oberli F., von Quadt A., Roddick J.C., Spiegel W. (1995) Three natural zircon standards for U-Th-Pb, Lu-Hf, trace element and REE analyses. *Geostandards Newsletter*, Vol. 19, No. 1, pp. 1–23, https://doi.org/10.1111/j.1751-908X.1995.tb00147.x
Wong J., Verdel C., Allen C.M. (2017) Trace-element compositions of sapphire and ruby from the eastern Australian gemstone belt. *Mineralogical Magazine*, Vol. 81, No. 6, pp. 1551–1576, https://doi.org/10.1180/minmag.2017.081.012
Xu X.-S., Zhang M., Zhu K.-Y., Chen X.-M., He Z.-Y. (2012) Reverse age zonation of zircon formed by metamictisation and hydrothermal fluid leaching. *Lithos*, Vol. 150, pp. 256–267, https://doi.org/10.1016/j.lithos.2011.12.014
Zaw K. (2017) Chapter 24: Overview of mineralization styles and tectonic–metallogenic setting in Myanmar. *Geological Society, London, Memoirs*, Vol. 48, pp. 531–556, https://doi.org/10.1144/M48.24
Zaw K., Sutherland L., Yui T.-F., Meffre S., Thu K. (2015) Vanadium-rich ruby and sapphire within Mogok Gemfield, Myanmar: Implications for gem color and genesis. *Mineralium Deposita*, Vol. 50, pp. 25–39, https://doi.org/10.1007/s00126-014-0545-0
Zaw K., Swe W., Barber A.J., Crow M.J., Nwe Y.Y. (2017) Chapter 1: Introduction to the geology of Myanmar. *Geological Society, London, Memoirs*, Vol. 48, pp. 1–17, https://doi.org/10.13140/RG.2.2.33577.90723
Zhang D., Guo S., Chen Y., Li Q., Ling X., Liu C., Sein K. (2021) ~25 Ma ruby mineralization in the Mogok Stone Tract, Myanmar: New evidence from SIMS U–Pb dating of coexisting titanite. *Minerals*, Vol. 11, No. 5, article no. 536, https://doi.org/10.3390/min11050536
Zwaan J.C., Buter E., Mertz-Kraus R., Kane R.E. (2015) Alluvial sapphires from Montana: Inclusions, geochemistry, and indications of a metasomatic origin. *G&G*, Vol. 51, No. 4, pp. 370–391, https://doi.org/10.5741/GEMS.51.4.370

For online access to all issues of Gems & Gemology from 1934 to the present, visit:

gia.edu/gems-gemology

Jewelry Services

Our legacy of trust, now available for jewelry.

GIA®

For generations, the world has trusted GIA to provide accurate reports for loose gems.

Now, we're bringing our global leadership to new horizons by providing jewelry services.

Expect the same rigorous GIA standards, deep expertise, and advanced technology to add confidence and credibility to every jewelry report.

GIA.edu/Jewelry

Jewelry provided courtesy of The Clear Cut.

© 2002 - 2026 Gemological Institute of America, Inc. (GIA). All trademarks are registered trademarks owned by GIA. GIA is a nonprofit 501(c)(3) organization. All rights reserved.

Policy-Driven Sustainability in China's Freshwater Pearl Culturing Industry

Qishen Zhou, Yalan Xu, Deyi Xu, Jingping Hu, and Mancun Zhao

China, an early pioneer in pearl trading and culturing, is the world's leading producer of freshwater cultured pearls in terms of volume, industry scale, and supply chain integration. However, the industry continues to occupy lower tiers of the global value chain, with limited access to value-added activities. Pearl culturing is characterized by a volume-driven growth trap—high output, but with low profitability and value addition. This article systematically traces the evolution of Chinese freshwater pearl culturing since 1949, categorizing it into four phases—exploration and development, rapid expansion, regulation, and sustainable development—and further analyzes the impact of environmental regulations. Despite initial challenges such as a reduction in the number of culturing sites, water use restrictions, and income losses for pearl culturing stakeholders, these policies have catalyzed a transition from unsustainable practices to eco-friendly models. Additionally, sustainable transformation pathways are discussed, with a focus on eco-conscious culturing techniques, quality-driven value enhancement, and cross-sector integration. Lastly, possible future directions for China's freshwater pearl culturing industry are explored, highlighting supply-demand dynamics, development drivers, empowerment strategies, and foundational safeguards. The study aims to provide evidence-based insights and policy-relevant recommendations that can inform sustainable aquaculture transitions worldwide, particularly in countries with comparable industry structures and environmental constraints or those undergoing rural ecological restoration.

The earliest records of freshwater pearl culturing in China date back to the Song Dynasty (960–1279 CE) (Pang, 1958). During the Ming Dynasty (1368–1644), maritime bans and ecological degradation led to the loss of organized and documented culturing techniques (Liao, 2012; Yang and Zhang, 2016). Systematic exploration of freshwater pearl culturing techniques resumed shortly after the founding of the People's Republic of China in 1949. By 1962, China produced its first batch of non-bead cultured (NBC) pearls, marking the inception of modern freshwater pearl culturing (G.F. Zhang, 2004).

Following the launch of the "Reform and Opening Up" policy in 1978, which liberalized China's markets, expanded foreign trade, and established special economic zones, China experienced rapid economic growth and higher living standards. This transformation coincided with a global rise in demand for pearls, which Western and emerging countries began to view as accessible luxury items. China became not only a major consumer but also an increasingly prominent player in the international freshwater pearl market. Freshwater pearl culturing techniques became more sophisticated, and the industry saw significant advancements in scale and specialization. Major industrial clusters formed, encompassing the entire value chain from mussel breeding and pearl culturing to processing and sales. Wuyi County in Zhejiang Province has emerged as a major hub for spat breeding. In 2023, the county hosted approximately 28,000 breeding ponds, producing nearly 1.5 billion spat and accounting for more than 85% of China's total freshwater mussel spat (Q.P. Zhang, 2024). These spat supply major culturing regions across China, including the provinces of Zhejiang, Jiangsu, Anhui, Jiangxi, and Hunan. Shanxiahu Town (located within the city of Zhuji in Zhejiang Province, nearly 250 km south of Shanghai) is now recognized as a global capital for freshwater pearl culturing, processing, and trade. China's freshwater pearl culturing industry serves as a vital economic driver, contributing to income growth for

See end of article for About the Authors and Acknowledgments.
Gems & Gemology, Vol. 62, No. 2, pp. 136–163,
https://doi.org/10.5741/GEMS.62.2.136
© 2026 Gemological Institute of America

Figure 1. Freshwater bead cultured products from China, such as these "Gablily" pearls (11–13 mm, cultured 3–5 years), are available in the international market. Courtesy of Angeperle.

rural producers, both full-time and part-time, and households that engage in culturing as a side business (figure 1).

In the early twenty-first century, however, unsustainable production models marked by the excessive use of fertilizers and high culturing densities caused severe aquatic ecosystem degradation, creating an economic-environmental paradox. These practices initially boosted output but ultimately reduced profitability by degrading water quality, which compromised pearl quality, and by oversaturating the market, which drove down prices. This model directly violated China's "ecological civilization" doctrine for sustainable development, introduced in 2005 (C.L. Huang, 2025). In response, the State Council issued a series of stringent environmental protection policies, prompting major freshwater pearl–producing provinces to impose strict regulations. Consequently, China's freshwater cultured pearl production plummeted from 5,265 tonnes in 2006 to 454 tonnes in 2020, resulting in market price volatility and threatening the industry's long-term viability (figure 2). Although these measures initially disrupted production and income streams, they served to catalyze industry-wide restructuring. Since then, Chinese farmers, researchers, and enterprises have pioneered eco-friendly culturing innovations and best practices for sustainable value chain development.

This study reviews the development and current status of China's freshwater pearl culturing industry and explores future trends. It clarifies the institutional, technical, and market forces that have shaped the industry's evolution, offering a framework for understanding the transition to sustainability and potential upgrading in the global value chain.

EVOLUTION OF CHINA'S FRESHWATER PEARL CULTURING INDUSTRY

Following the establishment of the People's Republic of China in 1949, the central government launched systematic culturing research programs aimed at revitalizing the country's pearl industry. During the 1950s and 1960s, institutions such as the Shanghai Fisheries Research Institute and the Zhejiang Provincial Fisheries Bureau conducted experimental work to improve traditional shell blister culturing techniques. These efforts included controlled trials and biomanipulation of host mussels, laying the technical groundwork for China's eventual success in culturing NBC freshwater pearls in 1962 (G.F. Zhang, 2004). In 1984, China's freshwater pearl output exceeded 100 tonnes for the first time, surpassing Japan's total cultured pearl production of approximately 64 tonnes, which mostly consisted of akoya pearls (Bai et al., 2014). Since then, China has maintained global dominance in freshwater cultured pearl production.

In Brief

- The evolution of China's freshwater pearl industry is traced from 1949, starting with early exploration and development, followed by rapid expansion, to regulation-driven contraction, and most recently a transition toward sustainable development.
- Stringent environmental regulation policies initially reduced output but ultimately drove innovation in fish-mussel polyculture, smart biocycle systems, and ecologically responsible industrialized culturing.
- Advances in multi-site bead implantation, precision surgical instruments, regenerative culturing, and selective breeding have enabled production of high-quality bead cultured freshwater pearls and significantly shortened culturing cycles.
- Eco-friendly pearl culturing models are now being deployed in mining subsidence ponds and polluted rivers, achieving measurable water quality improvement while generating economic returns.

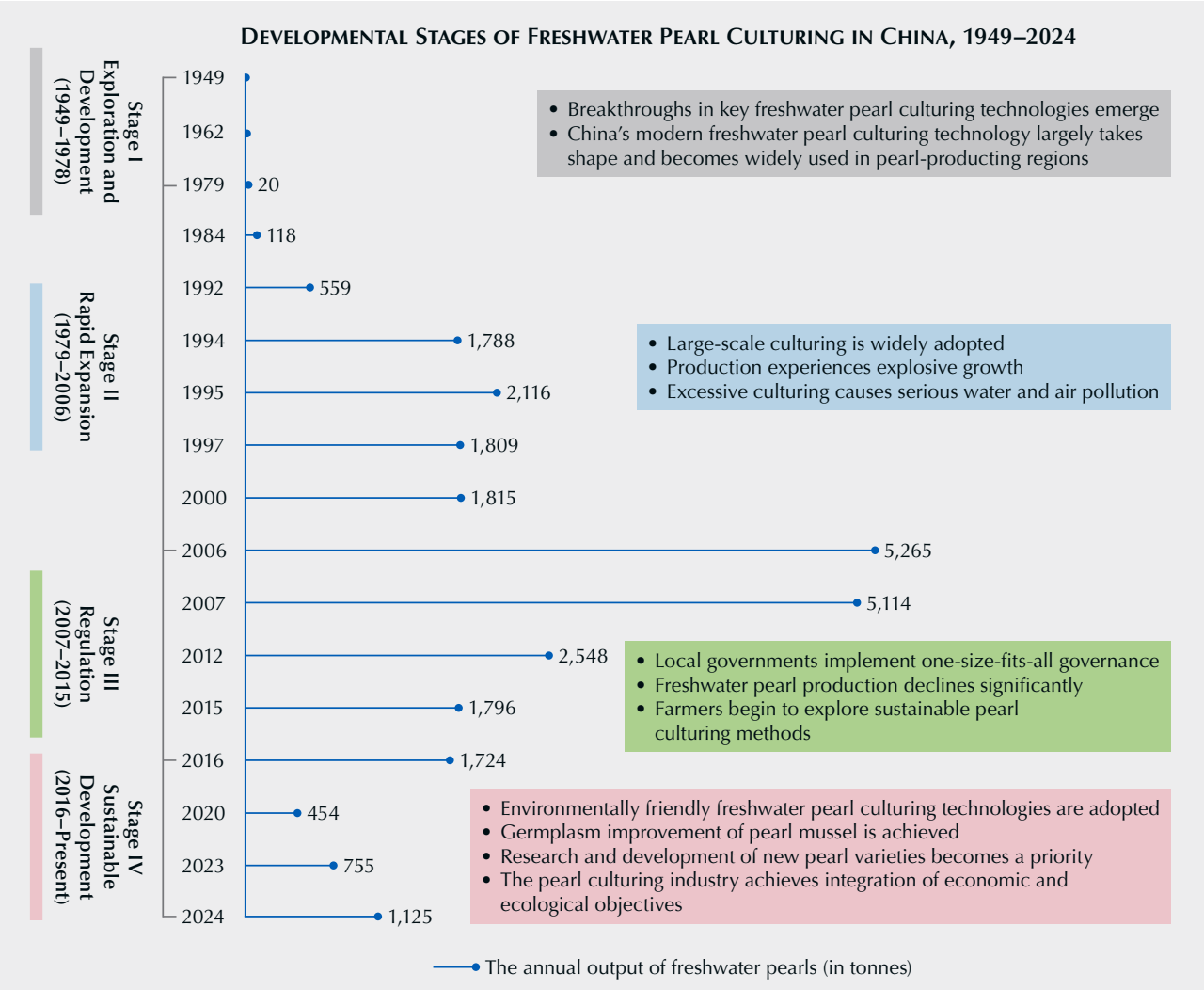

Figure 2. The four distinct developmental stages and key characteristics of freshwater pearl culturing in China are shown alongside representative annual production data. Output totals prior to 1979 are unavailable. For clarity, only milestone years are presented to illustrate overall trends and transitions in growth, regulation, and sustainability. Data sourced from China Fisheries Statistical Yearbook *(1980–2025).*

A significant turning point came in 1992, when China abolished the unified management and export licensing systems for pearls. This policy change encouraged individual pearl culturists to form cooperatives and private enterprises, fostering the emergence of modern commercial entities. The resulting industrial consolidation and specialization accelerated the growth of China's freshwater pearl culturing sector and contributed to another production peak. By 1994, annual production exceeded 1,000 tonnes, a year-on-year increase of 364%. Production reached an all-time high of 5,265 tonnes in 2006 (again, see figure 2).

After the peak in 2006, production scale and output declined. This downturn correlated with global economic shifts, market demand volatility, and the implementation of China's stringent environmental policies. Production fell to 454 tonnes in 2020, just 9% of the 2006 level. Since 2022, the industry has shown signs of recovery, supported by digital innovations such as livestream selling, e-commerce platforms, and intelligent culturing systems, alongside market expansion and promotion initiatives. Production rebounded to 1,125 tonnes in 2024.

Based on the historical evolution of China's freshwater pearl culturing industry since 1949, shown in figures 2 and 3, four distinct stages can be identified: exploration and development (1949–1978), rapid expansion (1979–2006), regulation (2007–2015), and sustainable development (2016–present).

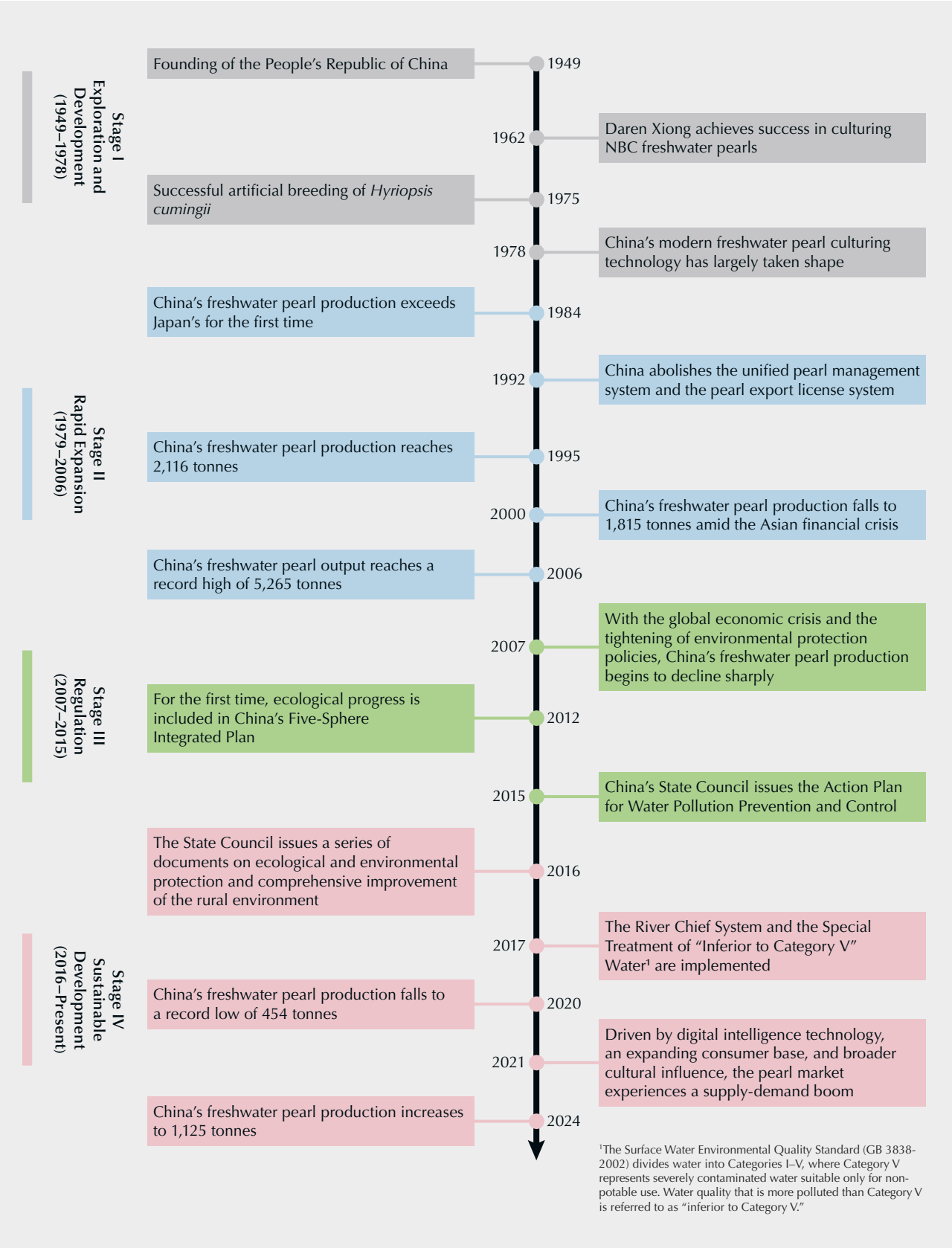

Figure 3. Timeline of major events in China's freshwater pearl culturing industry, grouped into four developmental stages.

Figure 4. Operations at the Dahaiyang Pearl Farm in 1979 in Deqing County, Zhejiang Province. Photo from Zheng (2021).

Exploration and Development (1949–1978). From the eleventh century until the 1950s, Chinese freshwater pearl culturing remained largely stagnant, and pearl production was almost exclusively reliant upon natural pearl harvesting. The 1950s marked a turning point, as research institutions in Shanghai, Zhejiang, and Hunan initiated systematic investigations into pearl culturing, successfully revitalizing the ancient Buddha-shaped shell blister culturing technique (Y.P. Zhang, 1973). Building upon this, researchers developed shell blisters with elaborate motifs such as dragons, pagodas, fish, vases, and human faces. However, breakthroughs in spherical whole freshwater pearl culturing were not yet achieved (Y.P. Zhang, 1973).

Researchers including Daren Xiong and Zhirong Shen conducted extensive studies in the 1960s, culminating in Xiong's 1962 breakthrough in NBC freshwater pearls. This achievement laid the foundation for modern freshwater pearl culturing in China (Xiong et al., 1980). In 1975, researchers developed artificial breeding techniques for *Hyriopsis cumingii*, eliminating the need for natural mussel spat collection and enabling large-scale culturing (Yao, 1978). Starting in the late 1970s, systematic studies were conducted on pearl formation mechanisms, surgical implantation techniques, growth optimization, water quality management, and disease control (Y.P. Zhang, 1973; G.F. Li, 1981). During this period, the foundation for modern freshwater pearl culturing was applied at scale. One example was a commercial NBC freshwater pearl farm in Deqing County, Zhejiang Province (figure 4), which demonstrated the application of these advancements.

Rapid Expansion (1979–2006). During this period, rapid industry growth prioritized short-term output gains at the expense of environmental sustainability. Most freshwater pearl farmers adopted extensive yield-driven culturing practices, with limited awareness of ecological impacts. Nutrient-overloaded feeding regimes and high stocking densities (figure 5) caused severe eutrophication, a condition in which excess nutrient enrichment (e.g., nitrogen and phosphorus) leads to algal blooms and oxygen depletion in aquatic ecosystems. Although widespread environmental degradation began during this stage, it initially drew little public or regulatory attention.

As ecological conditions worsened and the impacts on pearl quality and farm profitability became evident, the issue drew increasing scrutiny. These problems were subsequently documented through scientific assessments and media reports. For example, a 2016 monitoring report from Xianning City, Hubei Province, showed nitrogen and phosphorus levels in Futou Lake surpassing Category III thresholds by 100% and 300%, respectively (Xinhua Daily Telegraph, 2016). Deteriorating conditions led to increased prevalence of disease in *Hyriopsis cumingii* populations, reducing yield and pearl quality. This created a vicious cycle in which efforts to boost production resulted in diminishing economic returns, posing a significant setback for China's freshwater pearl culturing industry.

Regulation (2007–2015). China's rapid economic growth brought escalating challenges such as environmental pollution and ecosystem degradation. In response, the government prioritized systemic improvements to environmental governance. Water pollution emerged as a central focus of ecological management, with the establishment of quality and safety standards for wastewater management (Ministry of Agricultural and Rural Affairs, 2003) and pollutant discharge caps for key river basins (State Environmental Protection Administration, 2007). In 2012, ecological progress was first incorporated into China's Five-Sphere Integrated Plan, elevating environmental protection to a pillar of national strategy. The Water Pollution Prevention and Control Action Plan (State Council, 2015) mandated national standards and timelines for aquatic ecosystem restoration. The Chinese government issued a series of major policy documents aimed at further strengthening environmental quality. These included five-year plans for ecological protection (State Council, 2016) and comprehensive improvement of the

Figure 5. Top: Excessive stocking densities in a cage of Hyriopsis cumingii. *Photo from Yang and Zhang (2016). Bottom: Standard practice includes maintaining 2–4 adult mussels per cage, as shown here in the village of Xinjucheng. Photo by Yalan Xu.*

rural environment (Ministry of Ecology and Environment, and Ministry of Finance, 2016); a "river chiefs" system, in which government officials are responsible for the bodies of water in their jurisdiction (General Office of the CPC Central Committee & General Office of the State Council, 2016); regulations on environmental supervision (General Office of the CPC Central Committee & General Office of the State Council, 2019); and five actions for green aquaculture (Ministry of Agriculture and Rural Affairs, 2020). These efforts marked a shift toward more enforceable environmental governance.

Major freshwater pearl–producing provinces such as Zhejiang also enacted their own regulations and

Figure 6. Representative BC (A–D) and NBC (E and F) freshwater pearl products available in the international market. A: "Aurora" pearls (7–8 mm, cultured 2–3 years). B: "Edison" pearl necklace (12–13 mm, cultured 3–5 years). C: Star-shaped pearls (12–13 mm). D: Baroque-shaped pearl pendant (12 × 15 mm). E: Near-round pearl necklace (6–7 mm). F: Oval pearl earrings (8–10 mm). Courtesy of Angeperle (A, B, and D–F) and Qianzhu Jewelry (C).

remediation programs (Standing Committee of the People's Congress of Zhejiang Province, 2017; H.M. Wang, 2017). Meanwhile, several regions imposed outright bans on freshwater pearl culturing to protect water resources. Because these policies initially emphasized ecological preservation over pearl production, this approach proved unsustainable for long-term industry growth (Jia et al., 2023).

Sustainable Development (2016–present). The current period reflects a growing recognition that economic growth must align with ecological principles, with environmental protection an integral part of sustainable development (Horne et al., 2018). In response to increasingly stringent regulations, many traditional freshwater pearl culturing practices have been phased out or upgraded. The transition toward environmentally friendly practices represents both a continuation and an advancement of sustainable development principles, bringing new opportunities and challenges to China's freshwater pearl culturing industry. Chinese freshwater pearl enterprises have undertaken a series of industrial innovations and made significant progress in sustainable development through eco-friendly culturing, fish-mussel polyculture, and intelligent freshwater culturing techniques.

Meanwhile, companies have improved pearl quality via germplasm enhancement (the selective breeding of mussels with desirable traits) and the development of novel pearl shape and color varieties (J.L. Li et al., 2019; Z.Y. Wang, 2023; Y. Chen et al., 2024). The hubs of China's freshwater pearl industry now feature a full value chain that encompasses culturing, processing, design, marketing, educational and cultural experiences (museum exhibitions and pearl-themed tourism), and health and beauty products and treatments. These efforts have increased the industry's added value and competitiveness. The variety of Chinese freshwater cultured pearls on the international market has diversified, encompassing NBC pearls of various shapes and a wide range of bead cultured (BC) pearls (figure 6). A balanced strategy that integrates economic and ecological objectives is now seen as essential to the future of the freshwater pearl culturing industry (Hoang et al., 2019).

ENVIRONMENTAL REGULATION AND CHINA'S FRESHWATER PEARL INDUSTRY

China's freshwater pearl production is primarily from the filter-feeding mussel *Hyriopsis cumingii* (figure 7). The mussel feeds on particulate matter and organic detritus, with phytoplankton such as diatoms, chrysophytes, and chlorophytes forming the bulk of its diet. Studies indicate that a single *Hyriopsis cumingii* can filter more than 100 liters of water daily, reducing suspended solids by more than 50%. These mussels also help reduce ammonia-nitrogen and phosphorus concentrations, effectively controlling eutrophication and cyanobacterial blooms (Yu et al., 2020; Tang et al., 2021; Verma et al., 2025). When managed properly, freshwater pearl culturing not only helps prevent environmental contamination but also contributes to rehabilitating aquatic ecosystems. However, historically, excessive culturing practices have caused

Figure 7. External morphology (left; 10.08 × 6.36 cm) and internal structure (right; 13.43 × 10.21 cm) of Hyriopsis cumingii. *Photos by Qishen Zhou.*

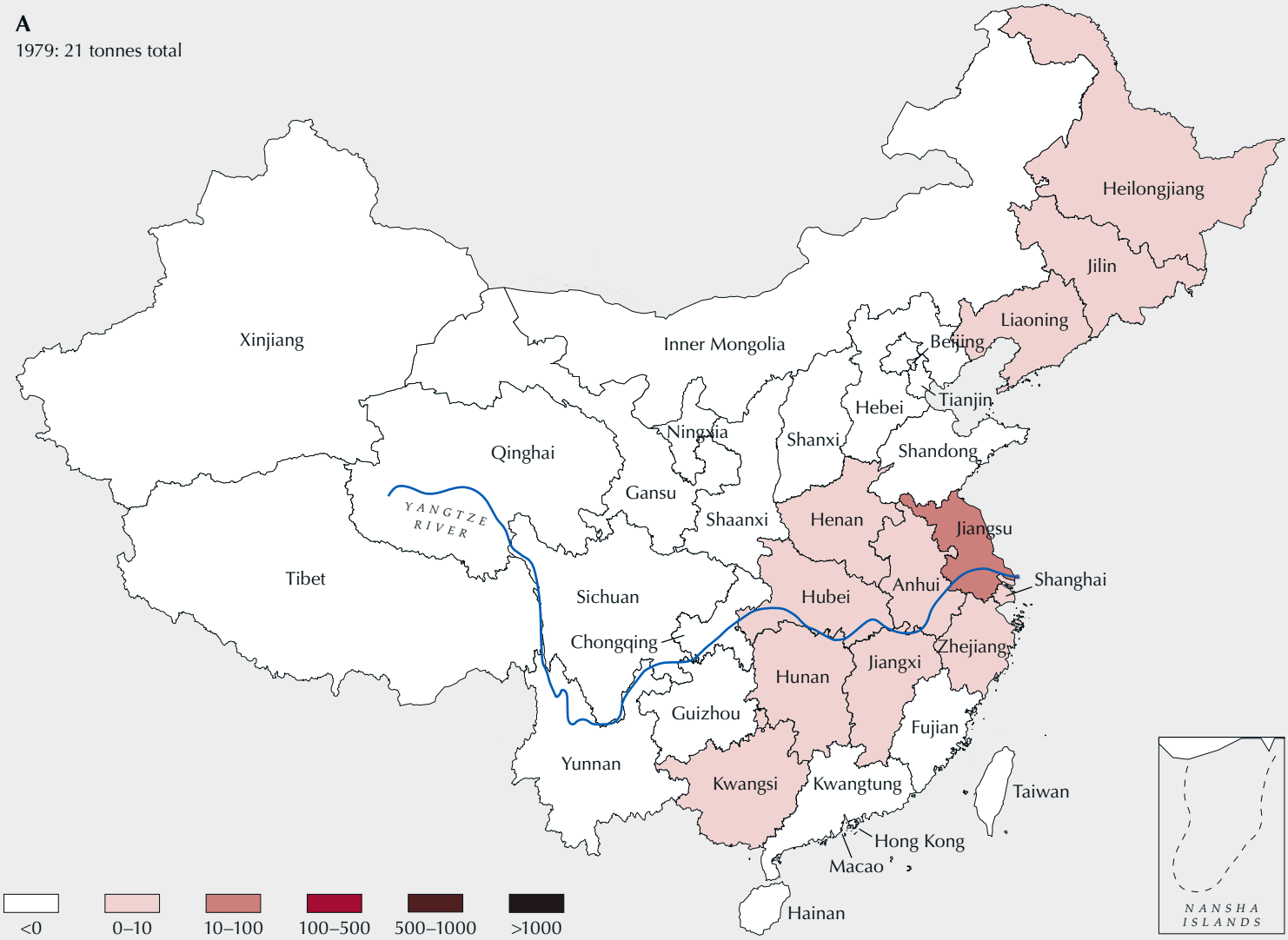

Figure 8. Regional distribution of freshwater pearl culturing in China by year in tonnes, beginning in 1979 (A). (For subsequent years, see maps B–G on opposite page.) Data sourced from China Fisheries Statistical Yearbook *(1980–2025).*

severe eutrophication. Since 2015, stringent environmental policies have reshaped the industry's spatial distribution and production practices.

Distribution of Freshwater Pearl Culturing Areas. China's freshwater pearl culturing areas have expanded markedly over time. The middle and lower reaches of the Yangtze River represent the traditional core culturing regions. Prior to the 1990s, major production areas were concentrated in Jiangsu, Zhejiang, and Shanghai, with minimal production in Liaoning, Jilin, Heilongjiang, Hunan, Hubei, Guangdong, Guangxi, Sichuan, and Chongqing (figure 8, A and B).

In the 1990s and early 2000s, freshwater culturing became more clustered, accompanied by a narrowing of production disparities between provinces. Six major culturing regions emerged: Jiangsu, Zhejiang, Anhui, Jiangxi, Hunan, and Hubei. Within these provinces, pearl culturing was concentrated in specific localities: Changzhou, Taizhou, Zhenjiang, and Huai'an in Jiangsu; Zhuji, Lanxi, and Yiwu in Zhejiang; Wuhu, Anqing, Chizhou, Xuancheng, and Chuzhou in Anhui; Poyang Lake (particularly Wannian and Duchang) in Jiangxi; Changde, Hanshou, and Yiyang in Hunan; and Honghu, Jiayu, and the outskirts of Wuhan in Hubei. Of these localities, Duchang and Wannian

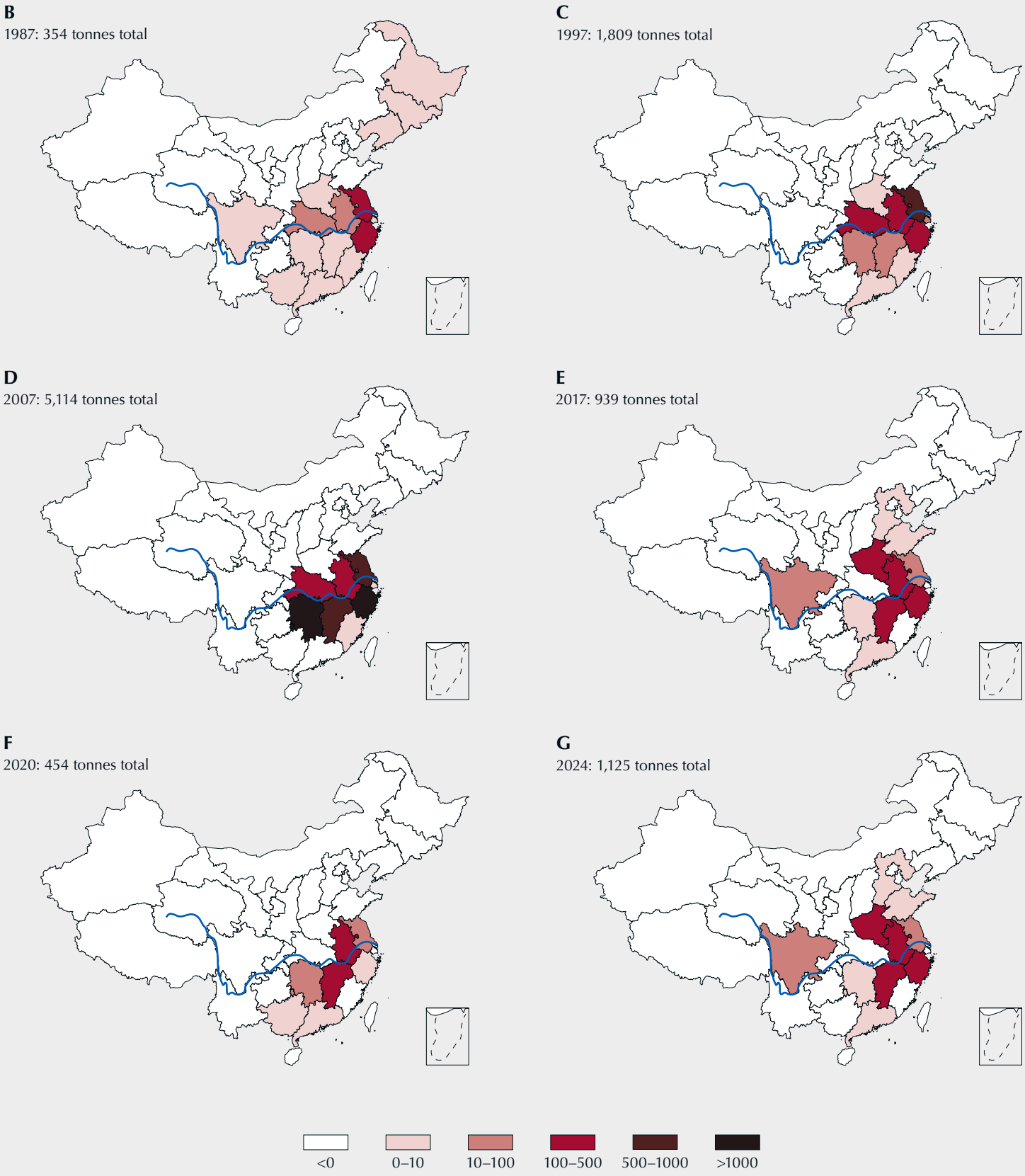
B
1987: 354 tonnes total
C
1997: 1,809 tonnes total
D
2007: 5,114 tonnes total
E
2017: 939 tonnes total
F
2020: 454 tonnes total
G
2024: 1,125 tonnes total
<0
0–10
10–100
100–500
500–1000
>1000

Counties in Jiangxi and Hanshou County in Hunan were officially recognized as "China's Freshwater Cultured Pearl Townships," establishing freshwater pearl culturing as a pillar industry (figure 8, C and D).

Stringent environmental policies enforced by local governments since 2007 have driven significant changes in freshwater pearl culturing areas. Along with the adoption of fertilizer-free culturing (which mitigates algal blooms by eliminating the use of organic fertilizers such as chicken manure), freshwater culturing in large natural water bodies such as lakes and reservoirs was officially banned in most regions. Production in Zhejiang and Hubei declined sharply, making Anhui and Jiangsu the leading producers (figure 8E).

Under sustained pressure from environmental policies, freshwater cultured pearl production fell to a record low in 2020 (figure 8F). Since 2021, increasing international demand, the adoption of eco-friendly techniques, and the rise of live streaming have spurred a recovery (China Jewelry and Jade Industry Association, 2024). By 2024, culturing areas had expanded to 10 provinces, and the distribution of production had shifted (figure 8G).

Zhejiang Province, an original pioneer of freshwater pearl culturing, offers a dramatic example of volatility over the past four decades. In the mid-1990s, epidemics of mussel disease resulting from unregulated high-density culturing forced companies to expand their production networks to Hunan, Hubei, and Jiangxi. Zhejiang introduced mandatory watershed monitoring and imposed limits on nutrient discharge for basins affected by culturing (Standing Committee of the People's Congress of Zhejiang Province, 2009). These regulations sharply reduced the scale of freshwater pearl culturing.

Zhejiang's "Five Waters Governance" initiative, launched in 2013, established integrated basin management protocols for coordinated water pollution control, flood prevention, drainage, water conservation, and water supply improvement (G. Xu and Y. Lu, 2019). By 2017, Zhejiang had instituted systematic elimination of substandard (Category V and below) water bodies, representing China's lowest water quality grades in terms of pollution and ecological degradation. As a result, freshwater pearl culturing output contracted dramatically, hitting a record low of 0.5 tonnes in 2021 (figure 9).

Hubei Province, known as the "Province of a Thousand Lakes," experienced rapid expansion of freshwater pearl culturing following the phased implementation of the Household Contract Responsibility System in the late 1970s and early 1980s (M.X. Yang et al., 2003). This rural reform policy, which allowed households to lease farmland from the collective and manage production independently, stimulated aquaculture expansion, including freshwater culturing, across the Yangtze River basins. According to provincial records, output rose from 1.7 tonnes in 1982 (Hubei's second year of culturing) to 37 tonnes by 1984, exceeding 100 tonnes annually after 1995 and peaking at 300 tonnes in 2008 (figure 9). Pearl culturing areas also expanded rapidly during this period. By 2007, freshwater pearl culturing

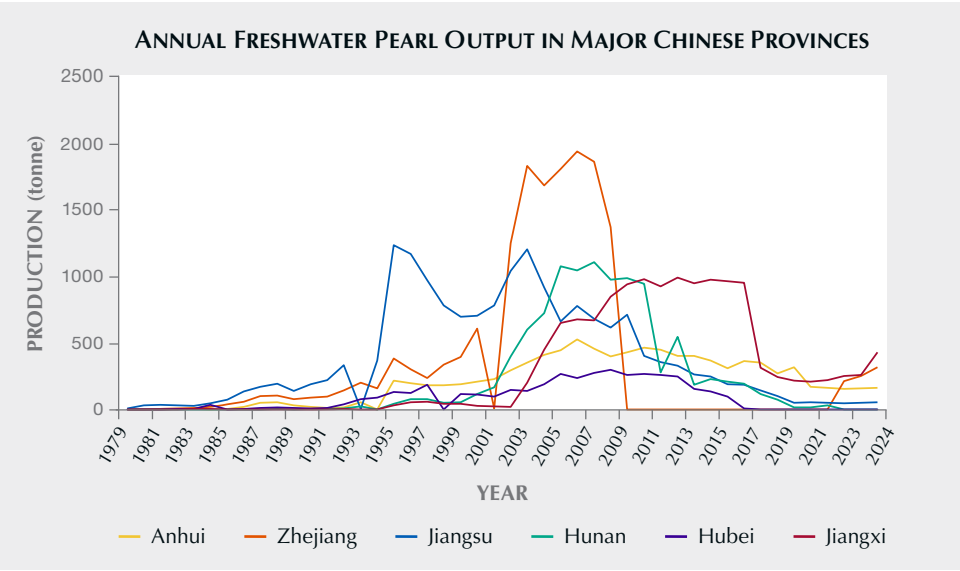

Figure 9. Annual freshwater pearl output in major Chinese provinces. Data sourced from China Fisheries Statistical Yearbook *(1980–2025).*

covered about 13,333 hectares, with a 2007 output of 278 tonnes valued at RMB 100 million (US$14.6 million) (F. Liu and L. Tu, 2007). Companies from Jiangsu and Zhejiang expanded their operations to Hubei during the 1990s, contributing to the province's emergence as a national production hub.

However, environmentally unfriendly culturing practices induced severe eutrophication and widespread algal blooms, causing heavy pollution in water bodies such as those in Caidian District (Wuhan), Huangshi, and Jingzhou. In 2007, Hubei banned freshwater pearl culturing in drinking water sources (Liu and Tu, 2007), and subsequent policies (Standing Committee of the People's Congress of Hubei Province, 2012; Hubei Provincial Department of Agriculture, 2016) further restricted the sector, collectively reducing output to 11 tonnes by 2016. Hubei completely withdrew from pearl culturing by 2017 (figure 9).

Other provinces have implemented similar measures to manage freshwater pearl culturing. Hunan enacted the most stringent regulations, reducing production from 1,113 tonnes in 2007 to 0.1 tonnes in 2022 through mandatory phase-out policies in key regions including Yueyang, Changde, and Yiyang (Zeng et al., 2007). Jiangsu Province, once China's largest freshwater pearl producer, saw output grow from 11 tonnes in 1979 to a peak of 1,242 tonnes in 1995. Under increasing regulatory pressure, Jiangsu gradually reduced production to 50 tonnes by 2022 through the establishment of non-culturing buffer zones and policy-driven exits from intensive production areas. Jiangxi Province, a later entrant, initially maintained low output before rapidly expanding post-2000, reaching a peak of 997 tonnes in 2015. Since then, Jiangxi has also adopted restrictive zoning and surface water protection measures, resulting in a steady decline to a record low of 210 tonnes in 2020. In Anhui, pearl culturing expanded rapidly from 0.5 tonnes in 1980, peaking at 530 tonnes in 2007. A series of environmental regulations and rising concerns over water quality gradually reduced that figure to approximately 156 tonnes by 2022 (figure 9).

After their respective troughs, output recovered in most provinces except Hubei, which remained at zero. Zhejiang rebounded most sharply from 0.5 tonnes in 2021 to 319 tonnes in 2024. Jiangxi climbed from its 2020 trough of 210 tonnes to 435 tonnes by 2024. By contrast, Jiangsu and Anhui saw only minimal increases, reaching just 55 and 167 tonnes, respectively. Hunan, although previously reduced to just 0.1 tonnes in 2022, recovered modestly to 3 tonnes by 2024, a level far below its historical peak but signaling a limited return under strict environmental controls. Sichuan, a newly emerging producer with no significant previous output, expanded to 28 tonnes by 2024 (figure 9).

Figure 10. An aquaculture pond used for culturing pearl mussels in Wuyi County. Photo by Yalan Xu.

Types of Water Bodies Used for Freshwater Pearl Culturing. Traditionally, freshwater pearl culturing was carried out in both natural water bodies (lakes, reservoirs, and rivers) and aquaculture ponds (J.L. Li et al., 2019). Major basins such as Poyang Lake (Jiangxi), Dongting Lake (Hunan), and Taihu Lake (Jiangsu) once served as primary production zones for high-quality cultured pearls. Characterized by moderate surface area, high dissolved oxygen content, and stable physicochemical properties, they provided optimal conditions for culturing. However, local bans and restrictions have shifted the focus away from large natural water bodies. Aquaculture ponds have become the primary sites, with only limited production in certain lakes and reservoirs under controlled conditions. In addition, pearl mussels are used for wastewater treatment in some degraded environments, such as mining subsidence ponds (water-filled depressions formed by ground collapse after underground mining activities) and eutrophic urban waterways.

Aquaculture Ponds. These ponds typically range from 0.8 to 6.7 hectares, with smaller ponds covering less than 0.7 hectares, and depths generally from 1.5 to 2.0 meters (figure 10). Annual rent averages RMB 18,000–30,000 (US$169–$282) per hectare (based on

interviews conducted by authors QZ, YX, and JH with pearl farm managers and industry association representatives in Zhejiang, Jiangsu, and Anhui in 2024). The shift to pond-based culturing has allowed for more manageable water quality control and easier compliance with environmental regulations. By containing nutrient discharge within controlled systems, ponds not only provide stable and predictable yields but also help reduce the risk of eutrophication in surrounding natural ecosystems. While pond-based systems prioritize the prevention of new pollution, the industry is simultaneously exploring the proactive remediation of existing environmental damage.

Polluted Water Bodies. As environmental regulations on freshwater pearl culturing tightened, traditional fertilization-based practices were gradually phased out. The ecological function of pearl culturing has been increasingly recognized, enabling pearl culturing to expand beyond traditional aquaculture zones into degraded environments. A prominent example is the town of Taiping in Zoucheng, Shandong Province, where a 53.3-hectare coal mining subsidence pond was repurposed in 2019 using smart biocycle culturing. This initiative yielded 300 kg of pearls per hectare and generated RMB 600,000 (US$5,640) per hectare (Shao, 2021), successfully integrating water purification with economic pearl production (figure 11). Following this success, the model was replicated in the coal mining subsidence areas of Huaibei and Fuyang in Anhui Province (Y. Yang and J. Liu, 2023; Y.M. Zhou, 2024). Furthermore, this culturing method has proven effective in urban water remediation. A pilot project in Binjiang District, Hangzhou, utilized pearl mussels as natural biofilters in the Xixinghou River (figure 12). The project successfully improved water quality from Category V to Category III (Binjiang District Water Treatment Office, 2022). Similar ecological restoration efforts have been extended to other severely polluted bodies, such as Gehu Lake in Yixing, Jiangsu Province, which serves as a critical upstream buffer for Taihu Lake (C.Q. He, 2024). These diverse cases demonstrate that pearl culturing has evolved from a traditional industry into a powerful tool for ecological remediation, transforming polluted water into productive assets. By aligning economic output with environmental restoration, this model offers a scalable win-win pathway for global sustainable aquaculture.

Policy Disparities and Economic Ramifications in China's Freshwater Pearl Culturing Phase-Out. China's major freshwater pearl–producing provinces have taken different approaches to phase out pearl culturing. In Zhejiang, local governments in Shanxiahu Town (Zhuji) and Jindong District (Jinhua) provided farmers with transitional subsidies of RMB 30,000 (US$290) per hectare to accelerate culturing termination (Zhuji Water Resources and Hydropower Bureau, 2017a; Jindong District Government Office of Jinhua City, 2017). Meanwhile, Hubei Province ended farming without compensation, forcing farmers to bear the full transition costs (Hubei Provincial Department of Agriculture, 2016).

Enforcement timelines also varied significantly, with implementation windows ranging from less than 30 days to more than six months. This often forced premature harvesting, leading to deterioration

Figure 11. Transformation of a coal mining subsidence pond in the town of Taiping (Zoucheng, Shandong Province), before (left) and after ecological remediation with pearl mussel culturing (right). Courtesy of Zhejiang Qinghu Holdings Co., Ltd.

Figure 12. Xixinghou River in Binjiang District, Hangzhou. Left: Turbid water with low transparency before treatment. Right: After treatment, water quality is noticeably improved. Mussels are submerged using an automated lifting system and are not visible during normal operation. Courtesy of Zhejiang Qinghu Holdings Co., Ltd.

in both yield and quality. With standard stocking densities of 6,667 mussels per hectare yielding market-grade pearls valued at RMB 10–25 (US$1.50–$3.80) per mussel, premature termination caused estimated losses of RMB 10,000–25,000 (US$1,500–$3,750) per hectare. The heaviest losses occurred in the wake of Hubei's culturing restrictions. Qianzu Pearl Group lost permits for 8,667 hectares of culturing waters, with verified losses exceeding RMB 100 million (US$15 million) by 2017. Ruan Shi Pearl Company faced a similar setback, relinquishing 133 hectares of licensed aquaculture waters in compliance with policy mandates. Angeperle, specializing in premium freshwater pearl products, experienced a 20% decline in output from contracted farmers between 2016 and 2018, while procurement prices rose by approximately 30% (Zhu, 2017).

RECENT INNOVATIONS IN THE FRESHWATER PEARL CULTURING INDUSTRY

While pearl mussels have the potential to play a positive role in water purification and the absorption of heavy metals, inadequate management practices such as excessive stocking densities, overfeeding, and lack of sediment treatment can exacerbate water pollution and degrade pearl quality. Strict environmental regulations have catalyzed technological innovation in wastewater recycling and the adoption of cleaner technologies. To maximize ecological, economic, and social benefits, Chinese companies and research institutes have implemented targeted strategies to promote the healthy and stable development of the industry. This section examines three pillars: sustainable practices, value chain optimization, and cross-sector integration.

Sustainable Freshwater Pearl Culturing Practices. In response to stricter environmental regulations, several freshwater pearl–producing regions have begun transitioning toward more sustainable models. A leading example is Zhuji in Zhejiang Province, which has pioneered ecologically responsible freshwater pearl culturing models with measurable outcomes. Since 2017, it has closed inefficient farms, strengthened oversight of operations, and established standardized freshwater pearl culturing demonstration zones (Zhuji Municipal People's Government Office, 2017; Zhuji Water Resources and Hydropower Bureau, 2017b). Eight demonstration zones, each covering 400 hectares, have been upgraded with internal circulation systems and reduced stocking densities. An investment of RMB 10 million (US$1.5 million) established a centralized facility for mussel meat processing (Pei et al., 2023).

By 2022, Zhuji's Shanxiahu Town, the epicenter of the city's pearl culturing industry, had decommissioned more than 190 hectares of culturing zones and upgraded more than 540 hectares with internal circulation-based ecological culturing systems. Water quality in pearl culturing areas improved significantly, rising from Category V or worse to Category III, with some areas even reaching Category II standards (Yan and Meng, 2022). Zhuji has also actively promoted new models such as fish-mussel polyculture, smart biocycle culturing, and industrialized ecological culturing. These

TABLE 1. Comparison of freshwater pearl culturing methods.

	Traditional freshwater pearl culturing	Fish-mussel polyculture	Smart biocycle culturing	Industrialized ecological freshwater pearl culturing
Culturing characteristics	Open-pond culturing	Symbiotic system of fish and mussels	Drip feeding; intelligent water quality control	Factory-based greenhouse culturing
Stocking area (hectares)	<15,000	<15,000	45,000–120,000	750,000
Culturing cycle[a] (years)	3–5	3–5	1.5–2.5	1.5
Water quality management	Natural purification or wastewater treatment facilities	Decomposition of fish waste into algae nutrients; reduced fertilizer use	Wastewater recycled after treatment	Wastewater recycled after treatment
Feeding method	Manual fertilizer application; no precision control	Ecological chain (fish waste fuels algae and mussels filter algae)	Automated feeding systems; targeted algae expansion	Network-connected precision feeding and real-time monitoring
Cost and efficiency	High organic fertilizer consumption; labor-intensive; moderate cost; limited efficiency	Lower fertilizer costs; improved economic returns	Labor reduction; high yield; high cost of supporting facilities	Energy-efficient; higher economic output; high cost of supporting facilities
Ecological outcome	Susceptible to eutrophication; pollution risk	Reduced eutrophication	Zero pollution	Zero pollution; high resource utilization

[a]*Using 9–13 mm "Edison" pearls as an example.*

approaches, summarized in table 1, are driving productivity enhancement, quality improvement, and environmental restoration.

Fish-Mussel Polyculture. Ecological aquaculture refers to a system in which organisms occupy distinct niches within the habitat, utilizing natural nutrient cycling mechanisms to maintain ecological balance and enhance production efficiency (Hui, 2014). One promising example is fish-mussel polyculture, which integrates grass carp (*Ctenopharyngodon idella*), silver carp (*Hypophthalmichthys molitrix*), bighead carp (*Hypophthalmichthys nobilis*), and other compatible species with pearl mussels such as *Hyriopsis cumingii*. In this system, fish release nitrogen and phosphorus through metabolic processes, contributing dissolved nutrients that stimulate phytoplankton growth. As filter-feeding bivalves, the mussels ingest suspended phytoplankton and organic particulates, reducing eutrophication risks through biofiltration. This synergy optimizes water resource efficiency and reduces nitrogen and phosphorus discharge. Cui et al. (2012) demonstrated through enclosure experiments that fish-mussel polyculture can suppress phytoplankton proliferation, strengthen biological purification capacity, stabilize ecosystems, and effectively improve water quality. Dai et al. (2013) found that optimizing freshwater fish species, fish-mussel ratios, and feed management all contribute to maximizing water quality. B. Wang et al. (2023) addressed a series of technical challenges associated with fish-mussel polyculture, including species compatibility, stocking density optimization, feed management, and disease control. B. Wang et al. (2023) also demonstrated that fish-mussel polyculture yields higher economic benefits than traditional monoculture practices.

By 2021, the fish-mussel polyculture pond in Lanxi City, Jinhua, Zhejiang Province, spanned 4,000 hectares, making Lanxi China's largest county-level city for this type of culturing (Ministry of Education, 2023). This model was published by the Department of Science, Technology and Education of the Ministry of Agriculture (2012) and promoted nationwide by the Ministry of Agriculture.

Smart Biocycle Culturing. Developed by Qinghu Agricultural Technology Co., Ltd. and Huazhong Agricultural University after a decade of research, smart biocycle culturing is a system that integrates precision culturing and targeted proliferation of

beneficial algae (Guo, 2022). This innovation not only significantly improves feed utilization and reduces culturing costs but also purifies the water and enhances the quality of pearls, earning it the reputation of a next-generation "water purifier."

The system moves the proliferation of beneficial bacteria, algae, and plankton that are essential for pearl mussel growth to an indoor environment. Primary water pipelines are installed in the lake, with mussels suspended beneath them. Mussel elevation is adjusted via water pressure to deliver nutrients directly to their "mouths" through an intelligent pipe network, decoupling the process from the surrounding water. The computer-controlled system monitors water quality and regulates feeding frequency and dosage according to the mussel's growth period as well as the season, temperature, and other factors (figure 13). This approach fundamentally prevents pollution during the pearl culturing process.

This system can sustain 45,000–120,000 mussels per hectare, compared to a maximum of 15,000 using

Figure 13. Diagram of the smart biocycle culturing system.

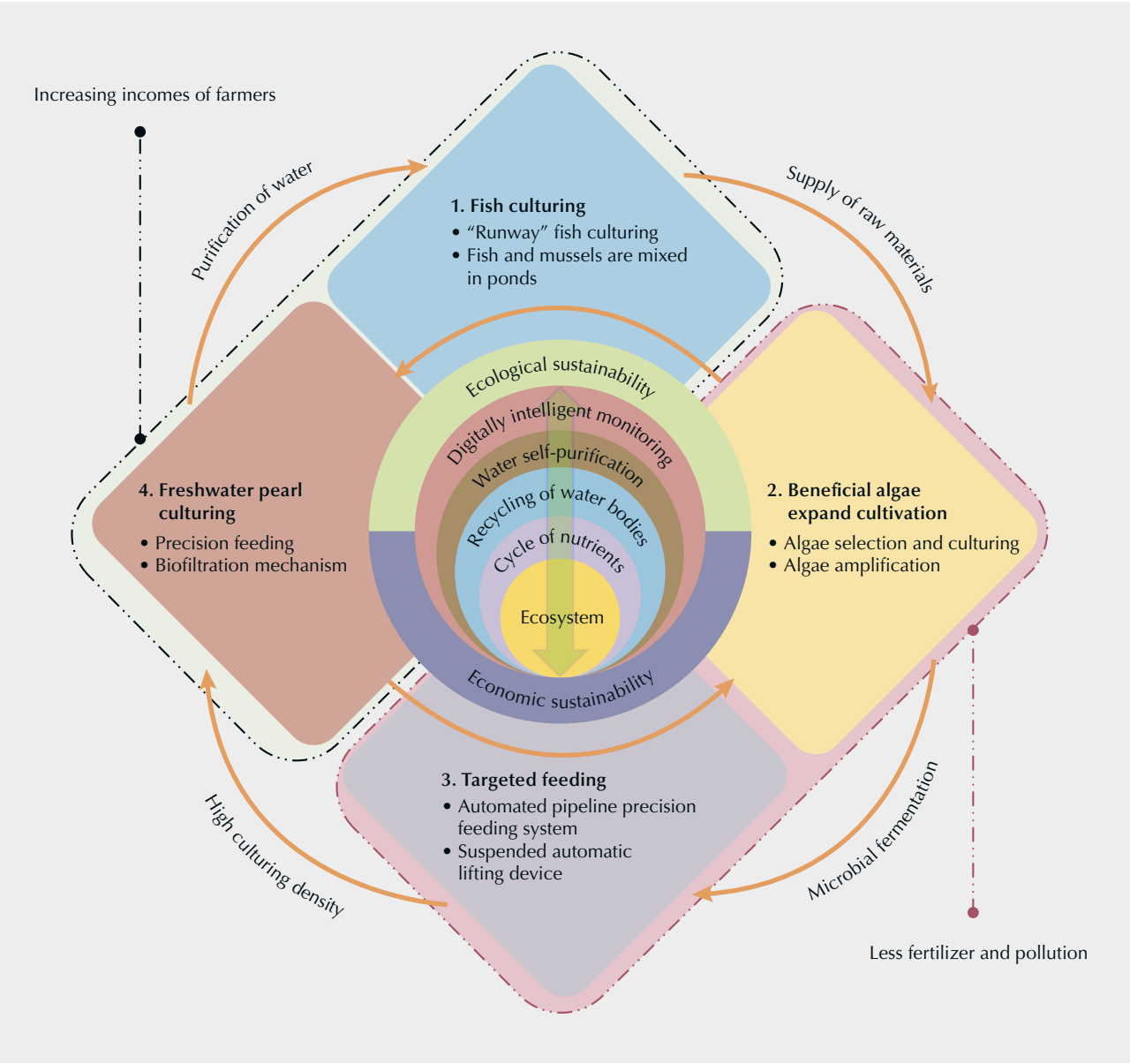

Figure 14. Industrialized ecological freshwater pearl culturing in Shanxiahu Town. Left: A greenhouse culturing environment. Right: Pearl mussels being cultured. Photos by Yalan Xu.

traditional models. Furthermore, this technology requires only 20 tonnes of specialized nutrient solution per year for 100,000 mussels, compared to 200 tonnes of organic fertilizer using traditional models. Network-connected management dramatically reduces labor costs. For a pond covering 66 hectares, only two personnel are needed to manage operations (G. Zhang et al., 2020; G.Y. Zhou, 2021).

Smart biocycle pearl culturing not only enhances efficiency and yield but also serves as an effective solution for managing eutrophication pollution while balancing ecological and economic benefits. In 2021, the Zhuji City Finance Bureau invested RMB 55 million (US$8.2 million) to further promote the system (W. Liu, 2021).

Industrialized Ecological Freshwater Pearl Culturing System. Since 2013, China has actively promoted research and development on industrialized ecological culturing, supported by national policies and advances in precision aquaculture technologies. Following several years of pilot experiments and technical refinement, Bairuila Agricultural Technology Co., Ltd. established China's first operational industrialized ecological freshwater pearl culturing system in 2019 (figure 14). This system replaces traditional open-air pond culturing by placing mussels on multi-layer shelves, enabling three-dimensional culturing within greenhouses. Meanwhile, the wastewater generated undergoes precipitation, filtration, disinfection, sterilization, and oxygenation before being recirculated into the culturing tanks, achieving zero discharge. The entire process is monitored in real time with a computerized control system regulating critical parameters including feeding schedules, water temperature (maintained at 28°C), and water quality (J.L. Li et al., 2025). With 9–13 mm "Edison" pearls, for example, industrialized ecological pearl culturing achieves a 50-fold increase in culturing density per unit area while reducing the production cycle from 3–5 years to 1.5 years (Zhuji City Association for Science and Technology, 2023; Fu et al., 2024).

Optimizing the Quality and Competitiveness of China's Freshwater Cultured Pearls. Although China has maintained its position as the world's largest producer of freshwater cultured pearls, quality remains a critical concern. Chinese customs data indicate that the average import price of pearls is significantly higher than the average export price (figure 15). In 2024, imported pearls averaged RMB 7,046 (US$972) per kg, while the export average was only RMB 1,236 (US$170) per kg. While import prices naturally reflect added costs such as transport, processing, and branding, a 7.3-fold gap far exceeds typical logistics and markup ratios in the pearl trade, which usually range from 1.5 to 3 times. This substantial discrepancy underscores persistent challenges in China's pearl industry, particularly in value creation, addition, and retention. Addressing these issues is essential for upgrading the industry's position in the global value chain. Enhancing the quality and increasing the yield of high-grade freshwater pearls will be crucial to overcoming the "low-end lock-in" dilemma in the global value chain—a condition in which producers remain trapped in low-value-added activities such as bulk culturing and unbranded exports. This approach will also serve as a fundamental driver for sustainable growth (C.R. Wang, 2024). To promote healthy and stable development, researchers have achieved phased innovations in two critical areas: mussel variety improvement and BC freshwater pearls.

Genetic Improvement of Freshwater Pearl–Producing Mussels. China's freshwater pearl culturing industry has entered a transition phase, shifting from volume-focused to quality-driven approaches. Culturing relies predominantly on *Hyriopsis cumingii* and its hybrid strains (Fiske and Shepherd, 2007). N. Xie et al. (2006) developed the kangle mussel (*Hyriopsis*

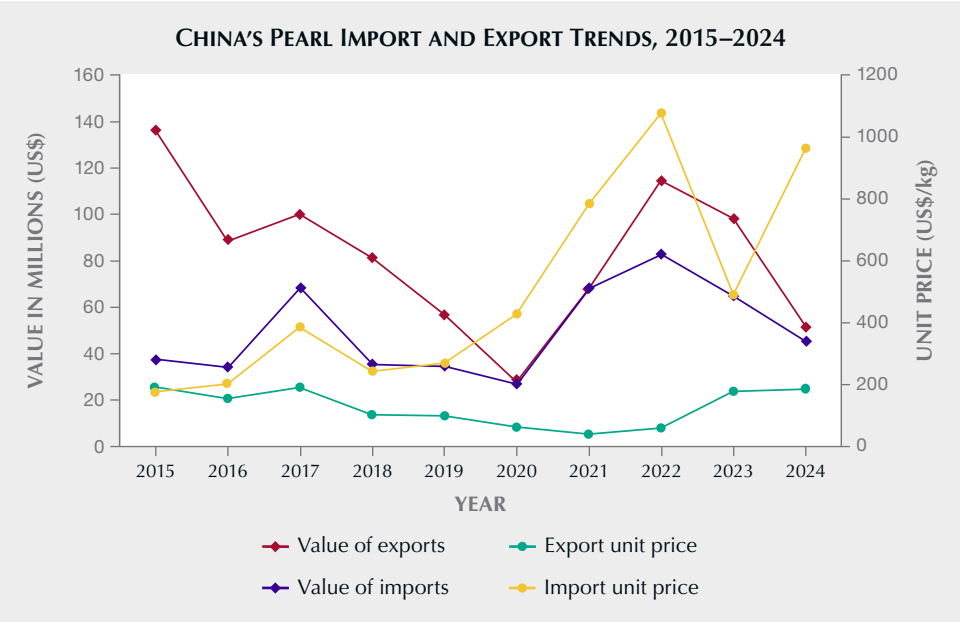

Figure 15. This graph is based on Chinese customs data from four product categories containing the term "cultured pearls." While these categories do not explicitly distinguish between freshwater and saltwater pearls, they broadly reflect trends in China's cultured pearl trade. Given that freshwater pearls dominate China's production and export volume, the import-export price gap revealed by the data highlights the Chinese industry's "low-end lock-in" in the global value chain.

schlegelii × *Hyriopsis cumingii*), achieving a nearly fourfold increase in the yield of premium-quality pearls (Li and Bai, 2007). G.F. Zhang et al. (2013) enhanced the color traits of *Hyriopsis cumingii* through mass and family selection, gradually developing four major donor mussel lines distinguished by nacre color—purple-red, violet, silver-white, and gold—as well as a recipient mussel line, known as the "Eagle Mussel," selected for its broad shell width and large body, which are favorable for cultivating larger pearls. These targeted breeding efforts enabled the large-scale production of uniformly colored freshwater pearls.

Subsequently, J.L. Li et al. (2019) investigated the genetic mechanisms underlying pearl coloration in *Hyriopsis cumingii*. In collaboration with Zhexing Pearl Trading Co., Ltd., they developed two novel subspecies: "Shen Zi No. 1" and "Shen Zhe No. 3" (figure 16). "Shen Zi No. 1" produces pearls with a 97.2% rate of purple coloration (Sun et al., 2019), while "Shen Zhe No. 3" has achieved an average 23% higher yield of BC pearls larger than 10 mm compared with non-hybrid *Hyriopsis cumingii* (J.L. Li et al., 2021).

Taken together, these genetic improvement efforts have significantly advanced the large-scale marketing of high-quality *Hyriopsis cumingii* varieties.

Figure 16. Selectively bred Hyriopsis cumingii *mussels. Left: "Shen Zi No. 1" (11.43 × 17.05 cm), displaying the distinctive purple nacre characteristic of this line. Photo by Qishen Zhou. Right: "Shen Zhe No. 3," showing multiple bead implantations (bead diameter ~5 mm) in the mantle tissue for BC pearl culturing. Photo from Gao et al. (2024).*

Bead Cultured Freshwater Pearls. Before the 1990s, BC freshwater pearls faced formidable technical barriers, including high surgical mortality rates, frequent bead rejection, and extremely low pearl yield (S.H. Xie, 2010). In 1985, Xie Shaohe's team achieved a milestone by producing the world's first 5 kg batch of BC freshwater pearls (Ye, 2015). This breakthrough initiated a paradigm shift from NBC to BC freshwater pearl production. Building on this advancement, China's BC freshwater pearl technology underwent continuous refinement over the following decades. Three core innovations matured between the late 1980s and the early 2010s: multi-site implantation, precision surgical instruments and management systems, and regenerative culturing. These advances significantly improved survival rates, resource efficiency, and pearl yield, laying the technical foundation for the industry's scaling-up, standardization, and global competitiveness.

1. *Multi-site implantation:* Traditional freshwater BC techniques were limited to single-site implantation at either the mantle or the visceral mass (S.H. Xie, 2010; Liang, 2015). Mantle implantation typically produces small BC freshwater pearls, while visceral mass implantation is used for cultivating larger pearls. Mantle site selection is largely standardized, with operations usually targeting the outer edge of the mantle tissue. Visceral site selection varies among producers, but practical implantation is confined to a few viable locations: beneath the labial palps, below the pericardial cavity on the dorsal side, and at the junction between the foot and the visceral mass (Akamatsu et al., 2001; S.H. Xie and Y. Xie, 2011; Liang et al., 2015). Of these, foot implantation yields the highest mussel survival rates and pearl quality (S.H. Xie and Y. Xie, 2014).

   Multi-site bead implantation has long been considered a key technical hurdle in the development of the pearl culturing industry. After years of systematic experimentation, a team led by S.H. Xie (2004a) achieved simultaneous culturing in the mantle and visceral mass, significantly increasing the yield (figure 17). This breakthrough improved mussel utilization by two to three times and reduced costs while shortening the culturing cycle, making it a practical solution for increasing production and income. Multi-site implantation has promoted scaling-up, standardization, and sustainable development (Ye, 2015).

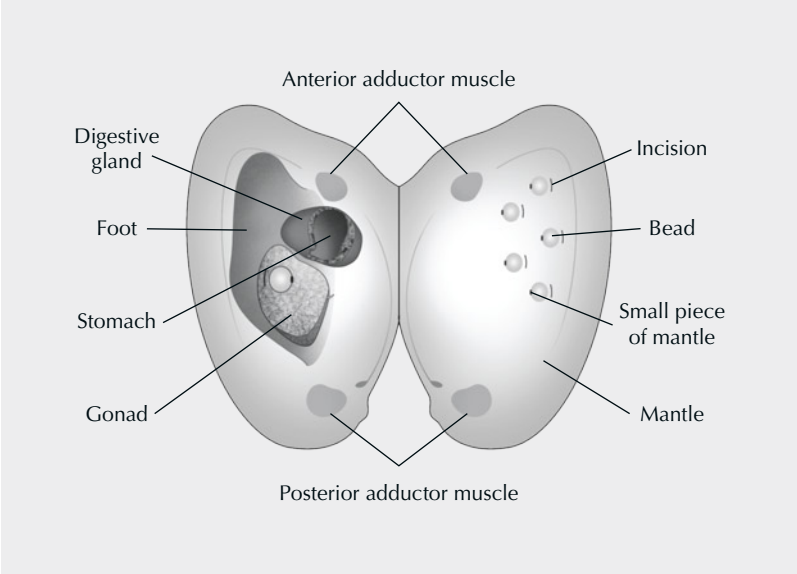

Figure 17. Simultaneous pearl culturing in the mantle and visceral mass of Hyriopsis cumingii.

2. *Precision surgical instruments and efficient culturing management technology development:* The development of specialized nutritional supplements and antimicrobial agents, along with a novel bead inserter offering adjustable functionality and precise positioning, has significantly improved the survival rates of pearl mussels undergoing multiple bead implantations (S.H. Xie and Y. Xie, 2009; H. Chen et al., 2015; X. He et al., 2021; X.H. Li et al., 2023). These innovations have overcome technical challenges in traditional devices, such as insufficient dynamic control and blurred positioning. Furthermore, pre- and post-surgical care protocols, dynamic optimization of stocking density, and real-time monitoring of water quality parameters (e.g., oxygen levels, pH, and ammonia concentration) have enhanced the precision and sustainability of freshwater pearl culturing (S.H. Xie and Y. Xie, 2009; S.H. Xie, 2010).
3. *Freshwater cultured pearl regeneration technology:* Traditional bead culturing techniques are limited to producing a pearl only once per site, severely limiting resource utilization. S.H. Xie (2004a) patented regenerative pearl culturing technology, which involves minimally invasive extraction that preserves the original pearl sac. Based on the size of the pearl sac, appropriately sized beads are selected for re-implantation, enabling the production of regenerated BC pearls. This innovation allows two or three sequential bead implantations during the mussel's typical eight-year lifespan.

TABLE 2. Common Chinese BC freshwater pearls in the international market.

	Baby pearl	"Freshwater akoya"	Gablily	"Edison"	Soufflé
Culturing cycle (years)	0.5–0.8	1–2	3–5	3–5	2–3
Implantation site	Mantle	Mantle	Mantle	Foot	Original pearl sac
Nacre thickness (mm)	0.5–1.5	1.0–3.0	1.5–3.1	0.8–3.0	2.0–4.0
Color	White, pink	White, light pink	White, purple, pink-orange	Deep purple, bronze, violet	Highly iridescent, with a wide variety of overtones
Luster	Strong to very strong	Very strong	Very strong	Very strong	Very strong
Dimension (mm)	≤5	3–9	8–12	11–20	≥12

Note: All freshwater cultured pearl varieties referenced are trade names.

Regenerative culturing produces a variety of high-quality BC pearls within a shorter time frame, reducing waste while significantly enhancing yield (S.H. Xie, 2004b; Y.S. Li and J.L. Li, 2007).

These breakthroughs have dramatically shortened culturing cycles, reduced costs, diversified BC freshwater pearl products, and enhanced the industry's economic, social, and ecological benefits (Gao et al., 2024). They have led to a variety of commercially available BC freshwater pearl products, including Baby pearls, "Edison" pearls, Gablily pearls, soufflé pearls,[2] and "freshwater akoya" pearls.[3] These varieties differ in size, shape, luster, and culturing techniques, as shown in table 2 and figure 18.

Industry Integration and Ecosystem Transformation. Industrial integration is a fundamental trend in modern economic development and a critical pathway for

[2]Soufflé pearls are an important category of regenerated BC freshwater pearls, named for their resemblance to the French dessert. Their bead is composed of a special composite material (a mixture of silt, incense ash, and bioadhesive).

[3]"Freshwater akoya" is a misnomer used by some producers to describe small, round, high-luster freshwater BC pearls that resemble traditional Japanese akoya pearls in appearance.

Figure 18. Commercial Chinese BC freshwater pearl varieties. A: Gablily pearl necklace, 11–13 mm round shape. B: "Edison" pearl necklace, 7.3–8.5 mm round shape. C: Soufflé pearl necklace, 13–19 mm baroque-shaped. Courtesy of Angeperle (A), Zhejiang Dongfang Shenzhou Pearl Group Co., Ltd. (B), and Nanchuang Beibei Ji (C).

achieving sustainable growth (Heo and Lee, 2019). The freshwater pearl culturing industry is shifting away from its traditional role as a primary sector activity (i.e., the extraction of raw materials). It is increasingly integrating with the secondary sector, which focuses on processing and value-added production, and the tertiary sector, which entails marketing, branding, and distribution. The "triple-industry integration" strategy is essential for extending, diversifying, and strengthening industrial chains in rural development contexts (Y. Wang, 2024).

Integration of Tourism, Culture, and Fisheries. The ecological resources of freshwater pearl culturing farms can be converted into added value through tourism, thereby increasing revenue and incentivizing farmers to adopt sustainable practices. For example, Deqing County in Zhejiang Province has developed an integrated "pearl culture and industrial tourism" model around its freshwater pearl culturing industry. This includes pearl-themed study tours (figure 19), museum-based science communication, live pearl harvesting experiences, and intangible cultural heritage workshops, showcasing how pearl culturing, culture, and tourism are jointly driving local income and employment (Shen, 2025). As a result of its achievements in sustainable culturing, Deqing's freshwater pearl composite culturing system was recognized by the Food and Agriculture Organization as a Globally Important Agricultural Heritage System in 2025 (Deqing County Bureau of Agriculture and Rural Affairs, 2025).

Value Chain Expansion. The freshwater pearl culturing industry must balance ecological protection with strategic leveraging of its ecological, social, and economic resources. The city of Zhuji, with strong support from the Collaborative Innovation Center for the Freshwater Pearl Culturing Industry since the center's establishment in 2021, has taken the lead in restructuring and upgrading the entire freshwater pearl culturing value chain. At the upstream level, Zhuji has integrated internal rural resources, such as local pearl farmers, culturing facilities, and traditional

Figure 19. Deqing County provides educational programs related to its freshwater pearl culturing industry, including the one shown here at the Osmun Pearl Museum. Courtesy of Zhejiang Osmun Group Co., Ltd.

Figure 20. Livestreaming from Shanxiahu Town, this host displays pearl jewelry and discusses product features for an online audience. Livestreaming has become an integral component of digital commerce in the freshwater cultured pearl value chain. Photo by Qishen Zhou.

know-how, with external inputs: university research teams, e-commerce platforms, and cross-regional investment. The city has also strengthened industry governance by promoting quality certification systems, traceability standards, and intellectual property protection (Pei et al., 2023).

Midstream, Zhuji has focused on technological upgrading and product diversification through the development of value-added pearl-derived products and the upcycling of low-value or residual pearl resources. For example, local enterprise Fenix Bio-Tech has applied nanotechnology to convert low-grade freshwater pearls into micrometer-sized powder for skincare, increasing product value more than tenfold (R. Xu and X. Lu, 2024). Similarly, pearl powder has been used in textile manufacturing, producing pearl fiber socks with UV resistance and far-infrared health benefits (Miao, 2018; P. Liu et al., 2020).

Downstream, Zhuji has embraced digital commerce to support industry transformation. Livestream selling has become a powerful tool to connect producers and consumers, enabling the transparent display of product, real-time interaction, and origin-based storytelling (figure 20). This innovation has strengthened consumer trust and brand identity, particularly among younger consumers. Online sales in Shanxiahu Town surged from RMB 1 billion (US$150 million) in 2017 to RMB 25 billion (US$3.8 billion) in 2022 (figure 21), highlighting the transformative impact of livestreaming and digital marketing.

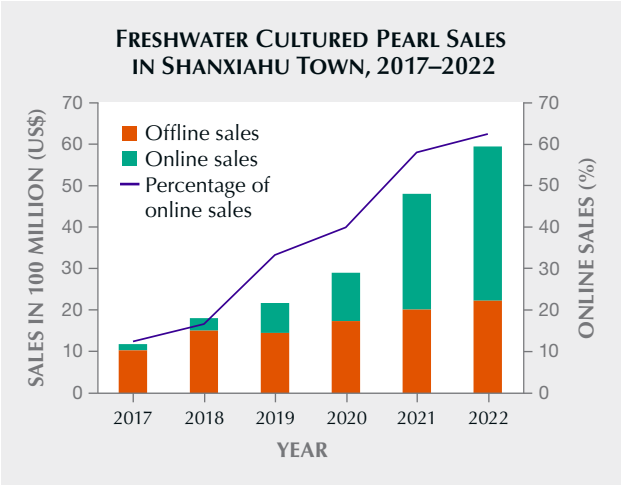

Figure 21. Official media reports indicate that annual gross revenue in Zhuji exceeded RMB 50 billion (US$7.1 billion) in 2023 and 2024, with more than 60% of sales occurring online (C.R. Wang, 2024; X. Huang, 2025). Data sourced from the 2023 World Pearl Conference promotional brochure.

FUTURE PATHWAYS FOR CHINA'S FRESHWATER PEARL CULTURING INDUSTRY

Although China's freshwater pearl culturing industry has largely transitioned to a sustainable development model, it is still at the early stage of developing a pearl production system grounded in circular economy principles (i.e., a closed-loop model in which waste is minimized, byproducts are reused, and nutrient cycles are restored to mimic natural ecosystems). Efforts to implement ecological culturing and closed-loop circular economy models such as resource recycling remain largely confined to the basic environmental management practices of pollution control and waste minimization. Such limited interventions fall short of establishing a comprehensive, regenerative circular system that fully integrates ecological, economic, and social dimensions. Despite the increasing emphasis on quality improvement, there are still notable weaknesses in research and development capacity, particularly in developing high-value-added pearl products. Diversifying the industry's value chain and fully aligning ecological sustainability with global value chain integration remains a long-term goal.

Supply and Demand. Between 2017 and 2020, due to the tightening of environmental protection policies, the global production of freshwater cultured pearls, as well as in China, declined year by year. Conversely, Chinese market demand rebounded in 2021 (China Jewelry and Jade Industry Association, 2024), driven in part by "revenge spending" after the COVID-19 pandemic—a phenomenon in which consumers compensated for prolonged lockdowns and suppressed desires through unusually high levels of consumption (Liu et al., 2023). The same lockdown conditions also accelerated the adoption of livestreaming e-commerce (Lu et al., 2025). This trend was particularly evident in Shanxiahu Town, China's foremost pearl distribution center, where online sales increased from 13% of total sales in 2017 to 63% in 2022, and online sales grew by nearly 25 times over the same period (again, see figure 21). This micro-market boom coincided with a strong global macroeconomic recovery in 2021, in which real gross domestic product (GDP) growth surged to 6.1% following the 3.1% decline in 2020 (International Monetary Fund, 2026). This release of pent-up consumer demand, coupled with the macroeconomic tailwinds, further bolstered the market's buoyancy.

Under the dual effects of supply contraction and surging demand, the supply-demand imbalance intensified, leading to a general rise in pearl prices. The price of ordinary freshwater pearls rose by 30–50%, while high-quality freshwater pearls increased by approximately 80% (CCTV Finance, 2023; Guan, 2023). Stimulated by high prices, Chinese pearl farmers significantly expanded production. However, the biological cycle of pearl cultivation created a delay in supply response. After bottoming out in 2020, China's freshwater pearl output began a steady recovery, climbing to 1,125 tonnes in 2024 (*China Fisheries Statistical Yearbook*, 1980–2025). The upstream segment of the culturing industry benefited significantly from this development. Mussel pond lease rates soared from RMB 4,500–7,500 (US$46–77) per hectare to RMB 30,000 (US$307) per hectare; daily wages of culturing technicians increased from RMB 200 (US$31) to RMB 600–800 (US$92–123); and mussel seeding spat prices more than tripled (based on author YX's field research data from October 2024).

However, the post-pandemic momentum soon dissipated. Following the 2021 rebound, global economic growth settled, stabilizing at a moderate level between 3.2% and 3.5% from 2022 to 2025 (International Monetary Fund, 2026). This macroeconomic deceleration, coupled with the fading of the post-pandemic "revenge spending," steered consumer behavior toward a more cautious and rational approach. Starting in 2024, the surge in supply coincided with a decline in demand, placing significant downward pressure on both the volume and price of ordinary pearls (Zhao and Huang, 2025). Over the next two to three years, as supply-and-demand dynamics gradually rebalance, production growth is expected to slow significantly, with a potential risk of decline.

Innovation and Sustainable Development. Disruptive technologies and frontier innovations have consistently driven industrial transformation (Musson and Robinson, 1989). China's freshwater pearl culturing sector currently stands at a strategic inflection point, where resource-intensive production models yield increasingly diminishing returns. Next-generation culturing technologies that are currently in the pilot phase require 7–10 years for nationwide adoption. Despite achieving vertical integration, the industry's global brand equity lags behind production. The industry's growth is now driven by innovation rather than resource inputs such as labor,

land, and capital. Firmly establishing "innovation empowerment" as the primary strategy and targeting the weaker segments of the value chain are essential for culturing enterprises to gain market advantage.

Overcoming longstanding technological bottlenecks in culturing and adopting advanced technologies will help boost production. Priority should be given to intelligent aquaculture systems and bleaching techniques to enhance luster. Enhancing pearl quality and developing new varieties that align with market demand are also critical. In terms of value chain integration, China's industry should pursue a strategic upgrade by making the culturing, processing, and design stages more advanced, intelligent, and eco-friendly. This approach will help transform China's production capacity advantage into a value advantage. Continuous investment in research and development is key to enhancing added value and competitiveness. Ultimately, the goal is to shift from outdated traditional production methods to more eco-friendly techniques. This transition will also redefine the industry from a source of water pollution to a water restoration and management contributor.

Digital-Intelligent Economy. Digital technologies and artificial intelligence are a natural fit for China's freshwater pearl culturing industry. The entire culturing process demands the kind of precision control that only advanced intelligent systems can provide. Digital transformation makes it possible to track multiple parameters (e.g., temperature, humidity, and microbiome dynamics) in real time, all managed visually through network-connected platforms. To advance the industry further, strategic investments from venture capital and e-commerce entities should be used to develop dedicated digital trading platforms. Emerging approaches such as livestream-enabled commerce should be embraced, supported by an integrated service architecture spanning culturing, sales, certification, and logistics. Finally, industry associations and local regulators should integrate critical resources—technological, financial, and market-related. By applying these integrated resources throughout the value chain, from culturing to product design and marketing, the industry can move toward a comprehensive ecosystem powered by intelligent systems.

Standardized Accountability Systems. As a global leader in water pollution control, China has tightened its environmental governance in recent years. However, unregulated culturing operations by certain producers jeopardize the sector's reputation, potentially hindering development in production and trading. Culturing associations, working jointly with provincial freshwater pearl culturing representatives, should establish eco-friendly standards addressing industrial sustainability and environmental protection and implement long-term pollution control mechanisms.

Moving forward, freshwater pearl culturing wastewater treatment projects should strictly adhere to the "Technical guideline for the development of local discharge and control standards of water pollutants for aquaculture" (Ministry of Ecology and Environment of the People's Republic of China, 2023). Specific measures include: (1) raising environmental awareness among members of the industry to ensure they understand the importance of wastewater treatment; (2) conducting regular wastewater monitoring, strengthening supervision and inspection efforts to promptly identify and resolve issues, and ensuring that wastewater treatment meets the required standards; and (3) exploring the potential of "carbon labeling" within the industry chain. By fully leveraging the carbon capture and storage potential of freshwater pearl culturing, the industry can establish carbon footprint and labeling management systems to certify products and mussel-shell-based crafts with carbon labels. This initiative not only enhances the value and low-carbon appeal of pearl and mussel shell products but also contributes to the industry's carbon reduction goals.

In conclusion, stakeholders across the freshwater pearl value chain—producers, processors, brands, and distributors—must recognize ecological challenges, eliminate outdated practices, and harmonize production with environmental responsibility to advance the industry toward eco-friendly, safe, and integrated development.

ABOUT THE AUTHORS

Dr. Qishen Zhou is an associate professor at the Gemmological Institute, China University of Geosciences (CUG) in Wuhan, and a researcher at Xinjiang University of Technology. Yalan Xu (xyl1673@cug.edu.cn, corresponding author) is a doctoral candidate at the School of Economics and Management, CUG in Wuhan, and a lecturer at the School of Jewelry and Art Design, Wuzhou University. Dr. Deyi Xu is a professor at the School of Economics and Management, CUG in Wuhan. Jingping Hu and Mancun Zhao are master's degree candidates at the Gemmological Institute, CUG in Wuhan.

ACKNOWLEDGMENTS

This research was supported by the 2024 Ministry of Education Humanities and Social Sciences Research General Project (Planning Fund Project) titled "Research on the Value-Addition and Upgrade of China's Pearl Industry within the Global Value Chain from a Hyper-Circular Economy Perspective" (Project no.: 24YJA790103), as well as the Center for Jewelry Heritage and Innovation, China University of Geosciences in Wuhan.

REFERENCES

Akamatsu S., Zansheng L.T., Moses T.M., Scarratt K. (2001) The current status of Chinese freshwater cultured pearls. *G&G*, Vol. 37, No. 2, pp. 96–109, https://doi.org/10.5741/GEMS.37.2.96

Bai Z.Y., Wang G.L., Liu X.J., Li J.L. (2014) The status and development trend of freshwater pearl seed industry in China. *Journal of Shanghai Ocean University*, Vol. 23, No. 6, pp. 874–881 [in Chinese].

Binjiang District Water Treatment Office (2022) River mussels for water treatment: Another attempt at scientific water management. April 19, https://www.hhtz.gov.cn/art/2022/4/19/art_1487008_59042390.html [in Chinese].

CCTV Finance (2023) Pearl prices soar: Some varieties double in price, young people become main consumers. *CNR News*, June 2, https://news.cnr.cn/native/gd/20230602/t20230602_526273207.shtml [in Chinese].

Chen H., Li X., Li X., Kong Q., He H. (2015) Nucleus treatment solution for freshwater nucleated pearls, its application, and treatment method. Patent no. CN103330717B, China.

Chen Y., Yao Y., Shen X., Fu Y., Bian X., Li W., Liu S. (2024) Transcription profiling reveals co-regulation mechanism of gene expression related to growth and mineralization induced by pearl cultivation in *Hyriopsis cumingii*. *Frontiers in Marine Science*, Vol. 11, article no. 1443863, https://doi.org/10.3389/fmars.2024.1443863

China Fisheries Statistical Yearbook (1980–2025) Compiled by the Ministry of Agriculture and Rural Affairs, the Fisheries and Fisheries Administration Bureau, the National Aquatic Technology Extension Center, and the China Society of Fisheries. China Agriculture Press, Beijing [in Chinese].

China Jewelry and Jade Industry Association (2024) China jewelry industry development report, 2019–2023, https://jewelleryupload.oss-cn-beijing.aliyuncs.com/temp/20241219102618_2910.pdf [in Chinese].

Cui Z.H., Zhou X.Y., Zhang G.F., Hu Z.J., Liu Q.G., Yan L.L., Li J.L. (2012) Effect of silver carp (*Hypophthalmichthys molitrix*) and bighead carp (*Aristichthys nobilis*) on growth and culturing water quality for pearl mussel (*Hyriopsis cumingii*). *Journal of Fisheries of China*, Vol. 36, No. 2, pp. 278–283 [in Chinese].

Dai Y.X., Wang Y., Tang J.Y, Li Y.M. (2013) Effects of different mixed culturing fish and feeding methods on the chemical characteristics of fish mussels in integrated culturing. *Chinese Fishery Science*, Vol. 2, pp. 351–360 [in Chinese].

Deqing County Bureau of Agriculture and Rural Affairs (2025) Our county's freshwater pearl composite farming system designated as a GIAHS. May 30, http://www.zgzhijiang.gov.cn/content-54-493677-1.html [in Chinese].

Department of Science, Technology and Education of the Ministry of Agriculture (2012) *Compilation of Practical Technologies for Agricultural Simplification*. China Agriculture Press [in Chinese].

Fiske D., Shepherd J. (2007) Continuity and change in Chinese freshwater pearl culturing. *G&G*, Vol. 43, No. 2, pp. 138–145, https://doi.org/10.5741/GEMS.43.2.138

Fu B., Liu S., Tao S., Yuan Y., Huang J. (2024) A fully controllable industrialized pearl culturing system. Patent no. CN109526851B, China.

Gao J.P., Li J.L., Bai Z.Y. (2024) Correlation and path analysis between the quality of nucleated pearls from the mantle of *Hyriopsis cumingii* and growth traits of host mussel. *Advances in Fisheries Science*, Vol. 45, No. 5, pp. 204–212, https://doi.org/10.19663/j.issn2095-9869.20230517001 [in Chinese].

General Office of the CPC Central Committee & General Office of the State Council (2016) Opinions on the comprehensive implementation of the river chief system, effective on December 11, https://www.gov.cn/gongbao/content/2017/content_5156731.htm [in Chinese].

——— (2019) Regulations on the central government's supervision of ecological environmental protection, effective on June 6, https://www.gov.cn/gongbao/content/2019/content_5404149.htm [in Chinese].

Guan Y. (2023) Some pearl prices soar to 10 times the original price! Sellers predict further increases. *Qilu Evening News*, October 24, https://m.gmw.cn/2023-10/24/content_1303549013.htm [in Chinese].

Guo W. (2022) Automated pipeline-based mussel supply and feeding system. Patent no. CN106305561B, China.

He C.Q. (2024) So impressive! Zhuji's pearl culturing technology to be used to improve water quality of Taihu Lake. *Shaoxing Daily*, August 28, https://www.shaoxing.com.cn/p/3234825.html [in Chinese].

He X., Zhang X., Zhan W. (2021) A method for bead insertion of freshwater bead cultured pearls. Patent no. CN113632753A, China.

Heo P.S., Lee D.H. (2019) Evolution patterns and network structural characteristics of industry convergence. *Structural Change and Economic Dynamics*, Vol. 51, pp. 405–426, https://doi.org/10.1016/j.strueco.2019.02.004

Hoang T.C., Black M.C., Knuteson S.L., Roberts A.P. (2019) Environmental pollution, management, and sustainable development: Strategies for Vietnam and other developing countries. *Environmental Management*, Vol. 63, No. 4, pp. 433–436, https://doi.org/10.1007/s00267-019-01144-z

Horne A.C., Kaur S., Szemis J.M., Costa A.M., Nathan R., Webb J.A., Stewardson M.J., Boland N. (2018) Active management of environmental water to improve ecological outcomes. *Journal of Water Resources Planning and Management*, Vol. 144, No.

12, article no. 04018079, https://doi.org/10.1061/(ASCE)WR.1943-5452.0000991
Hubei Provincial Department of Agriculture (2016) Notice on prohibiting fertilizer (manure) aquaculture and banning pearl cultivation, No. 272, effective on November 10, http://www.zgzhijiang.gov.cn/content-54-493677-1.html [in Chinese].
Huang C.L. (2025) The concept that "Green mountains and clear waters are as valuable as mountains of gold and silver": The "revolution of terminology" in human development concepts. *People's Daily*, http://theory.people.com.cn/n1/2025/0514/c40531-40479390.html [in Chinese].
Huang X. (2025) "Platform + industry" promotes pearls to the world. Xinhua News Agency, June 23, https://baijiahao.baidu.com/s?id=1835715387213652914&wfr=spider&for=pc [in Chinese].
Hui Y. (2014) Analysis on ecological culturing mode of raising fish, turtle, loach and crayfish in paddy fields of Fujian mountain area. *Journal of Fisheries Research*, Vol. 36, No. 5, pp. 391–397, https://doi.org/10.14012/j.cnki.fjsc.2014.05.008 [in Chinese].
International Monetary Fund (2026) Global economy in the shadow of war. https://www.imf.org/en/publications/weo/issues/2026/04/14/world-economic-outlook-april-2026
Jia J.X., Luo L.H., Gu J. (2023) Local government environmental regulation and high-quality economic development. *Chinese Industrial Economy*, No. 5, pp. 99–117, https://doi.org/10.19581/j.cnki.ciejournal.2023.05.006 [in Chinese].
Jindong District Government Office of Jinhua City (2017) Notice on issuing the work plan for the remediation of pearl cultivation pollution in Jindong District, Document No. 28, effective on May 5, https://www.jindong.gov.cn/art/2017/5/5/art_1229403632_1642601.html [in Chinese].
Li G.F. (1981) Experimental summary of freshwater pearl culturing technology. *Hebei Fisheries Science and Technology*, No. 3, pp. 18, 29–31 [in Chinese].
Li J.L., Bai Z.Y. (2007) A new breed of freshwater culturing—Kangle mussel. *Chinese Aquatic Products*, No. 10, pp. 44–45, https://doi.org/10.3969/j.issn.1002-6681.2007.10.027 [in Chinese].
Li J.L., Bai Z.Y., Ye W.X., Feng J.B., Wang Z. Chen W.M. (2021) Chinese triploidy freshwater mussel *Hyriopsis cumingii* "Shenzhen No. 3." *China Fisheries*, Vol. 12, pp. 102–106 [in Chinese].
Li J.L, Wang D.F., Bai Z.Y., Guan Y.B., Wu C.D., Chen L.S. (2019) Report on the development of freshwater pearl culturing industry in China. *Chinese Fisheries*, No. 3, pp. 23–29 [in Chinese].
Li J.L., Sun M.L., Bai Z.Y., Yuan Y., Fu B. (2025) Construction and application of industrial recirculating aquaculture system for high-quality freshwater pearls. *Journal of Fisheries Science*, Vol. 38, No. 4, pp. 67–76, https://doi.org/10.3969/j.issn.1005-3832.2025.04.010 [in Chinese]
Li Y.S., Li J.L. (2007) New culturing technology of regenerated non-bead pearls. *China Fisheries*, No. 7, pp. 44–45 [in Chinese].
Li X.H., Zhan Y., Jin W. (2023) A bead insertion tool for freshwater pearl mussel culturing. Patent no. CN220123714U, China.
Liang F.L., Xie S.H., Lin W.C. (2015) Advances in pearl culturing in *Hyriopsis cumingii*. *Bulletin of Marine and Limnology*, Vol. 2, pp. 113–118, https://doi.org/10.13984/j.cnki.cn37-1141.2015.02.016 [in Chinese].
Liao C.H. (2012) A preliminary study on the geographical distribution and trade of ancient pearls: Taking directionally named pearls as examples. *Agricultural Archaeology*, No. 1, pp. 221–225 [in Chinese].
Liu F., Tu L. (2007) Hubei completely bans pearl culturing in lakes and reservoirs. *Changjiang Business Daily*, August 22, https://news.sina.com.cn/c/2007-08-22/171813721008.shtml [in Chinese].
Liu P., Jia K.K., Wen L. (2020) Research progress and qualitative identification methods of pearl fiber. *Textile Testing and Standards*, Vol. 6, No. 6, pp. 1–4, https://doi.org/10.19391/j.cnki.cn31-2117.2020.06.001 [in Chinese].
Liu W. (2021) Zhuji, Zhejiang: Ecological aquaculture enriches people with mussels: "Pearl brilliance" reflects clear waters. *Economic Daily*, August 22, http://tuopin.ce.cn/zg/202112/23/t20211223_37196511.shtml [in Chinese].
Liu Y., Cai L., Ma F., Wang X. (2023) Revenge buying after the lockdown: Based on the SOR framework and TPB model. *Journal of Retailing and Consumer Services*, Vol. 72, article no. 103263, https://doi.org/10.1016/j.jretconser.2023.103263
Lu W., Ji X., Wu J. (2025) Retailer's information sharing and manufacturer's channel expansion in the live-streaming e-commerce era. *European Journal of Operational Research*, Vol. 320, No. 3, pp. 527–543, https://doi.org/10.1016/j.ejor.2024.09.008
Miao F.C. (2018) Properties and product development of pearl fiber. *Journal of Wuhan Textile University*, Vol. 31, No. 6, pp. 15–20 [in Chinese].
Ministry of Agriculture and Rural Affairs (2003) Regulations on quality and safety in culturing, effective on July 24, https://www.gov.cn/gongbao/content/2004/content_62952.htm [in Chinese].
——— (2020) Notice on the implementation of the "Five Major Actions" for green and healthy aquaculture in 2020, effective on March 30, https://www.gov.cn/zhengce/zhengceku/2020-04/01/content_5497877.htm [in Chinese].
Ministry of Ecology and Environment, and Ministry of Finance (2016) National rural environmental comprehensive improvement "13th Five-Year Plan," effective on December 28, https://www.eco.gov.cn/news_info/23887.html [in Chinese].
Ministry of Ecology and Environment of the People's Republic of China (2023) Technical guideline for the development of local discharge and control standards of water pollutants for aquaculture (HJ 1217—2023), effective on March 1, https://www.mee.gov.cn/ywgz/fgbz/bz/bzwb/shjbh/swrwpfbz/202302/t20230224_1017491.shtml [in Chinese].
Ministry of Education (2023) Promoting the upgrading of the pearl industry through innovative breeding models to support rural revitalization, effective on December 12, http://www.moe.gov.cn/jyb_xwfb/xw_zt/moe_357/jjyzt_2022/2022_zt04/dianxing/anli/202312/t20231212_1094340.html [in Chinese].
Musson A.E., Robinson E. (1989) *Science and Technology in the Industrial Revolution*. Gordon and Breach Science Publishers, New York.
Pang Y.Y. (1958) *Wenchang Miscellany*. Zhonghua Book Company, Beijing [in Chinese].
Pei X.Q., Guo S.Y., Zhu H.Y. (2023) The shining pearl town. *Farmers' Daily*, November 7, https://m.thepaper.cn/baijiahao_25206827 [in Chinese].
Shao K. (2021) Collapsed pits and ponds yield "shining pearls." *Xinhua News*, January 20, http://www.xinhuanet.com/2021-01/20/c_1127003696.htm [in Chinese].
Shen Y.X. (2025) Osmun ranks among top ten "fun factories" in Zhejiang. *Deqing News*, August 19, https://dqnews.zjol.com.cn/dqnews/system/2025/08/19/035030254.shtml
Standing Committee of the People's Congress of Hubei Province (2012) Hubei province lake protection regulations, effective on October 1, https://slt.hubei.gov.cn/fbjd/zcwj/zcfg/201206/t20120604_863704.shtml [in Chinese].
Standing Committee of the People's Congress of Zhejiang Province (2009) Zhejiang Province water pollution prevention and control regulations, effective on January 1, https://slt.zj.gov.cn/art/2021/8/18/art_1229560891_2322480.html [in Chinese].
——— (2017) Regulations on the river chief system in Zhejiang Province, effective on October 1, https://slt.zj.gov.cn/art/2021/8/18/art_1229560891_2322446.html [in Chinese].
State Council (2015) Water pollution prevention and control

action plan, effective on April 2, https://www.gov.cn/gongbao/content/2015/content_2853604.htm [in Chinese].
——— (2016) 13th five-year plan for ecological environmental protection, effective on November 24, https://www.gov.cn/gongbao/content/2016/content_5148753.htm [in Chinese].
State Environmental Protection Administration (2007) The implementation of "basin approval restrictions" in the heavily polluted waters of the Yangtze River Delta, Yellow River Delta, Huaihai River Delta should establish a unified water management mechanism and a new environmental and economic policy system, issued on July 3, https://www.mee.gov.cn/gkml/sthjbgw/qt/200910/t20091023_180094.htm [in Chinese].
Sun C.H., Bai Z.Y., Li Q.Q., Peng J.Q., Li J.L. (2019) Optimization of early composite selection for growth and shell color traits of *Hyriopsis cumingii*. *Progress of Fishery Science*, Vol. 40, No. 2, pp. 91–97, https://doi.org/10.19663/j.issn2095-9869.20180201001 [in Chinese].
Tang Y., Zhao L., Cheng Y., Yang Y., Sun Y., Liu Q. (2021) Control of cyanobacterial blooms in different polyculture patterns of filter feeders and effects of these patterns on water quality and microbial community in aquacultural ponds. *Aquaculture*, Vol. 542, article no. 736913, https://doi.org/10.1016/j.aquaculture.2021.736913
Verma A.K., Rahman A., Hussain S., Singh N.S. (2025) Freshwater mussels as multifaceted ecosystem engineers: Insights into their ecological importance, bioindication, and economic contributions. *Water*, Vol. 17, No. 11, article no. 1629, https://doi.org/10.3390/w17111629
Wang B., Min Q.W., Xue Y.H. (2023) Principle, benefits and influencing factors of fish-mussel mixed culturing. *Environmental Ecology*, Vol. 5, No. 3, pp. 66–69, 98 [in Chinese].
Wang C.R. (2024) Small pearls "string" together a billion-dollar industry. *China National Radio*, April 1, https://zj.cnr.cn/tdzj/20240201/t20240201_526578880.shtml [in Chinese].
Wang H.M. (2017) The "Five-Water Co-governance" initiative continues to make efforts, and Zhejiang Province aims to completely eliminate Inferior V water within the year. *People's Daily*, February 7, http://politics.people.com.cn/n1/2017/0207/c1001-29061838.html [in Chinese].
Wang Y. (2024) Enriching the people effect, realistic obstacles and coping strategies of industrial convergence. *Agricultural Economy*, No. 7, pp. 117–118 [in Chinese].
Wang Z.Y. (2023) Genome-wide association analysis and genome selection breeding of growth and inner shell color traits in *Hyriopsis cumingii*. Doctoral dissertation, Shanghai Ocean University [in Chinese].
Xie N., Li Y., Zheng H., Wang G., Li J., Oi N., Yuan W. (2006) Comparison of culture and pearl performances among *Hyriopsis schlegelii*, *Hyriopsis cumingii*, and their reciprocal hybrids. *Journal of Shanghai Fisheries University*, Vol. 15, No. 3, pp. 264–269 [in Chinese].
Xie S.H. (2004a) A method for culturing bead regenerated freshwater pearls. Patent no. CN1163121C, China.
——— (2004b) A method for inserting bead into mussels for freshwater pearl culturing. Patent no. CN1163120C, China.
——— (2010) Research on large area culturing technology of freshwater beaded pearl. *Journal of Guangdong Ocean University*, No. 1, pp. 55–58 [in Chinese].
Xie S.H., Xie Y. (2009) A device for inserting bead into freshwater mussels for pearl culturing. Patent no. N200820051856.1, China.
——— (2011) A method for culturing large pearls by bead implantation in the visceral sac of freshwater mussels. Patent no. 201010537371.5, China.
——— (2014) A high-efficiency pearl culturing method using foot implantation in freshwater mussels. Patent no. CN104187638A, China.
Xinhua Daily Telegraph (2016) Encountering environmental "eviction order": The transformation of the beautiful pearl industry under pressure. *Xinhuanet*, June 17, https://www.xinhuanet.com/politics/2016-06/17/c_129070223.htm [in Chinese].
Xiong D.R., Wu J.D., He X.J. (1980) A preliminary study on the formation of bead-free pearls in mussels. *Journal of Zhanjiang Fisheries College*, No. 2, pp. 1–7 [in Chinese].
Xu G., Lu Y. (2019) On the governance experience and future of the "Five Water Co-governance" project: Based on the perspective of collaborative governance theory. *Administration Reform*, No. 2, pp. 33–40, https://doi.org/10.14150/j.cnki.1674-7453.2019.02.007 [in Chinese].
Xu R., Lu X. (2024) Spring breeze sweeps across new horizons: Grinding sand into pearls blossoms. *Xinhuanet*, February 21, http://www.zj.xinhuanet.com/20240221/a5acb0eba2924d63b5b3c3224bfc1dfe/c.html [in Chinese].
Yan X.W., Meng Y.Z. (2022) The transformation of pearl lake. Central Commission for Discipline Inspection and the National Supervisory Commission, November 6, https://www.ccdi.gov.cn/yaowenn/202211/t20221106_229005.html [in Chinese].
Yang A., Zhang P. (2016) Deqing Have Bright Pearls—A Compilation of Research Results on the Source of Pearls. *China Friendship Press*, Beijing [in Chinese].
Yang M.X., Huang F.M., Zhou Y. (2003) Characteristics and genesis of the "waist constriction" feature of freshwater cultured pearls from Ezhou, Hubei Province. *Journal of Gems and Gemmology*, No. 2, pp. 11–14, 52, https://doi.org/10.15964/j.cnki.027jgg.2003.02.004 [in Chinese].
Yang Y., Liu J. (2023) Fuyang: Raising pearls in a subsiding area. *Fuyang Daily*, April 6, https://test.fynews.net/epaper/read.do?m=i&iid=2853&eid=27389&sid=95032&idate=1_2023-04-06 [in Chinese].
Yao K.L. (1978) Explored ways to shorten the production cycle of pearl culturing. *Aquatic Science and Technology Information*, No. 12, pp. 18–20 [in Chinese].
Ye Q. (2015) Shaohu Pearl pioneers China's "freshwater beaded pearl" culturing technology: "Multi-pearls per mussel" technology effectively enhances pearl production capacity. *Guangdong Science and Technology*, No. 5, pp. 25–27 [in Chinese].
Yu X.B., Zhao Z., Tang R., Xiong B., Wu Z.L., Su S.Q., Yao W.Z. (2020) Assessment of the environmental purification of triangle sail mussel (*Hyriopsis cumingii*) in recirculating aquaculture systems. *Applied Ecology and Environmental Research*, Vol. 18, No. 2, pp. 3439–3454, https://doi.org/10.15666/aeer/1802_34393454
Zeng N.H., Tang X.B., Peng K.X., Wang J.P. (2007) The status quo and development countermeasures of Hunan pearl industry. *Inland Aquatic Products*, Vol. 32, No. 10, pp. 4–7, https://doi.org/10.3969/j.issn.1674-9049.2007.10.001 [in Chinese].
Zhang G., Hu Y., Han X.L., Wang Z., Chen Y.H. (2020) Design of distributed water quality monitoring system under circulating water aquaculture mode of freshwater pearl mussels. *Transactions of Agricultural Engineering*, Vol. 36, No. 7, pp. 239–247, https://doi.org/10.11975/j.issn.1002-6819.2020.07.028 [in Chinese].
Zhang G.F. (2004) Freshwater pearl culturing techniques (Part 1). *Scientific Fish Farming*, No. 10, pp. 10–11 [in Chinese].
Zhang G.F., Xu S.J., Fang A.P. (2013) Effects of graft tissue on color genesis of non-bead cultured pearls produced in *Hyriopsis cumingii* mantle. *Acta Hydrobiologica Sinica*, Vol. 37, No. 3, pp. 581–587, https://doi.org/10.7541/2013.66 [in Chinese].
Zhang Q.P. (2024) Culturing mussel seedlings leads to a better life. *Wuyi County Media Center*, May 10 [in Chinese].
Zhang Y.P. (1973) Exploration of freshwater pearl culturing technology. *Freshwater Fishery*, No. 12, pp. 20–22 [in Chinese].
Zhao X., Huang Z.L. (2025) Overall decline in pearl prices as consumption gradually returns to rationality. *New Rural*

Technologies, No. 10, pp. 54–55, https://doi.org/10.3969/j.issn.1002-3542.2025.10.027 [in Chinese].
Zheng J.H. (2021) From fish farmer to freshwater pearl farmer, how did Shen Zhirong do it? *Farmers' Daily*, December 23, https://m.thepaper.cn/baijiahao_15974257 [in Chinese].
Zhou G.Y. (2021) From polluted water to purified water, Zhuji has launched a "green revolution" in pearl culturing. *Shaoxing Daily*, November 15, http://epaper.shaoxing.com.cn/sxrb/pc/content/202111/15/content_73166.html [in Chinese].
Zhou Y.M. (2024) Huaibei, Anhui Province: "Double harvest" of pearl culturing in coal mining subsiding area. *Xinhuanet*, October 24, http://www.ah.xinhuanet.com/20241024/4334161d019c475c9a8e61e6d0fe893a/c.html [in Chinese].
Zhu Y. (2017) Pearls in the dust: The critical moment of China's freshwater pearl industry. *Economic Observer*, September 1, https://www.eeo.com.cn/2017/0901/311913.shtml [in Chinese].
Zhuji City Association for Science and Technology (2023) The doctor has helped enterprises in Zhuji explore the precedent of factory-based pearl culturing, April 20, http://sxkx.sx.gov.cn/art/2023/4/20/art_1483462_58886756.html [in Chinese].
Zhuji Municipal People's Government Office (2017) Implementation opinions on accelerating the transformation and upgrading of the pearl industry (Zhuzhengbanfa, No. 85), effective on September 13, https://www.zhuji.gov.cn/art/2017/9/13/art_1229079889_423471.html [in Chinese].
Zhuji Water Resources and Hydropower Bureau (2017a) Supporting of transformation and upgrading of pearl culturing work notice, effective on September 13, https://www.zhuji.gov.cn/art/2020/6/4/art_1229561657_1804458.html [in Chinese].
——— (2017b) Implementation plan for accelerating the treatment of pond aquaculture wastewater in Zhuji City, effective on August 24, https://www.zhuji.gov.cn/art/2020/6/4/art_1229561657_1804462.html [in Chinese].

Glass-Ceramics as Imitation Gemstones: A Study on a Silicon-Aluminum-Magnesium-Zinc System

Wasura Soonthorntantikul, Wim Vertriest, and Karen Avakyan

Glass-ceramics are materials consisting of crystalline phases dispersed in an amorphous glassy matrix, produced by the controlled nucleation of forming crystallites from the molten glass host. With characteristics of both glasses and ceramics, they can be created in any color and transparency and in a wide array of refractive indices depending on their composition, making them ideal for use as imitation gemstones. Accurate identification requires a combination of standard and advanced gemological testing, using instruments available in major gemological laboratories. For glass-ceramics with a composition dominated by silicon, aluminum, magnesium, and zinc, the most effective identification method combines refractive index, major chemical composition, and photoluminescence and infrared absorption data. Key characteristics of this material include: a single refractive index between 1.60 and 1.63; an unusual combination of elements—mainly silicon, aluminum, magnesium, zinc, titanium, and zirconium—determined through bulk analysis with energy-dispersive X-ray fluorescence spectroscopy; infrared absorption bands around 3380 and 3440 cm^{-1} (which are absent in natural and manufactured glass); and a photoluminescence spectrum resembling that of spinel-group minerals. The properties of silicon-aluminum-magnesium-zinc glass-ceramics are consistent across the range of colors and transparencies.

At first, the concept of glass-ceramics might sound counterintuitive. Glasses are an amorphous solid lacking any crystal structure, while ceramics are typically composed of fine-grained crystallites fused together. Glass-ceramics combine characteristics of both, resulting in good mechanical strength, thermal shock resistance, and zero porosity or permeability, making them very suitable for gem and jewelry applications (figure 1).

This study examines the nature of glass-ceramic material and its use as an imitation gem, focusing on identification criteria for glass-ceramics of a specific chemical composition—silicon-aluminum-magnesium-zinc—to distinguish these from natural and laboratory-grown gemstones as well as glass imitations.

See end of article for About the Authors and Acknowledgments.
Gems & Gemology, Vol. 62, No. 2, pp. 164–176,
https://doi.org/10.5741/GEMS.62.2.164
© 2026 Gemological Institute of America

BACKGROUND

Glass-ceramics are inorganic, nonmetallic materials that start as a glass and, through controlled nucleation, form fine crystalline grains evenly dispersed in the glassy matrix. Within a glass-ceramic, the volume

In Brief

- Glass-ceramics form a unique category of materials, defined by one or more fine-grained crystalline phases dispersed in a glassy matrix. This structure results in improved mechanical strength, high thermal tolerance, and the ability to introduce a wide variety of coloring agents, making these materials ideal for use as imitation gemstones.
- Glass-ceramics can be produced in practically any color and transparency. They can be readily separated from natural stones and glasses through a combination of standard and advanced gemological methods.
- Their low cost, ease of manufacturing, and variety of colors and transparencies make them a popular choice for mass-produced fashion jewelry.

Figure 1. Glass-ceramics can be created in a full spectrum of colors to imitate a wide range of natural gemstones. Shown here are transparent samples (0.10–0.37 ct) donated for this study by the Formica Group, from left to right: GC-01 to GC-10 (top row) and GC-11 to GC-24 (bottom row). Photo by Nuttapol Kitdee.

percentage of crystalline phases is wide ranging and can vary from nearly 100% to less than 0.0001% (Deubener et al., 2018). Glass-ceramics have been used for decades in many industries, largely for their combination of mechanical strength and heat resistance (Höland and Beall, 2020). A familiar example is the glass-ceramic cooktop on induction stoves found in many kitchens. This surface is designed to withstand high heat and thermal shock, as well as constant impact from pots and pans.

For gem and jewelry applications, glass-ceramic materials are engineered to contain elements that act as chromophores to impart a desired color and highly uniform color distribution. A virtually unlimited array of hues, saturations, and transparencies can be created with the addition of certain trace elements. Glass-ceramics exhibit high heat tolerance, which facilitates their use in large-scale jewelry manufacturing processes. Most common gems (natural, laboratory-grown, and imitation) must be manually set after metal mountings are cast, because the temperatures required during casting exceed the gems' heat tolerance; setting them during the casting process would result in mechanical failure and color fading of the stones. Glass-ceramics, with their high heat tolerance, can be used in a direct casting process without losing their color. These physical properties make the material particularly suitable for use in jewelry (Vyshnevskyi et al., 2017; Dymshits and Zhilin, 2017). Nonetheless, significant development of glass-ceramics for the jewelry industry only started about a decade ago.

Glass-ceramics are conducive to large production volumes and high yields of finishable material, resulting in very low costs for finished goods—often retailing for less than US$1 per carat. This combination of affordability, variety and versatility, and ease of manufacturing makes them an attractive option for mass-produced costume jewelry.

This article will refer to the initial glass (prior to the development of internal crystalline phases) as "optical glass" to clearly differentiate it from the final glass-ceramic material. The phase diagram of silicon-aluminum-magnesium oxides shown in figure 2 approximates the composition of glass-ceramics in this study. In producing glass-ceramics, internal

Figure 2. Simplified ternary diagram of the silicon oxide (SiO_2)–aluminum oxide (Al_2O_3)–magnesium oxide (MgO) system for producing silicon-aluminum-magnesium-zinc glass-ceramics. Modified from Levin et al. (1964).

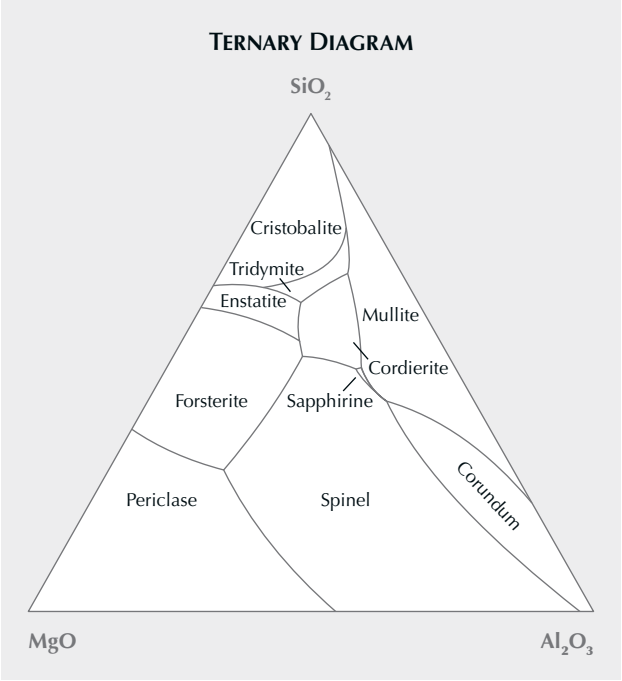

Box A: Producing Glass-Ceramics for Gem and Jewelry Applications

A team of GIA scientists observed the full process of creating glass-ceramics, from raw material to finished gems, at Formica's plant in Thailand in August 2024. These steps are outlined below.

First, the required chemicals are mixed thoroughly in large batches, each exceeding 40 kg. The bulk of the mixture consists of oxides of the major elements that make up the glass (silicon, aluminum, magnesium, and zinc). Oxides of zirconium and titanium are also added and serve as nucleating agents in aluminosilicate glasses, triggering the (controllable) formation of crystalline phases (Beall and Pinckney, 1999; DeCeanne et al., 2022). A specific combination of color-causing elements is also added to the mixture, ranging from just a few ppm up to 3% by weight. The exact ratios are important for the color of the final product.

After mixing, the powder is loaded into a large crucible and heated to a very high temperature while stirred continuously, resulting in a melt with the same composition as the original mixture. The molten glass is then poured into a slab (the added zinc helps lower viscosity at this stage) and cooled under a controlled temperature gradient. This gradual cooling prevents not only unwanted crystallization of certain minerals, but also thermal shock that could lead to mechanical defects during this stage.

When the glass cools to room temperature, it goes through quality control to remove any areas containing trapped gas bubbles—it is still a glass during this stage—or cloudy areas caused by unwanted crystallization. Only the clearest glass moves on to the next stage. The rejected material can be remelted and poured again or reused in subsequent batches.

In the final stage, the glass is placed in another furnace and subjected to a heating and cooling regime that determines the degree of crystallization. This in turn determines the final color and transparency of the glass-ceramic.

The final product can be manufactured just like any other gemstone or ornamental stone, through cutting, polishing, cabbing, sawing, or carving.

crystallization is carefully controlled with respect to temperature and duration, and the process is stopped before crystallization is brought to completion. Complete crystallization would result in the cordierite phase, $(Mg,Fe)_2Al_4Si_5O_{18}$. This controlled process yields various crystalline phases within glass-ceramics, most notably spinel ($MgAl_2O_4$). Adding significant concentrations of zinc oxide to the mixture can produce glass-ceramics based primarily on spinel crystals, ranging from traditional spinel ($MgAl_2O_4$) to gahnite ($ZnAl_2O_4$) (Pinckney and Beall, 1997; Beall and Pinckney, 1999). In glass-ceramics of the silicon-aluminum-magnesium-zinc oxide system, titanium and/or zirconium oxides are also added to act as heterogeneous nucleating agents (Höland and Beall, 2020). See box A for more details on the creation of glass-ceramics.

MATERIALS AND METHODS

Samples. Two sets of glass-ceramic imitation gemstones, 60 samples in all, were investigated for this study. The first set (GC-01 to GC-40), produced and donated by the Formica Group, consisted of 24 transparent round brilliants (again, see figure 1) and 16 translucent to opaque cabochons (figure 3, top) in a wide range of colors and weighing between 0.10 and 0.47 carats. The second set (GC-101 to GC-120), an additional 20 glass-ceramic imitation gemstones with compositions similar to the first set, was purchased by the authors (figure 3, bottom). The manufacturer of these samples is unknown. They had various colors, shapes, and transparencies, weighing between 0.03 and 1.13 carats. See table S1 in the supplementary material for descriptions of individual samples (https://www.gia.edu/gems-gemology/summer-2026-glass-ceramics).

For comparison, three optical glasses (OG-01 to OG-03) used to create green, blue, and red transparent glass-ceramics were also analyzed (see table 2). These were donated by the Formica Group.

Methods. In the field of materials science, glass-ceramics have been well studied, as evidenced by the many publications on this topic. These studies relied on methods for analyzing the crystalline phase development in the materials, such as X-ray diffraction, electron microscopy, and differential thermal analysis (Liu et al., 2018; Höland and Beall, 2020). However, these methods are generally not available in gemological laboratories.

To develop identification criteria for glass-ceramics of the silicon-aluminum-magnesium-zinc system from the perspective of gemologists, the glass-ceramics and the optical glass samples were examined at the GIA laboratory in Bangkok using the following analytical techniques.

Standard Gemological Testing. Standard gemological properties were recorded on all samples.

Figure 3. Top: Translucent to opaque glass-ceramic samples (0.10–0.16 ct) examined in this study, from left to right: GC-25 to GC-32 (top row) and GC-33 to GC-40 (bottom row). Bottom: Samples weighing 0.03–1.13 ct, from left to right: GC-101 to GC-110 (top row) and GC-111 to GC-120 (bottom row). Photos by Nuttapol Kitdee.

Refractive index (RI) was measured with a GIA-built refractometer, and specific gravity (SG) was determined by the hydrostatic method. A polariscope was used to determine whether the samples were singly refractive, doubly refractive, or uniaxial in optic character. A standard UV lamp with long-wave (365 nm) and short-wave (254 nm) excitation was used to observe fluorescence reaction. Microscopic examination was conducted at 10× to 60× magnification, using darkfield, brightfield, diffused, and fiber-optic illumination.

Fourier-Transform Infrared (FTIR) Spectroscopy. FTIR absorption spectra of all samples were recorded using a Thermo Nicolet iS50 FTIR spectrometer equipped with an XT-KBr beam splitter, a cryogenic MCT detector, and a DRIFTS accessory for cut glass-ceramics or a 4× beam condenser accessory for the optical glasses. The resolution was set at 4 cm^{-1}.

Ultraviolet/Visible/Near-Infrared (UV-Vis-NIR) Spectroscopy. UV-Vis-NIR absorption spectra of the transparent samples (GC-01 to GC-24, GC-101 to GC-103, GC-105 to GC-117, GC-119, and GC-120) were collected using a GIA custom-built UV-Vis-NIR system. The system included a DH-2000-BAL Ocean Optics deuterium and halogen light source, a QE Pro high-performance spectrometer, and a bifurcated fiber-optic probe for routing UV-Vis-NIR radiation from the light source to the sample and collecting its transmitted signal. Spectra were collected from 300 to 980 nm with an integration time of 1000 ms and one accumulation.

Photoluminescence (PL) Spectroscopy. PL spectra of all samples were collected at room temperature using a Renishaw inVia Raman microscope fitted with a 514 nm laser, 1800 lines/mm grating, and a 5× objective lens. The spectra were recorded between 520 and 850 nm.

Energy-Dispersive X-Ray Fluorescence (EDXRF) Spectroscopy. EDXRF spectra of all samples were collected for qualitative elemental analysis using a Thermo Quant'X EDXRF spectrometer, operating at 20 keV without a filter. The spectra were recorded between 0 and 20 keV.

Laser Ablation–Inductively Coupled Plasma–Mass Spectrometry (LA-ICP-MS). Trace element concentrations were measured quantitatively in all samples using LA-ICP-MS. Analyses were performed with a Thermo Fisher Scientific iCAP Q ICP-MS coupled with a Q-switched Nd:YAG laser ablation device operating at a wavelength of 213 nm. Faceted samples were analyzed on the girdle, while cabochons were analyzed close to the base. Laser ablation was carried out using 55 μm diameter spots, with a fluence of around 10 J/cm^2 and a 10 Hz repetition rate. The dwell time for each spot was 40 seconds. The ICP-MS was operated at a forward power of 1350 W, with a typical nebulizer gas flow of about 0.80 L/min. External calibration was performed using National Institute of Standards and Technology (NIST) 610 and U.S. Geological Survey glasses GSD-1G and GSE-1G as reference standards. The analyzed isotopes included ^{23}Na, ^{24}Mg, ^{27}Al, ^{29}Si, ^{43}Ca, ^{47}Ti, ^{53}Cr, ^{55}Mn, ^{57}Fe, ^{59}Co, ^{60}Ni, ^{63}Cu, ^{66}Zn, ^{88}Sr, ^{89}Y, ^{90}Zr, ^{118}Sn, ^{137}Ba, ^{139}La, ^{140}Ce, ^{141}Pr, ^{146}Nd, ^{147}Sm, ^{157}Gd, ^{166}Er, ^{174}Hf, and ^{197}Au.

RESULTS

The studied glass-ceramics generally showed consistent gemological properties, FTIR and PL spectra, and

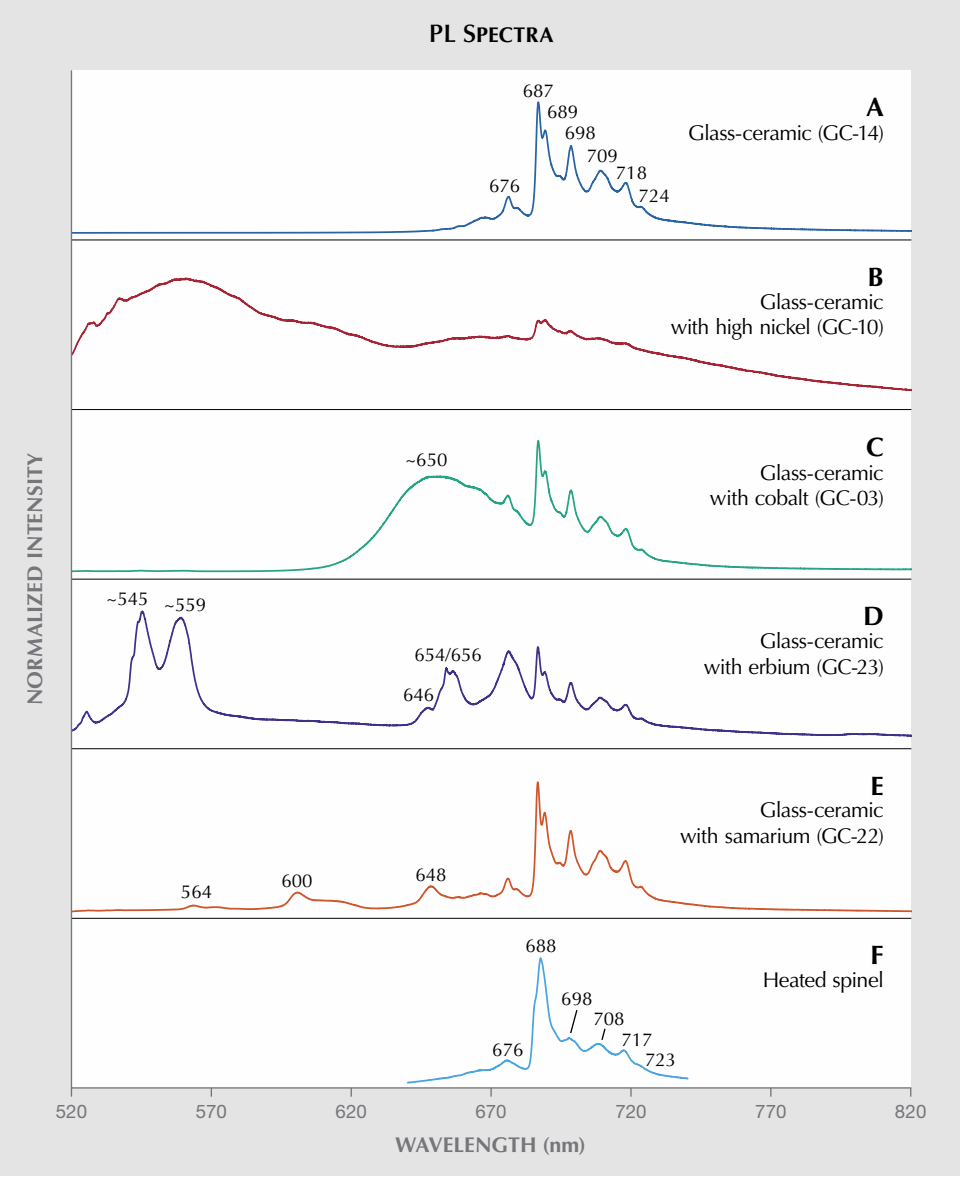

Figure 4. Representative PL spectra, collected using a 514 nm laser excitation at room temperature, for the glass-ceramic samples with a silicon-aluminum-magnesium-zinc composition (patterns A to E), showing emission bands at approximately 676, 687, 689, 698, 709, 718, and 724 nm—similar to chromium emission patterns in heated spinel (pattern F, from a spinel in GIA's colored stone reference collection).

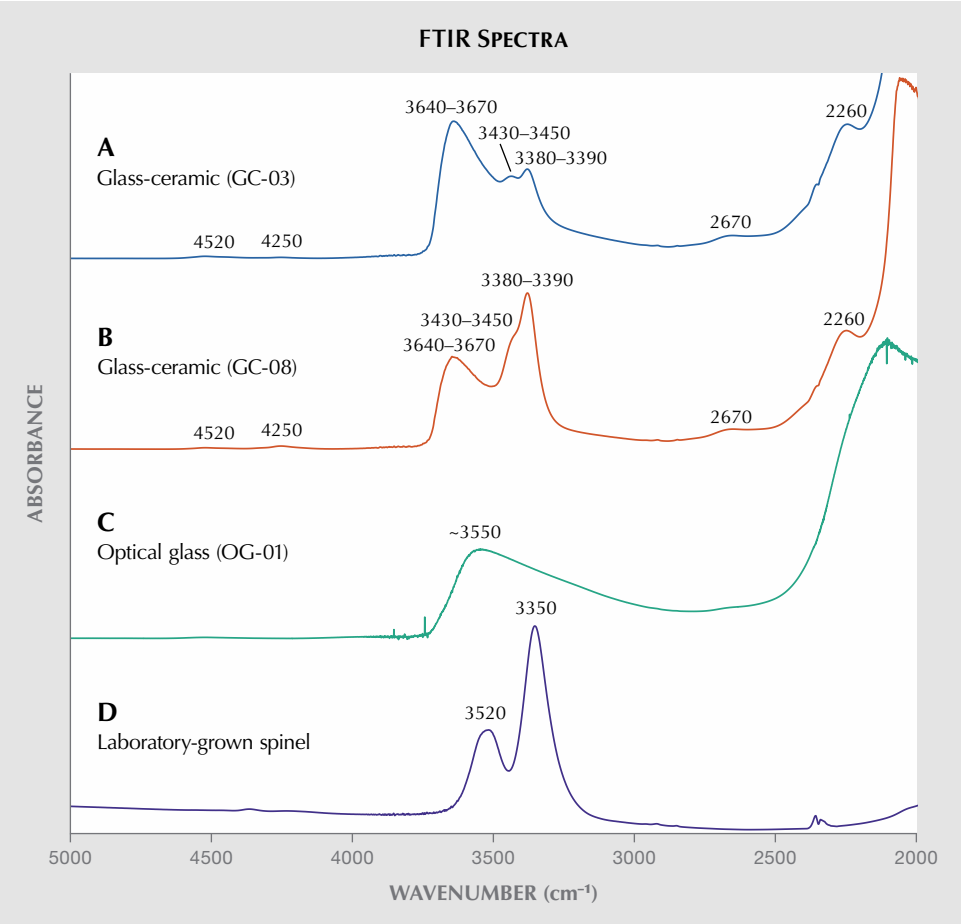

Figure 5. FTIR spectra comparing two representative blue glass-ceramics in the study with a blue optical glass and a blue laboratory-grown spinel produced by the flame-fusion method (from GIA's colored stone reference collection). The glass-ceramics show three absorption bands at 3640–3670 cm^{-1}, 3430–3450 cm^{-1}, and 3380–3390 cm^{-1}; weak bands at approximately 2260, 2670, 4250, and 4520 cm^{-1}; and strong absorption below 2150 cm^{-1}. Based on relative band intensity, the blue glass-ceramic spectra can be divided into two groups: 3640–3670 cm^{-1} > 3380–3390 cm^{-1} (pattern A) and 3380–3390 cm^{-1} < 3640–3670 cm^{-1} (pattern B). Spectra are offset vertically for clarity.

major chemical compositions, regardless of color and transparency (again, see the supplementary material). All were singly refractive, with RIs between 1.60 and 1.63, and hydrostatic SGs ranged between 2.85 and 3.42. Polariscope testing usually revealed single refraction, with occasional anomalous double refraction. A uniaxial optic character could be observed in some translucent samples. Most samples were inert under long-wave UV fluorescence but appeared chalky white, blue, or green under short-wave UV.

Microscopic examination revealed that the transparent stones were relatively clean, with uniform color distribution throughout. The inclusions in transparent samples were limited to minute gas bubbles, straight internal graining, and conchoidal fractures. Some of the transparent samples had light cloudy patches that were visible with fiber-optic illumination, while the translucent ones usually appeared milky throughout. In addition, semitranslucent blue samples (GC-35 and GC-37) appeared red when observed with transmitted light.

PL spectra of the glass-ceramics generally showed several emission peaks between 670 and 730 nm (figure 4). The main peaks were a doublet at 687 and 689 nm, with minor peaks at 676, 698, 709, 718, and 724 nm. Certain samples displayed additional PL features, such as a broad emission band at approximately 650 nm, or two emission peaks at around 545 and 559 nm. The series of peaks between 670 and 730 nm was not detected in three opaque samples—GC-35 (blue), GC-36 (greenish blue), and GC-40 (black)—or in transparent samples GC-119 (bluish green) and GC-120 (yellowish green).

FTIR spectra of the silicon-aluminum-magnesium-zinc glass-ceramic samples were generally consistent (figure 5), with three main broad absorption bands at ~3640–3670 cm^{-1}, 3430–3450 cm^{-1}, and 3380–3390 cm^{-1}. These results align with previous reports (Shen, 2010; Srisataporn et al., 2022). FTIR spectra of the studied glass-ceramics can be separated into two patterns. The majority of the samples (about 70%) showed a prominent band at 3640–3670 cm^{-1}, with weaker bands at 3430–3450 cm^{-1} and 3380–3390 cm^{-1} (figure 5A). The other pattern had a strong absorption band at 3380–3390 cm^{-1}, with weaker bands at 3430–3450 cm^{-1} and 3640–3670 cm^{-1}

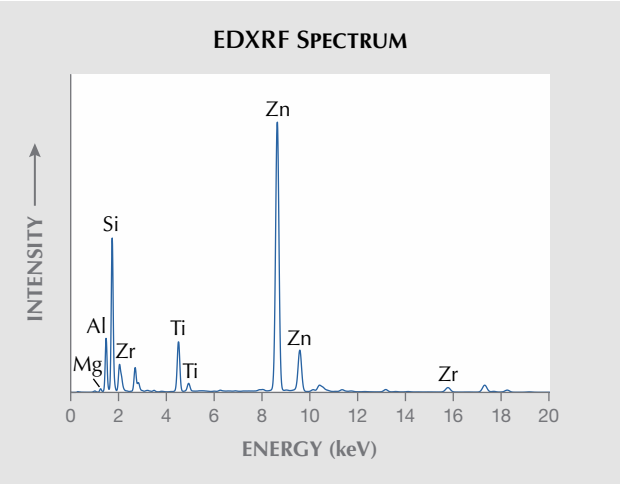

Figure 6. Representative EDXRF spectrum of sample GC-17 collected at 20 keV without a filter. This spectrum shows the six elements that were present in every silicon-aluminum-magnesium-zinc glass-ceramic. The combination of these six elements (silicon, aluminum, magnesium, zinc, titanium, and zirconium) is not seen in any natural material and serves as a strong indicator of a glass-ceramic.

(figure 5B); this was often observed in samples with green and yellow hues or black opaque samples. Some of the studied glass-ceramics had spectra that varied from these two patterns. The spectra for samples GC-35, GC-104, and GC-120 lacked the broad bands at 3430–3450 cm^{-1} and 3380–3390 cm^{-1}. Sample GC-119 had a distinct spectrum, with only a broad band at ~3520 cm^{-1}.

EDXRF spectra of the glass-ceramics displayed several visible bands consistently, confirming the presence of silicon, aluminum, magnesium, zinc, titanium, and zirconium (figure 6). Also detected were some additional elemental peaks corresponding to the color of the glass-ceramics: cobalt in blue samples, nickel in green, manganese and praseodymium in yellow, and neodymium and erbium in pink to red.

Analysis by LA-ICP-MS revealed a chemical composition mainly consisting of silicon (~36–44 wt.%) and aluminum (~22–34 wt.%) and other elements including magnesium, zinc, titanium, and zirconium. As shown in figure 7, a slight variation of each element concentration was observed in most

Figure 7. Variation in major chemical composition among the glass-ceramic samples from this study, measured by LA-ICP-MS. The silicon-aluminum-magnesium-zinc glass-ceramics show relatively consistent compositions in various colors and transparency. Each color represents an element: silicon, aluminum, zirconium, magnesium, zinc, and titanium, measured in transparent samples (open circles) and translucent to opaque samples (filled circles). See supplementary table S2 at https://www.gia.edu/gems-gemology/summer-2026-glass-ceramics for concentrations of all detectable elements.

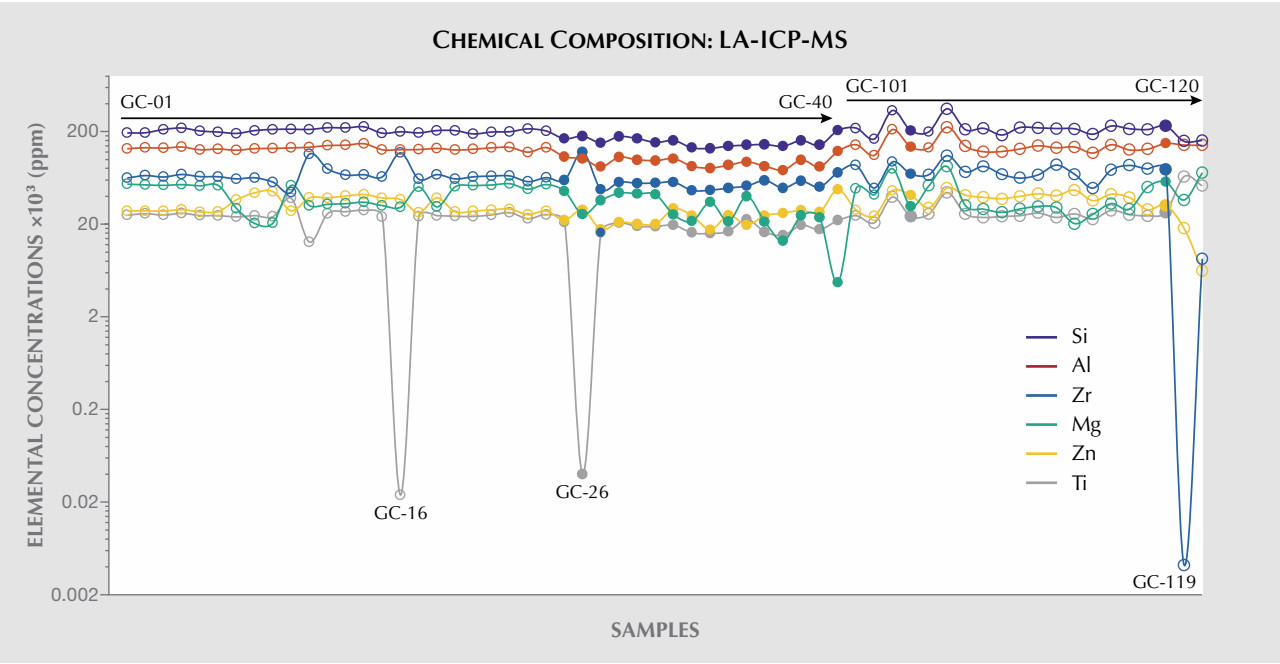

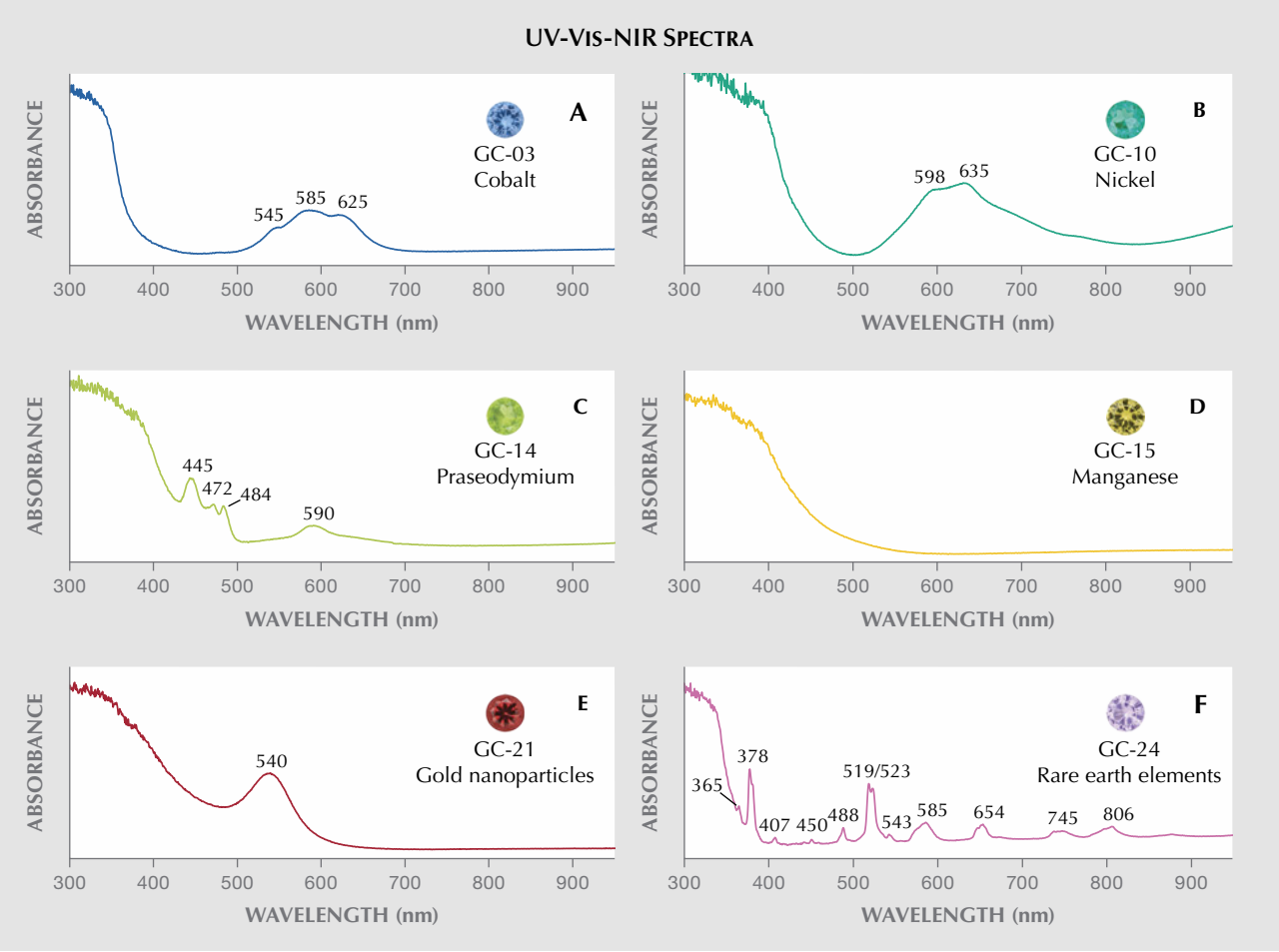

Figure 8. Representative UV-Vis-NIR spectra of variously colored glass-ceramics show different absorption features depending on the coloring agent(s) in each sample.

of the glass-ceramic samples, regardless of color and transparency. A variety of elements, including rare earth elements (REEs) and transition metals, were also detected at lower concentrations (see supplementary table S2). Significant concentrations of sodium and hafnium were detected in every sample. Consistent with the EDXRF results, some minor to trace elements correlated with sample color, as they were present in higher concentrations in samples of similar color. Any other elements detected at much lower concentrations (i.e., less than 500 ppm or 0.05%) are assumed to be accidental contaminants and not additives during the glass-ceramic manufacturing process.

UV-Vis-NIR spectra collected in the 300–980 nm range showed consistent absorption features in transparent glass-ceramics of similar colors (figure 8). Blue glass-ceramics mainly displayed broad bands at approximately 545, 585, and 625 nm, with absorption edges between 340 and 400 nm (figure 8A). Green samples generally showed broad bands at approximately 598 and 635 nm, with an absorption increase above 870 nm toward the near-infrared region and absorption edges between 365 and 445 nm (figure 8B). The green-yellow and some yellow samples showed similar absorption bands at ~445, 472, 484, and 590 nm and an absorption edge at approximately 380–400 nm (figure 8C). Many yellow and yellow-orange glass-ceramics showed strong absorption from the UV region to the visible spectrum at 520–590 nm (figure 8D). The red samples predominantly featured an absorption band at approximately 540 nm (figure 8E), while the pink glass-ceramics exhibited several bands at ~365, 378, 407, 442, 450, 488, 519, 523, 543, 585, 654, 745, 800, 878, and 970 nm (figure 8F).

TABLE 1. Summary of gemological, spectroscopic, and chemical properties of the studied glass-ceramics by color.

	Blue	Green	Yellow to orange	Purple, pink, and red	Other colors (e.g., white, black)
RI	1.61–1.63	1.61–1.63	1.61–1.62	1.60–1.63	1.61–1.62
SG	2.86–3.19	2.89–3.42	2.94–3.17	2.93–3.24	2.90–3.15
PL	Spinel-like features, mainly consisting of doublet peaks at 686.7 and 689 nm				
FTIR	Three prominent broad absorption bands at ~3640–3670 cm^{-1}, ~3430–3450 cm^{-1}, and ~3380–3390 cm^{-1}				
Major chemical composition	Aluminum, silicon, magnesium, titanium, zinc, zirconium				
Dominant chromophores	Cobalt, erbium, nickel	Nickel, praseodymium	Manganese, praseodymium	Gold, neodymium, erbium	na[a]

[a]*Not analyzed due to the samples' lack of transparency.*

DISCUSSION

Characterization of Silicon-Aluminum-Magnesium-Zinc Glass-Ceramics. The glass-ceramic samples generally showed consistent results when tested with standard and advanced gemological methods (table 1). However, samples with different colors often exhibited distinct properties, depending on their respective color-causing elements.

Standard Gemological Properties. Glass-ceramics can be used to imitate a variety of natural gemstones, including citrine, peridot, emerald, tsavorite, topaz, tourmaline, spinel, sapphire, ruby, garnet, and kunzite. The separation of glass-ceramics from these natural stones is straightforward with standard gemological testing. Many of the natural stones have an RI outside the range of glass-ceramics (1.60–1.63); those with a similar RI are generally doubly refractive, unlike glass-ceramics.

Variations in the properties of glass-ceramics (RI and SG) can be attributed to slight differences in chemical composition. A higher concentration of heavier elements can result in a denser material, while certain additives in the glass phase can affect optical properties such as refractive index. Transparency also varies, depending on the size of the crystal grains in the glassy matrix. When the grain size is smaller than the wavelength of visible light, light is not scattered and the sample appears transparent. Above a certain size threshold, the crystals start to reduce transparency due to light scattering (Beall and Pinckney, 1999). This scattering effect caused by very small crystallites can be observed as hazy/milky clouds in transparent and translucent glass-ceramics, as well as a reddish appearance in semitranslucent samples viewed in transmitted light (Jin et al., 2023).

While the goal of producing glass-ceramic imitation gemstones is to create an inclusion-free material—and this is technically feasible—it is also entirely possible to purposely introduce flaws to make the material appear more natural.

PL Spectra. PL spectroscopy is a very sensitive technique (Eaton-Magaña et al., 2024) and can detect chromium at extremely low concentrations. The series of emission peaks between 670 and 730 nm shown in figure 4 closely resembles chromium emission peaks in spinel (Widmer et al., 2015; Chen et al., 2024), consistent with previous reports for blue to green glass-ceramics (Srisataporn et al., 2022).

Based on the main chemical composition of glass-ceramics in the silicon-aluminum-magnesium-zinc system (Beall and Pinckney, 1999; Höland and Beall, 2020), a spinel-like PL spectra observed in the samples matched the main crystalline phases present, which ranged from spinel to gahnite. Certain elements had a significant impact on the PL spectrum. For example, cobalt (figure 4C) and erbium (figure 4D) were associated with additional emission bands at 650 nm and 545–559 nm, respectively. Notably, glass-ceramic samples containing relatively high nickel concentrations (~2000 ppm and higher) tended to show weaker spinel-like PL features, with broad bands below 650 nm (figure 4B). High nickel concentrations can act as a quencher for the typical chromium photoluminescence in spinel (Jouini et al., 2007).

FTIR Spectra. In figure 5, prominent broad bands between 3300 and 3700 cm^{-1} appear to be associated with hydroxyl stretching of water molecules and silanol groups in glass (Faulques et al., 2001; Efimov and Pogareva, 2006). These bands could also be related to the vibrations of hydroxyl groups in spinel-group materials, which make up the main crystalline phases of the studied glass-ceramics. These FTIR features have been observed in annealed gahnite produced using hydrothermal growth (Miron and Grozescu, 2012), as well as spinel grown by flame fusion (figure 5D). The glass-ceramic samples from this study also showed a discernible band at ~2260 cm^{-1}, caused by a combination of hydroxyl-group modes from the silica glassy matrix (Efimov and Pogareva, 2006).

FTIR spectra of natural glasses (e.g., moldavite and obsidian) and artificial glasses show a broad band around 3400–3600 cm^{-1}, similar to the region seen in silicon-aluminum-magnesium-zinc glass-ceramics. However, the FTIR spectra of glass-ceramics are clearly different from those of glasses, lacking both peaks in the 3380–3450 cm^{-1} region. The distinctive FTIR signature of glass-ceramics can be used to separate them from natural and laboratory-grown gemstones, as well as natural and artificial glasses.

Major Chemical Composition. Most of the glass-ceramic samples contained silicon, aluminum, magnesium, zinc, titanium, and zirconium oxides. The presence of a combination of silicon, aluminum, magnesium, and zinc oxides is directly related to the glass that is ultimately crystallized primarily to spinel or gahnite crystal phases in the glassy matrix (Beall and Pinckney, 1999; Höland and Beall, 2020). Zinc oxide is a common additive in glassmaking to help reduce viscosity. This allows the glass to be poured into slabs, and it is important for fast, temperature-controlled transfer of the material. During the annealing phase, the zinc is included in the growth of the spinel-like phases through diffusion. Titanium and zirconium oxides are introduced as nucleating agents to promote uniform crystal growth (Höland and Beall, 2020). The right amount of titanium and zirconium oxides results in a homogeneous distribution of crystals growing throughout the material. Notably, hafnium was detected in every sample, with the amount of hafnium oxide at approximately 2 wt.% of the zirconium oxide content. This strongly suggests that hafnium is a contaminant in zirconium oxide (again, see table S2 in the supplementary material).

Color-Causing Agents and Notable Trace Elements. Coloration in glass-ceramics can be created by transition metal ions, REE ions, metal nanoparticles, or a combination of the three. For the samples from this study, color appearance and UV-Vis-NIR spectra (again, see figure 8) corresponded well with the minor to trace element compositions measured using EDXRF and LA-ICP-MS. Glass-ceramics can be colored by various dominant elements, as follows:

- *Blue:* Cobalt was the primary cause of blue coloration. The blue samples had a typical cobalt UV-Vis-NIR absorption spectrum, with three broad absorption bands between 540 and 650 nm (Shen, 2010; D'Ippolito et al., 2015). This was consistent with the significant cobalt concentrations detected.
- *Green:* Nickel was responsible for light blue to green colors in many of the samples. A considerable nickel concentration was measured in these samples, which corresponded with two broad UV-Vis-NIR absorption bands between 590 and 640 nm (Shen, 2010; Jollands et al., 2023). Praseodymium, another chromophore detected, also contributed a green hue, with a unique UV-Vis absorption spectrum in the 440–600 nm range (Khomenko et al., 2017).
- *Yellow to Orange:* Yellow to orange coloration in the samples was generally created by manganese (Bosi et al., 2007). Strong absorption in the UV and blue regions below ~550 nm was observed in yellow samples, while strong absorption extended to ~610 nm to produce orange colors in samples with higher manganese concentrations. Praseodymium also contributed to a yellow-green coloration.
- *Purple, Pink, and Red:* Many gem materials with pink to red coloration would be expected to show similar absorption patterns with different absorption intensity—weaker for pink and more intense for red colors. This is not the case for pink to red glass-ceramics, however. Two main groups of chromophores were found in the samples within this color range:
    1. REEs, including neodymium and erbium, created a pinkish hue. REEs typically showed multiple narrow absorption peaks in the UV-visible region (Khomenko et al., 2017), consistent with the presence of these elements at high concentrations.

2. Gold nanoparticles in the glassy matrix resulted in a strongly saturated red color. The UV-Vis absorption caused by gold nanoparticles has a characteristic absorption spectrum defined by a broad absorption band at ~540 nm (figure 8E) (Alex and Tiwari, 2015). In this study, the red glass-ceramics colored by gold nanoparticles had gold concentrations around 20–40 ppm.

Multiple chromophores can be combined to produce a range of colors. Several other elements were detected in this study, but they are not known as chromophores (e.g., calcium, barium, sodium, lead, tin, and arsenic). Some of these elements, such as sodium and arsenic, are known additives in the glass-making process to adjust viscosity, but they might also be contaminants from other compounds.

Comparison Between Optical Glasses and Their Glass-Ceramic Products. Three optical glasses (OG-01 to OG-03) that would ultimately produce blue, red, and green glass-ceramics after controlled crystallization (table 2) were also examined. The differences in RI and SG values before and after crystallization were insignificant. In addition, the optical glasses and the glass-ceramics both showed a stronger chalky green-yellow fluorescence reaction to short-wave UV than to long-wave UV. These similarities indicate that standard gemological testing alone is not sufficient to differentiate optical glass from glass-ceramic products.

As shown in table 2, optical glasses can either resemble the final color of the glass-ceramic products, or the final color can be altered through a post-growth annealing process. For the blue optical glass (OG-01) and the blue glass-ceramic material (GC-02), a combination of cobalt and erbium was added to produce a blue hue. Co^{2+} is known to create blue coloration when incorporated in glass phases (Calas et al., 2021), so the color difference between the blue optical glass and the blue glass-ceramic product was insignificant.

Meanwhile, a significant color difference was observed between the near-colorless optical glass (OG-02) and its red glass-ceramic counterpart (GC-20), as well as between the dark brown optical glass (OG-03) and its green glass-ceramic counterpart (GC-12). The shift from near-colorless optical glass to a

TABLE 2. Three optical glasses (OG-01 to OG-03) and their faceted glass-ceramic products in blue (GC-02), red (GC-20), and green (GC-12).

	OG-01	GC-02	OG-02	GC-20	OG-03	GC-12
Color	Blue	Blue	Colorless	Red	Dark brown	Green
RI	1.618	1.622	1.600	1.618	1.610	1.618
SG	3.06	3.06	2.89	2.93	2.91	2.97
Long-wave UV	Strong chalky green	Moderate green	Weak red	Inert	Inert	Inert
Short-wave UV	Strong chalky greenish yellow	Strong chalky green	Strong chalky greenish yellow	Weak orange-red with strong chalky green	Weak chalky greenish yellow	Inert

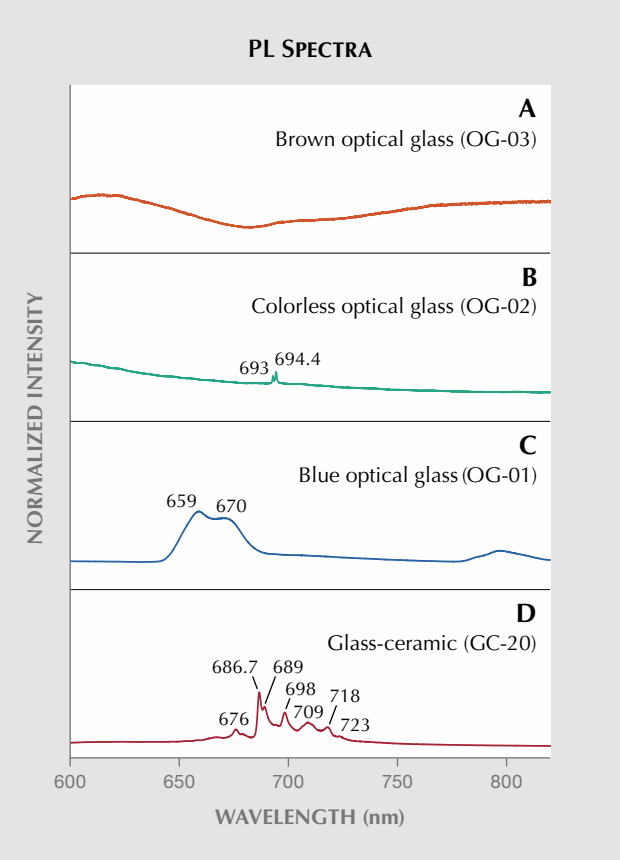

Figure 9. PL spectra of the three optical glasses in table 2, collected at room temperature, using a 514 nm laser, show distinct emission features compared to those typically observed in glass-ceramics (e.g., GC-20).

red glass-ceramic was due to the precipitation of gold nanoparticles with the presence of tin (Tilley, 2011; Calas et al., 2021). Nano-scale gold particles that developed next to the crystalline phases (e.g., spinel/gahnite) qualify the red sample as a glass-ceramic (Deubener et al., 2018). The dark brown optical glass contained a significant nickel concentration. When the optical glass was converted to a glass-ceramic, the nickel became incorporated into the spinel/gahnite-like crystalline phases, producing a green color. This determination that the nickel was incorporated into the spinel/gahnite crystalline phases is based on the UV-Vis-NIR absorption spectrum of green glass-ceramics (again, see figure 8B; e.g., Jollands et al., 2023).

Since the conversion of optical glasses to glass-ceramics requires no additives, chemical analysis using EDXRF and LA-ICP-MS showed no change in composition. In contrast, the FTIR (again, see figure 5) and PL (figure 9) spectra of the glass-ceramics displayed a significant shift from that of the optical glasses. These differences are related to the development of desired crystalline phases after controlled heat treatment.

As shown in figure 9, the glass-ceramics had a set of emission peaks between 670 and 730 nm that resembled spinel/gahnite PL features but were absent from the optical glass. Over the 650–750 nm range, the brown optical glass exhibited no emission peaks; the colorless optical glass showed narrow doublet peaks at 693 and 694.4 nm, similar to the Cr^{3+} emission peaks in corundum (Powell, 1998). The blue optical glass exhibited broad bands at around 659 and 670 nm, possibly related to REEs such as erbium. Although the corundum PL feature was detected in the colorless optical glass, this material is not considered a glass-ceramic, as corundum phases in this stage likely resulted from uncontrolled spontaneous crystallization.

CONCLUSIONS

Glass-ceramic materials can be produced in a broad range of colors and transparencies to imitate a wide variety of natural gemstones. Their gemological, spectroscopic, and chemical properties are generally consistent and can be used to distinguish glass-ceramics of the silicon-aluminum-magnesium-zinc system from natural and laboratory-grown gems as well as glass imitations.

The transparent glass-ceramic material currently being produced for gem use is inclusion-free, but manufacturers may eventually introduce flaws to more closely resemble natural stones. However, accurate identification can be achieved through a combination of standard and advanced gemological methods.

The proposed identification criteria for silicon-aluminum-magnesium-zinc system glass-ceramics are an RI between 1.60 and 1.63; a chemical composition dominated by magnesium, aluminum, silicon, titanium, zinc, and zirconium; spinel-like PL features; and a unique FTIR feature with a broad absorption band at ~3640–3650 cm^{-1}, together with bands at ~3430–3440 cm^{-1} and/or ~3380–3390 cm^{-1}.

It is important to note that these criteria are only valid for glass-ceramics of the silicon-aluminum-magnesium-zinc system. Creation of glass-ceramics in other chemical composition systems is possible, which could result in different gemological, spectroscopic, and chemical properties.

ABOUT THE AUTHORS

Dr. Wasura Soonthorntantikul is a senior research scientist at GIA in Bangkok. Wim Vertriest is the manager of field gemology at GIA in Bangkok. Dr. Karen Avakyan is the founder of the Formica Group companies and holds patents on the use of glass-ceramics in jewelry.

ACKNOWLEDGMENTS

The authors wish to thank Sasithorn Engniwat and Nuttapol Kitdee for their photography, Suwasan Wongchacree, Polthep Sakpanich, and Titapa Tanawansombat for their support on data collection, as well as Pichaporn Clarke for help with project coordination. We also thank Aaron Palke and Shiyun Jin for many helpful comments and suggestions during the writing of the manuscript.

REFERENCES

Alex S., Tiwari A. (2015) Functionalized gold nanoparticles: Synthesis, properties and applications—A review. *Journal of Nanoscience and Nanotechnology*, Vol. 15, No. 3, pp. 1869–1894, https://doi.org/10.1166/jnn.2015.9718

Beall G.H., Pinckney L.R. (1999) Nanophase glass-ceramics. *Journal of the American Ceramic Society*, Vol. 82, No. 1, pp. 5–16, https://doi.org/10.1111/j.1151-2916.1999.tb01716.x

Bosi F., Hålenius U., Andreozzi G.B., Skogby H., Lucchesi S. (2007) Structural refinement and crystal chemistry of Mn-doped spinel: A case for tetrahedrally coordinated Mn^{3+} in an oxygen-based structure. *American Mineralogist*, Vol. 92, No. 1, pp. 27–33, https://doi.org/10.2138/am.2007.2266

Calas G., Galoisy L., Cormier L. (2021) The color of glass. In P. Richet et al., Eds., *Encyclopedia of Glass Science, Technology, History, and Culture, Volume I*. American Ceramic Society, pp. 667–691, https://doi.org/10.1002/9781118801017.ch6.2

Chen Y., Zheng J., Lu M., Liu Z., Zhou Z. (2024) Gemological and spectral characteristics of gem-quality blue gahnite from Nigeria. *Journal of Spectroscopy*, Vol. 2024, article no. 6693346, https://doi.org/10.1155/2024/6693346

DeCeanne A.V., Rodrigues L.R., Wilkinson C.J., Mauro J.C., Zanotto E.D. (2022) Examining the role of nucleating agents within glass-ceramic systems. *Journal of Non-Crystalline Solids*, Vol. 591, article no. 121714, https://doi.org/10.1016/j.jnoncrysol.2022.121714

Deubener J., Allix M., Davis M.J., Duran A., Höche T., Honma T., Komatsu T., Krüger S., Mitra I., Müller R., Nakane S., Pascual M.J., Schmelzer J.W.P., Zanotto E.D., Zhou S. (2018) Updated definition of glass-ceramics. *Journal of Non-Crystalline Solids*, Vol. 501, pp. 3–10, https://doi.org/10.1016/j.jnoncrysol.2018.01.033

D'Ippolito V., Andreozzi G.B., Hålenius U., Skogby H., Hametner K., Günther D. (2015) Color mechanisms in spinel: Cobalt and iron interplay for the blue color. *Physics and Chemistry of Minerals*, Vol. 42, pp. 431–439, https://doi.org/10.1007/s00269-015-0734-0

Dymshits O.S., Zhilin A.A. (2017) Heat-resistant synthetic jewelry material. U.S. Patent No. 9,801,435 B2, issued October 31.

Eaton-Magaña S., Jones D.C., Turnier R.B., Breeding C.M. (2024) Shining a light on gemstone properties: An exploration of photoluminescence spectroscopy. *G&G*, Vol. 60, No. 4, pp. 494–517, https://doi.org/10.5741/GEMS.60.4.494

Efimov A.M., Pogareva V.G. (2006) IR absorption spectra of vitreous silica and silicate glasses: The nature of bands in the 1300 to 5000 cm^{-1} region. *Chemical Geology*, Vol. 229, No. 1-3, pp. 198–217, https://doi.org/10.1016/j.chemgeo.2006.01.022

Faulques E., Fritsch E., Ostroumov M. (2001) Spectroscopy of natural silica-rich glasses. *Journal of Mineralogical and Petrological Sciences*, Vol. 96, No. 3, pp. 120–128, https://doi.org/10.2465/jmps.96.120

Höland W., Beall G.H. (2020) *Glass-Ceramic Technology*, 3rd ed. Wiley and American Ceramic Society, 448 pp.

Jin S., Palke A.C., Renfro N.D., Sun Z. (2023) Special colors and optical effects of Oregon sunstone: Absorption, scattering, pleochroism, and color zoning. *G&G*, Vol. 59, No 3, pp. 298–322, https://doi.org/10.5741/GEMS.59.3.298

Jollands M., Ludlam A., Palke A.C., Vertriest W., Jin S., Cevallos P., Arden S., Myagkaya E., D'Haenens-Johannson U., Weeramongkhonlert V., Sun Z. (2023) Color modification of spinel by nickel diffusion: A new treatment. *G&G*, Vol. 59, No. 2, pp. 164–181, https://doi.org/10.5741/GEMS.59.2.164

Jouini A., Yoshikawa A., Guyot Y., Brenier A., Fukuda T., Boulon G. (2007) Potential candidate for new tunable solid-state laser between 1 and 2μm: Ni^{2+}-doped $MgAl_2O_4$ spinel grown by the micro-pulling-down method. *Optical Materials*, Vol. 30, No. 1, pp. 47–49, https://doi.org/10.1016/j.optmat.2006.11.027

Khomenko V.M., Tarashchan A.M., Ripenko V.V., Vyshnevskyi O.A., Kosorukov O. (2017) Glass-ceramics as imitation of gems. II. Optical spectra, luminescence, the natural of the opalescence of rare-earth glass-ceramics. *Mineralogical Journal (Ukraine)*, Vol. 39, No. 4, pp. 24–41, https://doi.org/10.15407/mineraljournal.39.04.024

Levin E.M., Robbins C.R., McMurdie H.F. (1964) *Phase Diagrams for Ceramists*. American Ceramic Society, Columbus, Ohio.

Liu X., Zhou J., Zhou S., Yeu Y., Qiu J. (2018) Transparent glass-ceramics functionalized by dispersed crystals. *Progress in Materials Science*, Vol. 97, pp. 38–96, https://doi.org/10.1016/j.pmatsci.2018.02.006

Miron I., Grozescu I. (2012) Cobalt-doped gahnite synthesized by hydrothermal method. *Optoelectronics and Advanced Materials—Rapid Communications*, Vol. 6, No. 9-10, pp. 931–934.

Pinckney L.R., Beall G.H. (1997) Nanocrystalline non-alkali glass-ceramics. *Journal of Non-Crystalline Solids*, Vol. 219, pp. 219–227, https://doi.org/10.1016/S0022-3093(97)00272-X

Powell R.C. (1998) *Physics of Solid-State Laser Materials*. Springer-Verlag, New York, 423 pp.

Shen A. (2010) Gem News International: "Nanogems"—A new glass-ceramic material. *G&G*, Vol. 46, No. 2, pp. 156–157.

Srisataporn B., Karava N., Buathong A. (2022) Gemological properties of blue and green "nanogem" imitation materials. *Proceedings of the 7th International Gem & Jewelry Conference (GIT 2021)*, Chanthaburi, Thailand, February 2–3, 2002, pp. 157–166, https://git.or.th/en/about/18/149/detail/1844

Tilley R.J.D. (2011) *Colour and the Optical Properties of Materials—An Exploration of the Relationship Between Light, the Optical Properties of Materials and Colour*, 2nd ed., Wiley, UK, 528 pp.

Vyshnevskyi O.A, Khomenko V.M., Kosorukov O.O., Ripenko V.V., Kalinichenko T.G. (2017) Glass-ceramics as imitation of gems. I. Gemological characteristic, composition, physical properties. *Mineralogical Journal (Ukraine)*, Vol. 39, No. 3, pp. 32–42, https://doi.org/10.15407/mineraljournal.39.03.032

Widmer R., Malsy A.-K., Armbruster T. (2015) Effects of heat treatment on red gemstone spinel: Single-crystal X-ray, Raman, and photoluminescence study. *Physics and Chemistry of Minerals*, Vol. 42, pp. 251–260, https://doi.org/10.1007/s00269-014-0716-7

GIA Colored Stone Reports

Every Gem Carries a Story — We Uncover It.

GIA®

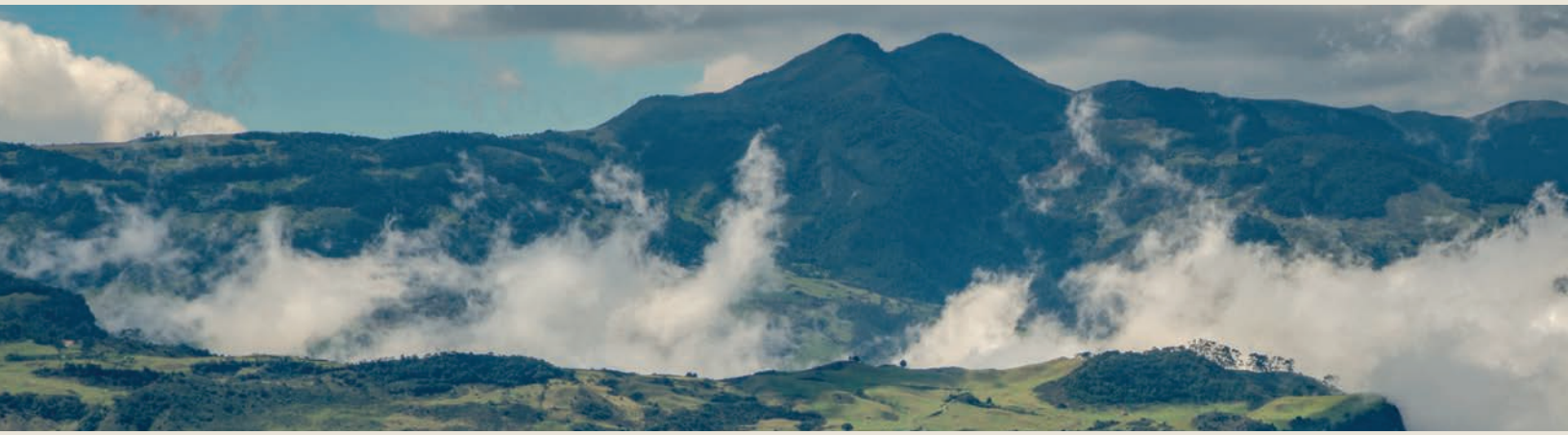

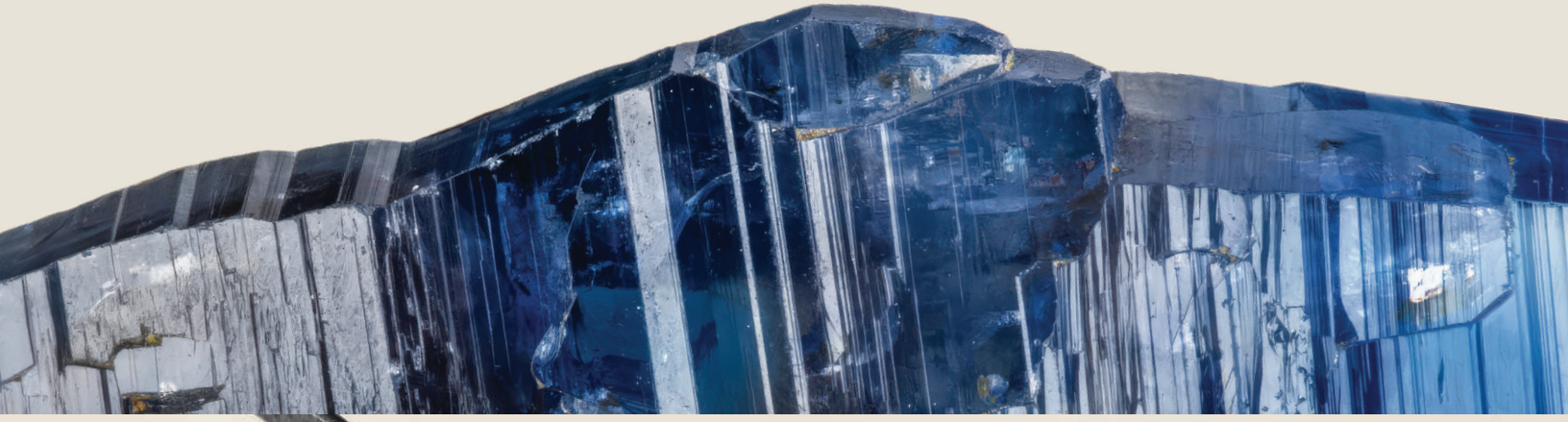

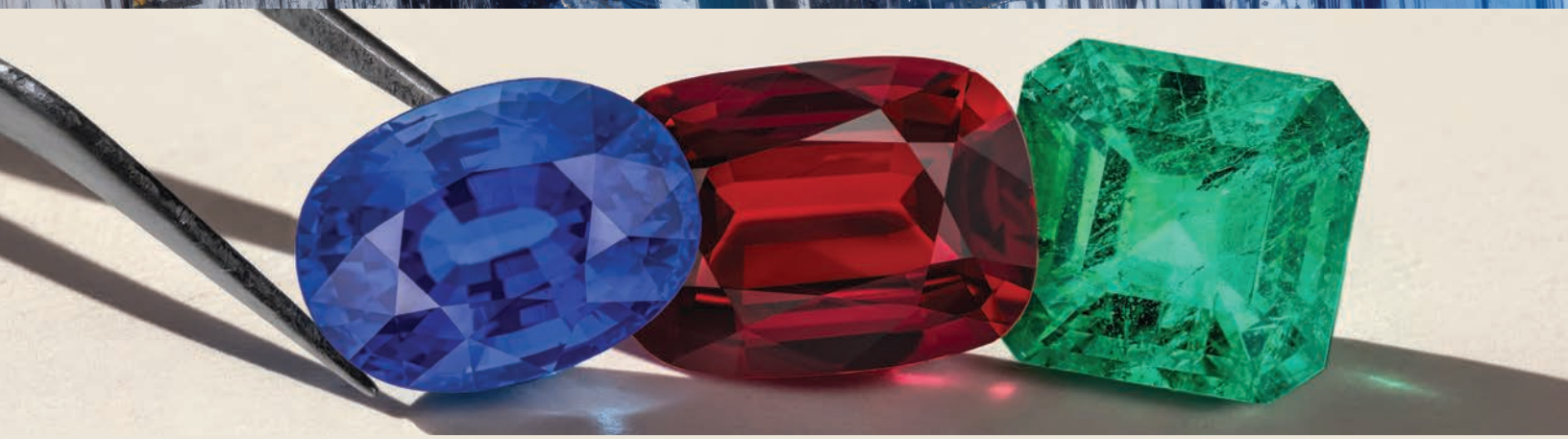

Our unrivaled field gemologists and researchers identify **colored stone treatments and geographic origins** with accuracy and precision, so we can offer you **trusted, industry-leading reports** that help earn customer confidence.

- 28,000+ gem reference samples
- 100+ field expeditions worldwide
- 70+ researchers and gemologists
- A global network of colored stone laboratories

GIA Colored Stone Reports

GIA.edu/coloredstones

Characterization of Red and Orange Spinel from Myanmar and Vietnam

Boonyapak Aksorn, Thitiphan Assawincharoenkij, Doan Thi Anh Vu, Dietmar Schwarz, Bhuwadol Wanthanachaisaeng, and Chakkaphan Sutthirat

This study investigated the gemological characteristics of red and orange spinel from Mogok in Myanmar and from Lang Chap and An Phu in Vietnam. In terms of standard gemological properties, all samples displayed a refractive index ranging from 1.710 to 1.728, specific gravity of 3.528 to 3.692, and red fluorescence under ultraviolet light. Advanced gemological methods, including ultraviolet/visible/near-infrared spectroscopy, electron probe microanalysis, and laser ablation–inductively coupled plasma–mass spectrometry, were employed to investigate chemical compositions, particularly focusing on chromophores and determination of diagnostic origin criteria. Both red and orange spinel samples exhibited chemical properties close to stoichiometric spinel. It was found that the diverse coloration in red and orange samples resulted from variations in chromium-to-vanadium ratios. The studied red spinels were chromium-rich, with chromium-to-vanadium ratios ≥1.7, whereas the orange spinels were vanadium-rich, with chromium-to-vanadium ratios ≤1.0. Trace element plots of titanium versus zinc for red spinel revealed separation between the three sources (Mogok, Lang Chap, and An Phu). Regarding orange spinel, plotting of vanadium versus zinc showed separation for Lang Chap and An Phu samples but due to the wide range of composition found in the Mogok samples, there was overlap between samples from Mogok and the two Vietnamese sources. Therefore, separation of the orange spinel from these sources is more difficult and will require investigating additional samples.

Spinel, as a gemstone, has continued to increase in popularity in recent years (figure 1). Despite high demand for this gem among collectors and in the jewelry trade, obtaining fine-quality spinel has proven challenging due to limited availability. Consequently, the price of spinel has consistently trended upward; moreover, the gemstone's geographic origin also plays a pivotal role in pricing. The origin of spinel is becoming an increasingly significant determinant of its value and is expected to soon be as significant as for emerald, ruby, and sapphire. For instance, blue spinel from Tanzania and Vietnam is more renowned than that from Madagascar or Myanmar, while red spinel from Myanmar and Vietnam is more highly regarded than that from other origins. However, reliable origin determination of spinel requires dependable data. Therefore, a comprehensive analysis of the physical and chemical characteristics of spinel from various origins is necessary. Color variation alone is insufficient to determine country of origin; similar appearing pink spinel might come from quite different

In Brief

- Red and orange spinels from Myanmar and Vietnam in this study revealed significant trace element composition data for further uses in gem-testing laboratories.
- Red spinel was characterized by a chromium-dominant chromophore composition with chromium-to-vanadium ratios ≥1.7, whereas orange spinel had a vanadium-dominant chromophore composition with chromium-to-vanadium ratios ≤1.0.
- UV-Vis-NIR spectroscopy confirmed that Cr^{3+} and V^{3+} were the primary chromophores controlling color variation in the studied spinels.
- Trace element plots (particularly titanium versus zinc) showed potential for partial separation of red spinel from different geographic origins.

See end of article for About the Authors and Acknowledgments.

Gems & Gemology, Vol. 62, No. 2, pp. 178–191,
https://doi.org/10.5741/GEMS.62.2.178
© 2026 Gemological Institute of America

Figure 1. Gem-quality spinel, such as these red (3.31 ct) and orange (2.53 ct) examples from Mogok, Myanmar, have increased in popularity in recent years. Photos by Robert Weldon; courtesy of GIA's Dr. Edward J. Gübelin collection (left) and Pillar & Stone International (right).

geological environments. For instance, Tajikistan spinel occurs in forsterite lenses within magnesian skarn (Liu et al., 2022), whereas the spinels studied here from the main commercial deposits in Myanmar (Mogok) and Vietnam (Lang Chap and An Phu) are both situated in marble hosts. These marbles formed under high-grade (granulite facies) metamorphic conditions and tectonic activity linked to the Himalayan orogeny (Garnier et al., 2005; Khoi et al., 2011; Huong et al., 2012; Fallick et al., 2019; Phyo et al., 2019; Chankhantha et al., 2020). The similarities in the marble hosts may result in comparable trace element chemistries and identical mineral inclusion assemblages. Consequently, these complicate the separation and origin determination of the studied spinels.

Spinel is the magnesium- and aluminum-containing member ($MgAl_2O_4$) of the spinel group of minerals with the general formula $(X^{2+})(Y^{3+})_2O_4$ (Sickafus et al., 1999) and crystallizes in the isometric (cubic) system. For spinel, the refractive index and specific gravity are approximately 1.72 and 3.55, respectively (Deer et al., 2013). However, solid solutions may form where different metals substitute for magnesium and aluminum in the X^{2+} and Y^{3+} sites and may slightly change those physical properties, introducing color. For instance, red, pink, and orange spinel may be attributed to the presence of Cr^{3+} and V^{3+} presumably in the octahedral (Y^{3+}) site, whereas blue spinel is attributed to Co^{2+} and/or Fe^{2+} predominantly in the tetrahedral (X^{2+}) site. However, spinel with a blue hue originating from cobalt tends to exhibit a more saturated and brighter color compared to spinel with a blue hue from iron. Chauviré et al. (2015) and Krzemnicki et al. (2023) also reported the presence of cobalt in blue spinel from Vietnam and Tanzania. Purple spinel can form when combinations of chromium and vanadium are accompanied by iron and/or cobalt substituting in the X^{2+} and/or Y^{3+} sites (Peretti and Günther, 2003; Chauviré et al., 2015; Andreozzi et al., 2019; Belley and Palke, 2021; Krzemnicki et al., 2023). However, the flexible nature of the octahedral and tetrahedral structures in spinel allows both sites to potentially accommodate either 2+ or 3+ ions (D'Ippolito et al., 2015; Andreozzi et al., 2019; Zhang et al., 2023). Investigations using quantitative analytical methods for trace element concentrations have been employed to separate natural from synthetic spinel, as well as to identify treatments (Saeseaw et al., 2009; Pluthametwisute et al., 2022). However, the trace element profiles of spinel from various origins remain largely unexplored.

GEOLOGICAL BACKGROUND

Mogok, Myanmar. Mogok is a significant global source of ruby, sapphire, and spinel. Gem mining has taken place in both primary and secondary deposits in this region since the fifteenth century (Iyer, 1953).

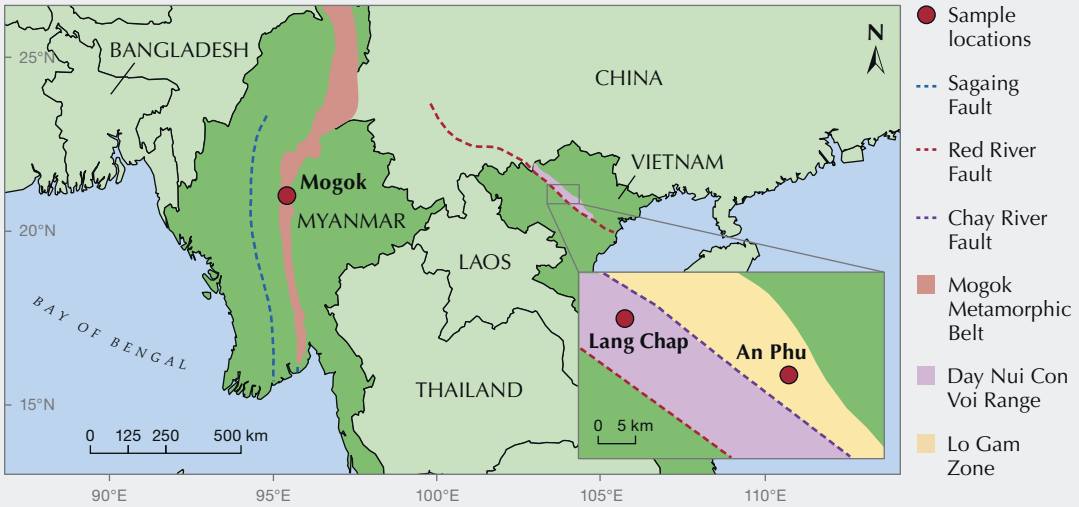

Figure 2. Map showing the main spinel locations in Southeast Asia: Mogok in Myanmar and Lang Chap and An Phu in Vietnam. Modified from Mattauer et al., 1999; Trinh et al., 2012; and Win et al., 2016.

Mogok is located in central Myanmar and is geologically part of the Mogok Metamorphic Belt (MMB) (figure 2) (Iyer, 1953; Phyo et al., 2019; Chankhantha et al., 2020), which experienced two major metamorphic events. The first occurred during the late Cretaceous to Paleocene, while the second took place during the late Eocene to Oligocene. Both events are linked to the collision between the Indian and Asian tectonic plates, which resulted in the formation of the Himalayan mountain range (Iyer, 1953; Searle et al., 2007, 2020; Phyo et al., 2019). The geologic setting of the Mogok region is highly complex, mainly consisting of high-grade metamorphic schists, gneisses, marble, calc-silicate rocks, and quartzite. Additionally, various igneous intrusions are present, including gem crystal–containing pegmatites and ultramafic rocks (Iyer, 1953; Thu, 2007; Phyo et al., 2019). Spinel has typically been found in marbles associated with metamorphism in granulite facies. Other minerals discovered in these marble formations include apatite, chondrodite, clinohumite, diopside, dravite, forsterite, graphite, phlogopite, pyrite, and corundum (ruby) (Zaw et al., 2015; Chankhantha et al., 2020). Moreover, anhydrite, apatite, calcite, chondrodite, dolomite, graphite, ilmenite, magnesite, forsterite, phlogopite, potassium feldspar, pyrite, quartz, rutile, sulfur, titanite, uraninite, and zircon have also been found as mineral inclusions in Mogok spinel (Phyo et al., 2019). Although mineral inclusions can provide valuable information for gemological characterization and origin determination, most of the samples examined in this study were free of inclusions, which limited detailed inclusion analysis.

Lang Chap, Vietnam. Here, gem spinel has been mined mostly from secondary deposits, beginning in February 2010. This area is particularly renowned for red to orange spinel (Khoi et al., 2011; Huong et al., 2012). The small village of Lang Chap is located in the Luc Yen District, Yen Bai Province, within the Day Nui Con Voi range. This area is positioned between the Red River Fault to the southwest and the Chay River Fault to the northeast (Trinh et al., 2012; again, see figure 2). In the Red River Fault zone, two main tectonic events contributed to the formation of gemstones; the Indosinian orogeny resulted from the collision between the Yangtze craton and the Indochinese shield in the Upper Proterozoic (Kušnír, 2000); the subsequent Himalayan orogeny produced similar high-grade metamorphic conditions to those of the MMB. Additionally, spinel from Lang Chap is associated with high-grade metamorphic rocks under amphibolite facies' conditions, including calc-silicates, gneisses, and marbles (Malsy et al., 2012; Chauviré et al., 2015; Giuliani et al., 2017). As a newly discovered deposit, detailed information on mineral inclusions in Lang Chap spinel is limited.

An Phu, Vietnam. This renowned gem mining location is also in Yen Bai Province and is known for high-quality spinel. These spinels formed within marble during granulite facies metamorphism; other minerals found in these marbles include chlorite, clinohumite, forsterite, pargasite, and phlogopite (Garnier et al., 2005; Fallick et al., 2019). In addition, inclusions of apatite, calcite, dolomite, goethite, graphite, magnesite, potassium feldspar, titanite, and zircon were discovered in these spinels (Giuliani et al., 2003). An Phu is part of a geological terrane, the Lo Gam zone, to the east of the Red River Fault (Malsy et al., 2012; again, see figure 2). Two significant tectonic processes in the Lo Gam zone were crucial to the formation of gemstones

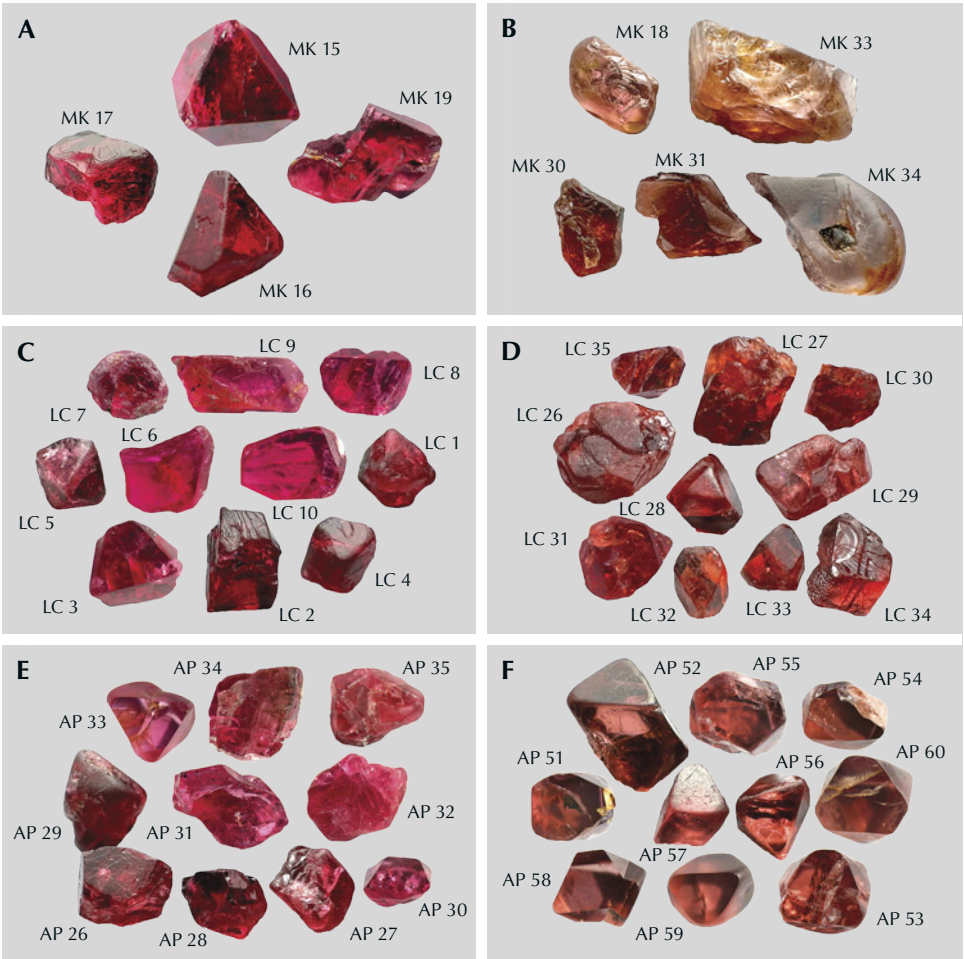

Figure 3. Representative red (left) and orange (right) spinel samples from Mogok (A: 0.19–0.60 ct and B: 0.35–2.59 ct), Lang Chap (C: 0.33–0.54 ct and D: 0.31–2.82 ct), and An Phu (E: 0.42–4.31 ct and F: 0.24–1.55 ct). Photos by Boonyapak Aksorn.

along the Red River Fault area. These were the Indosinian orogeny, resulting from the collision between the Yangtze craton and the Indochinese shield during the Upper Proterozoic, and the subsequent Himalayan orogeny, which is also associated with the metamorphic evolution of the MMB (Garnier et al., 2005; Chauviré et al., 2015; Giuliani et al., 2017; Chankhantha et al., 2020).

MATERIALS AND METHODS

Samples. All spinel samples for this study were acquired by the authors from either miners or local markets around the mining areas. Author DS bought all Mogok spinels directly from the local market around the mining area, and author DTAV bought spinels directly from the local miners in Lang Chap and An Phu, Vietnam. Red and orange spinels were meticulously selected and categorized based on their color and hue according to the Munsell color system. The red spinels' color codes ranged from 2.5R to 5R, and the orange spinels' color codes ranged from 7.5R to 10R. The red spinel collection comprised 13 samples from Mogok, 25 samples from Lang Chap, and 25 samples from An Phu. The orange spinel collection included 14 samples from Mogok, 25 samples from Lang Chap, and 25 samples from An Phu. All samples were labeled using abbreviations of locations followed by a number (e.g., MK 17). Double-sided polished wafers were fabricated from all 127 spinel samples for standard gemological testing, including determination of refractive index (RI), specific gravity (SG), ultraviolet (UV) reaction, and optical character with a polariscope. Furthermore, ultraviolet/visible/near-infrared (UV-Vis-NIR) spectroscopy, electron probe microanalysis (EPMA), and laser ablation–inductively coupled plasma–mass spectrometry (LA-ICP-MS) were applied to select samples representing each unique color (figure 3).

UV-Vis-NIR Spectroscopy. Absorption spectra in the UV-Vis-NIR range (250–1500 nm) were collected by a Perkin-Elmer Lambda 1050 spectrophotometer at

the Gem and Jewelry Institute of Thailand (GIT). Scan speed was set at 405 nm/min with a resolution of 3 nm. The thin double-sided polished wafer samples (≤4 mm thick) allowed for the use of transmission mode. The absorption coefficient was calculated using the formula $\alpha = 2.303A/t$, where α represents the Napierian true absorption coefficient in cm^{-1}, A is the decadic true absorbance (unitless), and t is the thickness of the sample in centimeters (Dubinsky et al., 2020).

EPMA. A JEOL model JXA-8100 electron probe microanalyzer at the Department of Geology, Chulalongkorn University, was used to determine major and minor oxide compositions. Standard materials for calibration included synthetic quartz (SiO_2) for silicon, synthetic rutile (TiO_2) for titanium, synthetic corundum (Al_2O_3) for aluminum, lead vanadium germanium oxide (PbV Geoxide) for vanadium, synthetic eskolaite (Cr_2O_3) for chromium, gadolinium gallium garnet (GGG) for gallium, fayalite (Fe_2SiO_4) for iron, synthetic periclase (MgO) for magnesium, synthetic manganosite (MnO) for manganese, cobalt oxide (CoO) for cobalt, zinc oxide (ZnO) for zinc, and wollastonite ($CaSiO_3$) for calcium. An acceleration voltage of 15 kV and a probe current of about 2.5×10^{-8} A with a focused electron beam (<1 μm) were applied to all analytical spots. Detection limits were empirically below 0.005 wt.%. Three spots were analyzed for each sample.

LA-ICP-MS. Trace element analyses were performed with LA-ICP-MS. This unit was comprised of a Thermo Scientific iCAP RQ ICP-MS attached to an Elemental Scientific Laser NWR-213 (laser ablation unit) based at GIT. The parameters employed for ICP-MS were a carrier gas flow of 0.75 L/min of helium, a plasma gas flow of 14 L/min of argon with plasma power set at 1550 W, and a radiofrequency generator supply of 40 V. Supplementary parameters for laser ablation included an output energy of 0.246 mJ, fluence around 10 J/cm^2, laser energy set at 65%, spot size of 85 μm, repetition rate of 10 Hz, dwell time of 60 s, and three analyzed spots for each sample. External standard calibration was performed using NIST SRM 610 (with lithium, beryllium, and boron concentrations of 485.0, 465.9–466.1, and 357.0 ppm, respectively) and NIST SRM 612 (with lithium, beryllium, and boron concentrations of 41.5, 36.2–38.4, and 35.0 ppm, respectively). The following masses were collected: ^{49}Ti, ^{51}V, ^{53}Cr, ^{55}Mn, ^{56}Fe, ^{59}Co, ^{60}Ni, ^{67}Zn, and ^{69}Ga. All analyses were reported as ppmw and converted to ppma on the basis of the molecular weight per atom approach, which is as follows: Molecular weight of spinel ($MgAl_2O_4$) is divided by the total number of atoms per formula unit (7 atoms) to obtain the average mass per atom. This value is then divided by the atomic weight of the target element and multiplied by its ppmw value to obtain the atomic concentration (ppma).

RESULTS

Standard Gemological Properties. A summary of the standard gemological properties for the red and orange spinels tested is presented in table 1. The samples

TABLE 1. Standard gemological properties of red and orange spinel samples.

Color group	Deposit	Color code	Refractive index	Specific gravity	Ultraviolet fluorescence
Red (*n* = 13)	Mogok, Myanmar	2.5R	1.713–1.728	3.551–3.692	LW: red to strong red SW: red to strong red
Red (*n* = 25)	Lang Chap, Vietnam	2.5R	1.710–1.725	3.554–3.653	LW: strong red SW: red to strong red
Red (*n* = 25)	An Phu, Vietnam	2.5R–5R	1.719–1.725	3.528–3.661	LW: strong red SW: red to strong red
Orange (*n* = 14)	Mogok, Myanmar	7.5R–10R	1.710–1.719	3.552–3.621	LW: red to strong red SW: weak red
Orange (*n* = 25)	Lang Chap, Vietnam	7.5R–10R	1.710–1.720	3.571–3.649	LW: strong red SW: weak red to red
Orange (*n* = 25)	An Phu, Vietnam	7.5R–10R	1.711–1.721	3.570–3.659	LW: red to strong red SW: inert to weak red

Note: n = number of samples; LW = long-wave; SW = short-wave.

ranged in RI from 1.710 to 1.728, all displaying single refraction. The SG values varied within a range of 3.528 to 3.692. Notably, all red spinel samples displayed red fluorescence under both long-wave (365 nm) and short-wave (254 nm) UV, while some orange spinel samples exhibited red fluorescence under long-wave UV but were inert or exhibited weak to medium red fluorescence under short-wave UV.

UV-Vis-NIR Spectroscopy. UV-Vis-NIR absorption spectra corrected for path length of all red and orange spinel samples showed absorption peaks at 390 nm and 534–540 nm (figure 4), attributed to overlapping contributions from Cr^{3+} and V^{3+}. Notably, the absorption feature associated with Cr^{3+} in red spinel shows a shoulder at 430 nm. In addition, orange spinels exhibited a reduced absorption intensity from 470 to 600 nm compared to their red counterparts, while also displaying a less pronounced peak at 534–540 nm. Moreover, their Cr^{3+} absorption range (350–490 nm) was broader than that observed in red spinels (350–470 nm). The referenced absorption peaks of Cr^{3+} and V^{3+} are from Belley and Palke (2021) and D'Ippolito et al. (2015).

Distinct absorption bands were evident for red spinel in the violet range (350–470 nm) and green to

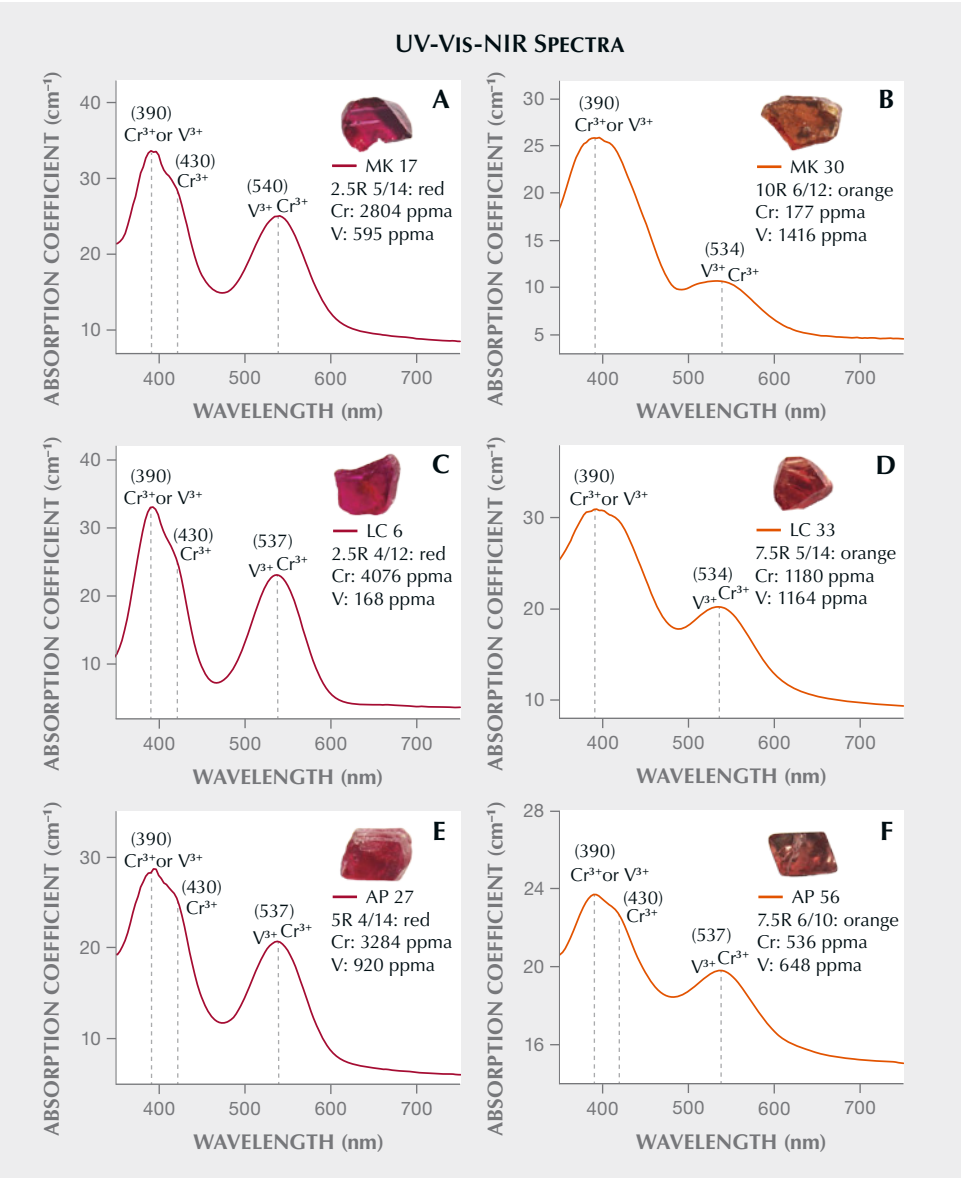

Figure 4. Representative UV-Vis-NIR absorption spectra of red (left) and orange (right) spinel samples from Mogok (A and B), Lang Chap (C and D), and An Phu (E and F). Munsell color notations (e.g., 2.5R 5/14) are provided to describe hue, value, and chroma.

TABLE 2. Representative EPMA analyses (in wt.%) of red spinel samples from Mogok, Lang Chap, and An Phu.

	Mogok			Lang Chap			An Phu		
	MK 15	MK 16	MK 17	LC 1	LC 2	LC 3	AP 27	AP 28	AP 32
SiO_2	0.04	0.03	bdl[a]	bdl	bdl	bdl	bdl	bdl	bdl
TiO_2	0.07	0.13	0.13	0.08	0.05	bdl	0.10	bdl	0.03
Al_2O_3	65.79	67.44	68.63	68.55	69.25	69.86	69.29	68.71	68.76
V_2O_3	0.21	0.37	0.23	0.39	0.10	0.34	0.36	0.11	0.18
Cr_2O_3	5.38	3.33	1.74	2.06	1.87	1.54	1.47	2.09	1.33
Ga_2O_3	bdl	0.06	0.05	0.07	bdl	0.01	0.10	bdl	bdl
FeO_{total}	0.15	0.15	0.20	0.45	0.94	0.40	0.20	0.58	0.36
MnO	bdl	bdl	bdl	0.01	0.02	bdl	bdl	0.03	0.02
MgO	28.56	27.56	28.25	27.92	27.18	27.82	27.49	27.37	27.53
CoO	bdl	bdl	bdl	bdl	bdl	bdl	bdl	bdl	bdl
ZnO	0.17	1.13	0.57	0.19	0.88	0.16	0.36	0.24	0.45
CaO	0.03	0.02	0.02	0.01	bdl	bdl	0.01	0.01	bdl
Total	100.39	100.22	99.81	99.72	100.29	100.13	99.37	99.14	98.66
Cation atoms per formula unit, based on four oxygen atoms per formula unit									
Si	0.001	0.001	—	—	—	—	—	—	—
Ti	0.001	0.002	0.002	0.001	0.001	—	0.002	—	0.001
Al	1.869	1.915	1.942	1.942	1.957	1.964	1.964	1.956	1.964
V	0.004	0.007	0.005	0.008	0.002	0.006	0.007	0.002	0.004
Cr	0.103	0.064	0.033	0.039	0.036	0.029	0.028	0.040	0.026
Ga	—	0.001	0.001	0.001	—	—	0.002	—	—
Fe^{3+}	0.014	0.005	0.010	0.005	0.002	—	—	0.001	0.004
Fe^{2+}	0.003	0.003	0.004	0.004	0.017	0.008	0.004	0.010	0.003
Mn	—	—	—	—	—	—	—	0.001	0.001
Mg	1.026	0.990	1.011	1.000	0.972	0.990	0.986	0.986	0.994
Co	—	—	—	—	—	—	—	—	—
Zn	0.003	0.020	0.010	0.004	0.016	0.003	0.006	0.004	0.008
Ca	0.001	0.001	—	—	—	—	—	—	—
Total	3.024	3.009	3.018	3.004	3.002	3.000	2.998	3.001	3.003
$\sum R^{2+}$	1.033	1.014	1.025	1.008	1.004	1.000	0.996	1.001	1.006
X(Mg)	0.984	0.992	0.986	0.991	0.981	0.992	0.996	0.989	0.993
X(Fe)	0.016	0.008	0.014	0.009	0.019	0.008	0.004	0.011	0.007
$\sum R^{3+}$	1.991	1.995	1.992	1.996	1.998	2.000	2.002	2.000	1.997
Y(Al)	0.946	0.964	0.981	0.976	0.981	0.982	0.982	0.979	0.985
Y(Cr)	0.052	0.032	0.017	0.020	0.018	0.015	0.014	0.020	0.013
Y(V)	0.002	0.004	0.003	0.004	0.001	0.003	0.004	0.001	0.002

[a]bdl = below detection limit (<0.005 wt.%).
Note: Fe^{2+} and Fe^{3+} recalculated using method described by Droop (1987).

TABLE 3. Representative EPMA analyses (in wt.%) of orange spinel samples from Mogok, Lang Chap, and An Phu.

	Mogok			Lang Chap			An Phu		
	MK 30	MK 31	MK 34	LC 32	LC 33	LC 35	AP 53	AP 54	AP 57
SiO_2	bdl[a]	bdl	bdl	bdl	bdl	bdl	0.01	bdl	bdl
TiO_2	bdl	0.11	bdl	bdl	0.08	0.04	0.04	bdl	bdl
Al_2O_3	70.77	70.63	70.36	70.89	70.62	70.49	70.51	71.17	71.66
V_2O_3	1.10	0.84	1.01	1.06	0.85	1.05	0.36	0.31	0.32
Cr_2O_3	0.10	0.24	0.15	0.20	0.45	0.51	0.12	0.07	0.23
Ga_2O_3	0.13	bdl	bdl	bdl	bdl	0.01	0.09	0.07	bdl
FeO_{total}	0.03	0.09	0.11	0.11	0.24	0.32	0.58	0.83	0.28
MnO	bdl	0.01	bdl	bdl	bdl	bdl	0.01	0.01	bdl
MgO	28.65	28.40	28.22	27.72	27.58	27.30	28.65	27.16	27.76
CoO	bdl	bdl	bdl	bdl	bdl	bdl	bdl	bdl	bdl
ZnO	0.09	0.01	0.31	0.05	0.08	0.16	0.14	0.06	bdl
CaO	0.01	bdl	0.01	0.02	0.01	bdl	bdl	0.03	bdl
Total	100.88	100.33	100.19	100.04	99.91	99.86	100.51	99.69	100.25
Cation atoms per formula unit, based on four oxygen atoms per formula unit									
Si	—	—	—	—	—	—	—	—	—
Ti	—	0.002	—	—	0.001	0.001	0.001	—	—
Al	1.968	1.973	1.972	1.986	1.983	1.982	1.970	2.002	1.999
V	0.021	0.016	0.019	0.020	0.016	0.020	0.007	0.006	0.006
Cr	0.002	0.005	0.003	0.004	0.009	0.010	0.002	0.001	0.004
Ga	0.002	—	—	—	—	—	0.001	0.001	—
Fe^{3+}	0.004	0.001	0.004	—	—	—	0.011	—	—
Fe^{2+}	0.001	—	0.002	0.002	0.005	0.006	—	0.017	0.006
Mn	—	—	—	—	—	—	—	—	—
Mg	1.008	1.004	1.001	0.982	0.980	0.971	1.013	0.966	0.980
Co	—	—	—	—	—	—	—	—	—
Zn	0.002	—	0.006	0.001	0.001	0.003	0.002	0.001	—
Ca	—	—	—	0.001	—	—	—	0.001	—
Total	3.007	3.001	3.006	2.995	2.995	2.993	3.009	2.995	2.995
$\sum R^{2+}$	1.010	1.004	1.009	0.986	0.986	0.980	1.016	0.985	0.985
X(Mg)	0.995	0.999	0.994	0.998	0.995	0.994	0.989	0.983	0.994
X(Fe)	0.005	0.001	0.006	0.002	0.005	0.006	0.011	0.017	0.006
$\sum R^{3+}$	1.997	1.997	1.998	2.009	2.009	2.013	1.993	2.010	2.010
Y(Al)	0.988	0.989	0.989	0.988	0.988	0.985	0.995	0.997	0.995
Y(Cr)	0.001	0.003	0.002	0.002	0.004	0.005	0.001	0.000	0.002
Y(V)	0.011	0.008	0.010	0.010	0.008	0.010	0.004	0.003	0.003

[a]bdl = below detection limit (<0.005 wt.%).
Note: Fe^{2+} and Fe^{3+} recalculated using method described by Droop (1987).

yellow range (500–600 nm), resulting in transmission in the blue and red regions of the spectrum (figure 4, A, C, and E). On the other hand, orange spinels exhibited similar absorption in the violet range (350–470 nm), extending into part of the blue region (490 nm), along with reduced absorption in the green to yellow range (500–600 nm), resulting in increased transmission in the orange region, as depicted in figure 4, B, D, and F.

The representative red spinel sample (LC 6 in figure 4C) revealed a chromium-rich and vanadium-poor composition, with 4076 ppma chromium and 168 ppma vanadium, and exhibited a peak at 390 nm, a shoulder peak at 430 nm, and a distinct absorption intensity at 534–540 nm. In contrast, the representative orange spinel sample (MK 30 in figure 4B) yielded chromium-poor and vanadium-rich contents of 177 ppma chromium and 1416 ppma vanadium and showed a peak at 390 nm, a broader peak width compared to the red spinel, and a much reduced peak at 534–540 nm.

Mineral Chemistry. *EPMA*. Representative EPMA analyses and the resulting calculated stoichiometric formulas based on four oxygen atoms are presented in tables 2 and 3. Moreover, Fe^{2+} and Fe^{3+} were recalculated using the method described by Droop (1987). According to the classification of Haggerty (1991) and Deer et al. (2013), spinels with major elements of magnesium and aluminum in an approximate stoichiometric ratio of 1:2 are classified as spinel ($MgAl_2O_4$).

Chemical analyses of red spinel samples from Mogok, Lang Chap, and An Phu demonstrated that all contained Al_2O_3 (65.79–69.86 wt.%) and MgO (27.18–28.65 wt.%). Consequently, the red samples exhibited 1.869–1.964 Al^{3+} atom per formula unit (apfu), incompletely occupying the octahedral site (2 apfu). The presence of Cr^{3+} (0.026–0.103 apfu) was observed, substituting for Al^{3+} in the octahedral site. Consequently, the mole fraction at the tetrahedral site showed that $X_{Mg^{2+}}$ ranged from 0.981 to 0.996, while $X_{Fe^{2+}}$ ranged from 0.004 to 0.019. At the octahedral site, $Y_{Al^{3+}}$ ranged from 0.946 to 0.985, $Y_{Cr^{3+}}$ ranged from 0.013 to 0.052, and $Y_{V^{3+}}$ ranged from 0.001 to 0.004 (table 2).

Orange spinel samples from Mogok, Lang Chap, and An Phu were predominantly comprised of Al_2O_3

TABLE 4. Representative LA-ICP-MS analyses (in ppmw) of red spinel samples. Corresponding ppma values are shown in parentheses.

	Mogok			Lang Chap			An Phu			Detection limit (ppmw)
	MK 15	MK 16	MK 17	LC 1	LC 2	LC 3	AP 27	AP 28	AP 32	
Ti	1110 (461)	522 (217)	939 (390)	155 (65)	41 (17)	140 (58)	45 (19)	16 (7)	19 (8)	0.88
V	1630 (650)	1230 (491)	1490 (595)	1175 (469)	423 (169)	1270 (507)	2307 (920)	882 (352)	1080 (431)	0.04
Cr	23623 (9243)	13785 (5394)	7166 (2804)	6842 (2677)	6374 (2494)	6002 (2348)	8393 (3284)	12149 (4754)	7967 (3117)	0.43
Mn	8 (3)	11 (4)	5 (2)	7 (3)	150 (55)	7 (3)	10 (4)	206 (76)	172 (64)	0.13
Fe	6158 (2238)	7554 (2745)	10274 (3733)	1909 (694)	4298 (1562)	1893 (688)	1756 (638)	4565 (1659)	3577 (1300)	3.02
Co	bdl[a]	3 (1)	2 (0.7)	4 (1)	5 (2)	4 (2)	4 (2)	12 (4)	1 (0.3)	0.07
Ni	13 (5)	142 (48)	82 (28)	18 (6)	7 (2)	19 (7)	79 (27)	42 (14)	1 (0.2)	0.27
Zn	2402 (764)	10569 (3360)	6713 (2134)	2046 (650)	9920 (3154)	1799 (572)	1325 (421)	1116 (355)	1456 (463)	0.25
Ga	107 (31)	225 (66)	169 (50)	184 (54)	175 (51)	177 (52)	258 (76)	206 (61)	393 (116)	0.11

[a]*bdl = below detection limit.*

TABLE 5. Representative LA-ICP-MS analyses (in ppmw) of orange spinel samples. Corresponding ppma values are shown in parentheses.

	Mogok			Lang Chap			An Phu			Detection limit (ppmw)
	MK 30	MK 31	MK 34	LC 27	LC 32	LC 35	AP 53	AP 54	AP 57	
Ti	209 (87)	415 (46)	79 (33)	95 (40)	77 (32)	152 (63)	116 (48)	79 (33)	149 (62)	0.88
V	3549 (1416)	2867 (1144)	470 (188)	3031 (1209)	3688 (1471)	4041 (1612)	1626 (649)	1340 (535)	1529 (610)	0.04
Cr	452 (177)	1541 (603)	265 (104)	1005 (393)	728 (285)	2431 (951)	904 (354)	589 (230)	1397 (547)	0.43
Mn	4 (2)	8 (3)	4 (1)	5 (2)	5 (2)	7 (2)	12 (5)	71 (26)	7 (3)	0.13
Fe	1877 (682)	5318 (1932)	5224 (1898)	1120 (407)	829 (301)	1994 (725)	3912 (1421)	6736 (2447)	2244 (815)	3.02
Co	bdl[a]	1 (0.2)	1 (0.4)	2 (0.8)	bdl	2 (0.7)	6 (2)	5 (2)	2 (0.5)	0.07
Ni	9 (3)	32 (11)	167 (57)	120 (41)	38 (13)	37 (13)	29 (10)	13 (4)	7 (2)	0.27
Zn	1145 (464)	588 (187)	725 (230)	1330 (422)	980 (311)	1291 (411)	1042 (331)	325 (103)	753 (239)	0.25
Ga	152 (45)	52 (15)	101 (30)	76 (22)	155 (46)	98 (29)	146 (43)	109 (32)	136 (40)	0.11

[a]*bdl = below detection limit.*

(70.36–71.66 wt.%) and MgO (27.16–28.65 wt.%). Therefore, recalculated Al^{3+} ions (1.968–2.002 apfu) occupied most of the octahedral sites. In addition, V^{3+} (0.006–0.021 apfu) was observed, substituting for Al^{3+} in the octahedral site. As a result, the mole fraction at the tetrahedral site showed that $X_{Mg^{2+}}$ ranged from 0.983 to 0.993, while $X_{Fe^{2+}}$ ranged from 0.001 to 0.017. At the octahedral site, $Y_{Al^{3+}}$ ranged from 0.985 to 0.997, $Y_{Cr^{3+}}$ ranged from 0 to 0.005, and $Y_{V^{3+}}$ ranged from 0.003 to 0.011 (table 3).

LA-ICP-MS. Representative trace analyses of impurities in red and orange spinel samples are presented in tables 4 and 5, respectively. It is well recognized that the red and orange colorations in spinel are primarily attributed to chromium and vanadium, as seen in these samples. The relationship between chromium and vanadium is illustrated in figure 5, highlighting the significantly higher chromium contents in red spinel compared to vanadium, while the reverse is observed in orange spinel. Notably, the chromium-to-vanadium ratios are ≥1.7 for red spinel

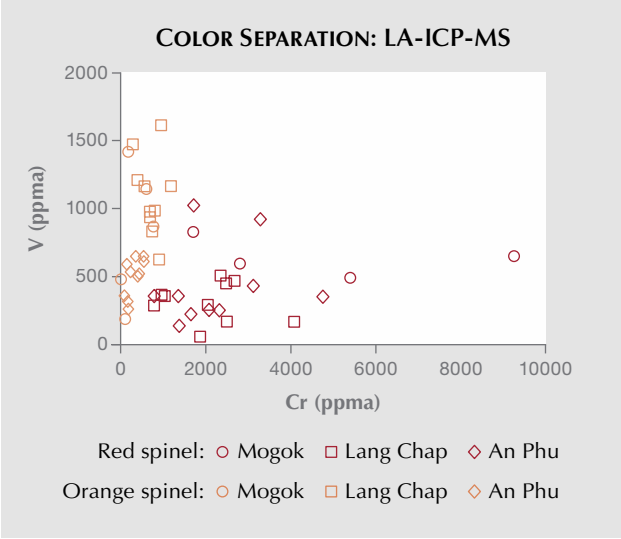

Figure 5. Plot of vanadium vs. chromium showing trends corresponding to red and orange colors in spinel samples from Mogok, Lang Chap, and An Phu.

TABLE 6. LA-ICP-MS analyses (in ppmw) of chromium, vanadium, and chromium-to-vanadium ratios affecting coloration in representative spinel samples. Corresponding ppma values are shown in parentheses.

Red spinel	MK 17	LC 6	AP 27	AP 35	LC 9
Cr	7166 (2804)	10417 (4076)	8393 (3284)	4380 (1714)	4776 (1869)
V	1490 (595)	420 (168)	2307 (920)	2565 (1023)	145 (58)
Cr/V	4.8 (4.7)	24.8 (24.3)	3.6 (3.6)	1.7 (1.7)	32.9 (32.2)
Orange spinel	**MK 30**	**LC 33**	**AP 56**	**LC 32**	**MK 33**
Cr	452 (177)	3016 (1180)	1371 (536)	728 (285)	16 (6)
V	3549 (1416)	2919 (1164)	1625 (648)	3688 (1471)	1203 (480)
Cr/V	0.1 (0.1)	1.0 (1.0)	0.8 (0.8)	0.2 (0.2)	0.01 (0.01)

and ≤1.0 for orange spinel (table 6). These ratios were determined using both ppmw and ppma and yielded similar values because chromium and vanadium have very similar atomic weights.

Trace analyses of red spinel (table 4) determined a vanadium range of 169 to 920 ppma, a chromium range of 2348 to 9243 ppma, and an iron range of 638 to 3733 ppma. The chromium-to-vanadium ratios displayed a range of 1.7 to 32, indicating chromium is always predominant over vanadium (mostly ≥1.7 times). Additionally, titanium versus zinc plots distinctly highlight a variation among different sources, with a decreasing trend in titanium content from Mogok to Lang Chap and An Phu, respectively (figure 6).

The orange spinel samples (table 5) were determined to have a range of vanadium from 188 to 1612 ppma, chromium from 104 to 951 ppma, and iron from 301 to 2447 ppma. In particular, chromium-to-vanadium ratios were clearly ≤1.0 (table 6). Iron content in orange spinel appears to be lower than in red spinel. Additionally, plots of vanadium versus zinc are distinctively different between Lang Chap and An Phu orange spinel; however, they both overlap with Mogok spinel (figure 7).

Figure 6. Plot of titanium vs. zinc shows clear separation among red spinels from Mogok, Lang Chap, and An Phu.

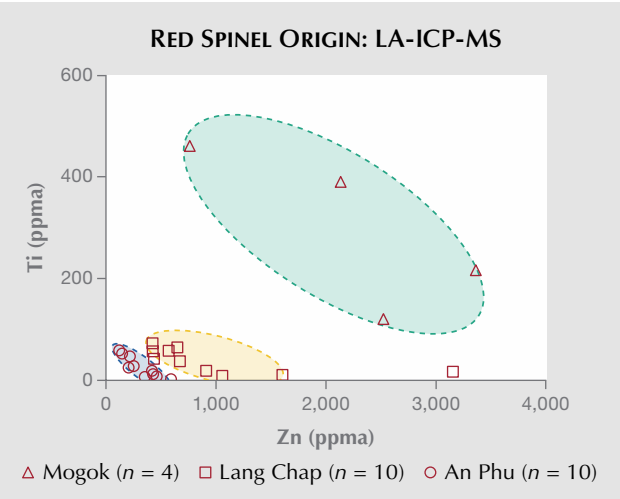

Figure 7. Plot of vanadium vs. zinc reveals clear separation between orange spinels from Lang Chap and An Phu, but both sets overlap with Mogok spinel samples.

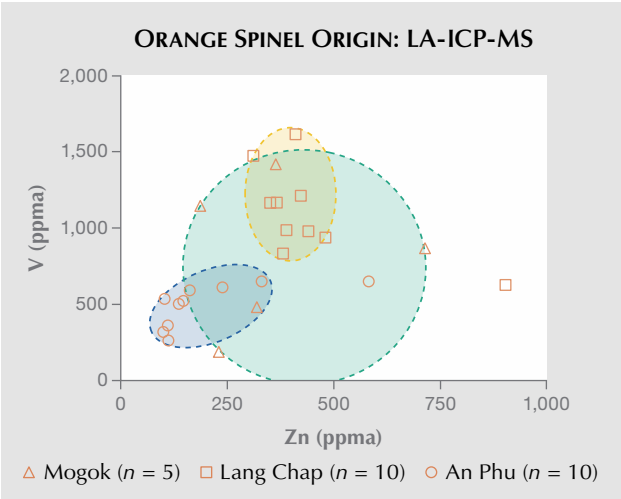

DISCUSSION

The colors observed in spinel are predominantly influenced by trace elements substituting in tetrahedral and/or octahedral sites, resulting in spin-allowed or spin-forbidden transitions that contribute to a diverse range of colors (Chauviré et al., 2015; Andreozzi et al., 2019). Specifically, the red and orange hues in spinel are attributed to Cr^{3+} and V^{3+} in spin-allowed transitions, leading to the absorption of light within the violet spectrum (350–470 nm) and the green to yellow spectrum (500–600 nm). The red spinel samples, characterized by chromium-to-vanadium ratios ≥1.7, exhibited a distinct peak at 390 nm (with a shoulder peak at 430 nm) and a band at 534–540 nm, resulting in a pronounced red hue. Conversely, the studied orange spinel, with chromium-to-vanadium ratios ≤1.0, exhibited a distinct peak at 390 nm (without a 430 nm shoulder peak) and a band at 534–540 nm, showed enhanced light absorption in the blue to green spectrum (350–490 nm), and displayed decreased absorption intensity in the green to yellow spectrum (500–600 nm), producing a distinct orange color due to the partial cancellation of the red range by the complementary green range. For example, samples LC 6, MK 17, and AP 27, with chromium-to-vanadium ratios of 24, 4.7, and 3.6, respectively (table 6), clearly demonstrated this effect. In contrast, sample MK 30, with a color code of 10R 6/12 and a chromium-to-vanadium ratio of 0.01, displayed a more prominent orange color compared to samples LC 33 and AP 56, which have chromium-to-vanadium ratios of 1.0 and 0.83, along with color codes of 7.5R 5/14 and 7.5R 6/10, respectively (again, see figure 4, D and F). Notably, spinel samples with chromium-to-vanadium ratios between 1.0 and 1.7 require further investigation, although their colors may be continuously superimposed within the ranges of orange and red. Consistent with the relative proportions of chromium and vanadium discussed above, higher vanadium versus chromium concentrations in spinel should exhibit an orange shade, whereas a prominent chromium content would result in a red coloration in spinel. Moreover, beyond relative chromium and vanadium concentrations in spinel, the absolute concentrations of chromium and vanadium in spinel play a substantial role in indicating the intensity of the resultant color. In red spinel, sample LC 6 (2.5R 4/12), with chromium and vanadium concentrations of 4076 and 168 ppma, respectively, displayed a deeper red hue compared to sample LC 9 (2.5R 6/10), with chromium and vanadium concentrations of 1869 and 58 ppma. Similarly, in orange spinel, sample LC 32 (7.5R 6/12), with chromium and vanadium concentrations of 285 and 1471 ppma, exhibited a deeper orange hue than sample MK 33 (7.5R 7/6), where chromium and vanadium concentrations were 177 and 1416 ppma.

Fluorescence of spinel under short-wave and long-wave UV light was evaluated in relation to chromium, vanadium, and iron contents. The results indicate that fluorescence in both red and orange spinel samples is significantly influenced by chromium content. In particular, chromium-rich red spinel exhibits strong red fluorescence under long-wave UV light, which is notably more intense than that observed in more chromium-poor orange spinel. On the other hand, the fluorescence appears to show no correlation with vanadium and iron contents. It is important to note that the presence of significant fractures in a few samples may have interfered with fluorescence observation and potentially affected the accuracy of the analysis.

The titanium versus zinc plots of red spinel can be used to clearly distinguish spinel from Mogok (high titanium) relative to those from Lang Chap or An Phu (much lower titanium), respectively. The titanium and zinc contents of Mogok spinel align with previous studies. Chankhantha et al. (2020) reported titanium concentrations ranging from 441 to 1270 ppmw and zinc concentrations ranging from 482 to 4320 ppmw. Similarly, Zhao et al. (2023) documented titanium concentrations ranging from 408 to 497 ppmw and zinc concentrations ranging from 339 to 549 ppmw, further supporting the compositional similarities of Mogok spinel. For orange spinel, Lang Chap's samples show notably higher concentrations of vanadium and zinc, whereas samples from An Phu have lower concentrations of these two trace elements. However, orange spinel from Mogok exhibits vanadium and zinc ranges overlapping with those from both Lang Chap and An Phu (again, see figure 7). This remains an issue requiring further investigation. However, the geologic settings of these deposits are similar; they appear to have all been closely related to the Himalayan orogeny. Moreover, their marble host rocks underwent granulite facies metamorphism within, leading them to resemble mineral assemblages found both in marbles and as mineral inclusions in spinel (Garnier et al., 2005; Khoi et al., 2011; Huong et al., 2012; Fallick et al., 2019; Phyo et al., 2019; Chankhantha et al., 2020).

CONCLUSION

Red and orange spinel from Mogok in Myanmar and from Lang Chap and An Phu in Vietnam are predominantly comprised of Al_2O_3 and MgO. The presence of Cr^{3+} imparts the distinctive red coloration in spinel, while a combination of V^{3+} and Cr^{3+} is responsible for an orange hue. Spectral analysis revealed prominent absorption peaks at 390 nm, a shoulder peak at 430 nm, and a band at 534–540 nm attributed to Cr^{3+} absorption, with V^{3+} peaks overlapping with Cr^{3+} peaks at 390 nm and 534–540 nm, characterized by a broader peak width at 390 nm and a minor contribution at 534–540 nm. The ratios of Cr^{3+} to V^{3+} correlate with the colors observed for the spinel samples studied, with ratios ≥1.7 indicating red spinel and ≤1.0 indicating orange spinel. Trace element analysis, particularly of titanium and zinc, aids in differentiating the origins of red spinel from Lang Chap and An Phu. Further research is necessary to address complexities arising from geological and tectonic variations among different sources. Additional sampling, including spinel from more geologically diverse origins, may further improve origin determination, particularly as the deposits examined in this study are hosted in similar marble-related environments, which increases the difficulty of separation compared to studies involving different types of host rocks.

ABOUT THE AUTHORS

Boonyapak Aksorn is a gemologist at the Gem and Jewelry Institute of Thailand (GIT) and has a master's degree in geology from Chulalongkorn University in Bangkok, Thailand. Dr. Thitiphan Assawincharoenkij is an associate professor at the Applied Mineral and Petrology of Research Unit (AMP RU), Chulalongkorn University. Dr. Doan Thi Anh Vu is a lecturer at the University of Science, Vietnam National University in Ho Chi Minh City. Dr. Dietmar Schwarz is a senior gemologist at Zmpery Gemology Laboratory in Shanghai, China. Dr. Bhuwadol Wanthanachaisaeng is chief of research and standard development at GIT. Dr. Chakkaphan Sutthirat is a professor of earth science at Chulalongkorn University and vice president of Thailand Science, Research and Innovation.

ACKNOWLEDGMENTS

The authors express their gratitude to the Gem and Jewelry Institute of Thailand (GIT) for use of their advanced analytical instruments, including LA-ICP-MS and UV-Vis-NIR. Sample preparation and electron probe microanalyzer were provided by the Department of Geology at Chulalongkorn University. Special thanks to Montira Seneewong-Na-Ayutthaya, Pimlapat Kamkaew, Sopit Poompuang, and Thanapong Lhuaamporn for technical assistance. This work is an initial collaboration with Hub of Talents in Gem and Jewelry Industry, supported by the National Research Council of Thailand (NRCT).

REFERENCES

Andreozzi G.B., D'Ippolito V., Skogby H., Hålenius U., Bosi F. (2019) Color mechanisms in spinel: A multi-analytical investigation of natural crystals with a wide range of coloration. *Physics and Chemistry of Minerals*, Vol. 46, pp. 343–360, https://doi.org/10.1007/s00269-018-1007-5

Belley P.M., Palke A.C. (2021) Purple gem spinel from Vietnam and Afghanistan: Comparison of trace element chemistry, cause of color, and inclusions. *G&G*, Vol. 57, No. 3, pp. 228–238, https://doi.org/10.5741/GEMS.57.3.228

Chankhantha C., Amphon R., Rehman H.U., Shen A.H. (2020) Characterisation of pink-to-red spinel from four important localities. *Journal of Gemmology*, Vol. 37, No. 4, pp. 393–403.

Chauviré B., Rondeau B., Fritsch E., Ressigeac P., Devidal J.-L. (2015) Blue spinel from the Luc Yen district of Vietnam. *G&G*, Vol. 51, No. 1, pp. 2–17, https://doi.org/10.5741/GEMS.51.1.2

D'Ippolito V., Andreozzi G.B., Hålenius U., Skogby H., Hametner K., Günther D. (2015) Color mechanisms in spinel: Cobalt and iron interplay for the blue color. *Physics and Chemistry of Minerals*, Vol. 42, pp. 431–439, https://doi.org/10.1007/s00269-015-0734-0

Deer W.A., Howie R.A., Zussman J. (2013) *An Introduction to the Rock-Forming Minerals*. Mineralogical Society of Great Britain and Ireland, Middlesex, UK.

Droop G.T.R. (1987) A general equation for estimating Fe^{3+} concentrations in ferromagnesian silicates and oxides from microprobe analyses, using stoichiometric criteria. *Mineralogical Magazine*, Vol. 51, No. 361, pp. 431–435, https://doi.org/10.1180/minmag.1987.051.361.10

Dubinsky E.V., Stone-Sundberg J., Emmett J.L. (2020) A quantitative description of the causes of color in corundum. *G&G*, Vol. 56, No. 1, pp. 1–27, https://doi.org/10.5741/GEMS.56.1.2

Fallick A.E., Giuliani G., Rigaudier T., Boyce A.J., Pham V.L., Pardieu V. (2019) Remarkably uniform oxygen isotope systematics for co-existing pairs of gem-spinel and calcite in marble, with special reference to Vietnamese deposits. *Comptes Rendus Geoscience*, Vol. 351, No. 1, pp. 27–36, https://doi.org/10.1016/j.crte.2018.11.008

Garnier V., Ohnenstetter D., Giuliani G., Maluski H., Deloule E., Trong T.P., Pham V.L., Hoàng Quang V. (2005) Age and significance of ruby-bearing marble from the Red River Shear Zone, northern Vietnam. *Canadian Mineralogist*, Vol. 43, No. 4, pp. 1315–1329, https://doi.org/10.2113/gscanmin.43.4.1315

Giuliani G., Dubessy J., Banks D., Quang V.H., Lhomme T., Pironon J., Garnier V., Trong T.P., Van L.P., Ohnenstetter D. (2003) CO_2–H_2S–COS–S_8–AlO(OH)-bearing fluid inclusions in ruby from marble-hosted deposits in Luc Yen area, North

Vietnam. *Chemical Geology*, Vol. 194, No. 1–3, pp. 167–185, https://doi.org/10.1016/s0009-2541(02)00276-0
Giuliani G., Fallick A.E., Boyce A.J., Pardieu V., Pham V.L. (2017) Pink and red spinels in marble: Trace elements, oxygen isotopes, and sources. *Canadian Mineralogist*, Vol. 55, No. 4, pp. 743–761, https://doi.org/10.3749/canmin.1700009
Haggerty S.E. (1991) Oxide mineralogy of the upper mantle. *Reviews in Mineralogy and Geochemistry*, Vol. 25, No. 1, pp. 355–416.
Huong L.T.-T., Häger T., Hofmeister W., Hauzenberger C., Schwarz D., Pham V.L., Wehmeister U., Khoi N.N., Nhung N.T. (2012) Gemstones from Vietnam: An update. *G&G*, Vol. 48, No. 3, pp. 158–176, https://doi.org/10.5741/GEMS.48.3.158
Iyer L.A.N. (1953) The Geology and Gem-stones of the Mogok Stone Tract, Burma. *Memoirs of the Geological Survey of India*, Vol. 82, 100 pp.
Khoi N.N., Sutthirat C., Tuan D.A., Van Nam N., Thuyet N.T.M., Nhung N.T. (2011) Ruby and sapphire from the Tan Huong–Truc Lau area, Yen Bai Province, northern Vietnam. *G&G*, Vol. 47, No. 3, pp. 182–195, https://doi.org/10.5741/GEMS.47.3.182
Krzemnicki M.S., Leuenberger A., Balmer W.A. (2023) Cobalt-bearing blue spinel from Lukande, near Mahenge, Tanzania. *Journal of Gemmology*, Vol. 38, No. 5, pp. 474–493.
Kušnír I. (2000) Mineral resources of Vietnam. *Acta Montanistica Slovaca*, Vol. 5, No. 2, pp. 165–172.
Liu Y., Qi L., Schwarz D., Zhou Z. (2022) Color mechanism and spectroscopic thermal variation of pink spinel reportedly from KuhiLal, Tajikistan. *G&G*, Vol. 58, No. 3, pp. 338–353, https://doi.org/10.5741/GEMS.58.3.338
Malsy A.-K., Karampelas S., Schwarz D., Klemm L., Armbruster T., Tuan D.A. (2012) Orangey-red to orangey-pink gem spinels from a new deposit at Lang Chap (Tan Huong–Truc Lau), Vietnam. *Journal of Gemmology*, Vol. 33, No. 1–4, pp. 19–27.
Mattauer M., Matte P., Olivet J.-L. (1999) A 3D model of the India–Asia collision at plate scale. *Comptes Rendus de l'Académie des Sciences – Series IIA: Earth and Planetary Science*, Vol. 328, No. 8, pp. 499–508, https://doi.org/10.1016/s1251-8050(99)80130-x
Peretti A., Günther D. (2003) Spinel from Namya. *Contributions to Gemology*, Vol. 2, pp. 15–18.
Phyo M.M., Bieler E., Franz L., Balmer W., Krzemnicki M.S. (2019) Spinel from Mogok, Myanmar: A detailed inclusion study by Raman microspectroscopy and scanning electron microscopy. *Journal of Gemmology*, Vol. 36, No. 5, pp. 418–435.
Pluthametwisute T., Wanthanachaisaeng B., Saiyasombat C., Sutthirat C. (2022) Minor elements and color-causing role in spinel: Multi-analytical approaches. *Minerals*, Vol. 12, No. 8, article no. 928, https://doi.org/10.3390/min12080928
Saeseaw S., Wang W., Scarratt K., Emmett J.L., Douthit T.R. (2009) Distinguishing heated spinels from unheated natural spinels and from synthetic spinels. *GIA Research News*, March 22, https://www.gia.edu/gia-news-research-NR32209A
Searle M.P., Noble S.R., Cottle J.M., Waters D.J., Mitchell A.H.G., Hlaing T., Horstwood M.S.A. (2007) Tectonic evolution of the Mogok metamorphic belt, Burma (Myanmar) constrained by U-Th-Pb dating of metamorphic and magmatic rocks. *Tectonics*, Vol. 26, No. 3, article no. TC3014, https://doi.org/10.1029/2006tc002083
Searle M.P., Garber J.M., Hacker B.R., Htun K., Gardiner N.J., Waters D.J., Robb L.J. (2020) Timing of syenite–charnockite magmatism and ruby and sapphire metamorphism in the Mogok Valley Region, Myanmar. *Tectonics*, Vol. 39, No. 3, article no. e2019TC005998, https://doi.org/10.1029/2019tc005998
Sickafus K.E., Wills J.M., Grimes N.W. (1999) Structure of spinel. *Journal of the American Ceramic Society*, Vol. 82, No. 12, pp. 3279–3292, https://doi.org/10.1111/j.1151-2916.1999.tb02241.x
Thu K. (2007) The Igneous Rocks of the Mogok Stone Tract: Their Distribution, Petrography, Petrochemistry, Sequence, Geochronology and Economic Geology. PhD Thesis, Yangon University, Yangon, Myanmar.
Trinh P.T., Van Liem N., Van Huong N., Vinh H.Q., Van Thom B., Thao B.T., Tan M.T., Hoang N. (2012) Late Quaternary tectonics and seismotectonics along the Red River fault zone, North Vietnam. *Earth-Science Reviews*, Vol. 114, No. 3–4, pp. 224–235, https://doi.org/10.1016/j.earscirev.2012.06.008
Win M.M., Enami M., Kato T. (2016) Metamorphic conditions and CHIME monazite ages of Late Eocene to Late Oligocene high-temperature Mogok metamorphic rocks in central Myanmar. *Journal of Asian Earth Sciences*, Vol. 117, pp. 304–316, https://doi.org/10.1016/j.jseaes.2015.11.023
Zaw K., Sutherland L., Yui T.-F., Meffre S., Thu K. (2015) Vanadium-rich ruby and sapphire within Mogok Gemfield, Myanmar: Implications for gem color and genesis. *Mineralium Deposita*, Vol. 50, pp. 25–39, https://doi.org/10.1007/s00126-014-0545-0
Zhang L., He K., Guo Q. (2023) Spectroscopic characteristics and coloring mechanisms of different colored spinels from Myanmar. *Crystals*, Vol. 13, No. 4, article no. 575, https://doi.org/10.3390/cryst13040575
Zhao Y., Xu B., Zhao Z., Xu Q., Li Z. (2023) Gemological and chemical characterization of varicolored gemgrade spinel from Mogok, Myanmar. *Crystals*, Vol. 13, No. 3, article no. 447, https://doi.org/10.3390/cryst13030447

For online access to all issues of GEMS & GEMOLOGY from 1934 to the present, visit:

gia.edu/gems-gemology

FROM THE FIELD
VIETNAM

Editor: Wim Vertriest

Field gemology highlights the connection among gemstones, the earth, the trade, and the communities involved in production. For decades, GIA gemologists have traveled the world to visit gem mining and trading locales, documenting conditions in the field and collecting research samples. This systematic collection of research samples on site is essential to ensuring that data supporting origin determination and related research areas remain current and robust. This *G&G* column provides contextual background and presents photos capturing the seemingly common and occasionally spectacular observations encountered during these visits to gemstone sources.

In November 2025, a team of GIA gemologists conducted a field visit to northern Vietnam to document the local mining and trading scene and to enhance their understanding of the region's gemstone culture.

Collecting samples in Vietnam often requires hiking to remote locations where miners are still finding gems. The GIA team spent several days making trips across narrow jungle trails into the surrounding hills to meet with local miners, observe their practices, and collect research samples alongside them. Engaging with gemstone miners is a valuable component of such fieldwork, as they represent the earliest stage of the supply chain, forming the connection between the earth and the trade.

Part of the GIA team in Vietnam, from left to right, including Jessa Rizzo, Yusuke Katsurada, Alex Goodsuhm, and Narint Jaisanit, along with a local ruby and spinel miner (center), in Luc Yen, Vietnam.

GEMSTONES

Deep in the hills of northern Vietnam lies the town of Luc Yen. The surrounding valleys, caves, and hill flanks are rich in gems, but were only discovered in the late 1980s. Since then, the region has been growing in popularity among gemstone connoisseurs, with more gems being discovered across a wider area in recent years.

Ruby was the primary gemstone that initiated the mining boom in northern Vietnam, with large-scale operations active in the surrounding valleys during the early 1990s. Today, ruby production is limited, as most of the easily accessible deposits have been depleted; however, material continues to be recovered from less accessible areas. While the relatively limited quantity of facet-grade material is typically directed to the international market, lower-grade rubies remain readily available in local markets, along with crystal specimens such as this ruby cluster shown to the right.

Editors' note: Questions or topics of interest should be directed to Wim Vertriest (wvertrie@gia.edu).

Gems & Gemology, Vol. 62, No. 2, pp. 192–199.

© 2026 Gemological Institute of America

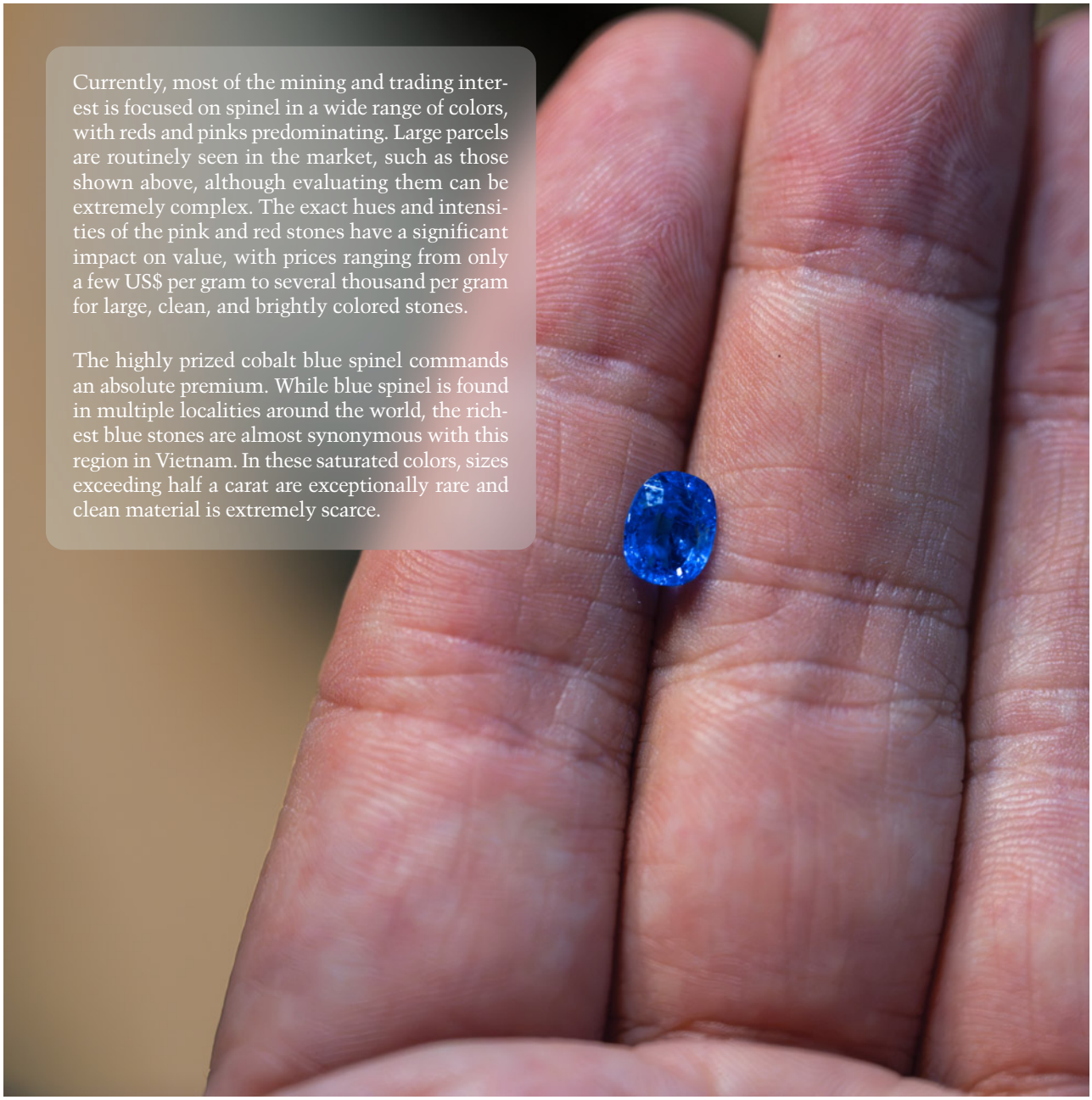

Currently, most of the mining and trading interest is focused on spinel in a wide range of colors, with reds and pinks predominating. Large parcels are routinely seen in the market, such as those shown above, although evaluating them can be extremely complex. The exact hues and intensities of the pink and red stones have a significant impact on value, with prices ranging from only a few US$ per gram to several thousand per gram for large, clean, and brightly colored stones.

The highly prized cobalt blue spinel commands an absolute premium. While blue spinel is found in multiple localities around the world, the richest blue stones are almost synonymous with this region in Vietnam. In these saturated colors, sizes exceeding half a carat are exceptionally rare and clean material is extremely scarce.

Over time, additional gem varieties have been discovered, including several types of garnet and tourmaline, with yellow colors being the most sought after. Opalescent sapphires have gained considerable popularity in recent months, combining a moonstone-like glow and cloudiness with the durability characteristic of sapphire.

MINING

Most of Luc Yen's gem resources can be traced to the abundance of marble that dominates the local geology. Initially regarded as the host rock for gems, marble has since become an important economic pillar for the local industry. In recent decades, numerous marble mining operations have established quarries to cater to the growing international demand for high-quality white marble. The photos to the right, taken 35 years apart from the same viewpoint, show the development of a large marble mining operation.

Near the village of An Phu lies a mining area known as Cuong Troi, which translates roughly to "gate to the sky." Higher on the hillsides, crews break the marble in pursuit of spinel crystals, leaving a prominent white scar across the landscape, where freshly exposed marble contrasts sharply with the surrounding jungle, as seen below.

In the early days of gem mining around Luc Yen, attention was focused on alluvial deposits located at the bases of narrow valleys. Over time, natural forces broke down the marble and released the gemstones from its matrix, resulting in thick beds of sediment that were rich in gems and easy to exploit. This photo to the right from 1992 illustrates how rubies were mined during that period, when heavy machinery enabled the efficient washing and screening of gravels to recover the stones.

Mining in Luc Yen continues today, though it is markedly different. Much of the easily accessible thick sediment layers have been depleted, and the remaining gem-bearing material is largely confined to small cracks and caves between boulders and rocks, where the use of heavy equipment is not feasible. Small crews of miners work these deposits manually, pumping water in to turn the accumulated mud into a slurry that drains away, leaving behind the heavier pebbles. This material is then scooped out and manually washed to reveal the gems. Throughout the narrow valleys and higher elevations of the surrounding jungles, small mining crews can be observed digging between boulders in search of gems.

THE MARKET

Given the abundance of gem material in the region, a vibrant trading scene quickly developed. While the majority of goods on display are locally sourced, globalization has extended to these mountainous areas of Vietnam. Gems from southern Vietnam, including sapphire and peridot, as well as stones from other continents, are increasingly available in the markets.

The main markets are located in Luc Yen city center, where gem traders set up tables every morning to display their stones. This allows potential buyers to efficiently scan the available goods; however, rare and high-value stones are not always openly exhibited.

In the alleys surrounding the markets, many gem dealers conduct business over a cup of tea. Stones are passed around and offers are made, typically involving higher-value material.

In the village of An Phu, located near several significant spinel mining areas, a small outdoor market takes place each afternoon, with dealers and miners gathering to display their parcels of rough stones.

With the strong demand for fine rough and the rapid development of the trading sector, the presence of fraudulent material is inevitable. During this most recent visit to the Luc Yen markets, this suspiciously large, clean, and bright piece of rough shown to the right attracted attention. Based on visual features (color concentrations and conchoidal fractures), it was immediately clear that the specimen was unusual. Examination with a 10× loupe revealed distinct gas bubbles, confirming this was a piece of glass fashioned to imitate a blue spinel crystal. Such stones highlight that even in close proximity to the mines, caution should always be exercised.

In the alleys around the Luc Yen markets, multiple workshops produce "gem paintings," such as the one pictured below. Using gems of intense color but small size and low clarity, artists create delicate patterns and scenes that often hold strong cultural meaning. This side industry complements traditional gem trading, as it relies on a steady supply of gem minerals not suitable for faceting.

Thanks to Hiep Tran (Hiep Tran Gemstones) and Geir Atle Gussias and Mai Tran (Baldergems) for assistance in Vietnam.

All images by Wim Vertriest, with the exception of pp. 196 and 197 (top photos) by Robert Kammerling.

For videos from this recent field expedition, visit: gia.edu/gems-gemology/summer-2026-from-the-field

Lab Notes

Editors
Shane F. McClure | Sally Eaton-Magaña | Artitaya Homkrajae

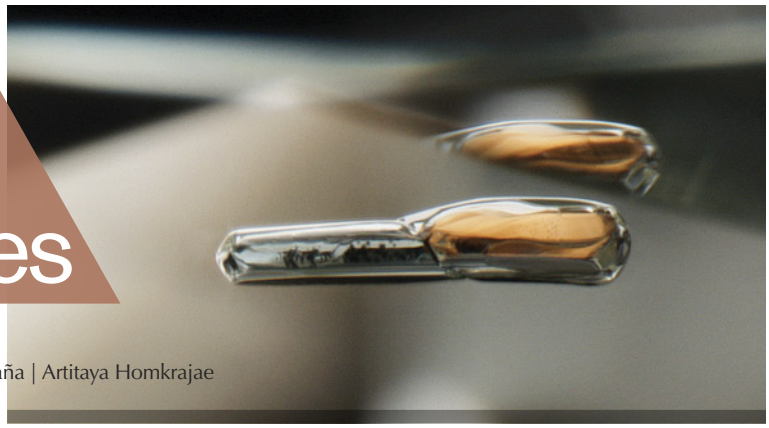

Figure 1. The 5.22 ct very light pinkish brown pear brilliant diamond (left) and the originally submitted 11.07 ct rough (right).

DIAMONDS

Atypical Color Center in Natural Pinkish Brown Diamond

GIA's New York laboratory received a 5.22 ct natural type IaAB pear brilliant diamond, graded as very light pinkish brown (figure 1, left). The finished diamond was matched to its previously submitted 11.07 ct rough (figure 1, right) through identical ultraviolet/visible and mid-infrared spectra.

An atypical absorption band centered at 525 nm and a triplet feature at 600, 608, and 618 nm were detected in the visible/near-infrared (Vis-NIR) absorption spectrum (figure 2). These spectral features are distinct from the typical broad 550 nm absorption band associated with pink coloration from plastic deformation of the diamond structure. The N3 center (415 nm), a defect involving three nitrogen atoms and a vacancy (3N+V), was also present. Mid-infrared spectra showed a natural type IaAB diamond in the one-phonon region (~1332–400 cm^{-1}), revealing nitrogen aggregation from prolonged residence at high mantle temperatures. The A-center (1282 cm^{-1}) results from two adjacent substitutional nitrogen atoms (N-N), and the B-center (1175 cm^{-1}) from four adjacent substitutional nitrogen atoms surrounding a vacancy (4N+V).

Microscopic observation revealed a cloud composed of needle-like inclusions, transparent internal graining, and color zoning caused by plastic deformation of the crystal structure. Mottled strain patterns were observed with high interference colors under cross-polarized light (figure 3, left), indicative of internal stress and crystal structure distortion during natural diamond formation. DiamondView fluorescence showed crystal growth patterns and blue emission caused by the presence of the N3 center in the crystal structure (figure 3, right). Gemological testing supported a natural diamond and natural color origin, with no evidence of surface coating, treatment, or laboratory growth.

The cause of the 525 nm absorption band and triplet feature at 600, 608, and 618 nm remains unknown. A prior study of a pink diamond with a 525 nm absorption band found high concentrations of nickel- and hydrogen-related defects (S. Caplan and W. Wang, "Natural pink diamond colored by the 525 nm absorption band," *GSA Abstracts with Programs*, Vol. 54, No. 5, 2022). However, no such

Editors' note: All items were written by staff members of GIA laboratories.

Gems & Gemology, Vol. 62, No. 2, pp. 200–207.
© 2026 Gemological Institute of America

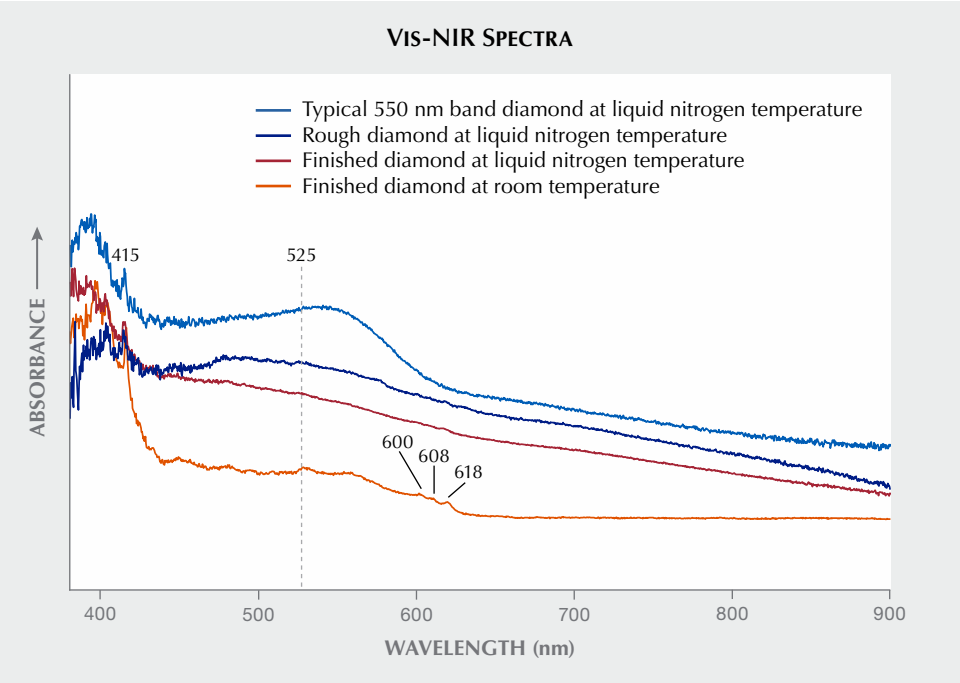

Figure 2. Overlay of the natural rough and finished diamond Vis-NIR spectra verifies matching absorption features. These spectra show the 415 nm peak, an atypical 525 nm band, and triplet at 600, 608, and 618 nm. The room temperature spectrum of the finished diamond shows more resolved features due to a higher signal-to-noise ratio. The typical broad 550 nm band from a different pinkish brown diamond is shown for comparison, highlighting the atypical absorption features. Spectra are offset vertically for clarity.

impurities were detected in this diamond, suggesting that the 525 nm absorption band, to the author's knowledge, has not been previously documented. Weak 600 and 609 nm peaks appear more prominently in type IIa and low nitrogen pink diamonds colored by the 550 nm band (S. Eaton-Magaña et al., "Comparison of gemological and spectroscopic features in type IIa and Ia natural pink diamonds," *Diamond and Related Materials*, Vol. 105, 2020, article no. 107784), possibly originating from unidentified point defects in the diamond structure, which differ from the spectral features seen in this diamond. The 525 nm band and triplet feature observed in this diamond are likely an atypical naturally occurring previously undocumented color center. These atypical absorption spectral features demonstrate the complexity of diamond color origin and the need for further research into natural diamond color centers.

Erica Watts

Figure 3. Left: Mottled strain patterns with high interference colors observed under cross-polarized light. Photomicrograph by Christopher Vendrell; field of view 7.19 mm. Right: DiamondView fluorescence image showing crystal growth patterns and the blue color commonly observed in type IaAB diamonds.

Figure 4. This piece, a diamond cut into the shape of a panther face and set with two natural Zambian emeralds, has a total weight of 67.18 ct. Photo by Gourav Bera.

Carved Natural Diamond Panther Face

Recently, the Mumbai laboratory received an intriguing submission for an identification report. The opaque gray stone was carved and faceted to resemble a panther's face, with two green marquise mixed-cut stones for eyes (figure 4). The piece weighed 67.18 ct and measured 28.45 × 24.17 × 11.37 mm.

Microscopic examination revealed no major surface-reaching features in the heavily included gem. The item, analyzed using Fourier-transform infrared absorption and photoluminescence (PL) spectroscopy at room temperature with 405 nm excitation, exhibited absorption features typical of a type Ia diamond, along with the presence of a hydrogen-related 3107 cm^{-1} peak. The PL spectroscopy showed emissions associated with the N3 defect.

According to the client, the finished piece, titled "Jade Fang," took nearly a year of dedicated craftsmanship to complete. The diamond initially weighed 113 carats and required the use of advanced cutting tools due to its heavy inclusions. Two natural Zambian emeralds weighing 0.29 ct and 0.27 ct, previously submitted to GIA, were added to finish the panther's face.

Unlike traditional cuts designed to maximize brilliance through symmetry, unique shapes such as this one challenge the cutter. This piece reminds us that the true value of a diamond lies not just in its gemological characteristics but also in the artistry that brings it to life.

Roxane Bhot Jain and Manisha Bhoir

PEARLS

Large South Sea Bead Cultured Pearl with *Mille-Feuille* Structure

An extraordinarily large undrilled light gray pearl (figure 5) was recently examined at GIA's New York laboratory. Despite its impressive size (76.79 ct and 42.97 × 33.43 × 31.00 mm), the pearl exhibited an unexpectedly light heft, suggesting the presence of a hollow interior. Real-time X-ray microradiography (RTX) imaging revealed an unusual internal structure for a bead cultured pearl characterized by widely spaced concentric nacre layers separated by translucent veil-like organic material (figure 6), rather than

Figure 5. The South Sea bead cultured pearl measuring 42.97 × 33.43 × 31.00 mm and a large chicken egg (57 × 43 mm). Photo by Sood Oil (Judy) Chia.

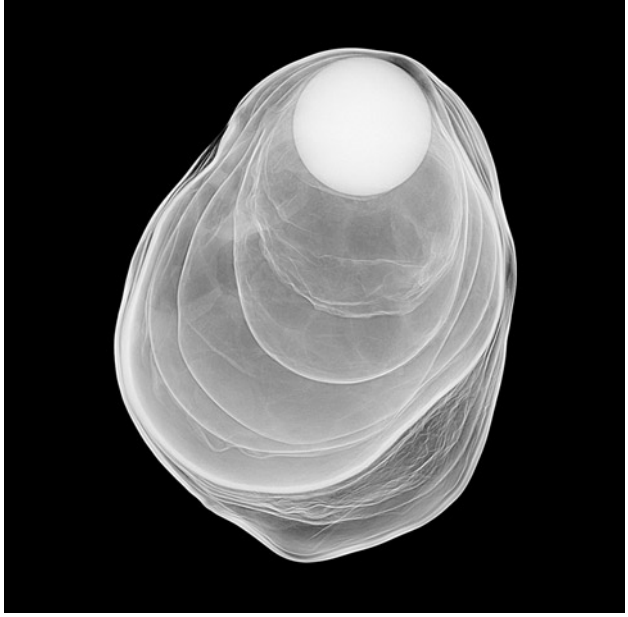

Figure 6. RTX image showing concentric nacre layers separated by translucent organic material.

the compact, continuous nacre typically observed in solid bead cultured pearls. The bead measured approximately 11 mm in diameter and was securely attached at one end of the pearl, with no internal movement or rattling detected when gently shaken. The thin nacre, measuring approximately 0.5 mm at its thickest portion, and hollow internal structure made the pearl extremely fragile.

Based on the gemological examination and the size of the pearl and the bead, the sample was identified as a South Sea bead cultured pearl. Patchy, uneven gray to brown material present underneath the surface appeared to be associated with an organic-rich internal structure; these features contributed to the pearl's bodycolor. While some South Sea pearls may be cultured with organic or inorganic materials to intentionally produce larger baroque-shaped pearls, this was not the case for this sample (L.E. Cartier and M.S. Krzemnicki, "New developments in cultured pearl production: Use of organic and baroque shell nuclei," *Australian Gemmologist*, Vol. 25, No. 1, 2013, pp. 6–13). In this instance, the mollusk may have been affected by unknown environmental or health factors, causing the pearl sac to inflate irregularly by gas or fluid accumulation, trapping organic materials between layers of nacre, ultimately creating a *mille-feuille*-like internal structure similar to a puff pastry layered with cream (L. Otter et al., "A look inside a remarkably large beaded South Sea cultured pearl," Spring 2014 *G&G*, pp. 58–62).

While average sizes of South Sea bead cultured pearls range between 10 mm and 13 mm, exceptional examples may occasionally exceed 20 mm. This remarkable South Sea bead cultured pearl, with its extraordinary size and uncommon structures, provides interesting insights into a highly unusual growth pattern.

Emiko Yazawa

Microscopic Marine Organisms in South Sea Cultured Pearls

GIA's Bangkok laboratory recently received five pearls ranging from cream to orangy yellow, weighing between 2.33 and 5.54 ct and measuring approximately 9.6 × 6.4 mm to 10.3 × 8.3 mm (figure 7). The pearls appeared similar to South Sea cultured pearls produced from *Pinctada maxima* mollusks. X-ray fluorescence imaging was used to confirm their saltwater origin; all samples were inert

*Figure 7. Five cream to orangy yellow South Sea cultured pearls (*Pinctada maxima*), ranging from 9.6 × 6.4 mm to 10.3 × 8.3 mm. Photo by Nuttapol Kitdee.*

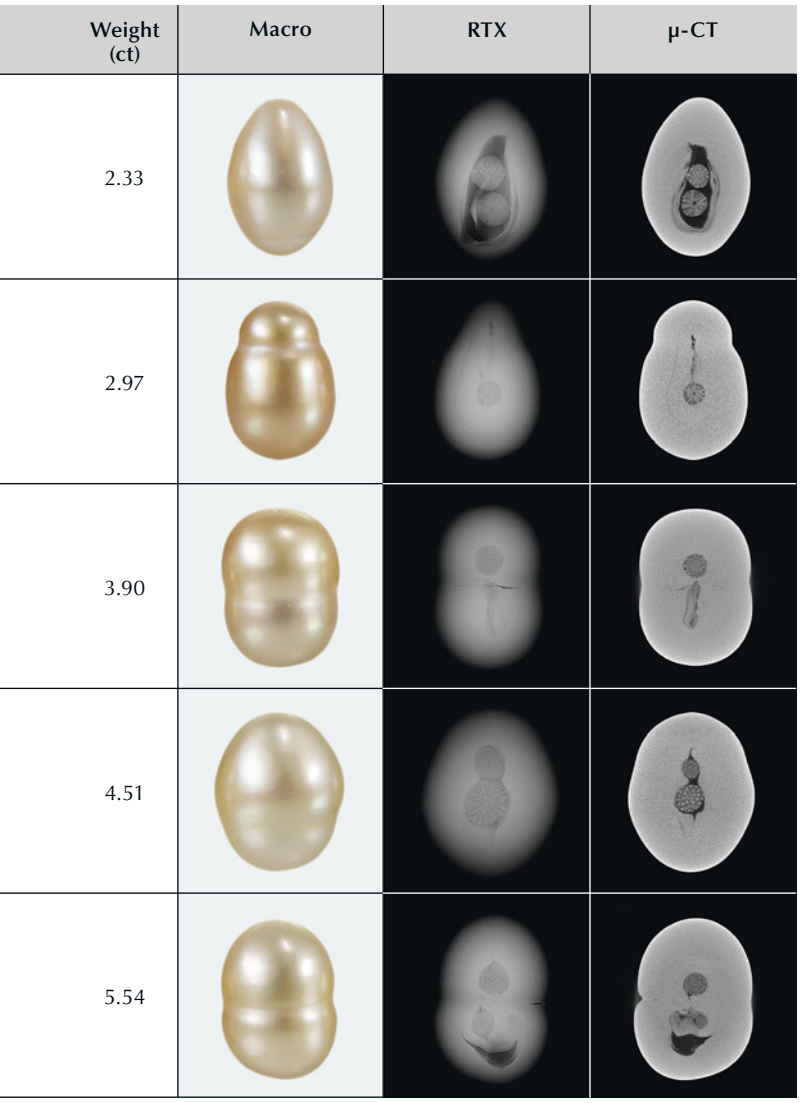

Figure 8. RTX and µ-CT images reveal varying forms of elongated void or linear features associated with one or two microscopic spheres of marine organisms. The spheres measure from 1.23 to 2.28 mm in diameter.

when exposed to X-rays, resulting from the absence of, or a very low level of, manganese, characteristic of saltwater pearls. The four orangy yellow pearls exhibited typical ultraviolet/visible/near-infrared reflectance spectra of natural color yellow South Sea pearls (S. Jin et al., "Application of UV-Vis-NIR spectroscopy to gemology," Winter 2024 *G&G*, pp. 456–473).

Real-time X-ray microradiography (RTX) analysis revealed that each sample contained one or two intriguing spherical radial objects in the center, positioned along the length of the pearl (figure 8). The objects were associated with varying forms of elongated void or linear features known to be diagnostic growth structures commonly found in South Sea non-bead cultured (NBC) pearls (A. Homkrajae et al., "Internal structures of known *Pinctada maxima* pearls: Cultured pearls from operated marine mollusks," Fall 2021 *G&G*, pp. 186–205). The pearls were further analyzed using X-ray computed microtomography (µ-CT) to enhance image resolution, which provided a more comprehensive understanding of the internal structures.

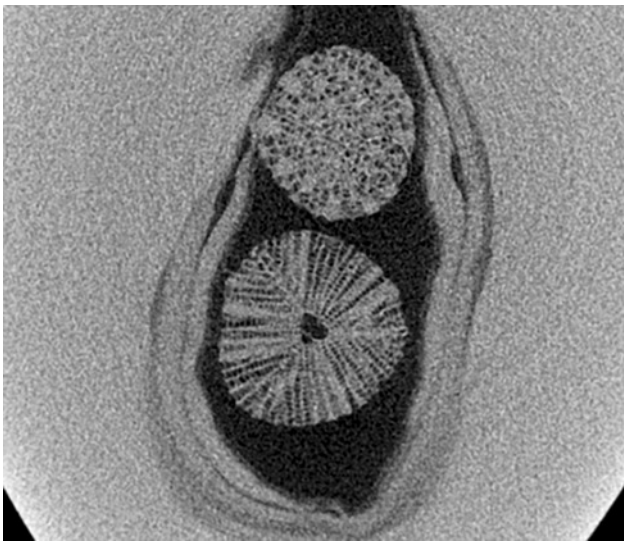

Figure 9. A distinctive porous and radial structure extends outward from the chamber central core of the two white microscopic marine organisms within the elongated dark gray void of the 2.33 ct pearl.

The spherical objects, along with the typical void and linear structures, were clearly visible in the µ-CT analysis. The 3D images revealed that each sphere possessed a distinctive porous and radial structure extending outward from the central core (figure 9; see video at www.gia.edu/gems-gemology/summer-2026-lab-notes-marine-organisms-in-cultured-pearls). Their morphology closely resembled foraminifera spheres found in a natural pearl previously examined at GIA's Bangkok laboratory (Winter 2015 Lab Notes, pp. 434–436). RTX analysis was used to obtain measurements of all the spherical objects, ranging from 1.23 to 2.28 mm in diameter, which are consistent with the size of previously reported microorganisms. However, the previously studied natural pearl exhibited dark organic- and conchiolin-rich growth layers around the rounded microorganism's central core and growth arcs within the surrounding nacre, a structural characteristic comparable with the formation of natural pearls. Conversely, all five studied pearls displayed a tight structure or minimal growth arcs in the surrounding nacre, consistent with NBC pearls and the so-called "atypical bead cultured pearls" previously studied ("Atypical 'beading' in the production of cultured pearls from Australian *Pinctada maxima*," *GIA Research News*, February 13, 2017).

Although previously reported microscopic marine organisms found within pearls were related to natural formations, the internal void and linear features of these studied samples, as well as their close resemblance to

South Sea cultured pearls, indicated that these were likely of cultured origin. Moreover, it is very unusual to encounter similar-looking pearls with identical internal structures of microorganisms rarely found inside pearls. These findings indicated that microorganisms were intentionally inserted into the host mollusk as bead nuclei for culturing. The use of these organisms may be intended to imitate natural pearl formation; thus, gemologists must take caution when interpreting organic materials as evidence of natural origin, and comprehensive analysis is needed for identification. This is the first reported discovery of microscopic marine organisms in South Sea cultured pearls at GIA's laboratories.

Kwanreun Lawanwong

Reversible Photochromism in a Heat-Treated Sri Lankan SAPPHIRE

A 2.38 ct very light blue gemstone was recently submitted to GIA's Bangkok laboratory for identification and geographic origin determination. Standard and advanced gemological testing results were consistent with a Sri Lankan sapphire that had undergone high-temperature heat treatment.

During routine gemological examination, an unexpected color change was observed. After approximately 30 to 40 seconds of exposure to short-wave (254 nm) ultraviolet radiation, the stone's bodycolor changed from an initial very light blue to a light yellow color. Given the unusual nature of this observation, the stone was subsequently subjected to fade testing under GIA color-stability testing conditions using a 150W halogen lamp. After approximately six hours, the yellow color gradually faded, and the bodycolor returned to an appearance similar to its original very light blue coloration (figure 10), confirming that the color change was temporary and reversible.

This behavior is consistent with activation of an unstable trapped-hole color center that can exist in either an inactive (ground) state or an activated state following exposure to ultraviolet radiation (K. Nassau and G.K. Valente, "The seven types of yellow sapphire and their stability to light," Winter 1987 *G&G*, pp. 222–231). In this case, short-wave UV radiation provided sufficient energy to activate the color center and produce a temporary yellow color. However, the induced color was not stable and gradually returned to its inactive state over time or under incandescent illumination. Color descriptions should be based on the color observed after color-stability testing.

Although color-stability testing is not routinely performed for sapphires in this color range, this behavior is consistent with previously documented examples of sapphires containing unstable color centers, particularly some Sri Lankan material. Similar reversible color changes have been reported in sapphires with color influenced by trapped-hole color centers, including yellow, orange, and pinkish orange to orangy pink sapphires ("An update on sapphires with unstable color," *GIA Research News*, December 12, 2022).

Ultraviolet/visible/near-infrared spectroscopic data support this interpretation. Before UV exposure, the stone showed spectral features typical of metamorphic blue sapphire; absorption in the 380–390 nm region (associated with Fe^{3+}) was relatively weak, consistent with low iron content, while a distinct absorption peak at 450 nm (attributed to Fe^{3+}-Fe^{3+} pair interactions) was observed, together with an Fe^{2+}/Ti^{4+} intervalence charge-transfer band

Figure 10. Reversible photochromism in a 2.38 ct heat-treated Sri Lankan sapphire. Exposure to short-wave ultraviolet radiation for 30 to 40 seconds produced a temporary yellow color. After approximately six hours under GIA color-stability testing conditions, the stone returned to an appearance similar to its original very light blue coloration. Photos by Lhapsin Nillapat.

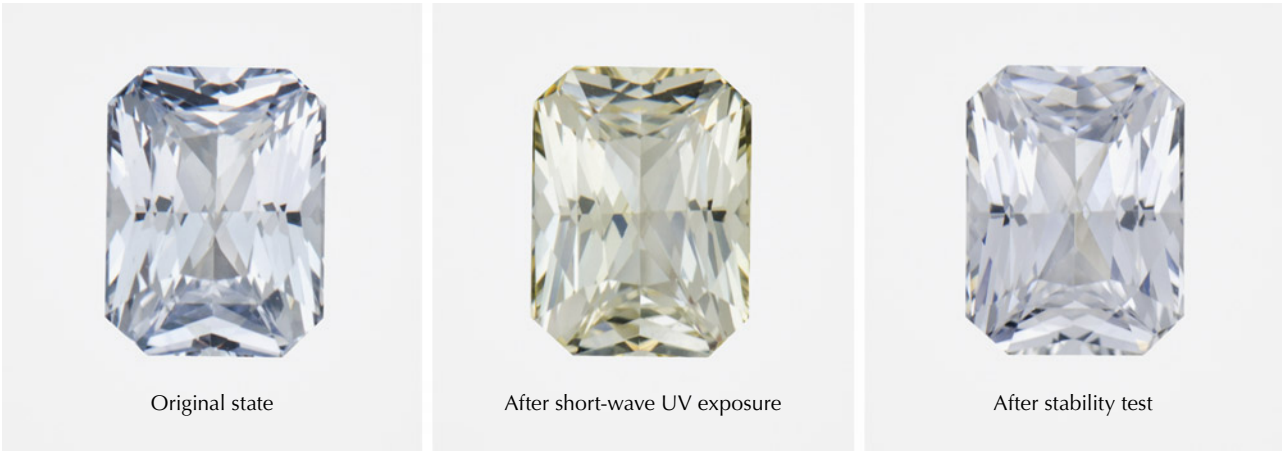

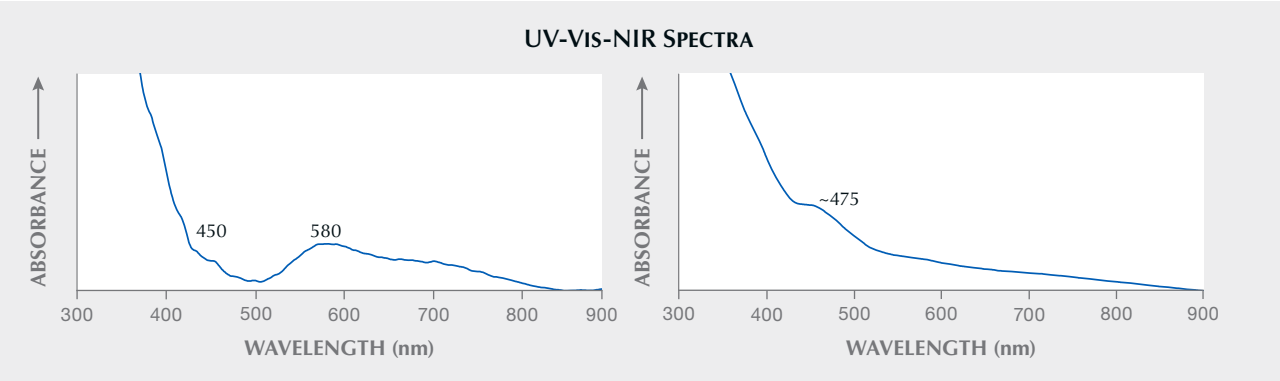

Figure 11. Left: The original state (before UV exposure) shows spectral features typical of metamorphic blue sapphire, including an Fe^{3+}-Fe^{3+} pair–related absorption peak at 450 nm and an Fe^{2+}/Ti^{4+} intervalence charge-transfer band near 580 nm. Right: After short-wave UV exposure, the spectrum is dominated by an absorption band centered near 475 nm, attributed to the activation of Fe^{3+}-related trapped-hole color centers. Different y-axis scales are used to better highlight the spectral changes following UV exposure.

near 580 nm. After short-wave UV exposure, the 580 nm absorption feature was no longer resolved, and the spectrum became dominated by an absorption band centered near 475 nm, consistent with the activation of Fe^{3+}-related trapped-hole color centers (figure 11) (E.V. Dubinsky et al., "A quantitative description of the causes of color in corundum," Spring 2020 *G&G*, pp. 2–28). After fading, the spectrum returned to its original state.

Importantly, this UV-activated and reversible color change is unrelated to the stone's high-temperature heat treatment. Previous studies have shown that heating does not stabilize color derived from unstable color centers (C.P. Smith et al., "Heated sapphires with unstable colour centres," *Journal of Gemmology*, Vol. 36, No. 7, 2019, pp. 602–604). The observations in this case, therefore, are consistent with established theoretical models and previously documented examples of unstable color-center behavior in Sri Lankan corundum.

Aprisara Semapongpan

Heat-Treated Red SPINEL

The Hong Kong laboratory recently received a 3.37 ct transparent purplish red oval mixed cut for identification (figure 12). Although the stone was submitted as a ruby, subsequent testing suggested a different identity. Standard gemological testing revealed a single refractive index (RI) of 1.717, consistent with spinel rather than doubly refractive ruby (1.760–1.768). Additionally, ruby and red spinel exhibit distinct absorption spectra. Ruby is characterized by a bright chromium fluorescent emission line at 693 nm, along with two fine dark lines in the blue portion of the spectrum at 468 nm and 476 nm. In the blue region where ruby shows distinct doublet lines, spinel typically shows a broad, featureless absorption band and lacks the sharp 476 nm line.

Microscopic examination revealed several features: altered crystal inclusions with discoidal fractures (figure 13), whitish healed fissures, and the presence of exogenous materials within surface-reaching fractures and cavities. Based on the combination of RI, specific gravity, absorption spectrum, and observed natural inclusion features, as well as laser ablation–inductively coupled plasma–mass spectrometry chemistry, the stone was identified as a natural spinel. Additionally, certain cavities displayed a granular texture with lower luster, indicative of filler material, suggesting artificial treatment (figure 14).

Heat treatment of spinel is considerably less common than that of ruby; however, heat-treated spinel does exist in the marketplace. For spinel specimens with exceptional clarity, microscopic examination alone is generally insufficient to detect evidence of heating. All spinel samples submitted to GIA are analyzed using photoluminescence (PL) spectroscopy as a primary method for evaluating potential heat treatment. The spectrum of the unheated reference spinel shows the peak with the highest counts positioned at 685.5 nm, with a full

Figure 12. This 3.37 ct purplish red oval mixed cut was submitted as a ruby. Photo by Tony Leung Yik Hang.

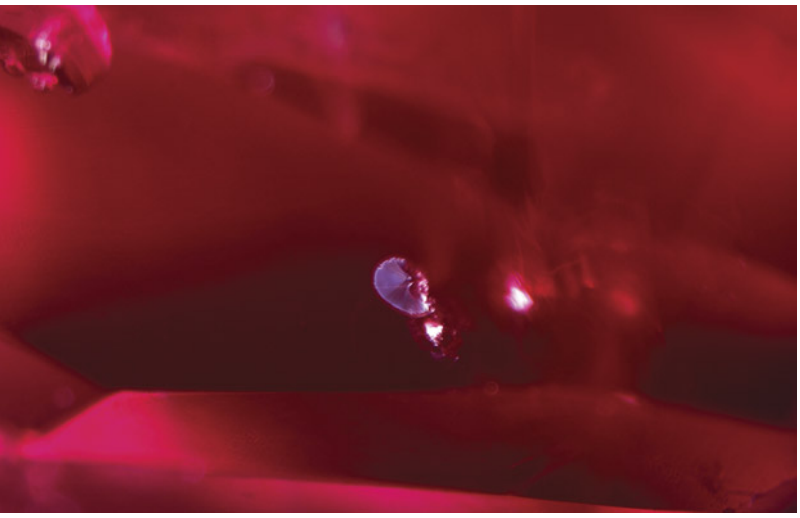

Figure 13. Heat-altered crystal inclusions surrounded by a discoid fracture, proving that the spinel underwent high-temperature treatment. Photomicrograph by Tsz Wing Lai; field of view 2.40 mm.

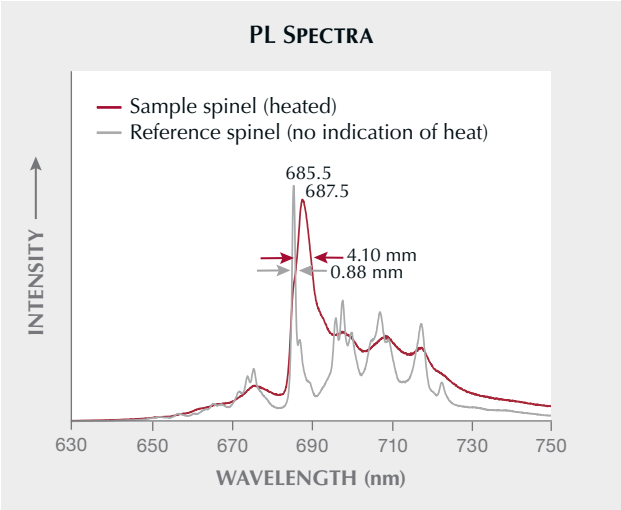

Figure 15. Comparison of the sample's PL spectrum to that of a natural unheated spinel proves that the sample is a heat-treated spinel.

width at half maximum (FWHM) of 0.88 nm (figure 15). In contrast, the sample spectrum exhibits a peak shifted to 687.5 nm, with a significantly broader FWHM of 4.10 nm. This peak broadening and wavelength shift are consistent with characteristics typically observed in heated spinel spectra (S. Saeseaw et al., "Distinguishing heated spinels from unheated natural spinels and from synthetic spinels," *GIA Research News*, April 2, 2009). Raman spectroscopic analysis further characterized the studied stone's filler as glass.

Historical evidence demonstrates that reliance on stone color alone can result in misclassification, underscoring the necessity of comprehensive analytical approaches for accurate gemstone identification. Red spinel has been the ultimate "imposter," famously misidentified as ruby for centuries. The most notable example is the Black Prince's Ruby set in the British Imperial State Crown.

The submitted spinel appears to have undergone unusually aggressive heating, possibly because it was misidentified as ruby prior to treatment. Such a scenario in the studied sample could explain the presence of glassy surface material and severely damaged inclusions, features atypical of heated spinel. While speculative, this possibility highlights the importance of accurate identification before treatment and the role of advanced spectroscopic methods in detecting such interventions.

Tsz Wing Lai and Amy Cooper

Figure 14. By manipulating different light sources, the filler material is uncovered. While standard lighting shows dull, low-luster patches in the filled cavities (left), fiber-optic illumination reveals a whitish granular texture (right). Photomicrographs by Tsz Wing Lai; fields of view 4.00 mm (left) and 1.50 mm (right).

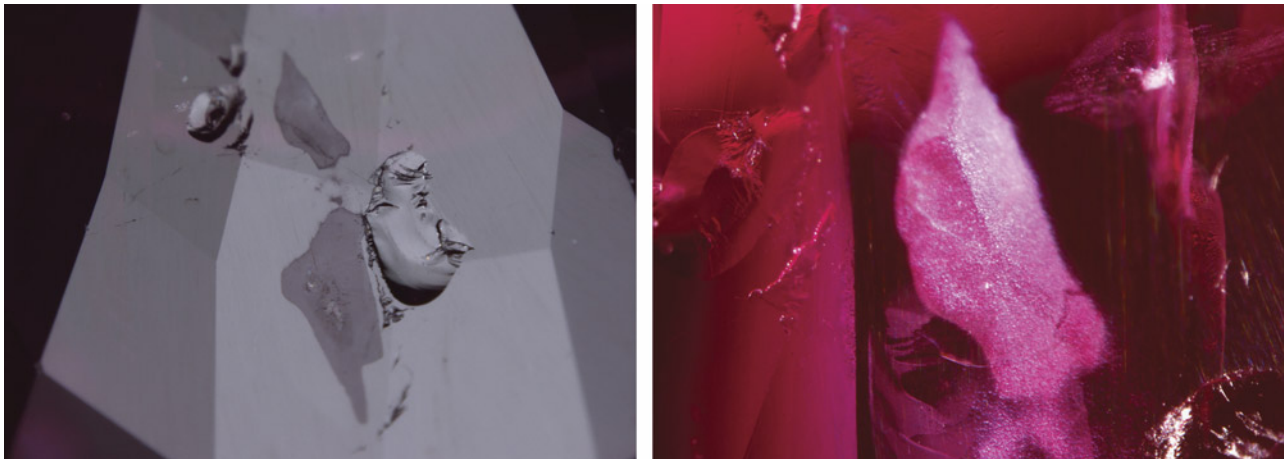

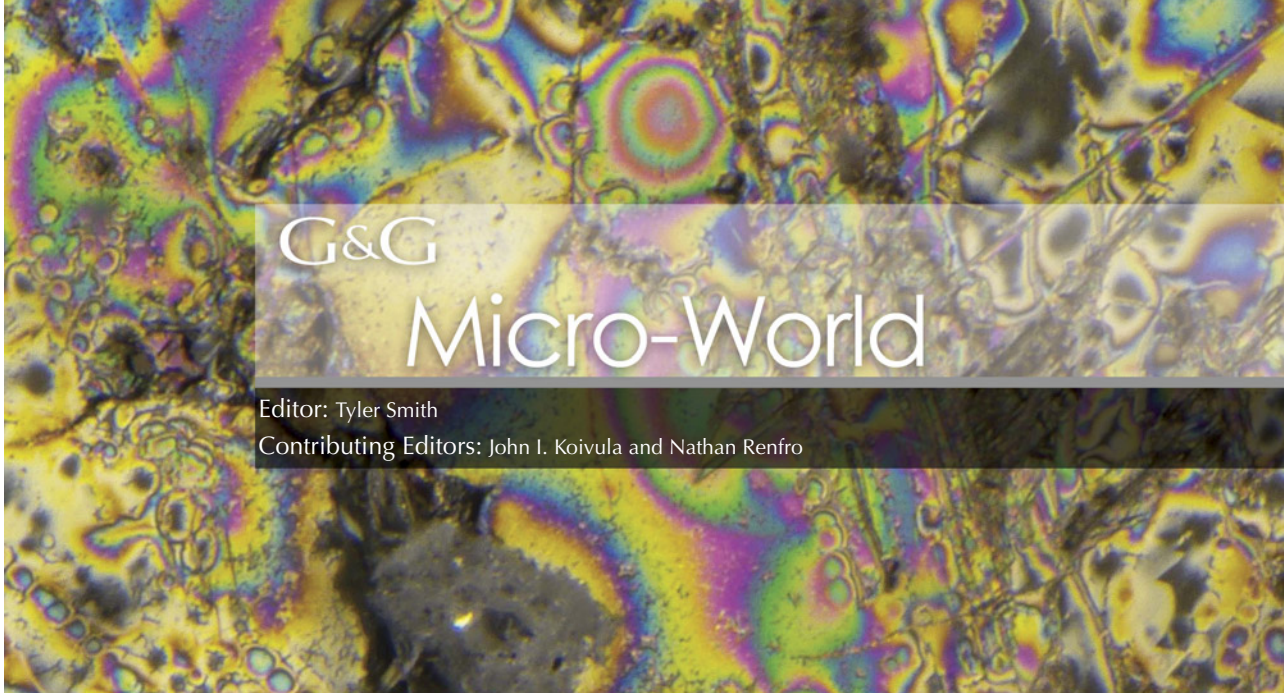

Figure 1. Left: Contact-twinned calcite host with scattered red realgar inclusions. Right: A closer view of one of the vivid inclusions. Photomicrographs by Wingtak Lui; fields of view 12 mm (left) and 3.2 mm (right).

Twinned Calcite with Realgar Inclusions

Microscopic examination of a transparent contact-twinned calcite crystal from the Jiepaiyu mine in Shimen County, Changde, Hunan, China, revealed vivid red to orange-red blebby to platy realgar (As_4S_4) inclusions scattered throughout the host, consistent with calcite's common e-twin law (figure 1). Raman microspectroscopy was targeted directly on the red inclusions using 785 nm excitation over shorter wavelengths. This approach was followed since the light-induced realgar-to-pararealgar conversion is reportedly most efficient under ~500–670 nm and is markedly decreased at longer wavelengths (>~670 nm) (D.L. Douglass et al., "The light-induced alteration of realgar to pararealgar," *American Mineralogist*, Vol. 77, No. 11-12, 1992, pp. 1266–1274). The resulting spectrum showed calcite bands together with diagnostic realgar bands. The occurrence of well-preserved realgar inclusions within transparent contact-twinned calcite is mineralogically noteworthy given realgar's tendency to alter under prolonged light exposure.

Wingtak Lui and Rui Rui Xing
Min De Minerals & Gem Research Co., Ltd.
Nanjing, China

Yu-Chen Huang
Taiwan Central Gem Laboratory Co., Ltd.

About the banner: An opaque plate of hematite displays iridescence in its rock crystal quartz host from the Rist mine in Alexander County, North Carolina. Photomicrograph by Nathan Renfro; field of view 5.99 mm.

Gems & Gemology, Vol. 62, No. 2, pp. 208–213.

© 2026 Gemological Institute of America

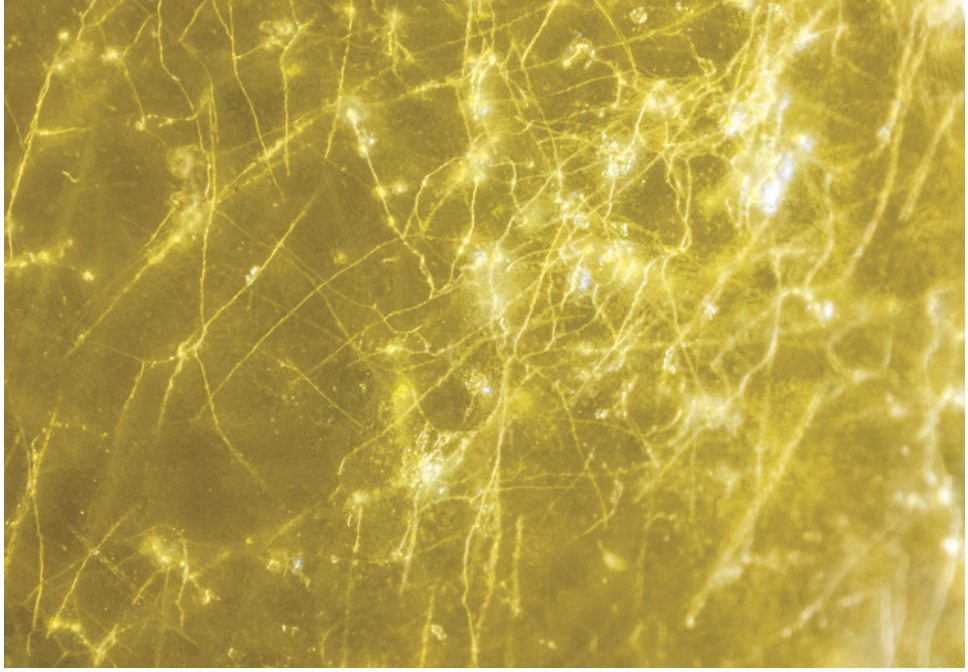

Figure 2. A fine, complex network of microscopic shell-boring parasitic tunnels with intersecting nodes resembling fungal hyphae in a mabe pearl. Photomicrograph by Gauri Sarvankar; field of view 1.65 mm.

"Fungal Hyphae" in a Mabe Pearl

Recently, the authors examined an intriguing white button-shaped assembled cultured shell blister, commonly referred to in the trade as a mabe pearl. This mabe pearl, which measured approximately 15.31 × 15.10 mm and was mounted in an earring, exhibited a semitranslucent surface with iridescence. When examined under higher magnification with fiber-optic illumination, an intricate network of fine branch-like structures was observed just beneath the nacreous surface. Closer examination revealed channels resembling a mass of fungal hyphae, the microscopic thread-like filaments found in fungi and molds (figure 2). These channels were likely formed by shell-boring parasites; parasitic worms often infest pearl-producing mollusks, resulting in the formation of elongated channels with varying patterns. Although parasitic boreholes have been previously documented in both shells and pearls (Spring 2024 *G&G* Micro-World, p. 78), this unique arrangement of intersecting tunnels displays a striking resemblance to the microscopic morphology of fungal hyphae, highlighting the complex biological interactions that can influence nacre formation.

Gauri Sarvankar and Abeer Al-Alawi
GIA, Mumbai

Leaf-Like Imprint on Non-Nacreous Pearl

Recently, a vein-like structure similar to that of a leaf was observed on the surface of a baroque-shaped non-nacreous natural pearl. The white and yellowish brown pearl weighed 12.54 ct and measured 13.40 × 13.12 × 12.22 mm (figure 3, left). Visually, it displayed a striking contrast between its white frosty surface and its underlying yellowish brown bodycolor. Higher magnification unveiled

Figure 3. A 12.54 ct natural non-nacreous pearl (left) with formations displaying a leaf-like imprint on its surface (right). Photos by Gourav Bera (left) and Jayesh Surve; field of view 1.30 mm (right).

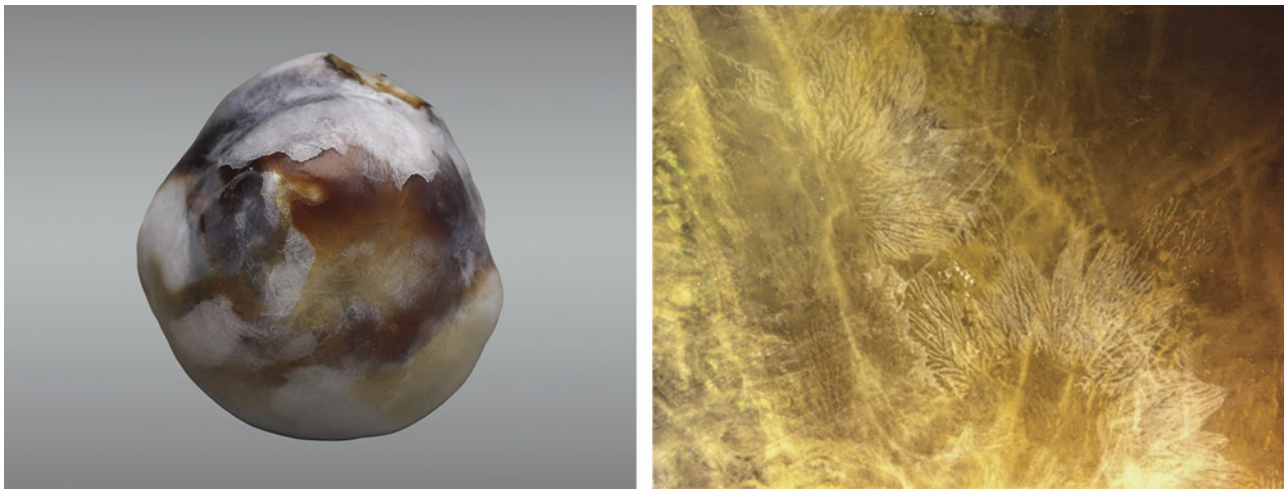

captivating formations resembling leaves with intricate vein structures (figure 3, right). While non-nacreous pearls exhibit various surface patterns, the distinctive leaf-like pattern observed on this specimen identifies it as a particularly intriguing non-nacreous natural pearl.

Jayesh Surve and Abeer Al-Alawi
GIA, Mumbai

Reticulated Pattern on Pearls' Surfaces

Pearls formed in an organic environment often show unique external and internal features. In a recently examined multistrand necklace composed of small natural pearls ranging from 3.45 × 2.49 mm to 6.51 × 6.30 mm, some pearls displayed an interesting surface pattern. Unlike typical hammering effects, which produce a series of flat facets or shallow indentations (Summer 2025 Gem News International, pp. 210–212), these pearls featured a reticulated pattern with deeper indentations and distinct ridges (figure 4). This unique surface texture is a result of natural pearl growth; no post-harvest treatment or alterations were detected.

Emiko Yazawa
GIA, New York

Two-Phase Inclusion in Peridot

Pakistani peridot is known for its diagnostic ludwigite inclusions, but something far rarer was recently observed in a 7.44 ct faceted stone—a fluid-filled cylindrical void among a myriad of needle-like ludwigite crystals (figure 5). The void also contained a spherical gas bubble that shifted within the liquid as the stone was moved. This feature is known as a two-phase inclusion due to the negative space containing a liquid and a gas. Cylindrical-shaped inclusions are uncommon in any stone, as cylinders do not conform to any crystallographic habit; however, a similar example has been documented in a pink euclase crystal (Fall 2021 *G&G* Micro-World, pp. 274–275).

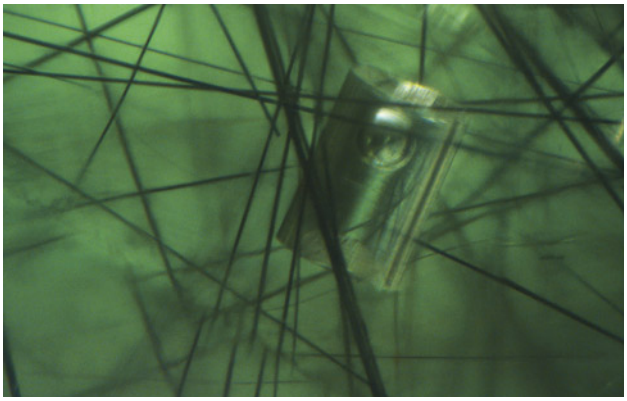

Figure 5. A cylindrical-shaped void encapsulates liquid and a gas bubble within a myriad of needle-like ludwigite inclusions in a Pakistani peridot. Photomicrograph by Britni LeCroy; field of view 1.42 mm.

Britni LeCroy
GIA, Carlsbad

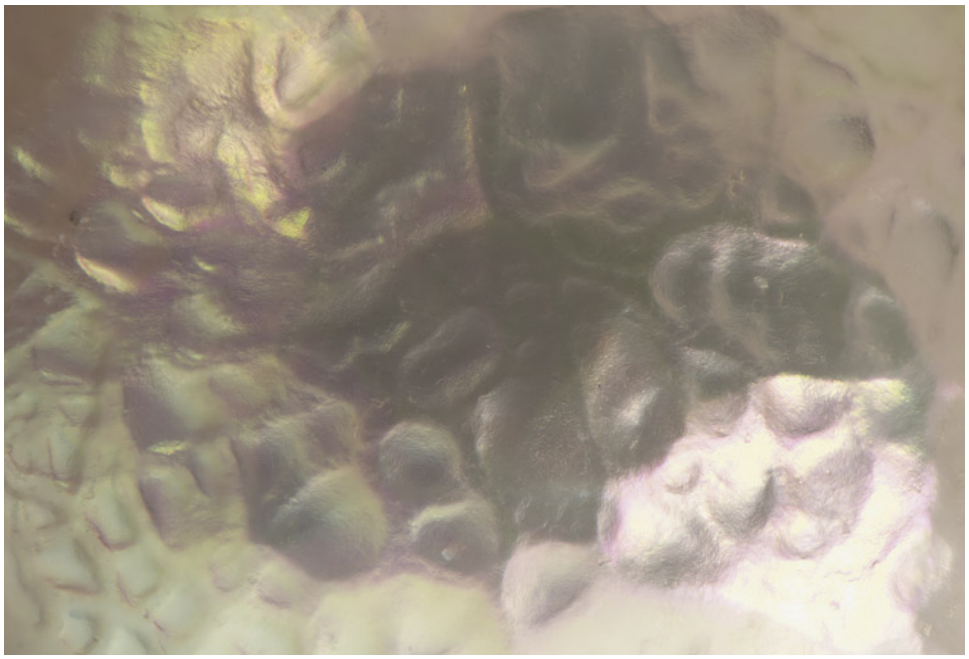

Figure 4. A small natural pearl displays a reticulated pattern with indentations and distinct ridges, differing from the hammered texture commonly observed in pearls. Photomicrograph by Emiko Yazawa; field of view 3.57 mm.

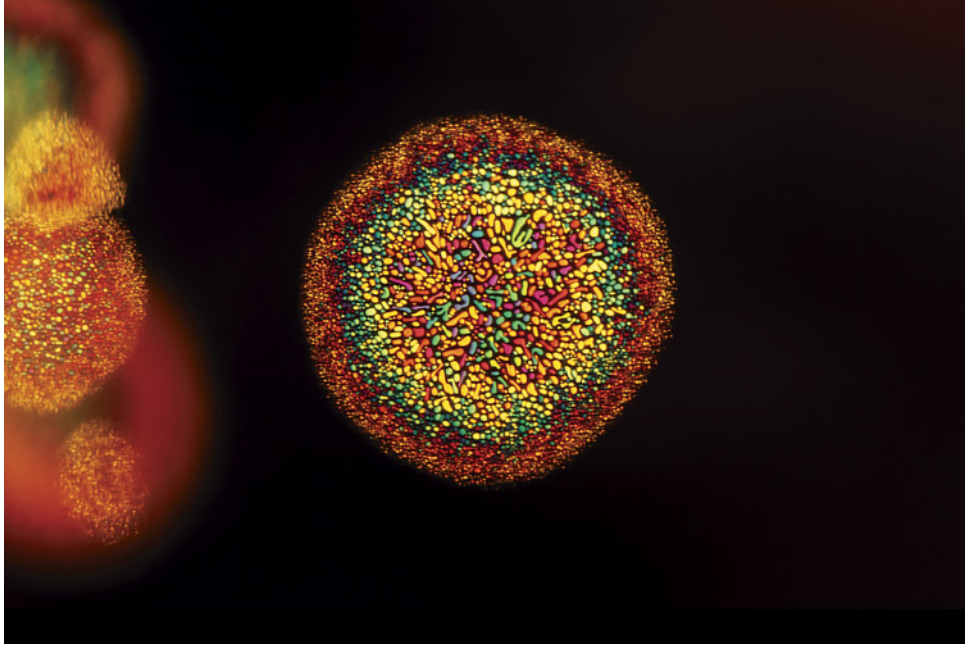

Figure 6. Thin-film decrepitation inclusions create a colorful mosaic pattern in a beryllium-diffused orange sapphire under diffused fiber-optic lighting. Photomicrograph by E. Billie Hughes; field of view 1.6 mm.

Colorful Mosaic Pattern in Heated Orange Sapphire

When viewing this inclusion scene (figure 6), one might wonder whether it represents a gemstone inclusion at all. This image has invoked comparisons to fireworks illuminating a night sky, a mosaic-like stained glass window, and the plates used in the Ishihara test for color blindness. In reality, the scene is composed of tiny thin-film decrepitation inclusions inside a beryllium-diffused orange sapphire. While this inclusion scene is not itself diagnostic of diffusion, it is likely the result of high-temperature heat treatment.

E. Billie Hughes
Lotus Gemology, Bangkok

"Shooting Stars" in Sapphire

The author recently examined a 3.46 ct bluish violet to purple color-change sapphire measuring 9.04 × 7.61 × 5.47 mm. Microscopic examination revealed a scene reminiscent of shooting stars in a night sky, created by numerous Rose channels against a backdrop of scattered zircon crystals (figure 7). Commonly occurring in various gems including calcite, diamond, and sapphire, Rose channels are created by intersecting twin lamellae, formed by twinning along the rhombohedral faces (F. Notari et al., "'Boehmite needles' in corundum are Rose channels," Fall 2018 *G&G*, p. 257).

Michaela Damba
GIA, Carlsbad

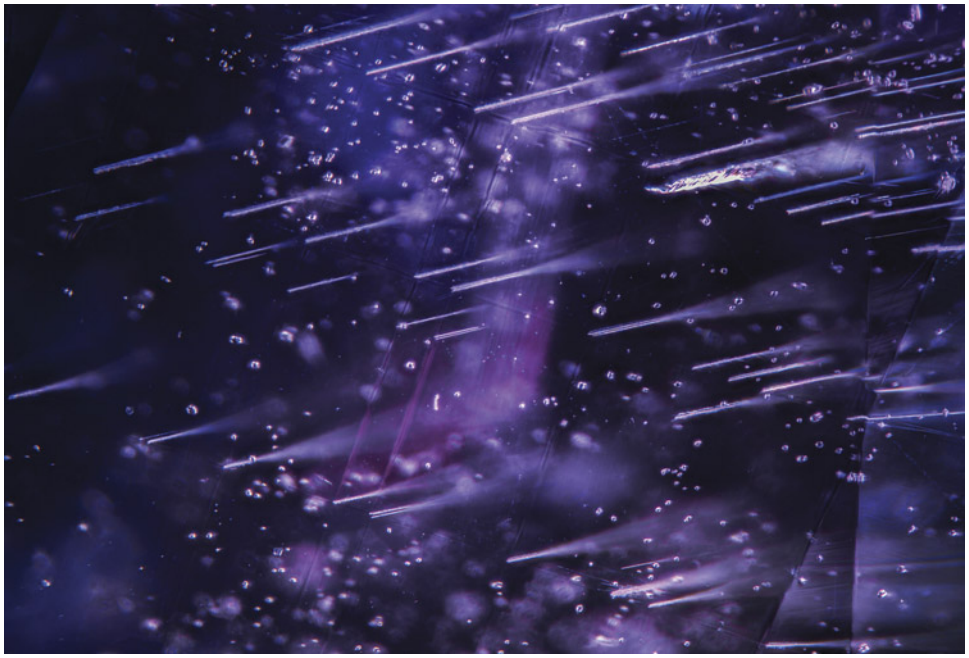

Figure 7. Numerous Rose channels with scattered zircon crystal inclusions in a 3.46 ct color-change sapphire. Photomicrograph by Michaela Damba; field of view 4.79 mm.

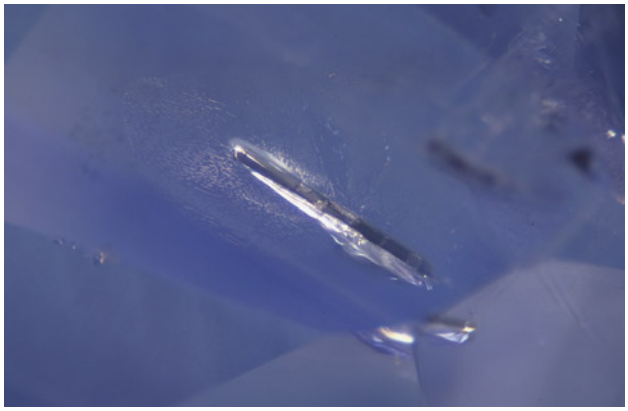

Figure 8. Elongated, rod-shaped vesuvianite crystal in sapphire associated with a partially healed fissure. Photomicrograph by Keith Chow; field of view 3.10 mm.

Vesuvianite in Sapphire

The author recently examined a sapphire containing an elongated, rod-shaped crystal associated with a partially healed fissure (figure 8). Due to its morphology and color, the inclusion appeared to be pargasite. However, subsequent analysis using Raman spectroscopy identified the inclusion as vesuvianite.

Vesuvianite is an accessory sorosilicate mineral that typically forms in skarn during metasomatism of carbonate rocks such as limestone. Exceptionally rare as an inclusion in gemstones, vesuvianite has previously only been documented in two rubies from Mogok, Myanmar (Winter 2017 *G&G* Micro-World, p. 469; C.P. Smith and R. Zellagui, "Vesuvianite (idocrase) and apatite inclusions in ruby identifiable by infrared spectroscopy," *Journal of Gemmology*, Vol. 37, No. 4, 2020, pp. 346–348). Given the association of vesuvianite with skarns, these inclusions may also occur in sapphires from skarn deposits, such as those in Andranondambo, Madagascar, and Kataragama and Elahera, Sri Lanka (G. Giuliani and L.A. Groat, "Geology of corundum and emerald gem deposits: A review," Winter 2019 *G&G*, pp. 464–489).

To the author's knowledge, this is the first report of vesuvianite as an inclusion in sapphire.

Sharon Tao
Gübelin Gem Lab, Lucerne, Switzerland

Distinctive Fluorescent Crystal Inclusions in Spinel

The authors examined a 7.01 ct spinel reportedly from Tanzania. Under short-wave (254 nm) ultraviolet light, a small fluorescent spot was observed on the stone's surface, caused by cut-through crystal inclusions. Micro-Raman analysis identified the inclusions as diopside, phlogopite, and edenite, forming a cluster of transparent crystals associated with a dark, opaque pyrite grain (figure 9A). In reflected light, the inclusions showed luster distinct from the spinel host, with the pyrite exhibiting a golden metallic luster (figure 9B). Under short-wave ultraviolet light, the crystals fluoresced in different colors: white for diopside, yellow for phlogopite, and blue for edenite (figure 9C). Fluorescence from inclusions is often overlooked but can provide important identification clues.

Natcha Rattana-anan and E. Billie Hughes
Lotus Gemology, Bangkok

Quarterly Crystal: Chromite in Diamond

Recognizable mineral inclusions in diamond are rather unusual. The most common inclusion in gem-quality diamond is often referred to as a "carbon spot," which is a collective term used to describe any dark inclusion in diamond. The most prominent dark mineral inclusions in diamond, carbon spots are typically chromite, graphite, or sulfides. Of the three, only graphite is composed of carbon. Sulfides are fairly common as inclusions, and chromite crystals are the only type of carbon spot that is actually rare.

This quarter's subject is a transparent, colorless, and partially etched diamond octahedron, which came from

Figure 9. A cluster of diopside, phlogopite, and edenite inclusions in spinel, associated with a dark, opaque pyrite crystal, shown in diffused fiber-optic light (A), reflected light (B), and short-wave ultraviolet light (C). Photomicrographs by Natcha Rattana-anan; field of view 3.6 mm.

Figure 10. Weighing 1.17 ct and measuring 6.61 mm in the largest dimension, this partially etched colorless diamond octahedron hosts numerous opaque black chromite crystals. Photo by Rhonda Wilson.

Sierra Leone, by way of David New in Tucson, Arizona. The diamond crystal, weighing 1.17 ct and measuring 6.61 × 5.94 × 3.09 mm, hosts numerous opaque black solids situated along octahedral planes (figure 10). Laser Raman microspectrometry identified one of the included crystals as chromite. As an inclusion in diamond, chromite is generally opaque and black with a submetallic to vitreous luster and typically forms as angular mineral grains (figure 11, top). In polarized light, the chromite inclusions are observed to cause strain in the diamond host (figure 11, bottom).

John I. Koivula and Nathan Renfro
GIA, Carlsbad

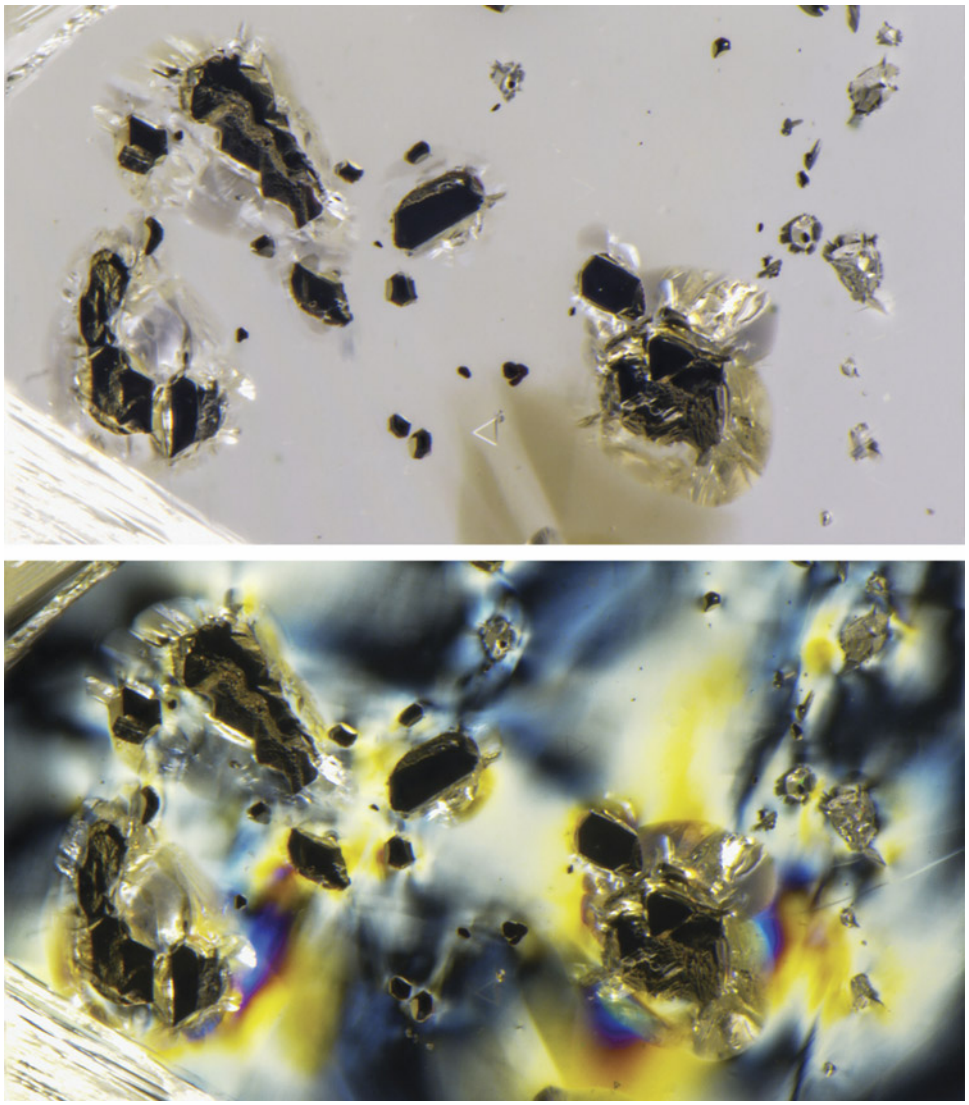

Figure 11. Top: Sometimes referred to as "carbon spots," opaque black crystals of chromite are uncommon inclusions in diamonds. Bottom: Polarized light reveals the strain surrounding the scattered chromite crystals. Photomicrographs by Nathan Renfro; field of view 3.73 mm.

GEM NEWS INTERNATIONAL

Contributing Editors

Gagan Choudhary, *IIGJ-Research & Laboratories Centre, Jaipur, India* (gagan.choudhary@iigjrlc.org)

Guanghai Shi, *School of Gemmology, China University of Geosciences, Beijing* (shigh@cugb.edu.cn)

Figure 1. Left: The polished pegmatite plate measures 3.28 m × 1.80 m × 2.5 cm and originates from the Governador Valadares area, Minas Gerais, Brazil. At the top of the plate, an unidentified bluish green translucent mineral is present (indicated by the arrow). Right: An enlargement of the 7.1 × 2.9 cm bluish green mineral, which formed in a vacuole between two crystals of perthitic microcline. Photo by Pierre Barbey.

COLORED STONES AND ORGANIC MATERIALS

Determination of aquamarine in a Brazilian pegmatite plate. A remarkable Brazilian pegmatite plate hangs on the ground-floor wall of the Centre for Petrographic and Geochemical Research (CRPG) in Vandœuvre, France. This rock, called "Patagonia granite" by the trade in reference to the granitic mountain peaks in southern Argentina, came from the Galiléia region, near Governador Valadares, in the state of Minas Gerais, Brazil. Famous for its gem-bearing pegmatites, the region, located north of Rio de Janeiro, is marked by the presence of granitoids belonging to the Neoproterozoic Galiléia magmatic suite formed by tonalites, granodiorites, granites, and pegmatites. Dating of these rocks by the uranium-lead method on zircon has given ages between 594 and 570 million years, characteristic of the Brasiliano or Pan-African orogeny.

The polished pegmatite plate, measuring 3.28 m × 1.80 m × 2.5 cm, exhibits three distinct mineral assemblages from the border to the core (figure 1, left): (1) the edges composed of quartz, feldspar, and large brownish laths of mica (black in the photo) ending at the top with a close association of wedge-shaped quartz and potassium-feldspar (graphic texture); (2) large and zoned euhedral perthitic microcline feldspar crystals hosting disseminated centimetric schorlite and an unidentified 7.1 × 2.9 cm bluish green translucent mineral (figure 1, right); and (3) the whole core filled by translucent and healed grayish quartz.

Editors' note: Interested contributors should send information and illustrations to gandgeditorial@gia.edu.

Gems & Gemology, Vol. 62, No. 2, pp. 214–220.

© 2026 Gemological Institute of America

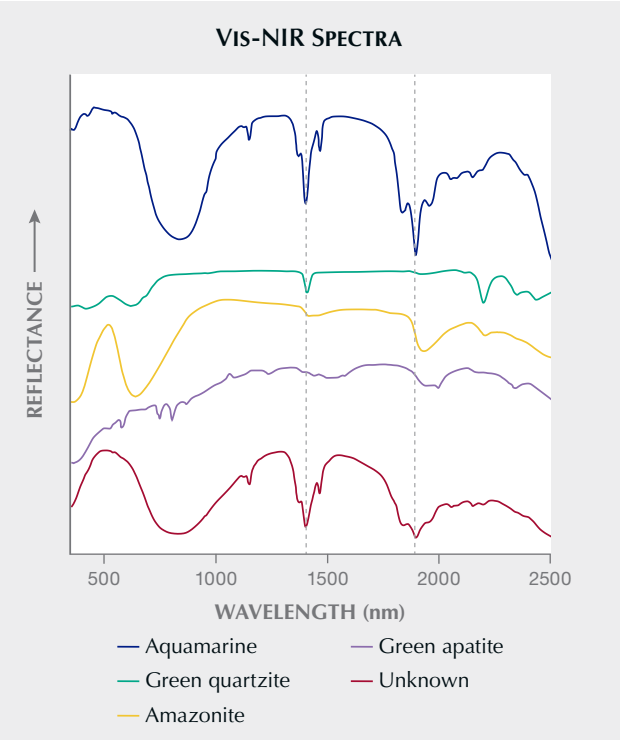

Figure 2. Comparison of Vis-NIR reflectance spectra for four samples from the CRPG standards database to the spectrum of the unknown mineral, matching the aquamarine reference. Thus, the unknown mineral belongs to the beryl family. Spectra are offset vertically for clarity.

The unidentified bluish green mineral was analyzed using visible/near-infrared (Vis-NIR) reflectance spectroscopy with an analytical point-spectrometer. The technique allows for the acquisition of a reflectance spectrum of a 1 cm diameter surface area. Spectra collected in the 500–2500 nm range are sometimes used to analyze the mineralogical composition of rocks based on the position and shape of the absorption band.

The spectrum of the bluish green mineral was compared with that obtained from sample standards in the CRPG database (amazonite, green apatite, aquamarine, and green quartzite; figure 2). The positions of the two absorption bands at 1400 nm and 1900 nm are linked to the vibration of water molecules in the structure, while the wide absorption band centered at 800 nm is due to an electronic transition of iron. Therefore, the unknown mineral was positively identified as a member of the beryl family.

Chemical analysis on the bluish green beryl by a handheld X-ray fluorescence (XRF) spectrometer showed the following analytical ranges for trace elements, in ppmw: iron = 3000 (±100), titanium = 447–474 (±27), zinc = 305–350 (±13), and cesium = 157–180 (±6). Chromium and vanadium were not detected, ruling out emerald and identifying the mineral as aquamarine, with its color attributed to the combination of iron and titanium. The presence of cesium confirmed the magmatic source of the aquamarine.

The determination of aquamarine on the large plate of Brazilian pegmatite combining handheld Vis-NIR reflectance and XRF spectrometers underscores the importance of the use of nondestructive methods on polished petrological sections in galleries of mineralogical museums. These qualitative point chemical analyses offer insight into the knowledge of mineral associations across diverse geological environments and enhance understanding of the genesis of gems.

Gaston Giuliani, Marie Barthez,
Jean-Marc Montel, and Pierre Barbey
Université de Lorraine, CRPG/CNRS-UL,
Vandœuvre, France

Rare colors of Chinese freshwater cultured pearls. The Gemmological Institute at the China University of Geosciences recently received 53 freshwater cultured pearls displaying rare colors (figure 3): 21 purple, 7 green, 7 blue, and 18 orange pearls with rich hues. While white, orange, pink, and purple freshwater cultured pearls are common in the market, green, blue, and yellow colors are scarce. These pearls were nearly round, ranging from 7 to 14 mm in diameter, with most exhibiting good luster and smooth surfaces. The pearls were sourced from Menghao Jewelry, a supplier working directly with local pearl farmers in Zhejiang Province. With the increasing advancement of nucleated freshwater pearl cultivation technology in China, dozens of farms are capable of producing such rare-colored pearls, which typically range from 4 to 15 mm in diameter and require one to two years

Figure 3. These 10 representative pearls from the 53 studied, selected for Raman analysis, range in color from deep purple to orange-red. Photos by Chuting Zhang.

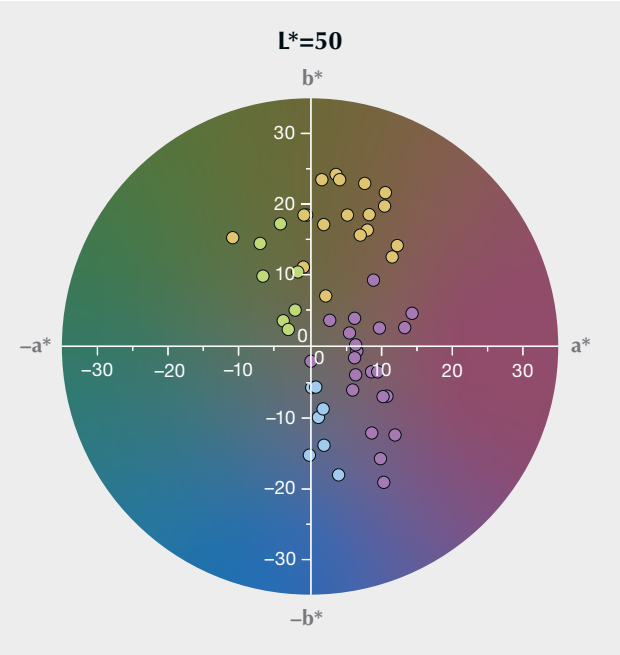

Figure 4. The color parameters of all samples are presented as point plots on the two-dimensional cross section at L = 50. The colorimetric data are defined in the CIE L*a*b* color space as follows: L* (lightness) represents the brightness of color, ranging from 0 (absolute black) to 100 (absolute white); a* represents the position on the red-green axis (positive values indicate red tones, while negative values indicate green tones); and b* represents the position on the yellow-blue axis (positive values indicate yellow tones, while negative values indicate blue tones).*

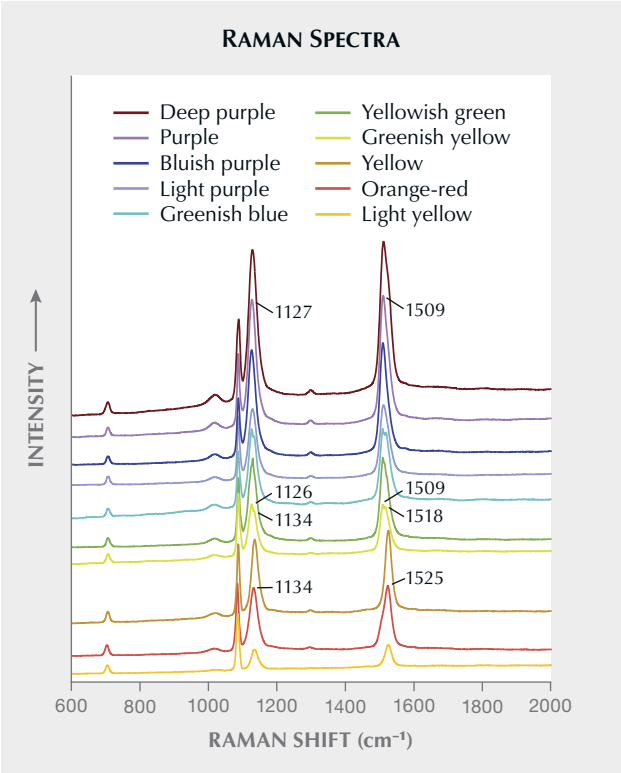

Figure 5. Raman spectra of the 10 representative pearls studied. Spectra are offset vertically for clarity.

to grow. The main mollusk species used for their cultivation are *Hyriopsis cumingii* and *Hyriopsis schlegelii*.

Microscopic observation of the studied pearls revealed clear surface contour textures with no artificial staining. The ultraviolet/visible spectroscopy analysis exhibited a stable characteristic absorption peak at 280 nm, typical of natural pearls, with no abnormal absorption signals, thus confirming the natural coloration of the samples. L*a*b* color parameters were collected for all samples, captured under a standard D65 light source and measured from the edges of pearl images. The L*a*b* parameters were widely distributed in CIE L*a*b* color space. The L* values of the purple-hued pearls were relatively lower than those of the orange-yellow-hued pearls. To provide an intuitive understanding of the color distribution, the data points were projected onto a two-dimensional cross section at L* = 50 (figure 4). The a* values of the 53 studied pearls ranged from a more greenish hue (a* = –11) to a more reddish hue (a* = 15). The b* values ranged from –20 to 25, covering both yellow and blue tones.

Of the 53 pearls, 10 representative samples were selected for Raman analysis (again, see figure 3). Two sets of Raman peaks related to natural polyenic pigments were detected in the pearls, including 1127/1509 cm^{-1} and 1134/1525 cm^{-1} (figure 5). The former is associated with purple pigment, while the latter is linked to orange pigment. Interestingly, the pearls with 1509 cm^{-1} Raman peaks not only exhibited the common hue of purple, but also rare hues of green and blue. The pearls with 1525 cm^{-1} Raman peaks were not limited to the yellow color, but presented a gradient series ranging from light yellow to orange-red. Additionally, two unusual Raman peaks were detected. The greenish yellow and greenish blue pearls exhibited double peaks at 1509 and 1518 cm^{-1}, indicating the presence of mixed pigments within the pearls (S. Karampelas et al., "Role of polyenes in the coloration of cultured freshwater pearls," *European Journal of Mineralogy*, Vol. 21, No. 1, 2009, pp. 85–97).

According to scientific studies, the rare colors of these types of pearls are primarily determined by the donor oyster's nacre color (S. Karampelas and A. Lombard, "Gemological characteristics of saltwater cultured pearls produced after xenotransplantation," Spring 2013 *G&G*, pp. 36–41; Z. Wang et al., "How cultured pearls acquire their colour," *Aquaculture Research*, Vol. 51, No. 10,

2020, pp. 3925–3934). For example, *Hyriopsis cumingii* "Shenzi No. 1," cultivated in China, can grow purple pearls, while another golden strain of *Hyriopsis cumingii* can grow yellow pearls.

However, some artificial treatments, such as dyeing, irradiation, bleaching, or coating, may be used to change the natural color to rare yellow, green, or blue colors, thus misleading less experienced buyers. Therefore, careful analysis is required to accurately distinguish between natural and artificial colors.

Chuting Zhang, Jing Yu, and Kexin Zhang
Gemmological Institute, China University of Geosciences, Wuhan

Figure 6. Six-rayed star quartz specimens: 5.77 ct, 13 × 9.5 × 6.5 mm (left) and 13.23 ct, 15.5 × 13 × 9 mm (right). Photo by Haoran Zhu.

Six-rayed star quartz containing exsolved rutile needles. Asterism, the optical phenomenon producing a star-like pattern on the surface of a cabochon, arises from the reflection and scattering of light due to the presence of oriented groups of parallel needle-like inclusions. In quartz, two distinct forms of asterism have been reported: the star effect in rose quartz, typically caused by multiple sets of oriented fibrous inclusions (K. Schmetzer and M. Krzemnicki, "The orientation and symmetry of light spots and asterism in rose quartz spheres from Madagascar," *Journal of Gemmology*, Vol. 30, No. 4, 2006, pp. 183–191), and three-rayed asterism induced by intersecting rutile needles (Summer 2022 GNI, pp. 249–252).

Recently, author JL acquired two quartz specimens from the Donghai Crystal Market in Jiangsu Province, China, each displaying a well-defined six-rayed star under point-source illumination (figure 6). Standard gemological analysis yielded a refractive index of 1.54 and a specific gravity of 2.68, with Raman spectroscopy confirming the specimens as quartz. Microscopic observation revealed reflective layers composed of three mutually interlaced sets of parallel acicular inclusions oriented at approximately 120° to one another (figure 7). These inclusions caused the observed asterism and consisted of two morphologically distinct types: fine silvery white needles and thicker yellowish brown needles.

Both the silvery white and yellowish brown needles exhibited Raman peaks at 142, 238, 446, and 614 cm^{-1},

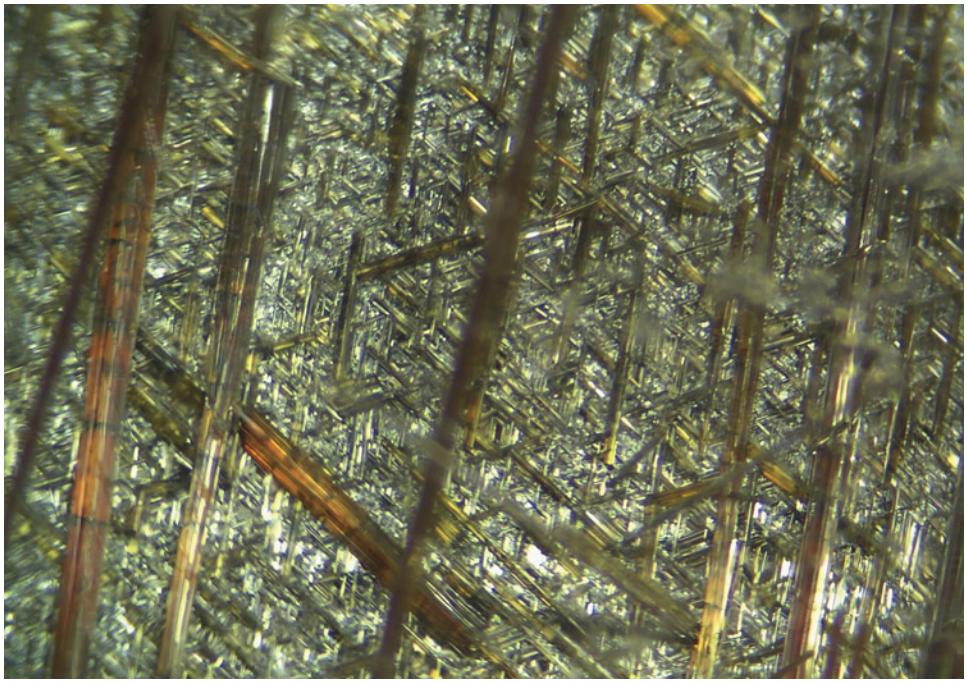

Figure 7. Three sets of interwoven needle-like hematite and rutile inclusions within a six-rayed star quartz. Photomicrograph by Haoran Zhu; field of view 5.00 mm.

characteristic of rutile, whereas certain inclusions displayed additional peaks at 225, 244, 290, 410, 493, 614, and 663 cm^{-1}, consistent with hematite. These findings suggested that some rutile needles contained hematite precipitates. This coexistence likely originated from titanium- and iron-rich hydrothermal fluids; under highly oxidizing conditions, titanium crystallized preferentially as rutile, followed by iron oxidation and subsequent hematite precipitation, resulting in a tightly intergrown microstructure responsible for the distinct six-rayed star effect.

Although rutile-induced asterism is common in quartz and the three-rayed star effect associated with asteriated rutile networks has been previously reported, the phenomenon observed in this specimen—arising from the synergistic presence of hematite and rutile needles—is both attractive and unique. To the best of the authors' knowledge, it has not been documented previously.

Jie Luo, Xiaoxu Yan, Xia Deng, and Zida Tong
Guangzhou City University of Technology, China

Suwei Yue
Guangzhou Polytechnic University, China

TABLE 1. XRF analysis (in wt.%) of the sample substrate and spot regions. Average values are shown in parentheses.

Oxide	Substrate	Raindrops	Ideal turquoise	Detection limit (wt. %)
Al_2O_3	35.21–35.82 (35.62)	35.32–35.91 (35.57)	45.70	0.2
SiO_2	1.85–2.11 (1.99)	1.08–1.65 (1.37)	—	0.3
P_2O_5	44.11–44.56 (44.30)	43.99–44.49 (44.28)	42.41	0.1
FeO_T	5.75–6.14 (5.85)	5.98–6.65 (6.44)	—	0.004
CuO	10.46–10.70 (10.60)	10.66–10.87 (10.78)	11.89	0.004
ZnO	0.09–0.10 (0.10)	0.08–0.10 (0.09)	—	0.01
K_2O	0.30–0.41 (0.36)	0.28–0.41 (0.34)	—	0.006
CaO	0.05–0.06 (0.05)	0.05–0.06 (0.05)	—	0.005
Total	—	—	100	—

An unusual yellow raindrop turquoise. Recently, author YYL encountered a unique specimen of turquoise characterized by yellow raindrop-like patterns in the Zhushan County turquoise market in Hubei Province, China. The sample exhibited a blue-green substrate, with bright yellow spots distributed individually and in clusters across its surface. Both the substrate and the spots were opaque, with the individual spots nearly round and measuring between 2 mm and 1 cm in size (figure 8).

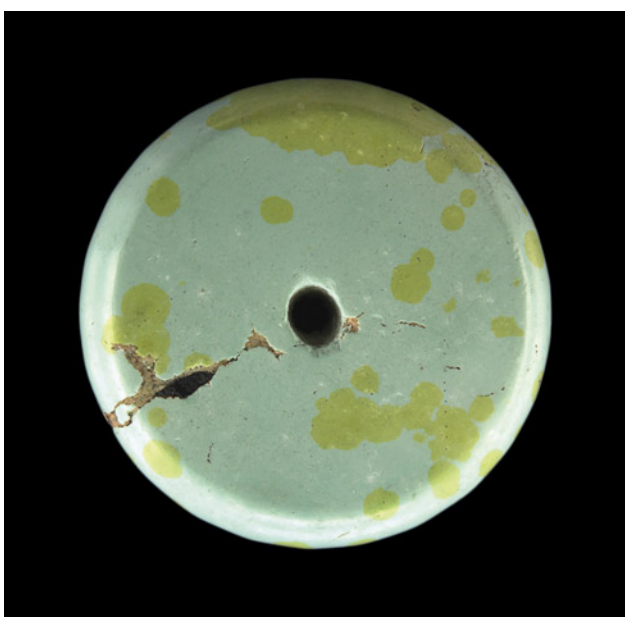

Figure 8. An unusual raindrop turquoise measuring 23 × 23 × 5 mm. Photo by Yunyu Liu.

Fourier-transform infrared (FTIR) analysis of both the substrate and the raindrop-like spots revealed turquoise vibrational peaks. Two absorption peaks attributed to a stretching vibration were noted at 2858 and 2979 cm^{-1}, indicative of wax (Fall 2015 GNI, pp. 343–345). The stronger absorptions for these two features in the substrate suggested a higher wax content, likely from residual wax after polishing due to the sample's lower hardness.

To determine the compositions of the substrate and the spots, four points in each of these regions were tested with X-ray fluorescence (XRF) spectroscopy using a quantitative method developed by the School of Jewellery laboratory, China University of Geosciences, Wuhan, with the total content of major oxides ranging from 98 to 100 wt.%. The results indicated that the primary chemical compositions of the yellow spots and the substrate were largely consistent (table 1). Specifically, the average Al_2O_3 content was 35.57 wt.% for the yellow spots and 35.62 wt.% for the substrate. Similarly for the yellow spots and substrate, the CuO content was 10.78 wt.% and 10.60 wt.%, respectively, while the total iron oxide (FeO_T) content was 6.44 wt.% and 5.85 wt.%, respectively.

Trace element analysis was performed using laser ablation–inductively coupled plasma–mass spectrometry on three spots each in the substrate and raindrop areas across both sides of the sample, with the results demonstrating broadly consistent element enrichment patterns between the substrate and raindrops. No significant con-

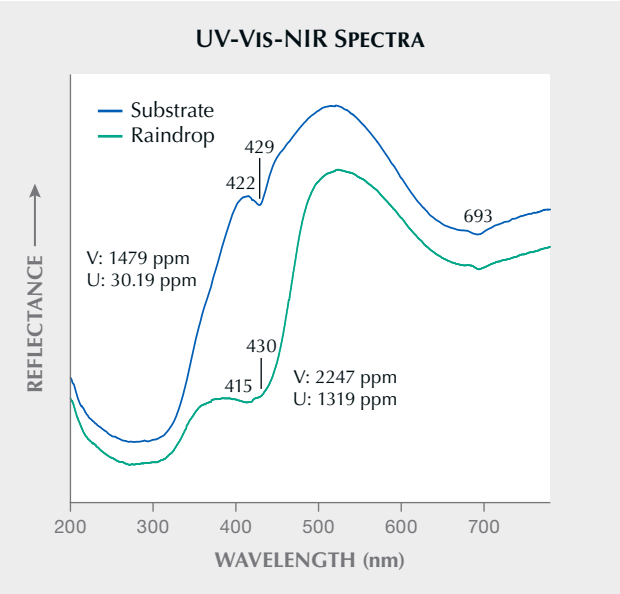

Figure 9. In the UV-Vis-NIR spectrum, both the substrate and the spots exhibit absorption in the blue-violet and red regions, with stronger absorption observed in the spots.

centration differences between the yellow raindrop regions and the blue-green substrate were observed for the trace elements analyzed, with the exception of vanadium and uranium, which were both significantly higher in concentration in the yellow regions.

The ultraviolet/visible/near-infrared (UV-Vis-NIR) reflectance spectra of the substrate exhibited characteristics typical of turquoise (figure 9). In contrast, the yellow spots displayed a strong absorption band at 415 nm, accompanied by a shoulder band at 430 nm. The violet-blue region showed significant absorption, while the red region exhibited a broader absorption band, albeit with lower intensity compared to the blue-violet region. From a compositional perspective, the primary distinction between the substrate and the yellow spots lies in their uranium and vanadium contents. Uranium exhibits a strong absorption band at 415 nm in the violet region, forming a broad absorption feature. The low-energy end of this absorption extends to approximately 460 nm, which is attributed to the magnetic dipole transition of the uranyl ion (A.N. Platonov and C. Jin, "Color of uranyl-containing minerals," *World Nuclear Geoscience Journal*, Vol. 1, 1975, pp. 38–42). An increase in vanadium content causes the absorption related to iron ions (Fe^{3+}) at 422 nm to shift toward the red region, resulting in an absorption feature at 430 nm (X. Wang and Y. Guo, "The impact of trace metal cations and absorbed water on colour transition of turquoise," *Royal Society Open Science*, Vol. 8, No. 2, 2021, article no. 201110). In summary, absorption in the violet region is primarily caused by uranium, vanadium, and iron, while copper contributes to absorption in the red region. These elemental contributions collectively account for the intense yellow coloration observed in the spots.

Although this raindrop turquoise exhibits distinct color variations, there were no significant differences observed in the FTIR spectral characteristics or bulk chemical composition between the substrate and the yellow spots. However, when looking at trace element chemistry, significantly higher levels of vanadium and uranium were identified in the spots compared to the substrate. A slightly higher concentration of iron was also observed in the yellow spots.

Yunyu Liu and Quanli Chen
Gemmological Institute, China University of Geosciences, Wuhan

IN MEMORIAM

Harold Van Pelt, 1925–2026. Pioneer of gem photography Harold Van Pelt—"Van" to his friends and colleagues—passed away at the age of 100 (figure 10). Over three decades, he and his wife, Erica, contributed hundreds of photographs—including 93 covers—to *Gems & Gemology*.

Born in Paola, Kansas, Van graduated from the Brooks Institute of Photography in Santa Barbara, California, in 1953. After he and Erica married in the early 1960s, they made a good living photographing commercial furniture. Since this work was seasonal, they used their downtime to visit Europe, Africa, and Asia. Shooting thousands of photographs in museums during their travels, they became attracted to minerals and ultimately gems. By the late 1960s and early '70s, they began attending the Tucson gem and mineral shows, soon photographing major gem crystals and, inevitably, fashioned gems.

In 1981, when *G&G* transitioned to a larger, full-color format with an expanded editorial review board, the Van Pelts played a pivotal role in the journal's growing accept-

Figure 10. Harold Van Pelt with his wife, Erica, in his studio. Photo by Harold & Erica Van Pelt.

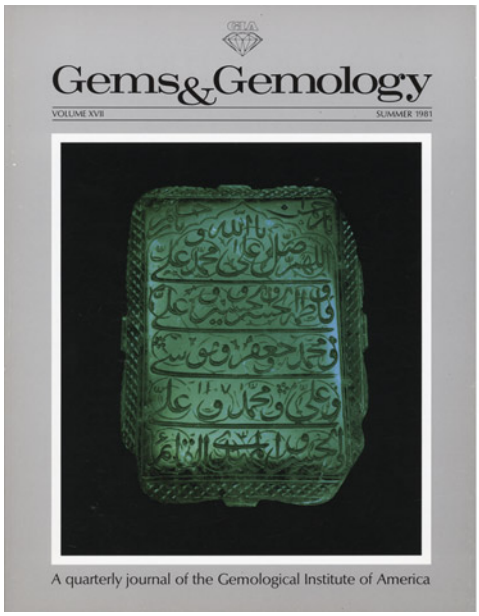

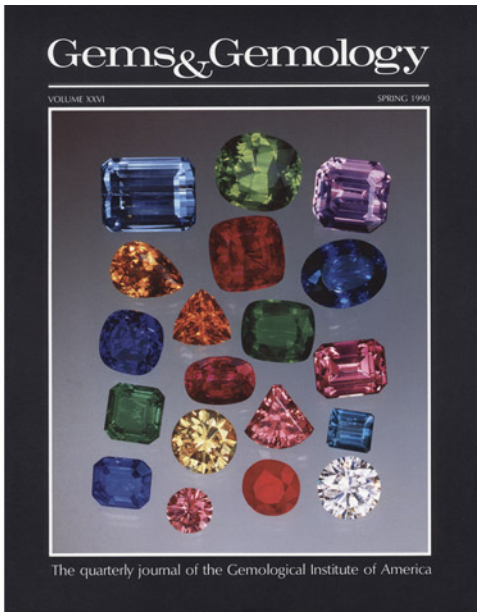

Figure 11. Left: The Van Pelts' first G&G cover (Summer 1981) featuring the 217.8 ct engraved Mogul emerald. Right: Taken in a single shot, these gemstones demonstrate the Van Pelts' ability to accurately capture color (Spring 1990). Photos by Harold & Erica Van Pelt.

ance by both the gem industry and the scientific community. Their first cover, the 217.8 ct Mogul emerald featured on the Summer 1981 issue (figure 11, left), and the many superb images they provided for Peter Keller's landmark article on Colombian emeralds in that issue, demonstrated that a scientific article could be beautiful and substantive at the same time.

While the Van Pelts published gem and mineral photos in numerous books and magazines during their career, their collaboration with *G&G* is one of their longest and, perhaps, most demanding professional relationships. Unlike images produced today, where gems are photographed individually and then composited into a single picture, they photographed multiple gems in a single shot. Their attention to lighting and color typically required many hours of setup for a single 8 × 10 transparency. Readers often commented that the accuracy of their color was unmatched in the field (figure 11, right).

More than a gifted photographer, Van was also an accomplished gem carver. Inspired by the museum collections seen during their world travels, he fashioned large pieces of rock crystal, agate, and other gem materials into exquisite objects that have been displayed at museums in the United States and Germany (figure 12). Using machinery he made or modified, he carved hundreds of items over 60-plus years.

We share our heartfelt condolences with Erica and Van's extended family, friends, and colleagues. May Van's legacy live on in the many extraordinary photos he and Erica produced—and in the beautiful objects he created—with skill, patience, and the eye of a true artist.

Alice Keller
Editor-in-Chief Emerita, Gems & Gemology

Dona Dirlam
GIA Librarian Emerita

Figure 12. The Winter 1982 cover depicts a quartz egg with an aquamarine and quartz base carved by Harold Van Pelt. The issue also includes an article detailing the techniques and equipment Van used to fashion the egg. Photo by Harold & Erica Van Pelt.